618-802

VOYAGER
IMAGING SCIENCE SUBSYSTEM
CALIBRATION REPORT

M. Benesh and P. Jepsen

July 31, 1978

Approved by:

F. E. Vescelus
Manager,
Space Photography Section

JET PROPULSION LABORATORY
CALIFORNIA INSTITUTE OF TECHNOLOGY
PASADENA, CALIFORNIA

ACKNOWLEDGMENTS

Calibration of the Voyager Imaging Science Subsystem (ISS) cameras was the result of well-organized teamwork. Many individuals participated in these activities and their dedicated efforts contributed significantly to the success of the calibration program. Their help and contributions are greatly appreciated by all concerned.

The authors wish to express their special appreciation to D. Norris and L. Snyder for their continued organizational and moral support, as well as to M. Brownell, A. Collins, G. Danielson, P. Kupferman, and F. Popescu, Voyager Imaging Science Experiment Representatives, for their scientific assistance.

Special thanks are due to members of the Calibration Team who were instrumental in obtaining the calibration data, sometimes under difficult and demanding conditions: L. Douglass, C. Kurzweil, D. Perrenoud, and S. Seng.

Particular acknowledgments are expressed to the Engineering Team under the coordinating direction of R. Lockhart for their unfailing technical assistance: L. Adams, G. Bailey, W. Cunningham, H. Enmark, C. Fondacaro, J. Genofsky, W. Magruder, E. Manning, D. Mullen, G. Perkins, W. Porter, W. Sleigh, and R. Steinkraus.

Last, but not least, the authors are indebted to the Image Processing Laboratory (IPL) personnel for their untiring support in data processing and analysis: C. Avis, G. Garneau, J. Gustavson, J. Kreznar, J. Lorre, D. Lynn, J. Mosher, R. Quiros, B. Wagie, and G. Yagi.

DEFINITION OF ABBREVIATIONS

ISS	Imaging Science Subsystem
IPL	Image Processing Laboratory (at JPL)
SAF	Spacecraft Assembly Facility (at JPL)
ETR	Eastern Test Range (at Cape Canaveral, Florida)
N/A	narrow-angle
W/A	wide-angle
BCE	bench checkout equipment
S/N	serial number
FDS	Flight Data Subsystem
D/C	dark current

CONTENTS

Figures

Figures

Figures

Figures

Figures

Figures

Figures

Figures

Figures

Tables

Tables

SECTION I

INTRODUCTION

This calibration report compiles the results of calibrations and tests performed on ISS cameras S/N 01 - S/N 08, which were designed and built for the Voyager mission to Jupiter and Saturn. A comprehensive analysis of the data obtained and a detailed discussion of their accuracy are also included. Brief descriptions of the methods, techniques, and equipment are provided so that the report can also be used as a convenient calibration manual for future space-flight projects.

The ultimate goal of this report is to provide information and data that will satisfy the basic purpose of the Voyager imaging experiment, which is to perform exploratory reconnaissance of Jupiter, Saturn, their satellites, and the rings of Saturn. The objective of ISS calibrations, then, was to define the characteristics of the instrument so that data obtained by it can be reliably interpreted without limitations because of uncertainties about instrumental performance.

The calibration program can be divided into four parts:

(a) Component calibrations.

(b) Subsystem calibrations (bench and thermal-vacuum chamber).

(c) System calibrations (SAF and ETR).

(d) In-flight calibrations.

Parts (a) and (b) are fully documented in this report. Part (c) is also described here, but it should be realized that system calibrations have been minimal for the Voyager project because of time and budgetary constraints. Part (d) will be performed several times between the launch and the encounter, and these calibration results will be discussed in a separate report. The in-flight calibrations are very important because they will verify and update the data contained in this document and will enable the IPL to finalize the ISS calibration program.

Every effort has been made to include all substantial and important calibration results, but a great deal of supplementary data has been omitted to reduce this document to a size technically and economically feasible for publication. These data have been filed at JPL and can be made available to all users upon request to the Voyager Project Representative.

A number of abbreviations are used throughout this report. Most of them are widely known or self-explanatory, but it may be beneficial for the user to become familiar with them before attempting to read the report (see "Definition of Abbreviations" on page iv).

The ISS cameras S/N 01 - S/N 08 were assigned and reassigned several times to different spacecraft in the months preceding the launch. To simplify the results, all calibration data in this report are listed consistently by the ISS camera serial number (S/N). The Voyager ISS component and camera assignment is then explained in Table 1-1.

Table 1-1. Voyager-ISS component and camera assignment

ISS Camera S/N	Optics S/N	Filter Wheel S/N	Shutter S/N	Camera Head S/N	Vidicon S/N	Electron-ics S/N	SAF Spacecraft	ETR Spacecraft	Scan Platform S/N	Spacecraft S/N	Mission ID	Launch Date	Spacecraft Trajectory Name
01	NAO-2	003	005	001	155 1341	001	Prototype						
02	WAO-3	004	004	002	155 1342	002	Prototype						
03	NAO-3	005	007	003	115 9880	003	Flight 1	Spare					
04	WAO-4	006	006	004	305 2719	004	Flight 1	Flight 2	002	VGR77-3	Voyager 2	8/20/77	JSX
05	NAO-4	007	009	005	225 1901	005	Flight 2	Flight 2	002	VGR77-3	Voyager 2	8/20/77	JSX
06	WAO-6	010	012	006	115 9903	006	Flight 3	Flight 1	003	VGR77-2	Voyager 1	9/5/77	JST
07	NAO-5	009	011	007	165 1402	007	Flight 3	Flight 1	003	VGR77-2	Voyager 1	9/5/77	JST
08	WAO-5	008	008	008	165 1407	008	Flight 2	Spare					

SECTION II

SUPPORT EQUIPMENT

Successful implementation of all Voyager ISS tests and calibrations required by Reference 2-1 necessitated utilization of a complex support equipment, which included the bench checkout equipment (BCE), the JPL light cannons, several collimators, and a set of specially designed targets. Their purpose and technical mode of application are described in this section.

A. BENCH CHECKOUT EQUIPMENT

The BCE[1] provides a means of functional testing and calibration of the Voyager-ISS cameras. (For detailed description and information about the BCE, see Reference 2-2.) The BCE consists of three basic units: the tape recorder, the processor/simulator, and the monitor (see Figure 2-1). A commercial automatic card reader, which is not shown in Figure 2-1, was also connected to the BCE.

The BCE tape recorder is a commercial unit which received IBM-compatible formatted information on a nine-track magnetic tape at 95.25 cm/s. The tape transport unit has both a read and write capability. The maximum number of frames that can be recorded on a single tape is 20. All ISS calibration procedures had to comply with this constraint.

A printer is mounted below the tape unit. This printer continuously prints all kinds of input and output data, as well as the most critical engineering parameters. During ISS calibrations, the printout proved to be valuable for troubleshooting, verification, and various other purposes.

The BCE processor/simulator was used for sending commands such as shutter speed, filter-wheel position, camera mode, frame scan rate, low/high gain, light-flood on/off, etc., to the tested ISS cameras. In this respect, the Voyager-ISS BCE was similar to that of previous space missions. However, it did have two new useful features; namely, the temperature indicators of various camera components and the pixel average video-signal indicator for any selected area.

The main unit of the BCE monitor is a commercial high-resolution television video monitor which mounts in a standard 48-cm rack. The monitor is a fully solid-state, 43-cm diagonal monitor with 1000-TV line resolution and 33-mHz bandwidth. The video display format consists not only of the frame picture itself, but also of various test data and a

---

[1] Designed and manufactured by Xerox Electro-Optical Systems, Pasadena, California from components supplied by various manufacturers.

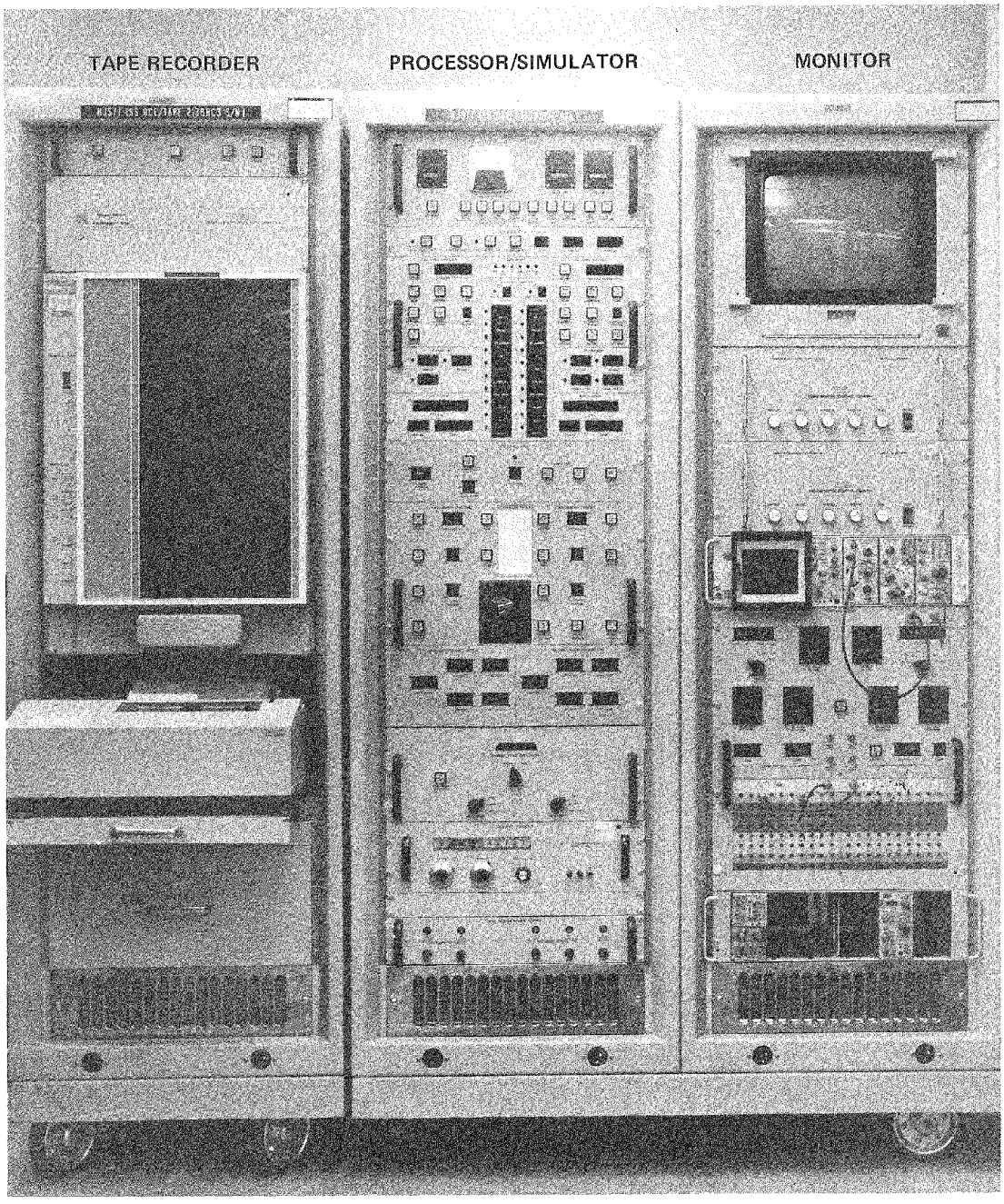

Figure 2-1. Voyager-ISS bench checkout equipment (BCE)

video data histogram, as indicated in Figure 2-2. A Tektronix Model C-53 camera could be attached to the video monitor by means of specially designed mounting bracketry, thus providing the capability of photographing the video monitor display during normal test operations.

An oscilloscope is mounted in the center part of the BCE monitor. A Polaroid camera, also provided as part of the BCE equipment, records the oscilloscope images. Both the video monitor described above and the oscilloscope were extensively used for planning and verification of the ISS calibration procedures.

The BCE card reader (not shown in Figure 2-1) can be used to supply automatic control of the BCE. Cards can be programmed to set the BCE test switches or to provide a video test pattern through the BCE for testing its various video-oriented functions. With the exception of a few emergencies, when manual control had to be used, all ISS calibrations were performed in the automatic mode using the card reader. This automation resulted in an outstanding repeatability of all tests and calibrations, and it also enabled an excellent on-line data recording and analysis.

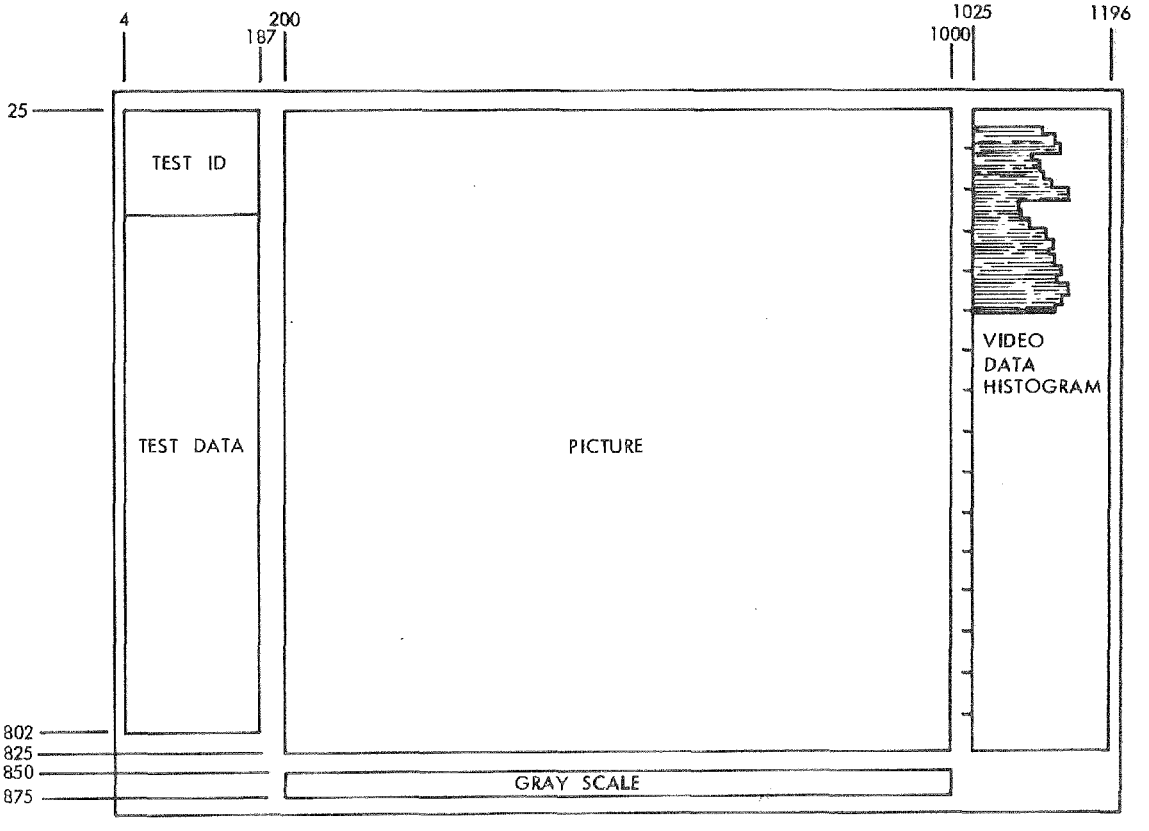

Figure 2-2. BCE video display format

B. LIGHT CANNONS

Three different JPL light cannons were used as light sources for ISS calibrations:

(1) The 30-cm light cannon No. 1 (Figure 2-3) for various radiometric calibrations of the narrow-angle cameras.

(2) The 30-cm light cannon No. 2 for illumination of targets in the Fairchild collimator (see Section II-C and -D). This light cannon is almost identical to light cannon No. 1, except for a shorter cone and different spectral irradiance characteristics.

(3) The 13-cm light cannon (Figure 2-4) for various radiometric calibrations of the wide-angle cameras.

Each of the two 30-cm light cannons is equipped with two 1600-W xenon high-pressure arc discharge lamps in an integrating cavity, a variable iris diaphragm for brightness regulation, a second conical integrating cavity, and finally, a 30-cm neutral plexiglass diffuser. Two 2000-W power supplies are required for operation of each of these light cannons. The 13-cm light cannon is considerably smaller, has only one lamp, and requires only one power supply.

1. Spectral Curves

The spectral irradiance of all three light cannons was measured for comparison of the calibration data, particularly the light transfer curves. The light cannon irradiance was compared on the JPL spectroradiometer to that of a 200-W quartz iodine spectral irradiance standard. Three reference standards of the National Bureau of Standards were used to calibrate the standard itself. The spectral curves, which were obtained at a 100-fL brightness, are shown in Figures 2-5(a) and (b) through 2-7. The approximate color temperature of the spectral irradiance standard was 3000 K and of the light cannon, 5600 K, i.e., similar to that of the Sun.

Spectral curves of three 100-fL standards, which were used for absolute brightness calibration of the light cannons (Section II-B-3), were also measured in a similar way. These results are documented in Figures 2-8 through 2-10.

Some users may prefer numerical data for computer applications and, for this purpose, all spectral curves were summarized in Tables 2-1 and 2-2.

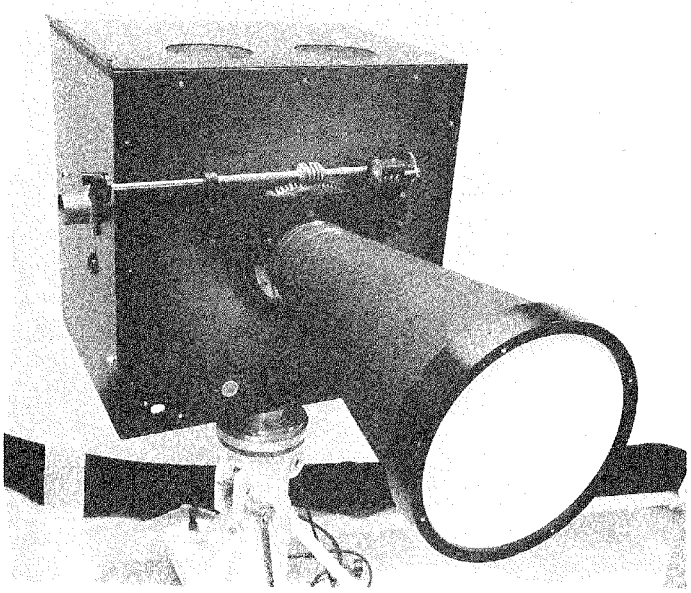

Figure 2-3. JPL 30-cm light cannon No. 1

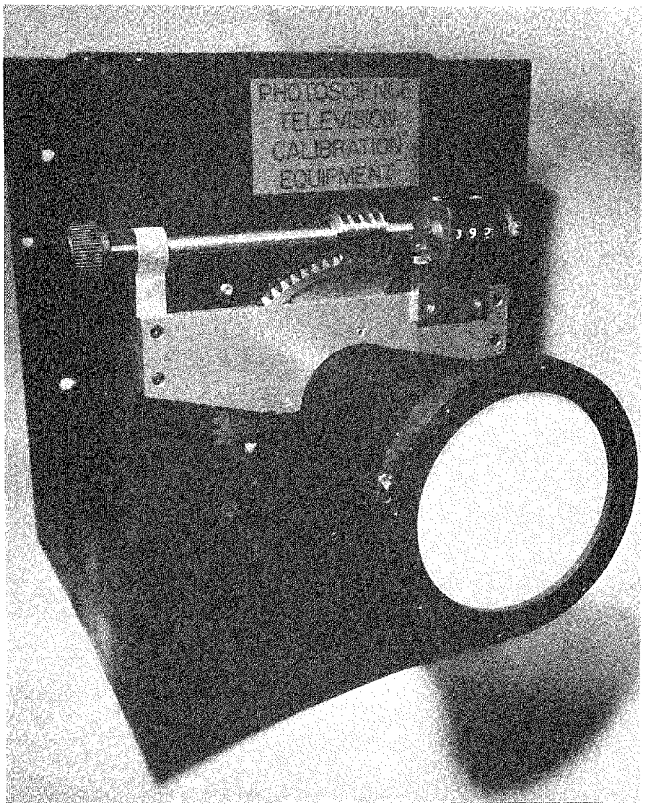

Figure 2-4. JPL 13-cm light cannon

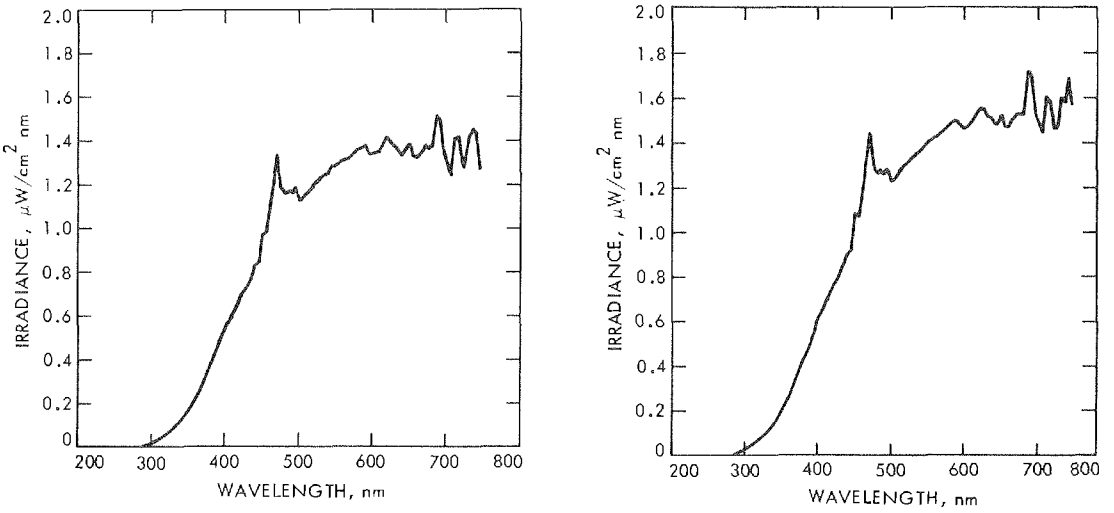

Figure 2-5. Spectral curve of the 30-cm light cannon No. 1: (a) old lamps until February 4, 1977, (b) new lamps from February 4, 1977

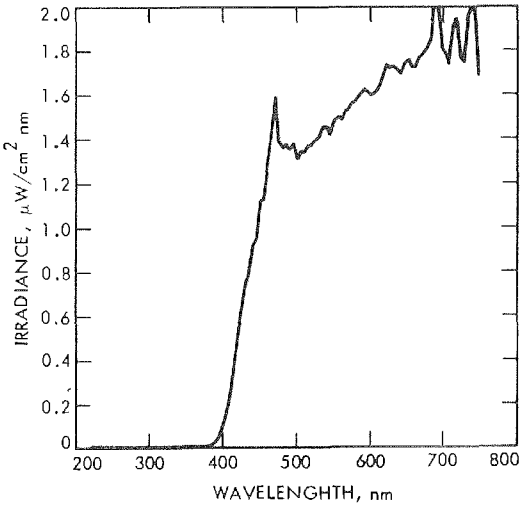

Figure 2-6. Spectral curve of the 30-cm light cannon No. 2

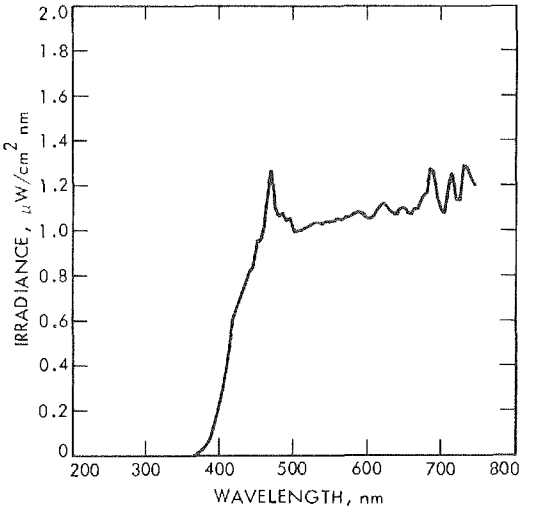

Figure 2-7. Spectral curve of the 13-cm light cannon

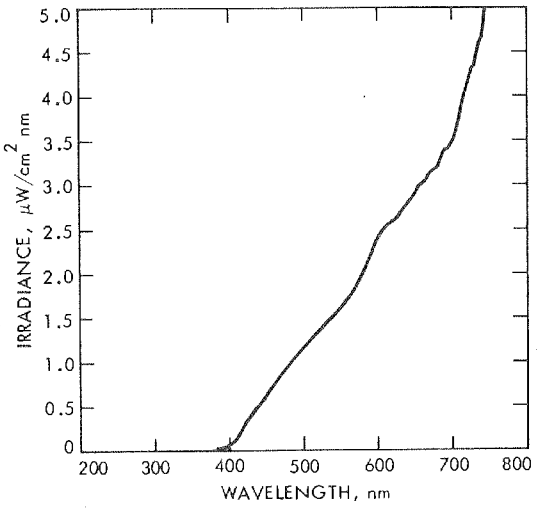

Figure 2-8. Spectral curve of the 100-fL standard No. 152

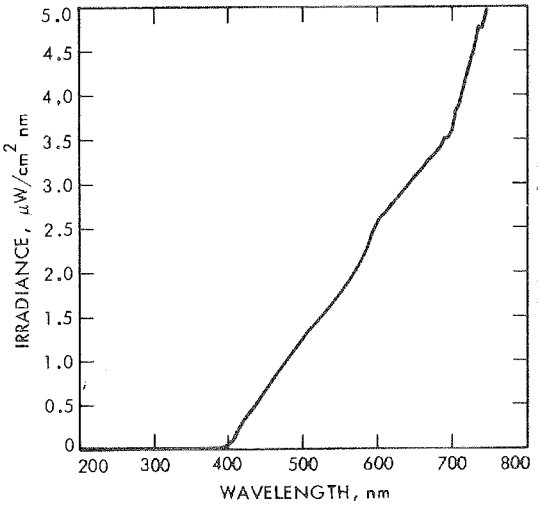

Figure 2-9. Spectral curve of the 100-fL standard No. 185

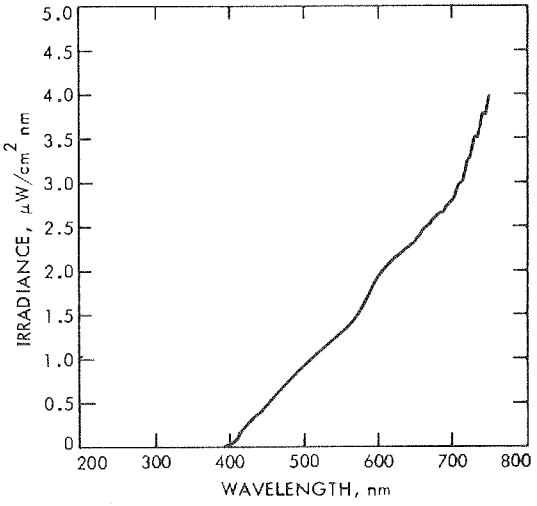

Figure 2-10. Spectral curve of the 100-fL standard No. 531

Table 2-1. Spectral irradiance of JPL light cannons

Wavelength, nm	Spectral irradiance, $\mu W/cm^2$ nm			
	30-cm light cannon No. 1 (old lamps)	30-cm light cannon No. 1 (new lamps)	30-cm light cannon No. 2	13-cm light cannon
200	0.0000	0.0000		0.0000
205	0.0001	0.0000		0.0001
210	0.0000	0.0003		0.0002
215	0.0002	0.0003	0.0001	0.0005
220	0.0001	0.0001	0.0003	0.0002
225	0.0002	0.0001	0.0002	0.0001
230	0.0001	0.0001	0.0001	0.0002
235	0.0000	0.0001	0.0002	0.0001
240	0.0000	0.0001	0.0002	0.0001
245	0.0000	0.0000	0.0002	0.0001
250	0.0000	0.0001	0.0002	0.0001
255	0.0001	0.0001	0.0003	0.0001
260	0.0000	0.0003	0.0005	0.0001
265	0.0001	0.0002	0.0005	0.0001
270	0.0002	0.0005	0.0005	0.0001
275	0.0004	0.0015	0.0005	0.0001
280	0.0011	0.0030	0.0006	0.0002
285	0.0021	0.0058	0.0004	0.0001
290	0.0047	0.0109	0.0005	0.0001
295	0.0075	0.0169	0.0004	0.0001
300	0.0119	0.0248	0.0003	0.0000
305	0.0178	0.0356	0.0003	0.0000
310	0.0264	0.0462	0.0003	0.0000
315	0.0352	0.0591	0.0003	0.0000
320	0.0461	0.0729	0.0003	0.0000
325	0.0579	0.0882	0.0003	0.0000
330	0.0736	0.1060	0.0002	0.0001
335	0.0883	0.1257	0.0003	0.0000
340	0.1090	0.1472	0.0003	0.0000
345	0.1313	0.1707	0.0003	0.0001
350	0.1529	0.1961	0.0002	0.0001
355	0.1778	0.2291	0.0002	0.0003
360	0.2105	0.2615	0.0003	0.0009
365	0.2501	0.3027	0.0004	0.0023
370	0.2855	0.3443	0.0009	0.0060
375	0.3224	0.3869	0.0026	0.0139
380	0.3672	0.4312	0.0064	0.0289
385	0.4086	0.4696	0.0144	0.0521
390	0.4528	0.5202	0.0301	0.0895

Table 2-1 (contd)

Wavelength, nm	Spectral irradiance, $\mu W/cm^2$ nm			
	30-cm light cannon No. 1 (old lamps)	30-cm light cannon No. 1 (new lamps)	30-cm light cannon No. 2	13-cm light cannon
395	0.5086	0.5806	0.0582	0.1505
400	0.5465	0.6148	0.1009	0.2214
405	0.5675	0.6398	0.1643	0.3057
410	0.6094	0.6822	0.2643	0.4102
415	0.6413	0.7166	0.3945	0.5168
420	0.6868	0.7688	0.5431	0.6214
425	0.7054	0.7797	0.6248	0.6768
430	0.7301	0.8050	0.7577	0.7204
435	0.7706	0.8425	0.7879	0.7724
440	0.8270	0.9014	0.9147	0.8228
445	0.8475	0.9205	0.9527	0.8375
450	0.9676	1.0840	1.1230	0.9608
455	0.9815	1.0666	1.1362	0.9537
460	1.0758	1.1695	1.2613	1.0288
465	1.2311	1.3237	1.4451	1.1813
470	1.3352	1.4450	1.5943	1.2724
475	1.1831	1.2944	1.3858	1.0939
480	1.1571	1.2620	1.3597	1.0584
485	1.1679	1.2803	1.3823	1.0761
490	1.1622	1.2606	1.3534	1.0412
495	1.1871	1.2885	1.3886	1.0518
500	1.1227	1.2185	1.3079	0.9912
505	1.1431	1.2468	1.3432	0.9952
510	1.1584	1.2635	1.3413	0.9964
515	1.1758	1.2864	1.3794	1.0065
520	1.2027	1.2986	1.3831	1.0155
525	1.2167	1.3229	1.4027	1.0251
530	1.2344	1.3457	1.4168	1.0297
535	1.2443	1.3528	1.4602	1.0293
540	1.2564	1.3726	1.4582	1.0253
545	1.2826	1.3912	1.4155	1.0386
550	1.2848	1.3991	1.4890	1.0386
555	1.3014	1.4156	1.5114	1.0404
560	1.3098	1.4203	1.4893	1.0501
565	1.3169	1.4357	1.5378	1.0427
570	1.3245	1.4558	1.5467	1.0568
575	1.3405	1.4577	1.5745	1.0590
580	1.3608	1.4752	1.5828	1.0639
585	1.3687	1.4952	1.6075	1.0801

Table 2-1 (contd)

Wavelength, nm	Spectral irradiance, $\mu W/cm^2$ nm			
	30-cm light cannon No. 1 (old lamps)	30-cm light cannon No. 1 (new lamps)	30-cm light cannon No. 2	13-cm light cannon
590	1.3757	1.5003	1.6294	1.0817
595	1.3352	1.4683	1.6178	1.0694
600	1.3390	1.4638	1.5981	1.0516
605	1.3459	1.4717	1.6080	1.0512
610	1.3526	1.4983	1.6293	1.0647
615	1.3822	1.5351	1.6814	1.0990
620	1.4127	1.5543	1.7442	1.1220
625	1.3873	1.5452	1.7261	1.1111
630	1.3748	1.5140	1.7314	1.0874
635	1.3549	1.5069	1.7125	1.0716
640	1.3264	1.4687	1.6938	1.0651
645	1.3641	1.5101	1.7450	1.1005
650	1.3828	1.5271	1.7645	1.1024
655	1.3264	1.4604	1.7254	1.0706
660	1.3211	1.4736	1.7294	1.0684
665	1.3373	1.5114	1.7709	1.1024
670	1.3767	1.5190	1.7894	1.1052
675	1.3567	1.5389	1.8188	1.1476
680	1.3853	1.5427	1.8616	1.1695
685	1.5163	1.7211	2.0530	1.2826
690	1.4916	1.6934	2.0551	1.2612
695	1.3507	1.5241	1.8167	1.1347
700	1.2871	1.4783	1.7860	1.0812
705	1.2341	1.4410	1.7423	1.0699
710	1.4115	1.6083	1.9169	1.1982
715	1.4219	1.5907	1.9619	1.2581
720	1.3101	1.4517	1.7730	1.1384
725	1.2724	1.4747	1.7469	1.1266
730	1.4081	1.6029	1.9636	1.2885
735	1.4518	1.5710	2.0000	1.2845
740	1.4377	1.6891	1.9886	1.2309
745	1.2699	1.5676	1.6849	1.1994

Table 2-2. Spectral irradiance of JPL 100-fL standards

Wavelength, nm	Spectral irradiance, $\mu W/cm^2$ nm		
	100-fL standard No. 152	100-fL standard No. 185	100-fL standard No. 531
200	0.0000	0.0000	0.0000
205	0.0000	0.0000	0.0000
210	0.0000	0.0001	0.0000
215	0.0001	0.0001	0.0001
220	0.0000	0.0002	0.0002
225	0.0001	0.0000	0.0000
230	0.0001	0.0001	0.0001
235	0.0001	0.0002	0.0000
240	0.0000	0.0000	0.0001
245	0.0002	0.0000	0.0001
250	0.0001	0.0000	0.0000
255	0.0001	0.0000	0.0001
260	0.0000	0.0001	0.0001
265	0.0001	0.0000	0.0000
270	0.0000	0.0000	0.0000
275	0.0000	0.0000	0.0000
280	0.0000	0.0001	0.0000
285	0.0000	0.0000	0.0000
290	0.0001	0.0001	0.0000
295	0.0000	0.0000	0.0001
300	0.0000	0.0000	0.0000
305	0.0000	0.0000	0.0000
310	0.0000	0.0000	0.0000
315	0.0000	0.0000	0.0001
320	0.0000	0.0001	0.0000
325	0.0000	0.0001	0.0000
330	0.0001	0.0000	0.0000
335	0.0000	0.0000	0.0000
340	0.0000	0.0000	0.0000
345	0.0000	0.0000	0.0001
350	0.0000	0.0000	0.0000
355	0.0000	0.0000	0.0000
360	0.0000	0.0000	0.0000
365	0.0001	0.0001	0.0000
370	0.0003	0.0003	0.0002
375	0.0008	0.0010	0.0006
380	0.0021	0.0025	0.0016
385	0.0045	0.0055	0.0033

Table 2-2 (contd)

Wavelength, nm	Spectral irradiance, $\mu W/cm^2$ nm		
	100-fL standard No. 152	100-fL standard No. 185	100-fL standard No. 531
390	0.0092	0.0114	0.0071
395	0.0177	0.0222	0.0143
400	0.0339	0.0411	0.0277
405	0.0663	0.0785	0.0545
410	0.1244	0.1420	0.1009
415	0.2031	0.2251	0.1622
420	0.2819	0.3034	0.2236
425	0.3463	0.3662	0.2735
430	0.3995	0.4228	0.3131
435	0.4493	0.4720	0.3517
440	0.4944	0.5247	0.3891
445	0.5479	0.5757	0.4301
450	0.6068	0.6400	0.4777
455	0.6592	0.6989	0.5213
460	0.7222	0.7596	0.5683
465	0.7826	0.8252	0.6148
470	0.8392	0.8836	0.6648
475	0.8958	0.9470	0.7109
480	0.9439	1.0007	0.7521
485	1.0029	1.0584	0.7967
490	1.0474	1.1172	0.8388
495	1.1011	1.1728	0.8829
500	1.1483	1.2282	0.9229
505	1.2034	1.2824	0.9661
510	1.2473	1.3309	1.0020
515	1.2895	1.3702	1.0322
520	1.3247	1.4205	1.0726
525	1.3771	1.4738	1.1098
530	1.4053	1.5111	1.1393
535	1.4488	1.5562	1.1782
540	1.4881	1.6054	1.2074
545	1.5461	1.6664	1.2580
550	1.5931	1.7231	1.2986
555	1.6383	1.7748	1.3367
560	1.7069	1.8471	1.3935
565	1.7665	1.9118	1.4399
570	1.8365	1.9813	1.4928
575	1.9073	2.0563	1.5538

Table 2-2 (contd)

Wavelength, nm	Spectral irradiance, $\mu W/cm^2$ nm		
	100-fL standard No. 152	100-fL standard No. 185	100-fL standard No. 531
580	1.9941	2.1518	1.6262
585	2.0752	2.2398	1.6998
590	2.1729	2.3460	1.7763
595	2.2739	2.4377	1.8527
600	2.3736	2.5444	1.9331
605	2.4481	2.6347	1.9881
610	2.5088	2.6795	2.0411
615	2.5512	2.7299	2.0812
620	2.5853	2.7882	2.1245
625	2.6138	2.8236	2.1625
630	2.6528	2.8664	2.1871
635	2.7255	2.9271	2.2444
640	2.7827	2.9758	2.2844
645	2.8358	3.0244	2.3062
650	2.9021	3.0883	2.3642
655	2.9696	3.1371	2.4250
660	2.9856	3.1852	2.4693
665	3.0523	3.2456	2.5205
670	3.1266	3.3078	2.5547
675	3.1749	3.3516	2.6269
680	3.1934	3.3749	2.6476
685	3.2971	3.4404	2.6751
690	3.4033	3.5266	2.7481
695	3.4012	3.5177	2.7879
700	3.4850	3.5909	2.8409
705	3.6292	3.8248	2.9735
710	3.7929	3.9109	3.0115
715	3.9849	4.0574	3.2019
720	4.1551	4.2371	3.2778
725	4.3104	4.4143	3.5207
730	4.3412	4.5203	3.5112
735	4.5973	4.7808	3.7908
740	4.6898	4.7471	3.7554
745	5.0699	4.9656	3.9978

2. Field Flatness

The field flatness (brightness distribution) across the plexiglass diffuser of the JPL light cannons was measured using the Gamma model 700 photometer at 12.5-mm intervals in a cross pattern, in both the horizontal and the vertical direction. All three light cannons were measured at three different light levels. The results are shown in Figures 2-11(a), (b), and (c); 2-12(a), (b), and (c); and 2-13(a), (b), and (c). The curves may seem to be rather poor, but their effect upon radiometric calibrations, especially as it pertains to shading, is insignificant for reasons described below.

The 30-cm light cannon No. 1 and the 13-cm light cannon (Figures 2-11 and 2-13) were always carefully aligned within ±5 mm with the boresight axis at a distance of approximately 30 mm from the ISS camera. In this position, the diffuser was out of focus, which meant that each light-source point was blurred across a large part of the vidicon faceplate. The net result then, was an extremely flat field illumination in the image plane. Also, because of the secondary mirror center obscuration, the narrow-angle camera can see only an annulus of diameter between 89 and 181 mm, as indicated in the upper portion of Figure 2-11.

The 30-cm light cannon No. 2 (Figure 2-12) presents a somewhat different story. In this instance, both the tested narrow-angle camera and the light cannon were always aligned with the optical axis of the Fairchild collimator (see Section II-C), which means that the light cannon shading was more or less in focus and collimated. However, the vidicon could see only an area of approximately 35 x 35 mm in the target plane (including the camera obscuration), where the illumination is very flat. Moreover, field flatness is not so critical for imaging as it is for radiometric calibrations.

3. Brightness Calibration

The success of radiometric calibrations is dependent, to a large degree, upon the reliability of the light cannons to produce consistent illumination levels over an extended period of time. Therefore, the light cannons were equipped with a variable iris mechanism and a Veeder root counter, which allow regulation of the iris diameter (see Figures 2-14 and 2-15. To determine the Veeder root-brightness relationship, a calibration variable transmittance standard of the crossed polarizer type was used in combination with the Gamma 700 photometer, as shown schematically in Figure 2-14. Based on the method of constant output, the resulting Veeder-root count versus inverse-filter transmittance was plotted on a log-log paper, forming the light cannon relative brightness curve.

The Veeder root counts are linearly proportional to the iris diameter and, hence, to the square root of the light generated in the second conical integrating cavity; however, the zero point on the dial usually does not correspond to a fully closed iris. This absolute

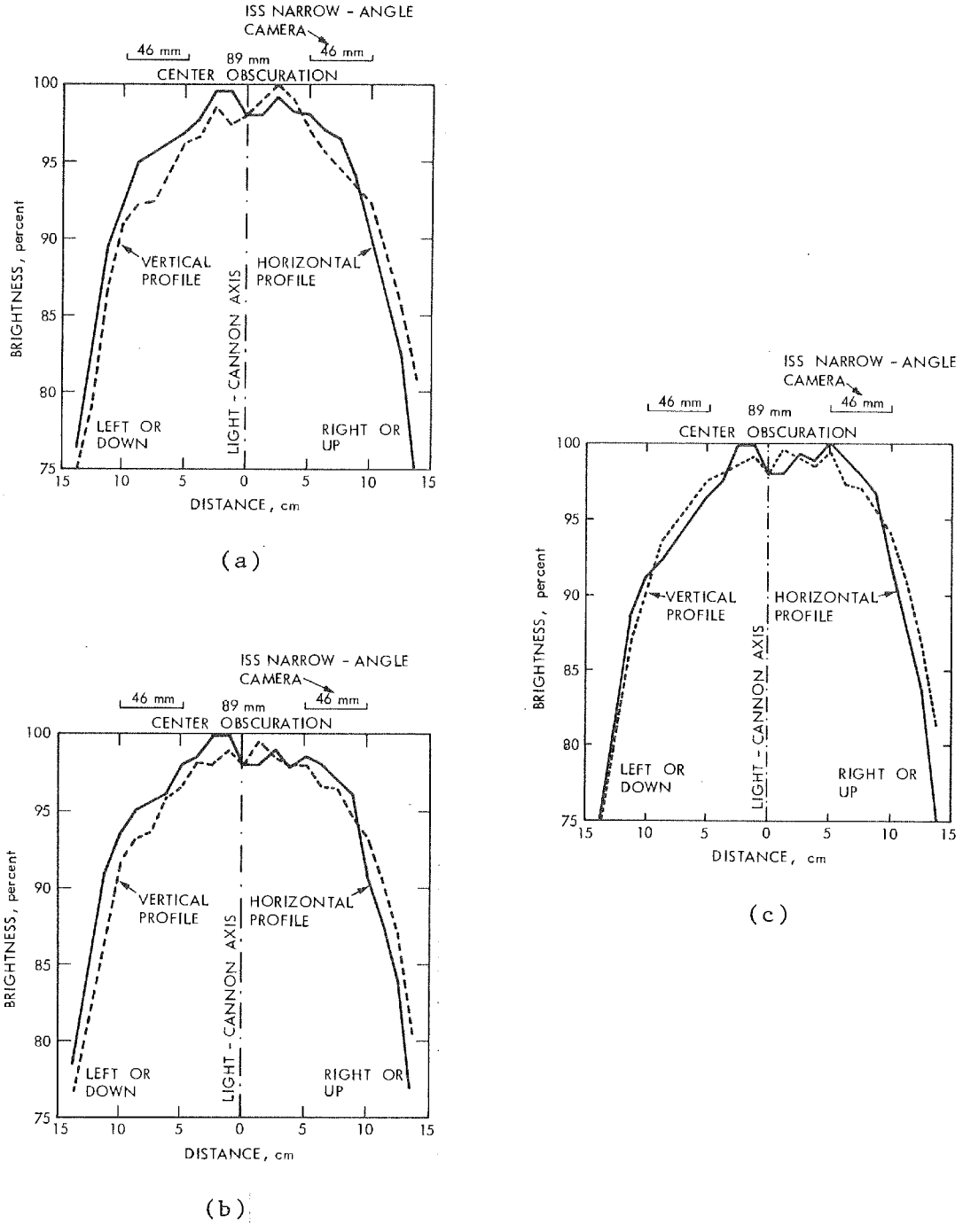

Figure 2-11. Field flatness of the 30-cm light cannon No. 1: (a) 100 fL, (b) 500 fL, (c) 1000 fL

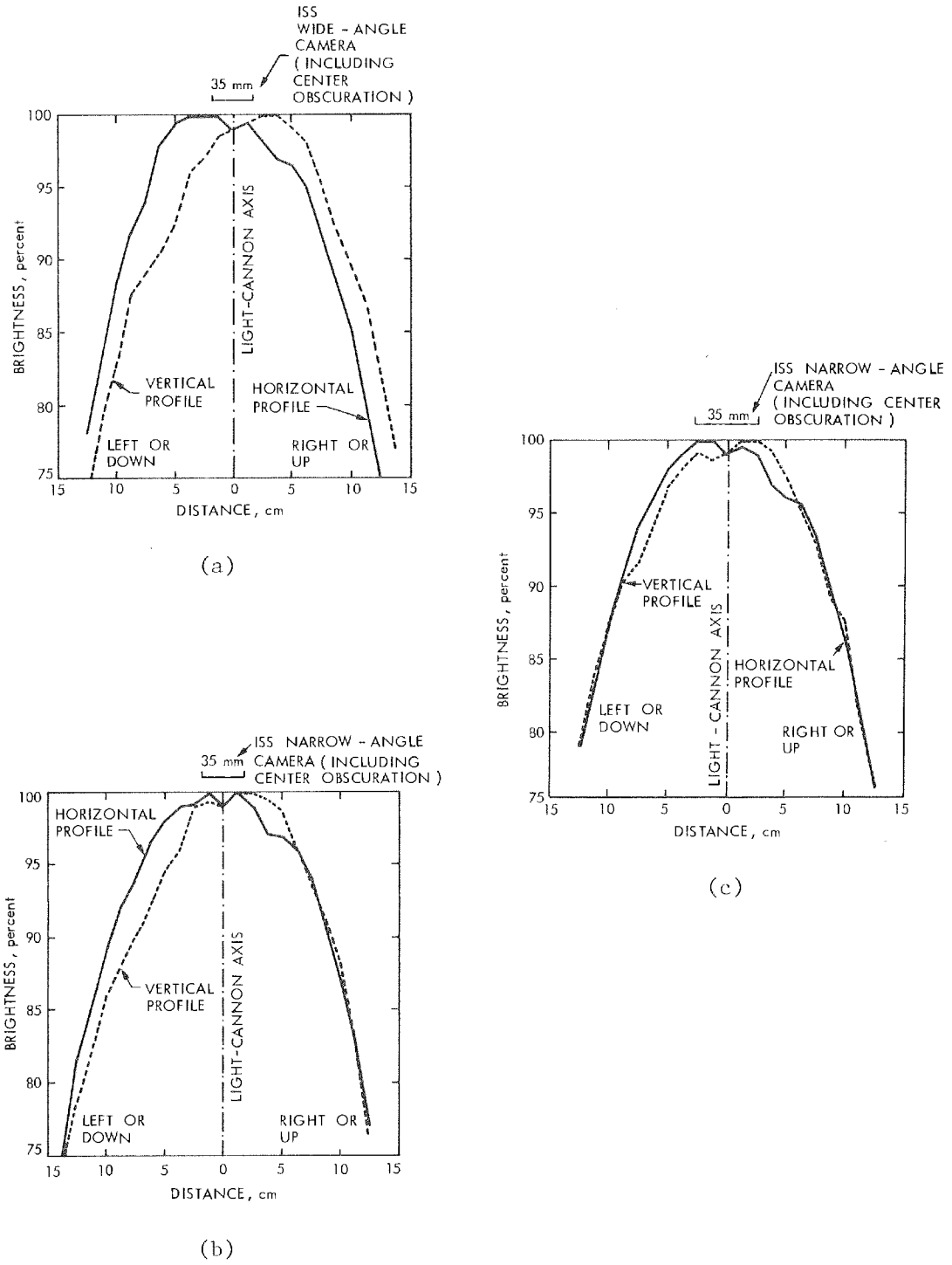

Figure 2-12. Field flatness of the 30-cm light cannon No. 2: (a) 100 fL, (b) 500 fL, (c) 1000 fL

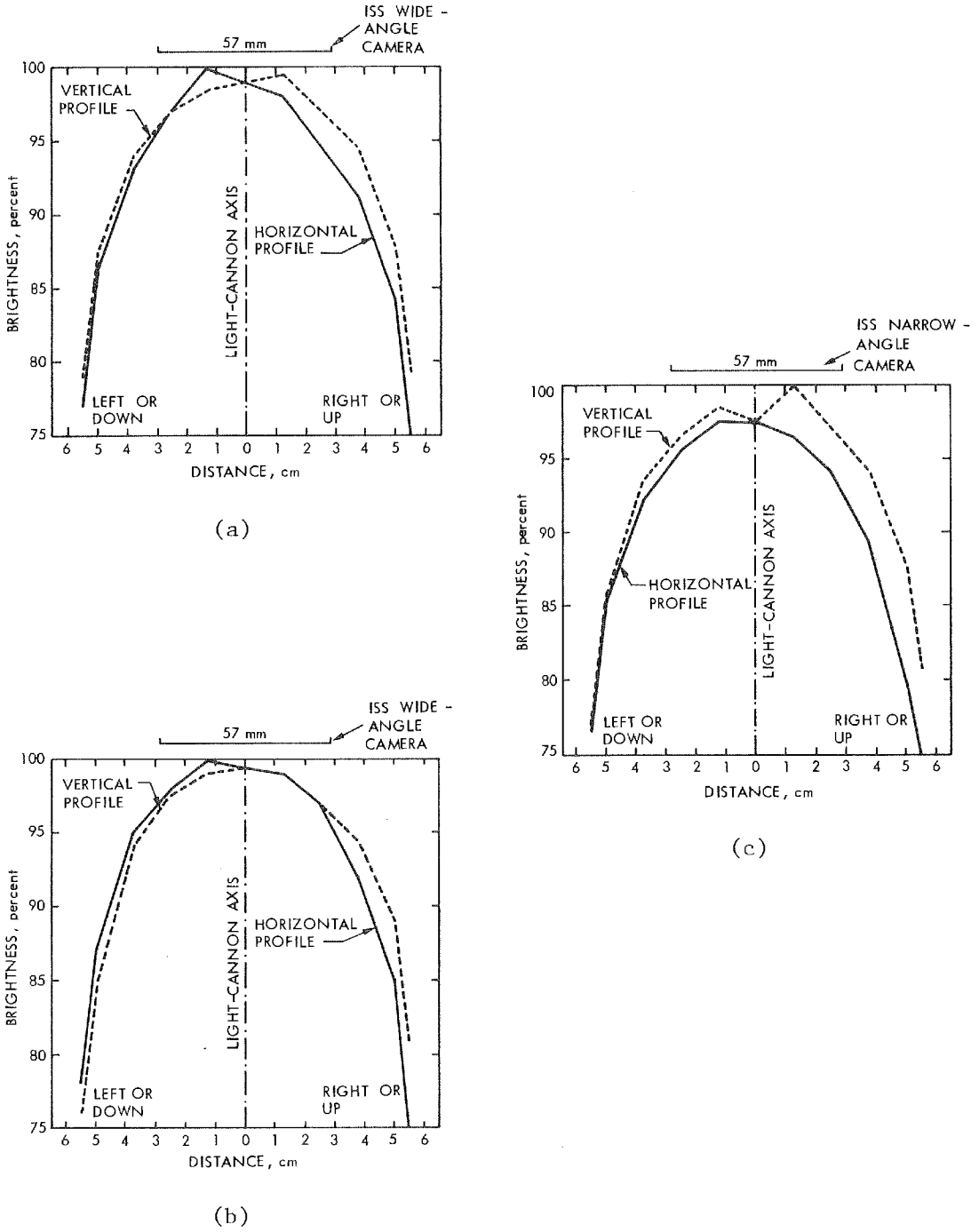

Figure 2-13. Field flatness of the 13-cm light cannon: (a) 100 fL, (b) 500 fL, (c) 1000 fL

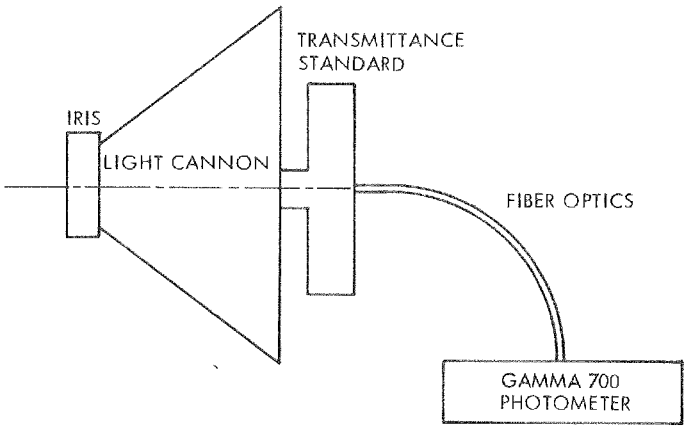

Figure 2-14. Relative brightness calibration of a JPL light cannon

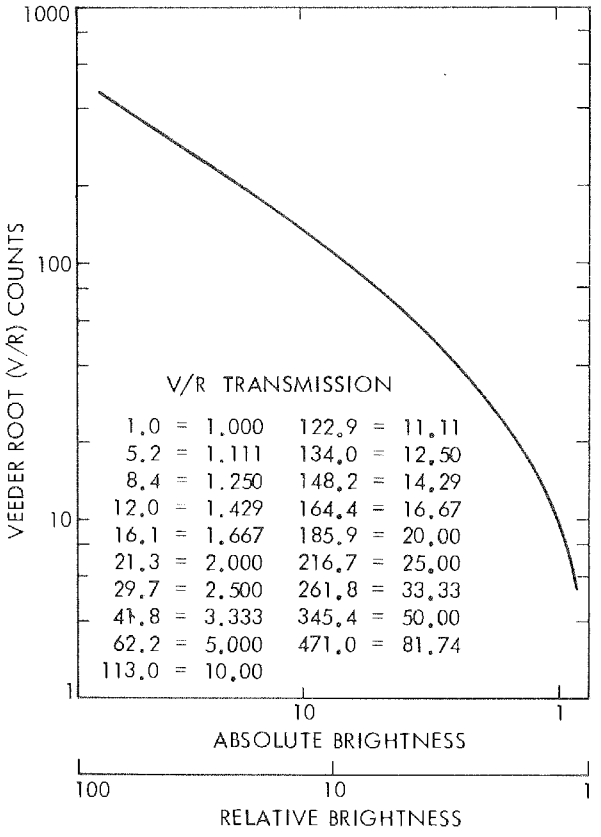

Figure 2-15. A typical light cannon brightness-calibration curve

scaling had to be determined by comparing the light cannon output with a known 100-fL light standard source by using a Gamma scientific telephotometer, model 2000. A typical light-cannon calibration curve, showing both the relative and absolute scales, is presented in Figure 2-15.

Although the relative brightness curve remained fairly constant throughout the ISS calibrations, it was checked regularly every third month. However, determination of the absolute brightness scale required constant attention because of the considerable drift in the brightness Veeder-root-count relationship.

Therefore, the absolute brightness scale was reestablished by using the telephotometer in connection with the 100-fL light standard at the beginning and end of each calibration, and by applying linear interpolation between these two readings. In the case of the wide-angle cameras, the center point of the plexiglass diffuser was used for this purpose; but, considering the center obscuration of the ISS narrow-angle cameras, two points lying at a 50-mm distance from the axis were measured. The projected field of view of the telephotometer on the diffuser was between 7 and 11 mm in diameter, depending upon its distance from the light cannon.

The precautions and techniques described above have allowed a consistent series of radiometric measurements over the entire ISS calibration phase. The limiting accuracy of the light cannon output was a function of random variations of the 100-fL light standards (up to ±2%) and also by the backlash of the variable iris mechanism, which results in an approximate ±0.5-Veeder-root-count accuracy, or in terms of brightness, ±1.6% at 100 fL to ±0.4% at 5000 fL.

C. COLLIMATORS

Six different types of collimators were used for ISS imaging calibrations, such as geometric distortion, beam bending, modulation transfer function, point response function, color reconstruction, and the special gray-scale target test. Three types of collimators were designed and built for the narrow-angle cameras and three for the wide-angle cameras.

The narrow-angle-camera bench calibrations utilized the traditional Fairchild collimator (Figure 2-16), which is located in the JPL optical tunnel, where its axis is aligned with the axis of the Askania optical bench (see Section II-E). However, for the Voyager project, the Fairchild collimator was thoroughly cleaned and completely rebuilt, thereby considerably increasing its optical quality: transmission was increased from 3 to 14%, shading became negligible, and optical distortion was reduced to practically zero. The absolute spectral transmittance of the Fairchild collimator, which was used for data analysis of certain imaging frames (particularly for color reconstruction), is shown in Figure 2-17 and listed in Table 2-3.

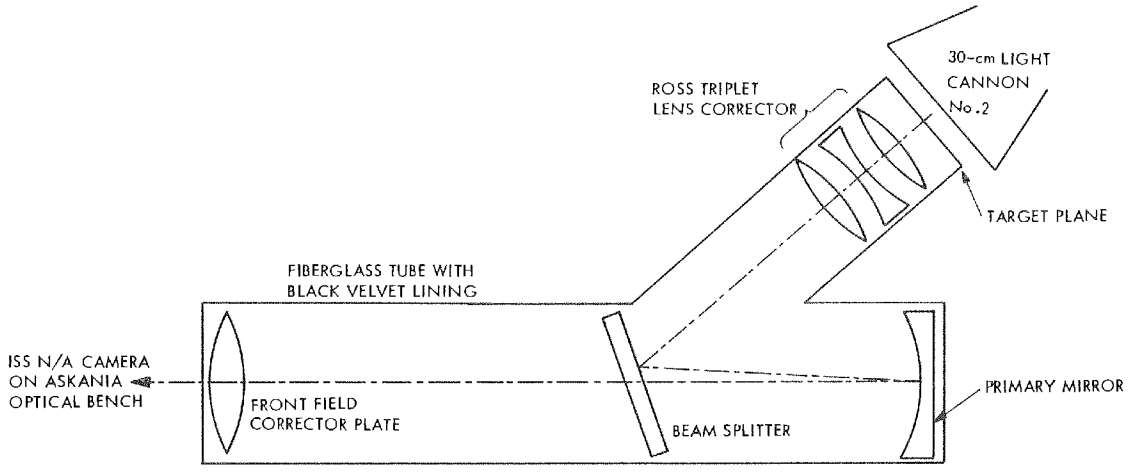

Figure 2-16. JPL Fairchild collimator (schematic, not drawn to scale)

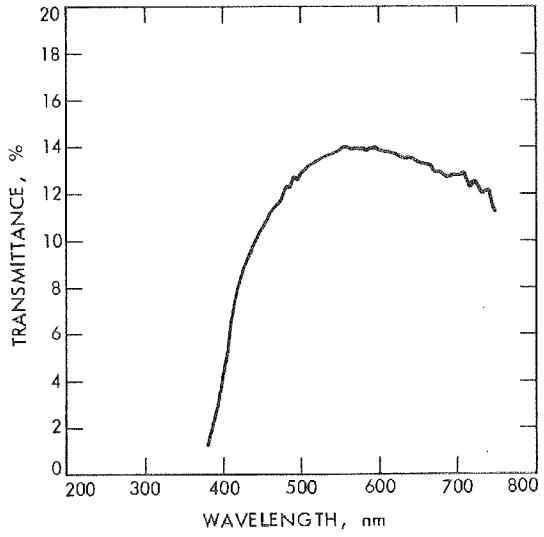

Figure 2-17. Absolute spectral transmittance of the Fairchild collimator

Table 2-3. Absolute spectral transmittance of the Fairchild collimator

Wavelength, nm	Spectral Transmittance, %	Wavelength, nm	Spectral Transmittance, %
380	1.16	565	13.89
385	1.80	570	13.96
390	2.37	575	13.87
395	3.10	580	13.90
400	4.07	585	13.80
405	5.10	590	13.99
410	6.17	595	13.90
415	7.09	600	13.84
420	7.90	605	13.82
425	8.46	610	13.77
430	9.07	615	13.75
435	9.44	620	13.63
440	9.82	625	13.62
445	10.29	630	13.52
450	10.61	635	13.51
455	10.87	640	13.52
460	11.23	645	13.42
465	11.44	650	13.30
470	11.50	655	13.29
475	11.75	660	13.21
480	12.28	665	13.15
485	12.21	670	12.89
490	12.71	675	12.94
495	12.53	680	12.80
500	12.93	685	12.77
505	13.05	690	12.66
510	13.21	695	12.82
515	13.28	700	12.75
520	13.43	705	12.76
525	13.49	710	12.92
530	13.60	715	12.21
535	13.69	720	12.47
540	13.74	725	12.37
545	13.80	730	11.93
550	13.84	735	12.09
555	14.00	740	12.19
560	13.96	745	11.23

The Fairchild collimator consists of four basic elements, mounted in a fiberglass tube with black velvet lining:

(1) Ross triplet lens corrector.

(2) Beam splitter.

(3) Primary mirror with a 10.668-m spherical radius of curvature.

(4) Front-field corrector plate.

A special holder was constructed to hold the targets in the focal plane of the collimator to prevent focusing inaccuracies. The targets were illuminated with the 30-cm light cannon No. 2 (see Section II-B). During calibrations, a special black metal tube was always placed between the collimator and the tested narrow-angle camera to prevent any outside stray illumination (see Section II-E). The Fairchild collimator was also utilized for various engineering purposes, as well as for the opto/mechanical alignment measurements for both the narrow- and the wide-angle cameras (see Section IV-B-3). However, like all collimators, it is not suitable for flat-field light transfer calibrations because of the focused field-flatness shading of the light cannon and other inaccuracies of the entire optical system.

Two Fecker collimators were built[2] according to JPL design and specifications. However, only one collimator, Fecker "A", was used for wide-angle-camera imaging calibration. In Figure 2-18, it is shown set up on the auxiliary Gaertner optical bench, together with its light source (a parabolic 5-cm xenon-Varian light cannon) and an ISS wide-angle camera. As in the case of the Fairchild collimator, only one target at a time could be inserted into the target holder. The other collimator, Fecker "B", was kept as a spare and finally was shipped to Cape Canaveral, Florida, for eventual emergency wide-angle-camera engineering testing.

The narrow-angle and the wide-angle optics collimators were designed and built for thermal/vacuum calibrations of the ISS cameras. They were both mounted on the same base. Figure 2-19 shows their actual calibration setup in front of the thermal/vacuum chamber window. The light sources were two quartz-iodide 5-cm lamps, and only one target at a time could be inserted in the target holder between the lamp and the optics. The narrow-angle optics is a spare MVM 1973 telescope, and the wide-angle optics collimator is a spare ISS wide-angle lens. With this arrangement, practically identical opto/mechanical conditions were established between the collimators and the tested cameras, thereby resulting in a 1:1 scale factor.

---

[2]By the Contraves-Goerz Optical Company, Pittsburgh, Pennsylvania.

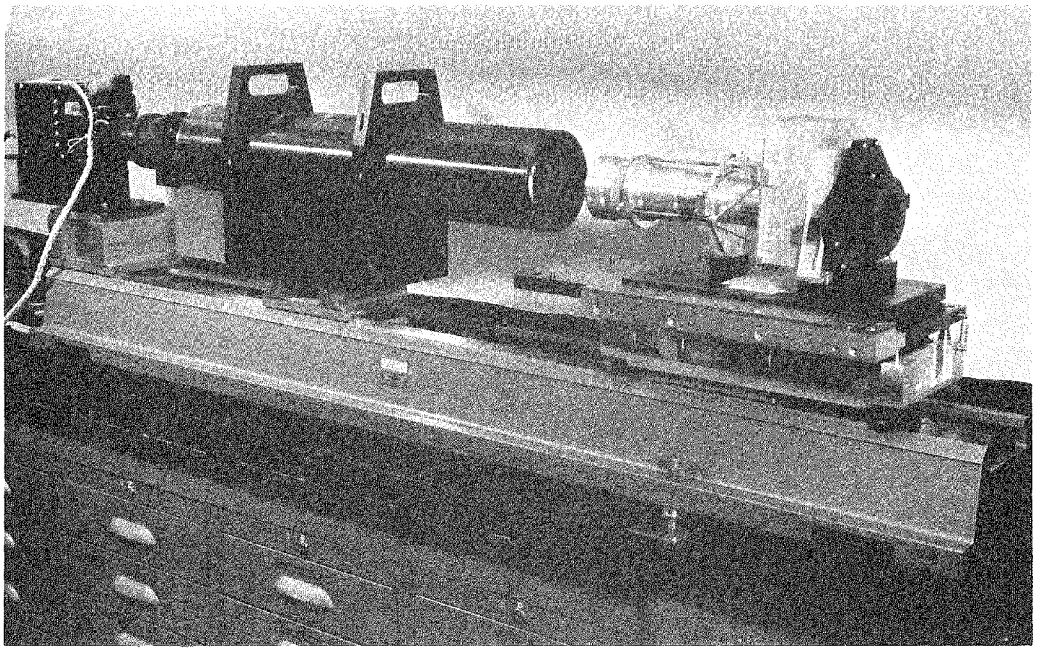

Figure 2-18. Fecker "A" collimator on optical bench with light cannon and ISS wide-angle camera

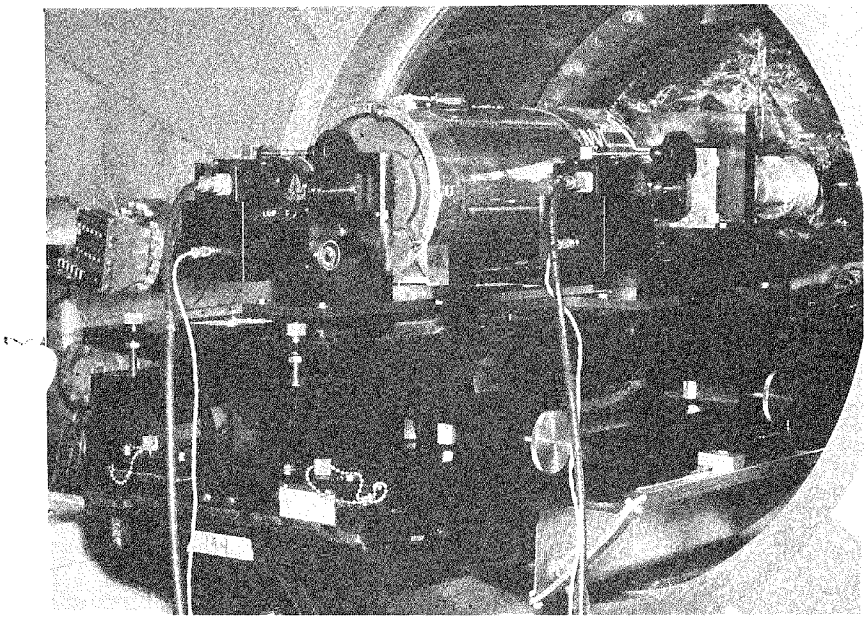

Figure 2-19. ISS narrow-angle optics and wide-angle optics collimators

Finally, two sets of collimators (SAF Unit 1 and SAF Unit 2) were provided for SAF and ETR system-calibration verifications of the ISS cameras mounted on the spacecraft scan platform. Each unit (Figure 2-20) consists of a Celestron telescope (narrow-angle cameras) and a Soligor lens (wide-angle cameras) mounted, like the thermal/vacuum collimators described above, on the same base. Two modified 5-cm parabolic xenon-Varian lamps were used for light sources, but contrary to the other collimators, the construction of the target holder is different. A target wheel was manufactured and mounted in the focal plane of each Celestron and Soligor lens, thereby enabling an automatic selection of any desired target.

Focal lengths of all collimators were measured by using the geometric grid target (see Section II-D) and the same measurement method as described in Section IV-B-1. The results obtained are summarized in Table 2-4, together with other most pertinent technical parameters of the collimators. No significant optical distortion was discovered for any of the collimators, but, nevertheless, they are not recommended for any accurate radiometric calibrations (such as flat-field light transfer) because of the focused shading of the light cannons used for light sources and because of some other eventual optical anomalies of a particular system as well.

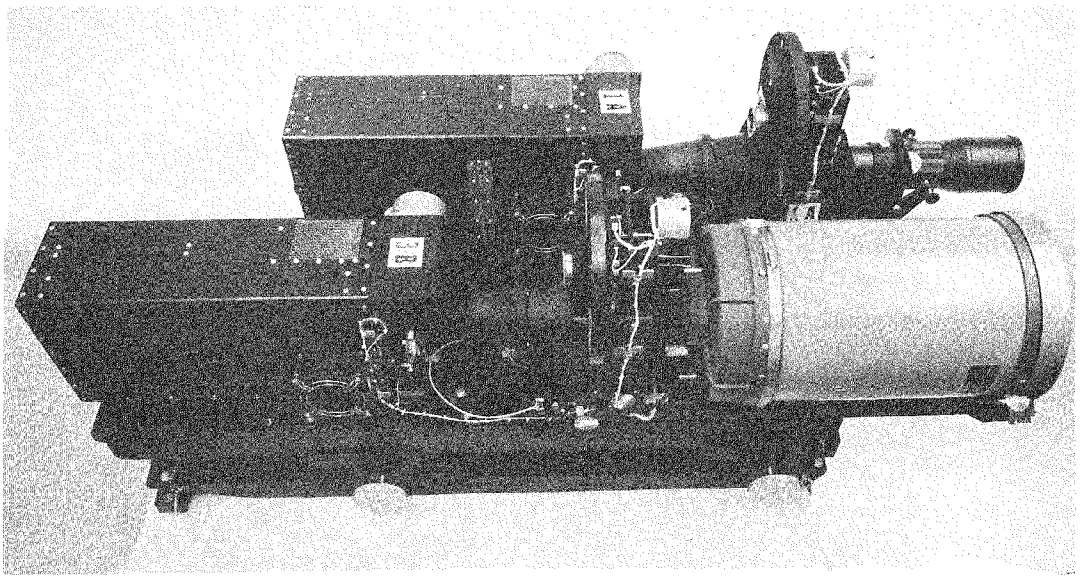

Figure 2-20. SAF collimators (Celestron and Soligor)

Table 2-4. Technical parameters of Voyager-ISS collimators

Collimator	Calibration	ISS camera focal length, mm	Collimator focal length, mm	Scale factor[a] (target/image)
Fairchild	Bench	Narrow-angle, 1500.00	4040.05	2.693
Fecker "A"	Bench	Wide-angle, 200.000	628.435	3.142
Fecker "B"	Bench	Wide-angle, 200.000	628.030	3.140
Narrow-angle optics	Thermal/vacuum	Narrow-angle, 1500.00	1500.241	1.000 161
Wide-angle optics	Thermal/vacuum	Wide-angle, 200.000	199.952	0.999 760
SAF Unit 1, Celestron 3B	SAF and ETR	Narrow-angle, 1500.00	1992.68	1.328
SAF Unit 1, Soligor 3A	SAF and ETR	Wide-angle, 200.000	401.421	2.007
SAF Unit 2, Celestron 1B	SAF and ETR	Narrow-angle, 1500.00	2023.49	1.349
SAF Unit 2, Celestron 1A	SAF and ETR	Wide-angle, 200.000	401.274	2.006

[a]For actual ISS data reduction, the true scale factor based on true camera focal length must be used (see Section IV-B-1).

D. TARGETS

The following targets were used for various Voyager-ISS photoscience tests and calibrations in connection with the applicable collimators, which were described in Section II-C:

(1) Geometric grid target (Figure 2-21) - geometric distortion calibration.

(2) MTF target (Figure 2-22) - modulation transfer function calibration.

(3) Pinhole target (Figure 2-23) - point spread function test (star simulation).

(4) Bull's eye target (Figure 2-24) - beam bending calibration.

(5) Color reconstruction target (Figure 2-25) - color reconstruction test.

(6) Calibration plaque (Figure 2-26) - in-flight calibration test.

The geometric grid target was manufactured according to JPL specifications. Coordinates of all grid intersections were measured by the manufacturer[3] and then verified at JPL on the Moore measuring machine in the same way as the vidicon reseau marks (Section III-D-2). The resulting positional accuracy is approximately ±1 μm.

The intersection points were also measured with a Wild T3 theodolite through all collimators to determine their equivalent focal length and eventual optical distortion (none of any practical significance was discovered). It would serve little purpose to list all the hundreds of grid coordinates in this report, but they were given to the JPL Image Processing Laboratory (IPL), where they were used for geometric distortion data reduction (discussed in Section IV-B-2).

The modulation transfer function (MTF) target is based on a completely new design. For all previous space flight projects, the MTF target always consisted of a number of different frequency fields, but the new MTF method developed by IPL (Section IV-C-1) calls for equal-width black and white bars spread across the entire camera field of view. The target seems to be very simple; however, the edges of the bars must be straight and sharp within ±1 μm to guarantee reliable results. During ISS calibrations, the MTF target was used in both its horizontal and vertical positions.

The pinhole target, designed and built at JPL, was used for the point spread function test (star simulation), as described in Section IV-C-3.

---

[3] Electromask Co., Woodland Hills, California.

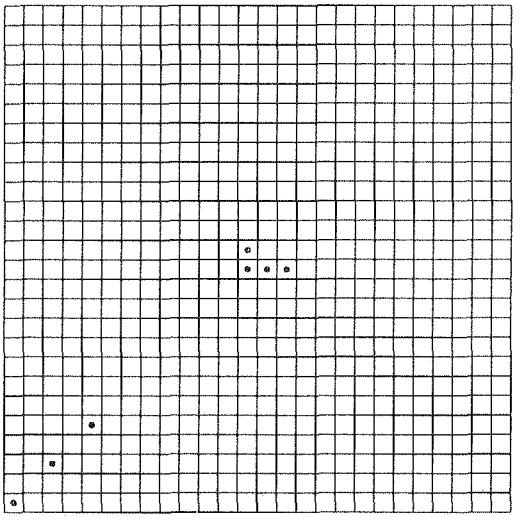

Figure 2-21. ISS geometric grid target

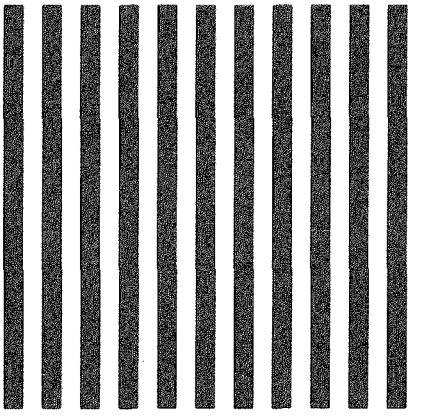

Figure 2-22. ISS modulation transfer-function target

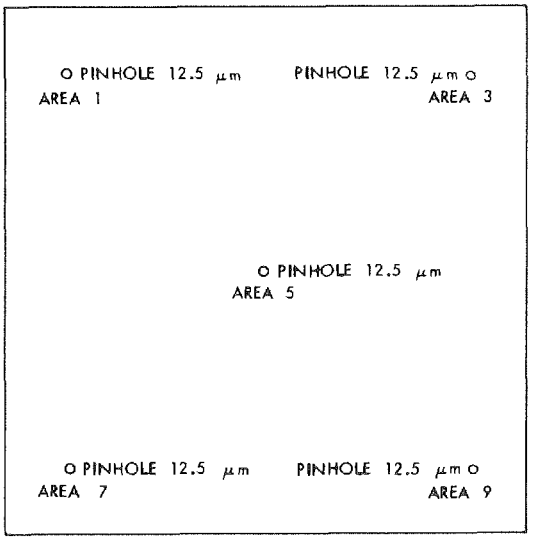

Figure 2-23. ISS pinhole target

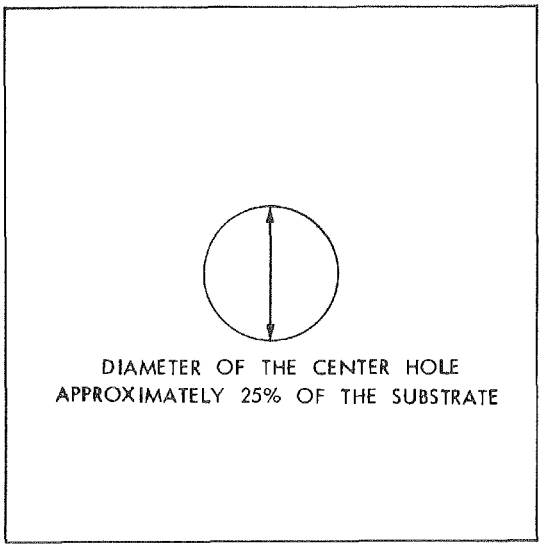

Figure 2-24. ISS bull's-eye target (either a full-moon or half-moon hole)

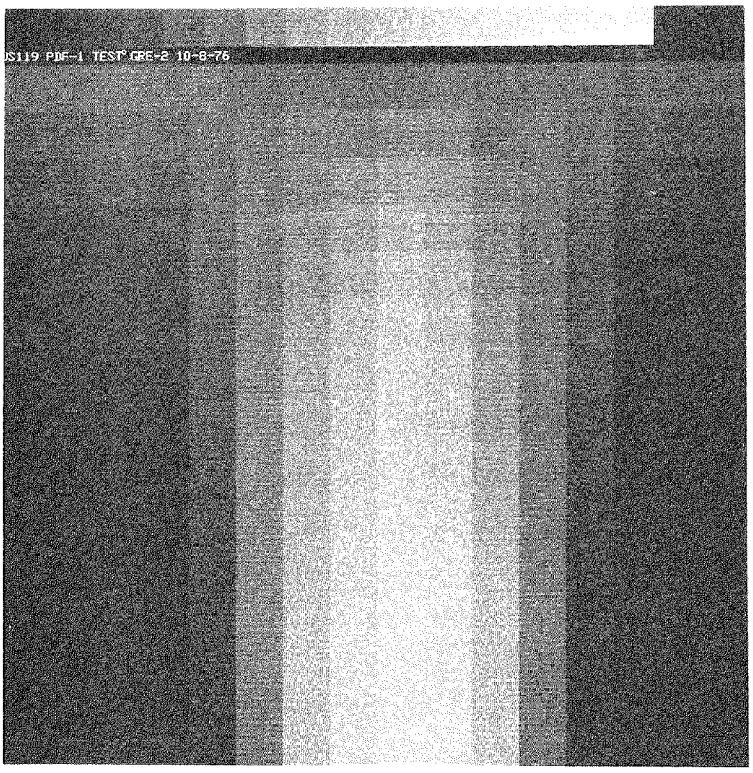

Figure 2-25. ISS color reconstruction target

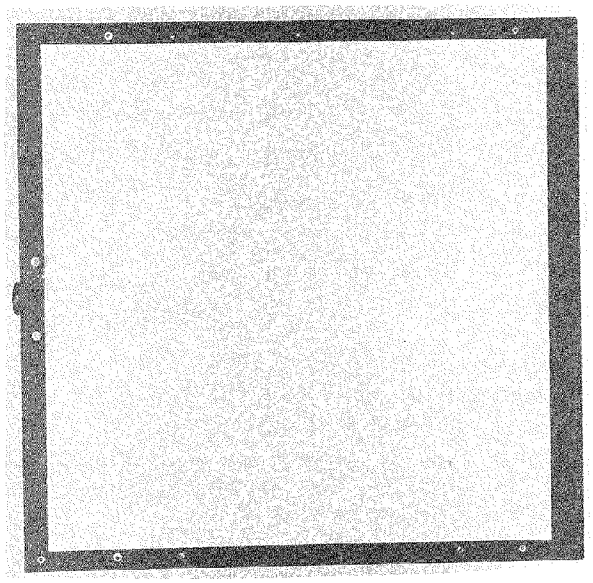

Figure 2-26. Calibration plaque

The bull's eye target is very simple and self-explanatory. This target was used for the beam bending test (Section IV-B-4), both in its full-moon and half-moon version.

The color reconstruction target, designed and computer-generated by IPL, was calibrated to develop a method of color simulation from black and white ISS photographs (see Section IV-A-6).

The calibration plaque was used for in-flight calibrations in the JPL optical tunnel (see Section IV-A-8), and it will also be used for extensive in-flight calibrations during the mission. It is a 60- x 60-cm target with an aluminum honeycomb surface, which was prepared by a grit blast method [150 grit aluminum oxide at 60 psi] to obtain a uniform field flatness and over 90% spectral reflectance. Inasmuch as the calibration plaques were in short supply, some of the tests utilized only a 30- x 30-cm segment of the plaque, called the witness plate.

E. CALIBRATION ENVIRONMENT

The ISS subsystem-level calibrations, which utilized the support equipment described in Sections II-A through II-D, were performed at two locations:

(1) JPL optical tunnel (bench calibrations).

(2) JPL thermal-vacuum chamber (environmental calibrations).

The JPL optical tunnel employs an Askania optical bench, which is aligned with the Fairchild collimator. Figure 2-27 shows a view of the optical tunnel area. A TV camera with its electronics assembly is mounted on the optical bench and pointed along the optical axis of the Fairchild collimator. The black metal tube, designed to eliminate outside stray illumination and veiling glare, is visible between the camera and the collimator front-field corrector plate. The 30-cm light cannon No. 2, which was used for illumination of the collimator targets, is hidden behind the far end (focal/target plane) of the collimator. This picture was staged for documentation purposes only, at a time when the collimator fiberglass tube was removed for cleaning.

Figure 2-28 shows a narrow-angle ISS camera and a wide-angle ISS camera set up on the Askania optical bench in the optical tunnel. The electronics assembly is shown in the foreground. During bench calibrations, this assembly and the cameras were connected to the BCE (Section II-A); and then the cameras were aligned either with their respective light cannon (30-cm light cannon No. 1 or 13-cm light cannon) for various radiometric calibrations, or with the applicable collimator (Fairchild or Fecker) for calibrations requiring images of targets.

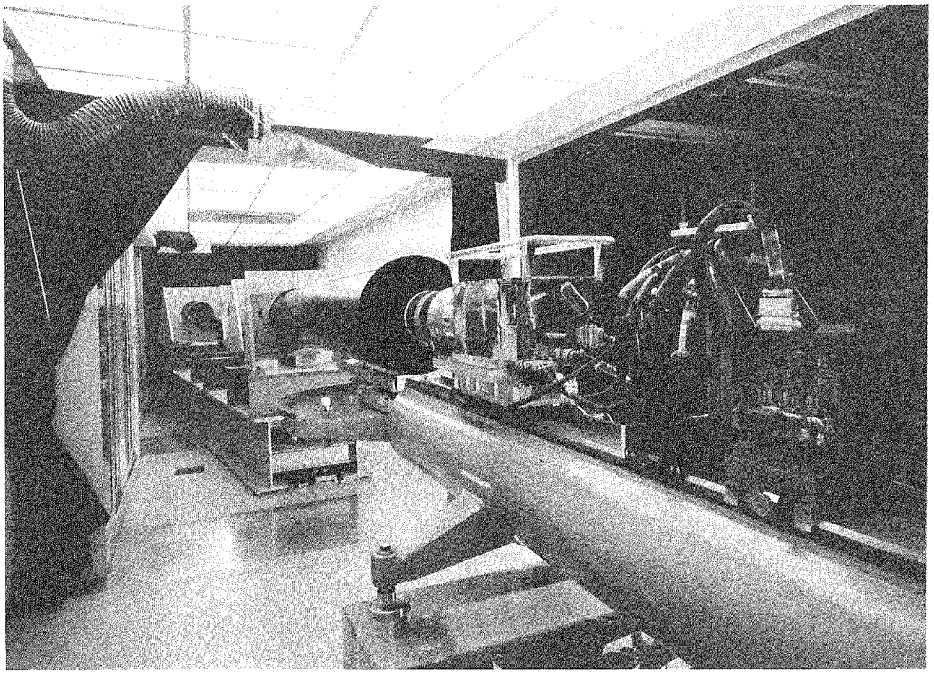

Figure 2-27. General view of the JPL optical tunnel test and calibration area

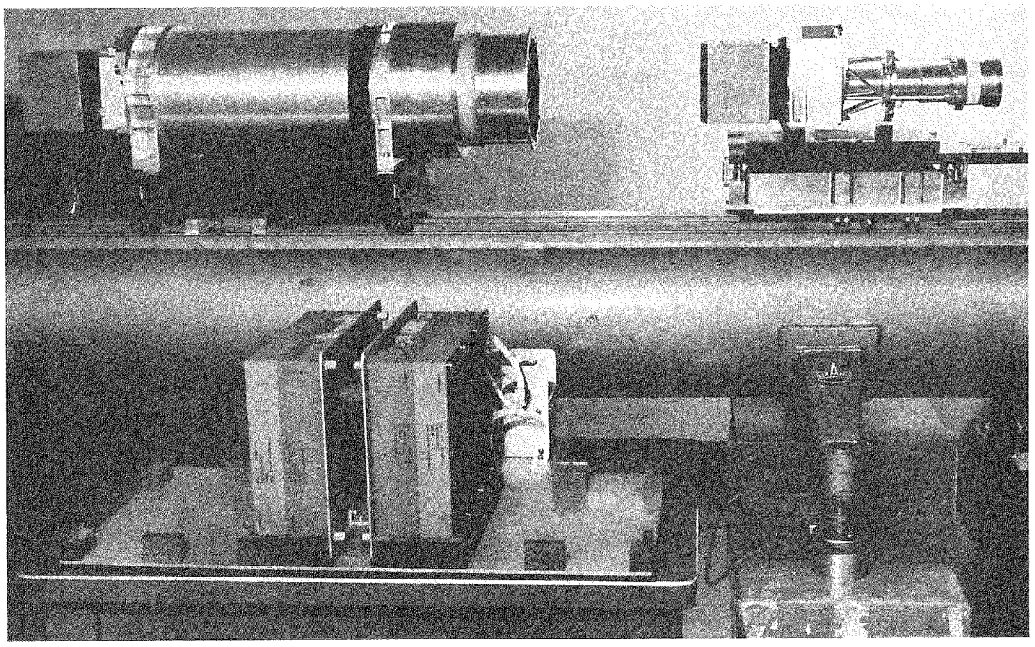

Figure 2-28. ISS camera calibration setup on the Askania optical bench

The temperature in the tunnel was approximately 23°C at the beginning of each bench calibration, but it rose 3 to 5° during the test as a result of the heat generated by the light cannon. The humidity was kept in a confortable narrow range between 60 and 66%.

The thermal-vacuum chamber, which is located in the JPL Environmental Laboratory, is shown in Figures 2-29 through 2-32. Figure 2-29 shows a general view of the entire thermal-vacuum chamber area. The chamber itself stands on the right side with the collimators mounted in front of the chamber window. The BCE and other calibration support equipment is located around the chamber, and the chamber control console can be seen on the left side of the picture. Figure 2-30 presents a detailed view of the thermal-vacuum chamber in its sealed position, ready for calibrations.

The ISS cameras were mounted inside the chamber as indicated in Figures 2-31 and 2-32, and the corresponding collimators were set up on a special rack in front of the chamber window and then carefully aligned with the boresight axis of each camera (Figure 2-31). When the 30-cm light cannon No. 1 was used for radiometric calibrations, the portable stimulus rack had to be removed, and the light cannon, which was mounted on an extended tripod, was set up in front of the chamber window. During calibrations, a black velvet cloth was always wrapped around the window to eliminate any eventual outside glare.

The absolute spectral transmittance of the chamber window[4] is documented in Figure 2-33 and Table 2-5. Without this information, comparison between the bench and thermal/vacuum results, particularly the flat-field light transfer curves, would be very difficult. A portable spectroradiometer had to be used because it was not possible to dismount the chamber window and ship it to the optical tunnel, where the JPL spectroradiometer is located. Unfortunately, this portable instrument could produce reliable readings from only 390 nm (380 and 385 nm are unreliable with large sigmas), and the ultraviolet ranges had to be determined by different means (see the dashed curve in Figure 2-33).

A mere extrapolation would be too inaccurate for this purpose; therefore, the ultraviolet extension was based on comparison with the spectral transmission curves of the Viking chamber window (Figure 2-35 in Reference 2-3) and with those of glass 1R81-E, which has a very similar coating. The resulting curve should thus be very close to the real Voyager chamber-window conditions, and it can be used for decalibrations with a great degree of confidence.

---

[4]Measured by Gamma Scientific, Inc. of San Diego, California.

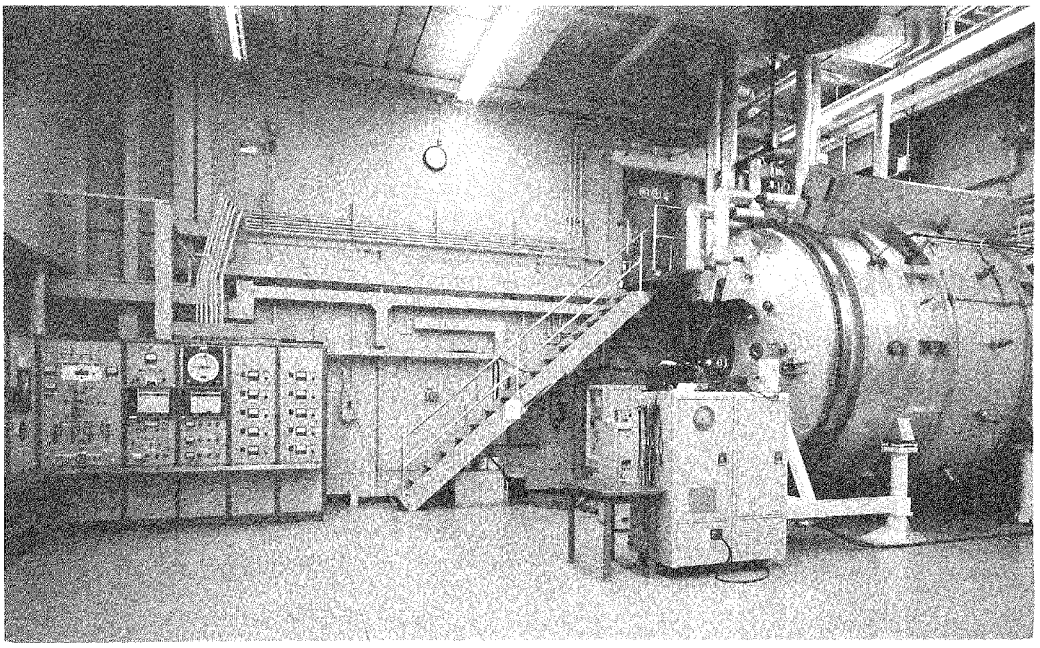

Figure 2-29. General view of the entire JPL thermal-vacuum chamber area

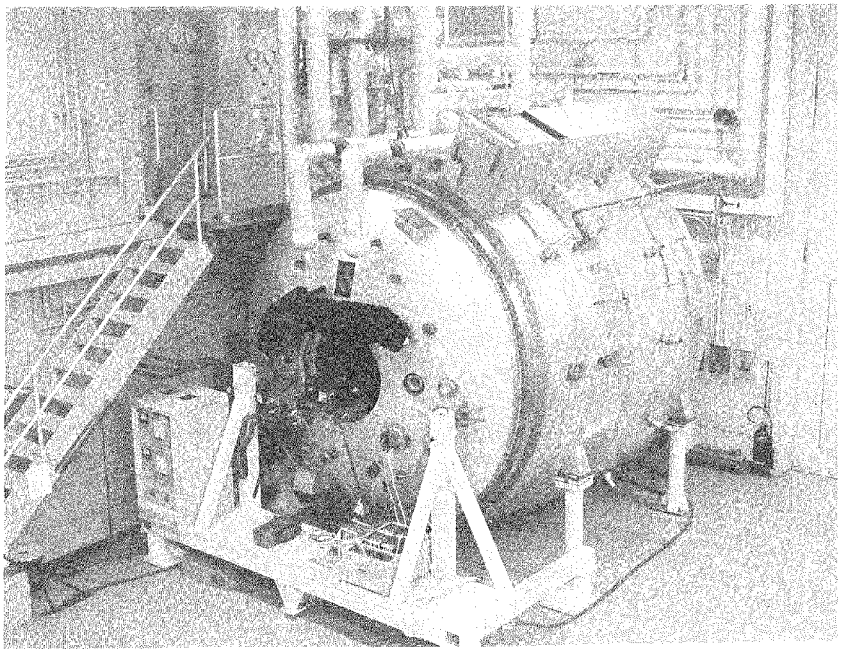

Figure 2-30. A detailed view of the JPL thermal-vacuum chamber

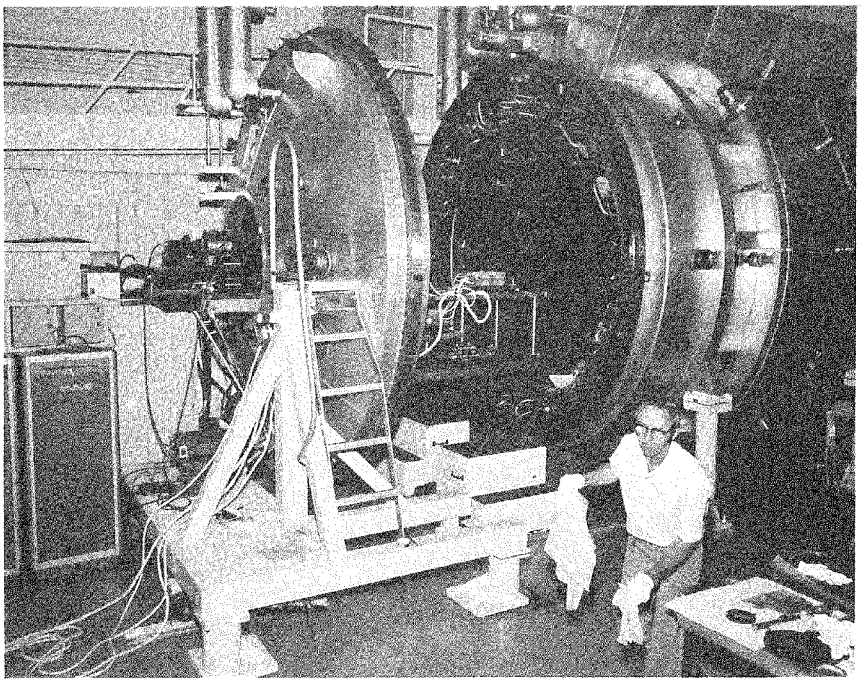

Figure 2-31. JPL thermal-vacuum chamber in its open position

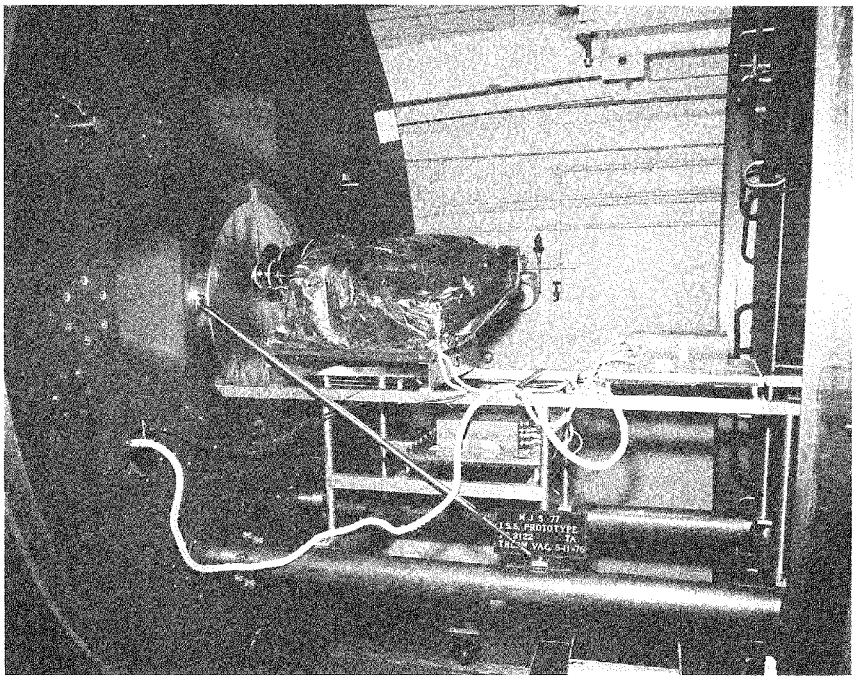

Figure 2-32. ISS cameras mounted inside the JPL thermal-vacuum chamber

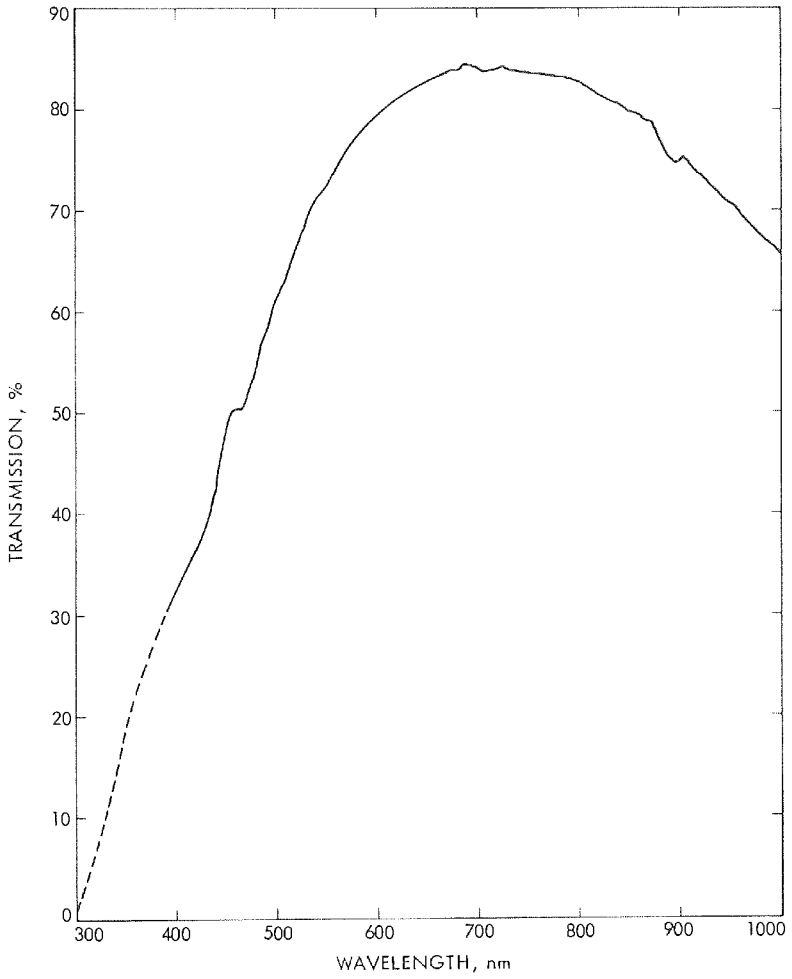

Figure 2-33. Absolute spectral transmission of the JPL thermal-vacuum chamber window

Table 2-5. Absolute spectral transmittance of the JPL thermal-vacuum chamber window

Wavelength, nm	Transmission, %	Wavelength, nm	Transmission, %	Wavelength, nm	Transmission, %
380	(29.9325)	560	74.1424	740	83.8284
385	(29.8907)	565	75.1448	745	83.6609
390	30.3421	570	76.0167	750	83.6422
395	31.1749	575	76.7265	755	83.6266
400	32.1636	580	77.3438	760	83.4049
405	33.9048	585	77.9537	765	83.3274
410	34.6179	590	78.4740	770	83.3594
415	35.4777	595	78.9622	775	83.2009
420	36.5969	600	79.4034	780	83.0832
425	37.8201	605	79.8867	785	82.9573
430	39.3904	610	80.3200	790	82.7589
435	40.9730	615	80.8257	795	82.5939
440	43.7058	620	81.1154	800	82.4846
445	46.2104	625	81.3587	805	82.2202
450	48.3294	630	81.6339	810	81.9270
455	49.9561	635	82.0148	815	81.6659
460	50.5258	640	82.3683	820	81.2996
465	50.1695	645	82.7275	825	81.0555
470	51.5511	650	82.8570	830	80.7507
475	52.9361	655	83.1144	835	80.4442
480	54.7453	660	83.3413	840	80.2578
485	56.8751	665	83.4591	845	79.9932
490	58.5427	670	83.6974	850	79.7220
495	59.8887	675	83.7573	855	79.4967
500	61.2215	680	83.8594	860	79.1372
505	62.6615	685	84.3361	865	78.6758
510	64.0574	690	84.2408	870	78.2971
515	65.5150	695	84.1192	875	78.1929
520	66.6885	700	83.9911	880	76.9317
525	67.7467	705	83.8511	885	75.8211
530	68.8762	710	83.7627	890	75.0644
535	70.0768	715	84.0597	895	74.6592
540	71.0521	720	84.0583	900	74.6657
545	71.9147	725	84.0823	905	75.0264
550	72.5587	730	83.9463	910	74.1714
555	73.2485	735	83.8721	915	73.5803

Table 2-5 (cont)

Wavelength, nm	Transmission, %	Wavelength, nm	Transmission, %	Wavelength, nm	Transmission, %
920	73.1921	980	67.3013	1040	61.5389
925	72.7856	985	66.8031	1045	60.9853
930	72.2074	990	66.3996	1050	60.1801
935	71.8234	995	65.9591	1055	60.0759
940	71.3538	1000	65.4187	1060	59.7459
945	70.9000	1005	64.8913	1065	59.9115
950	70.6071	1010	64.5031	1070	59.3628
955	70.1273	1015	64.1786	1075	58.8976
960	69.6129	1020	63.7189	1080	58.4535
965	69.1573	1025	63.2833	1085	58.7203
970	68.5172	1030	62.7935	1090	60.1833
975	67.8041	1035	62.5567		

In addition to the bench and environmental calibrations, a few calibration verification tests were performed in SAF and at the ETR. In these tests, the ISS cameras were mounted in their final position on the spacecraft scan-platform, and the regular ISS support calibration equipment was supplemented by the complex spacecraft support and control equipment.

REFERENCES

2-1. A. Collins and M. Benesh, Mariner Jupiter/Saturn 1977, Imaging Science Subsystem, Calibration Requirements Document, JPL Document 618-659, August 20, 1976.

2-2. MJS'77 ISSE, Bench Checkout Equipment, Operations Manual, Data Item Eng-010, Xerox Electro-Optical Systems, March 1976.

2-3 M. Benesh and T. Thorpe, Viking Orbiter 1975, Visual Imaging Subsystem, Calibration Report, JPL Document 611-125, March 1976.

SECTION III

COMPONENT CALIBRATIONS

The Voyager ISS consists of a narrow-angle and a wide-angle TV camera, each comprising the following four basic parts:

(a) The optics.

(b) The filter wheel/shutter assembly.

(c) The camera head housing the vidicon.

(d) The electronics assembly (power supply and support electronics).

Figure 3-1(a) shows the ISS cameras fully assembled with their electronics assemblies, and (b) gives a separate view of the shutter, filter wheel, and optics (the rectangular railing on top of the narrow-angle telescope was for handling purposes only). The optics of each camera is equipped with a sunshade, which is attached to the main telescope body by means of a plastic isolation ring. It may be of interest to mention that the ISS narrow-angle cameras were built according to a modified design of the original MVM 1973 cameras (Reference 3-1).

A unique "first" in space photography was achieved by installing the in-flight calibration lamps in the ISS cameras (their capabilities and application are described in detail in Section IV-A-5). There are eight in-flight calibration lamps for each narrow-angle camera mounted on the front circumference of the sunshade [Figure 3-1(a)], but the wide-angle cameras required only one such lamp, which was mounted on the optical axis at the rear end of the sunshade by means of a spider.

All components were subjected to a series of engineering acceptance tests, but additional tests and calibrations prior to their integration into the imaging subsystem were made on the optics, filters, shutters, and vidicons. There were three main reasons for these additional calibrations:

(a) It was necessary to verify the compatibility of the manufactured component with the photoscience requirements.

(b) Various radiometric calculations required knowledge of such parameters as spectral characteristics, actual shutter times, vidicon light-transfer curves, etc.

(c) Reseau mapping, the results of which were instrumental in subsystem-level geometric and focal-length calibrations, could be done only at the component level, when there was unrestricted accessibility to the vidicon tube.

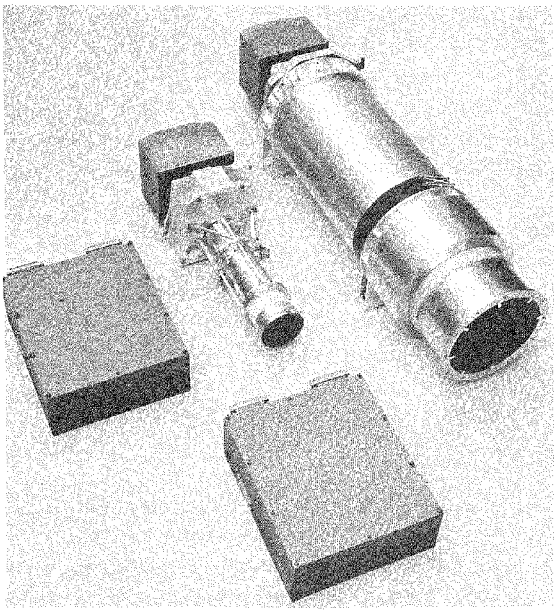

(a)

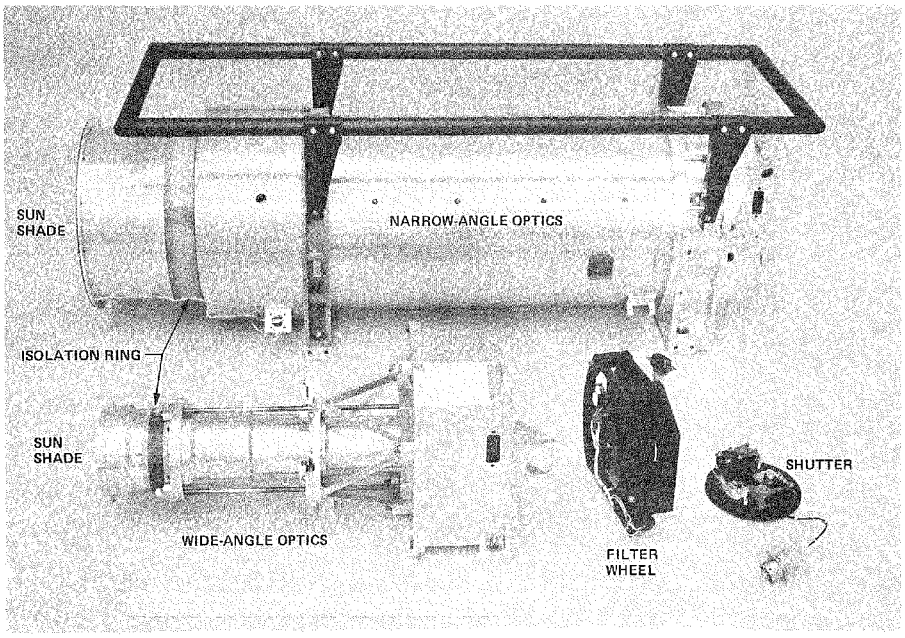

(b)

Figure 3-1. Voyager ISS cameras: (a) fully assembled with electronics assemblies, (b) optics, filter wheel, and shutter

Only results pertaining to ISS S/N 03 - S/N 08 cameras are documented in this report. However, many component-level calibrations were performed on other cameras and other spare-part components as well. These results were catalogued and filed in case of retrofitting or any other future needs. The assignment of individual components is summarized by their serial numbers as listed in Section I, Table 1-1.

All component-level calibration procedures were based on technical requirements documented in Reference 2-1. They were designed and performed in a way to fully satisfy the specified accuracy criteria.

A. OPTICS

The narrow-angle camera optics is a 1500-mm focal length all-spherical, catadioptric cassegrain telescope [a modified MVM 1973 design (see Reference 3-1)] consisting of five elements plus an additional dust lens located between the shutter and the vidicon [Figures 3-1(a) and b)]. The f-stop number (f/#) is 8.5.

The wide-angle camera optics is a 200-mm focal length six-element lens of the Petzval-type. The sixth element, like the dust lens in the narrow-angle optics, is also located between the shutter and the vidicon [Figures 3-1(a) and (b)]. The f/# is 3.5.

The purpose of the sunshade is to screen out scattered light causing veiling glare and, in the case of narrow-angle optics, to provide additional baffle effect eliminating direct light from reaching the vidicon. The sunshade also holds the Carley tungsten filament in-flight calibration lamps (type 715 AS15, 5 V, 0.115 A), as already mentioned in this section.

The narrow-angle optics refractive elements were fabricated from T-20 Suprasil II, an extremely stable optical material, and ultra low-expansion materials were used for the mirrors, which resulted in an essentially diffraction-limited performance. The wide-angle optics elements were manufactured[5] according to JPL specifications. The optical coatings are capable of withstanding radiation environments without degradation. (References 3-2 and 3-3 may be consulted for further technical details of the optical designs.)

The theoretical computer-generated modulation transfer function (MTF) curves of the ISS optics are shown in Figures 3-2 and 3-3. The minimum resolution, which was based on tests using the high contrast Air Force resolution target, is summarized in Table 3-1. The requirements for optical quality of ISS optics were defined in References 3-4 and 3-5, as follows: spatial frequency of at least 36 line-pairs/mm (LP/mm) at 50% modulation and 120 LP/mm at 15% modulation for narrow-angle optics, and a minimum resolution of 300 LP/mm for wide-angle

---

[5]By Schott Optical Glass Co., Duryea, Pennsylvania.

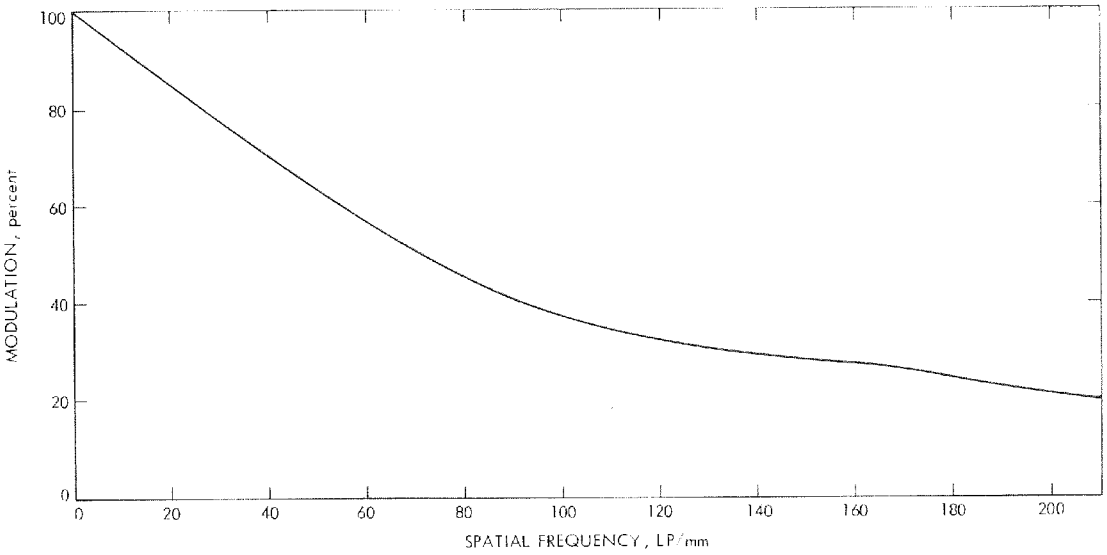

Figure 3-2. Theoretical computer-generated MTF curve of ISS narrow-angle optics

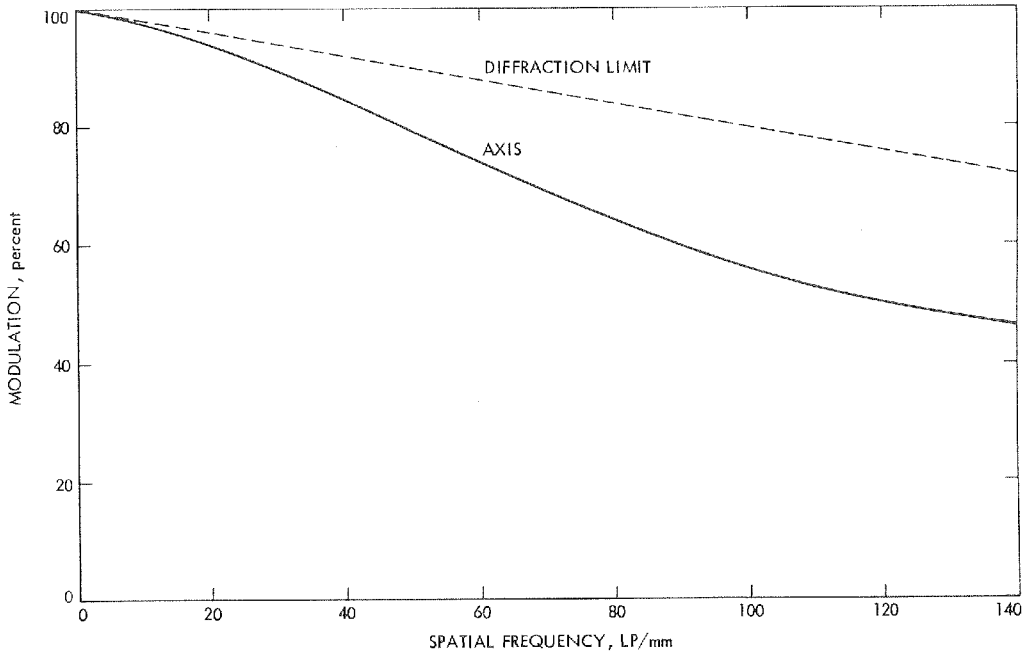

Figure 3-3. Theoretical computer-generated MTF curves of ISS wide-angle optics

Table 3-1. Minimum resolution of ISS optics

ISS S/N	Optics S/N	Peak Wavefront, λ	Minimum Resolution LP/mm	
			Center	Edge
03	NAO-3	0.30	173	154
04	WAO-4	Not available	390	390
05	NAO-4	0.15	194	194
06	WAO-6	Not available	390	390
07	NAO-5	0.13	194	194
08	WAO-5	Not available	390	390

optics. As can be seen from Figure 3-2 and Table 3-1, all these constraints were fully met.

1. Spectral Transmittance

Spectral transmittance of ISS telescopes was measured on the JPL spectroradiometer. The method and the typical test set-up are described in detail in Reference 2-3.

The results obtained are documented in Figures 3-4 through 3-9, and they include the effect of center obscuration, dust lens (sixth element), and the light ring. The curves are scaled to show absolute transmittance at 555 nm, which was deduced from T-stop number (T/#) measurements described in Section III-A-2.

The spectroradiometer was operated between 250 and 745 nm at 5-nm intervals. The accuracy of these spectral measurements is very difficult to measure, but based on past experience, as well as on several comparison tests, it should be better than the ±2% required by Reference 2-1.

Some users may prefer numerical data of spectral transmittance for computer applications, and Table 3-2 was included for this purpose.

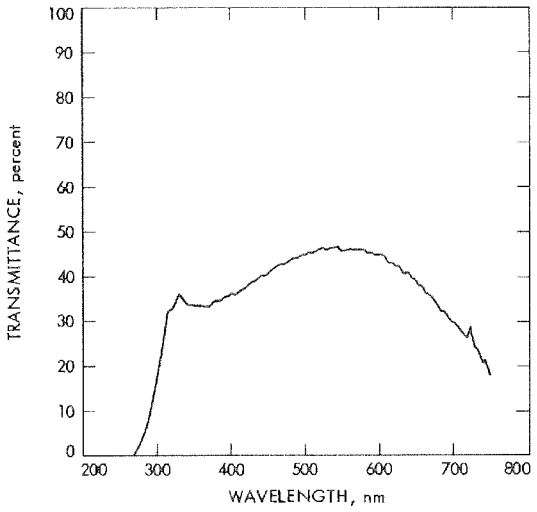

Figure 3-4. Spectral transmittance, ISS S/N 03 (narrow-angle optics S/N 03)

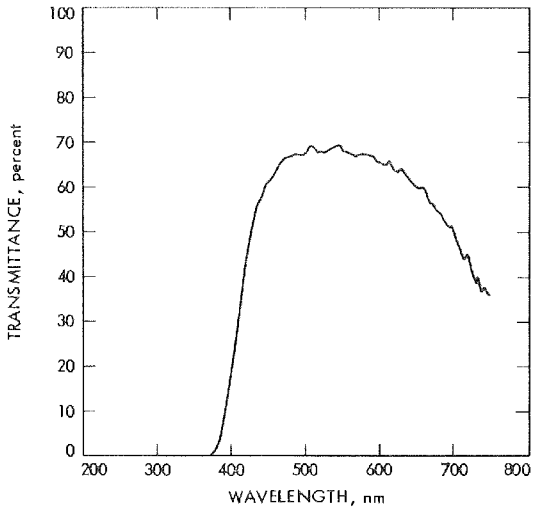

Figure 3-5. Spectral transmittance, ISS S/N 04 (wide-angle optics S/N 04)

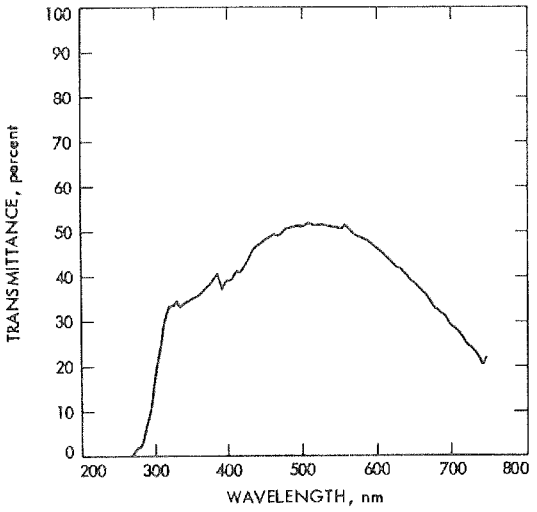

Figure 3-6. Spectral transmittance, ISS S/N 05 (narrow-angle optics S/N 04)

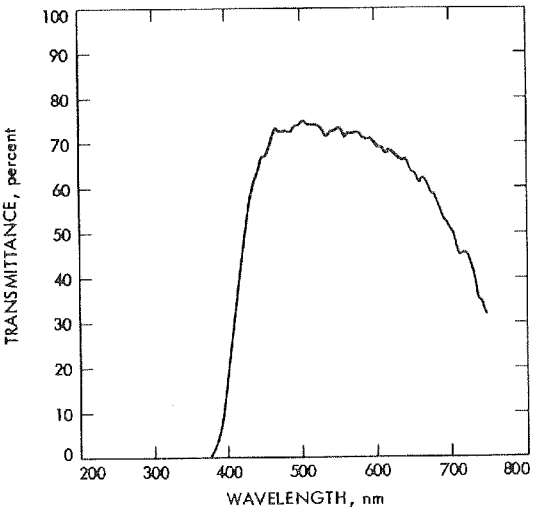

Figure 3-7. Spectral transmittance, ISS S/N 06 (wide-angle optics S/N 06)

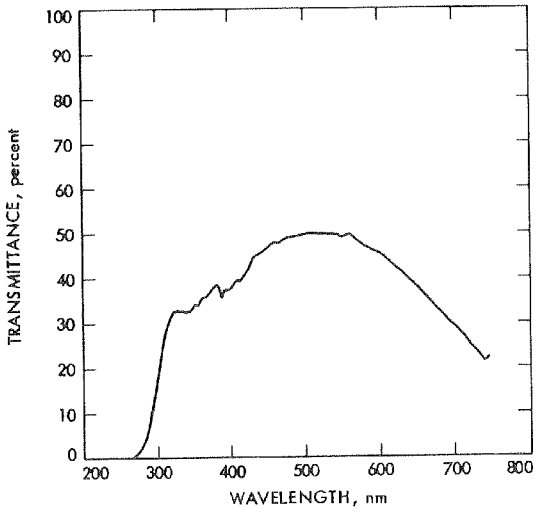

Figure 3-8. Spectral transmittance, ISS S/N 07 (narrow-angle optics S/N 05)

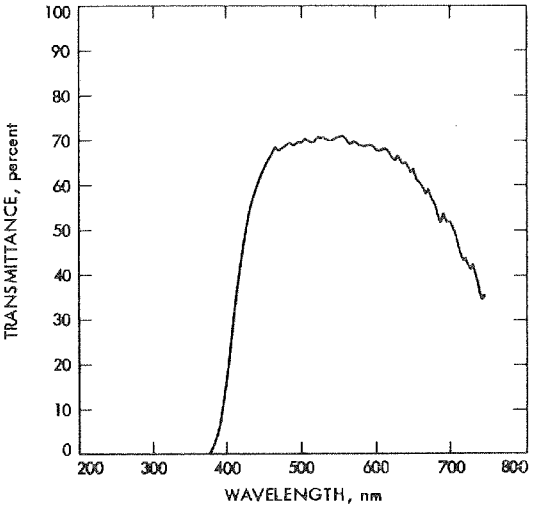

Figure 3-9. Spectral transmittance, ISS S/N 08 (wide-angle optics S/N 05)

Table 3-2. Spectral transmittance of ISS S/N 03-08 (narrow-angle and wide-angle optics)

Wavelength, nm	Spectral transmittance, %					
	ISS S/N 03 (NAO S/N 03)	ISS S/N 04 (WAO S/N 04)	ISS S/N 05 (NAO S/N 04)	ISS S/N 06 (WAO S/N 06)	ISS S/N 07 (NAO S/N 05)	ISS S/N 08 (WAO S/N 05)
250	0.00		0.00			
255	0.00		0.00			
260	0.00		0.00		0.00	
265	0.00		0.00		0.32	
270	0.00		0.00		0.00	
275	1.59		1.59		0.56	
280	2.89		1.99		1.67	
285	4.81		3.77		2.85	
290	8.37		7.21		5.25	
295	12.45		10.87		8.97	
300	16.01		16.25		14.21	
305	21.57		21.44		19.01	
310	27.30		25.46		24.67	
315	32.52		31.18		28.49	
320	32.86		33.80		31.55	
325	34.20		33.67		32.48	
330	36.44		34.84		33.14	
335	34.93		33.42		32.71	
340	33.76		34.28		32.88	
345	33.34		34.53		32.46	
350	33.70	0.04	35.14		33.04	
355	33.62	0.03	35.70		34.36	
360	33.57	0.05	36.12	0.03	34.08	
365	33.43	0.03	36.88	0.02	35.84	0.03
370	33.21	0.04	37.76	0.02	35.89	0.03
375	34.39	0.11	38.50	0.10	37.02	0.10
380	34.62	0.56	40.04	0.59	38.17	0.55
385	34.68	2.04	41.06	1.97	38.62	2.02
390	35.62	4.89	37.01	4.97	35.36	5.15
395	35.63	9.39	39.29	9.81	37.60	9.63
400	36.61	15.38	39.32	16.19	37.56	15.86
405	35.87	21.77	39.74	23.36	38.11	22.81
410	36.93	28.63	41.45	31.88	39.54	30.24
415	37.18	35.82	41.03	38.46	39.23	37.28
420	37.87	41.52	42.34	45.51	40.56	44.17
425	38.77	47.86	43.87	52.94	41.87	49.95
430	38.73	51.72	45.54	56.85	43.96	54.20
435	39.76	56.34	46.83	61.54	44.95	57.15

Table 3-2 (contd)

Wavelength, nm	Spectral transmittance, %					
	ISS S/N 03 (NAO S/N 03)	ISS S/N 04 (WAO S/N 04)	ISS S/N 05 (NAO S/N 04)	ISS S/N 06 (WAO S/N 06)	ISS S/N 07 (NAO S/N 05)	ISS S/N 08 (WAO S/N 05)
440	40.46	57.25	47.47	63.62	45.36	59.91
445	40.22	60.47	48.09	66.94	45.77	62.17
450	41.12	61.08	48.80	67.01	46.30	63.74
455	41.57	62.31	49.07	69.21	47.11	65.49
460	42.57	64.42	49.66	71.21	47.78	66.74
465	42.96	65.33	49.32	73.30	47.67	68.57
470	42.64	66.52	49.83	72.51	48.25	67.88
475	43.41	66.43	50.88	72.46	48.98	68.28
480	44.27	67.09	51.09	72.78	49.01	68.88
485	44.13	67.42	51.45	72.17	49.18	69.52
490	44.46	66.97	51.43	73.75	49.41	68.68
495	45.03	67.10	51.61	73.88	49.62	69.82
500	44.96	68.47	51.32	75.21	49.51	69.36
505	45.31	69.42	52.03	74.25	49.88	70.51
510	45.28	68.86	51.72	74.06	49.98	69.89
515	46.06	67.42	51.50	74.10	49.79	69.29
520	46.59	67.97	51.57	74.08	49.88	70.81
525	46.10	67.43	51.60	73.47	49.75	70.54
530	46.34	68.14	51.47	71.42	49.82	70.76
535	46.47	68.47	51.33	72.59	49.57	70.06
540	46.80	68.91	51.16	73.02	49.67	69.55
545	45.64	69.40	50.98	73.21	49.61	70.27
550	45.72	67.81	50.70	73.56	48.81	70.65
555	46.30	67.60	51.60	71.40	49.25	70.80
560	46.01	67.12	50.66	72.59	49.61	69.72
565	45.79	67.11	49.86	72.34	48.87	69.09
570	45.96	67.40	49.41	72.59	48.32	69.82
575	46.06	67.41	48.81	72.36	47.60	69.09
580	45.23	67.36	48.59	70.97	47.06	68.71
585	45.28	67.02	48.22	70.71	46.65	68.98
590	45.00	66.81	47.40	70.73	46.14	69.04
595	45.03	65.32	46.78	69.61	45.88	68.58
600	45.25	65.29	46.04	68.79	45.55	67.51
605	43.77	64.78	45.38	68.98	45.08	67.57
610	43.11	65.92	44.60	67.67	44.29	68.23
615	43.13	63.94	43.91	68.71	43.36	67.34
620	42.40	63.20	43.26	67.91	42.63	65.83
625	42.46	64.31	42.05	66.43	41.67	65.38

Table 3-2 (contd)

Wave-length, nm	Spectral transmittance, %					
	ISS S/N 03 (NAO S/N 03)	ISS S/N 04 (WAO S/N 04)	ISS S/N 05 (NAO S/N 04)	ISS S/N 06 (WAO S/N 06)	ISS S/N 07 (NAO S/N 05)	ISS S/N 08 (WAO S/N 05)
630	40.45	63.40	41.87	66.07	41.32	66.55
635	41.00	62.33	40.80	66.68	40.52	64.69
640	39.82	61.05	40.21	64.73	39.60	65.05
645	39.50	60.20	39.20	63.37	38.63	62.75
650	38.15	59.52	38.66	63.15	38.09	63.57
655	38.04	60.17	37.48	61.11	37.16	60.91
660	36.14	59.02	36.69	62.02	35.92	60.31
665	36.12	56.30	35.83	61.28	35.25	57.90
670	34.98	55.78	34.89	58.98	34.16	59.31
675	33.66	54.59	33.15	58.66	33.49	56.60
680	32.21	54.37	32.87	55.07	32.62	55.54
685	32.40	51.95	32.07	53.13	31.99	51.73
690	30.69	50.90	31.63	52.31	30.48	53.86
695	29.80	51.65	29.67	50.90	29.70	51.58
700	29.56	48.07	28.61	50.02	29.24	52.03
705	28.18	45.60	28.35	45.34	28.16	49.75
710	27.17	43.74	27.67	44.93	27.57	45.62
715	26.35	45.27	26.13	45.38	26.43	43.37
720	29.00	42.77	24.74	45.38	24.72	43.95
725	24.20	38.84	24.17	41.84	24.07	41.35
730	23.44	40.07	23.59	39.74	23.65	42.32
735	20.67	36.41	22.26	35.26	22.12	38.18
740	21.37	37.53	20.10	34.65	21.05	34.33
745	17.70	35.78	22.32	31.79	22.37	35.28

2. T-Stop Number

The T/# of an optical system is a function of its f/# and its absolute transmittance, t, which in the case of ISS cameras includes the center obscuration of the telescope (narrow-angle), the in-flight calibration lamp and its spider (wide-angle), the dust lens (narrow-angle), the sixth element (wide-angle), and the light ring:

$$T/\# = \frac{f/\#}{\sqrt{t}}$$

The method of T/# determination, which is based upon this relation, was described in detail in Reference 2-3. The results obtained are summarized in Table 3-3 and, as can be seen, they are all well within the ±2% accuracy limit required by Reference 2-1. The values are based upon at least three independent measurements of each telescope.

Once the T/# is known, the absolute transmittance at 555 nm can be computed from

$$t = \left(\frac{f/\#}{T/\#}\right)^2$$

where f/# is the anticipated f-stop number of the narrow-angle or wide-angle ISS camera.

The calculated absolute transmittance, t, was then used as scale factor for the spectral transmittance curves described in Section III-A-1.

Table 3-3. Results of T-stop number measurements

ISS S/N	Telescope S/N	Anticipated f/#	True T/#	Absolute Transmittance, %
03	NAO-03	8.5	12.49 ±0.14	46.3
04	WAO-04	3.5	4.26 ±0.02	67.6
05	NAO-04	8.5	11.83 ±0.09	51.6
06	WAO-06	3.5	4.14 ±0.02	71.4
07	NAO-05	8.5	12.11 ±0.11	49.25
08	WAO-05	3.5	4.16 ±0.02	70.8

3. Focal Length

The anticipated focal length of the ISS narrow-angle telescope is 1500 mm and the focal ratio, F/# = 8.5. The same parameters for the wide-angle optics are 200 mm and 3.5, respectively. However, no attempt was made to measure the focal length at component-level calibrations because these results would be of little practical use. Instead, the focal length of each ISS camera was determined by direct theodolite observations of the vidicon reseau grid through the optics. This approach ensures measurement of the true subsystem focal length. The method and its application to the ISS cameras are described in Section IV-B-1.

B. FILTER SPECTRAL TRANSMITTANCE

Each narrow-angle and wide-angle ISS camera is equipped with a filter wheel [Figure 3-1(b)] containing eight filter positions. This wheel can be stepped one through seven positions in forward direction per frame. A typical set of narrow-angle camera filters is shown in Figure 3-10; and the wide-angle camera filters, in Figure 3-11. The filter wheel positions are also summarized in Table 3-4.

The filter substrates were made from T-20 suprasil #2 [6]. To meet Jupiter radiation requirements, they were coated as follows:

(1) All clear filters were coated[7] with modified mark 8 anti-reflectance coating with a range of 350 to 570 nm for 0.6% or less reflectance per side. The resulting representative reflectance curve is shown in Figure 3-12.

(2) With three exceptions, all color filters were coated with all-dielectric material.[8] Of the two spectral curves supplied, one was at ambient conditions; the other, at a vacuum level of 1×10^{-5} torr and a temperature of 0°C. All ambient curves were also verified at JPL.

(3) The three exceptions, mentioned in (2), are the 1CW sodium-D, 2CW methane (6190) and 3CW methane (Uranus) filters. These filters were of a sandwich-type of construction with a fused-quartz spacer. The void was filled with suitable filter material, and the edges were sealed with a space-proven epoxy glue. No spectral curves were furnished with

---

[6] By Optical Components, Inc., Irwindale, California.

[7] By Herron Optics, Long Beach, California.

[8] Ibid.

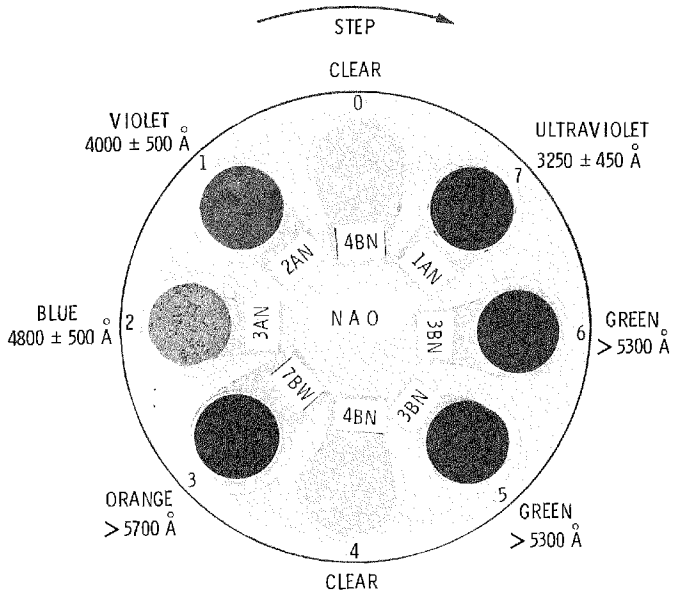

Figure 3-10. Narrow-angle ISS camera filter-wheel positions (as seen from front of optics)

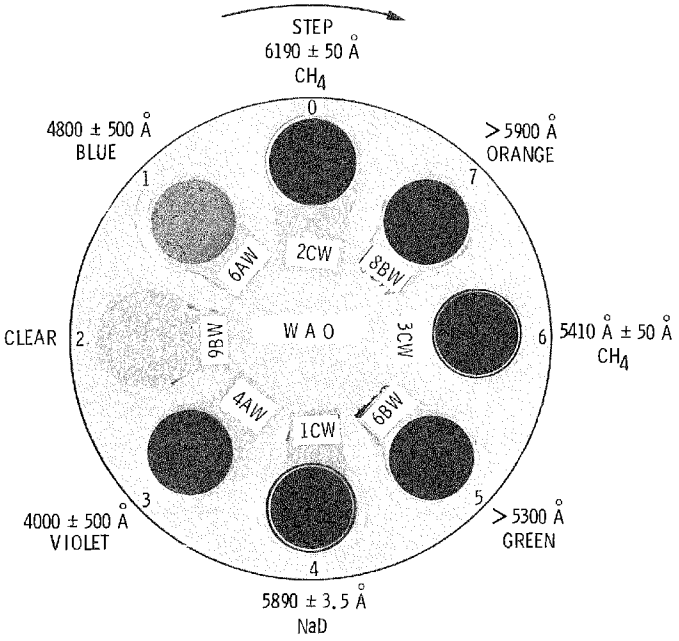

Figure 3-11. Wide-angle ISS camera filter-wheel positions (as seen from front of optics)

Table 3-4. A typical set of ISS camera filters

ISS camera	Filter-wheel position	Filter	Filter class ID	Wavelength, Å	Type
Narrow-angle	0	Clear	4BN	—	Interference
	1	Violet	2AN	4000 ±500	
	2	Blue	3AN	4800 ±500	
	3	Orange	7BW (thick)	>5700	
	4	Clear	4BN	—	
	5	Green	3BN	>5300	
	6	Green	3BN	>5300	
	7	UV	1AN	3250 ±450	
Wide-angle	0	Methane (6190)	2CW	6190 ±50	
	1	Blue	6AW	4800 ±500	
	2	Clear	9BW	—	
	3	Violet	4AW	4000 ±500	
	4	Sodium-D	1CW	5890	
	5	Green	6BW	>5300	
	6	Methane (Uranus)	3CW	5410 ±50	
	7	Orange	8BW	>5900	

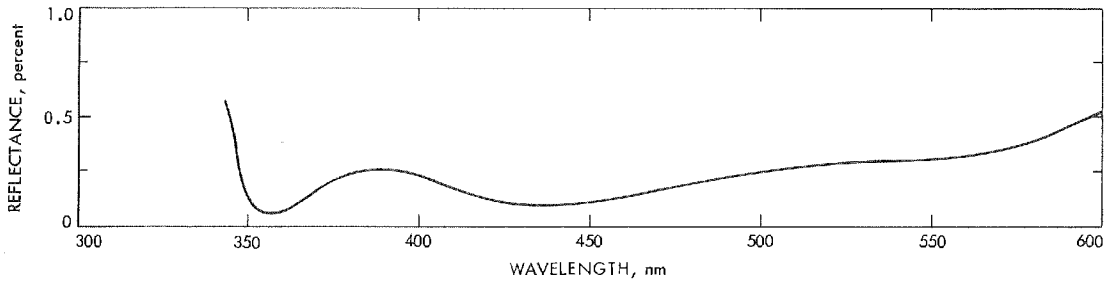

Figure 3-12. Reflectance of ISS camera clear filters after coating

these filters,[9] but the basic spectral information supplied was verified at JPL under ambient conditions. A few selected filters were also tested by several independent sources under extended conditions and were found to be satisfactory in performance.

Spectral measurements at source were taken on Beckman spectrophotometers, and verifications at JPL were made with a Cary 14 spectrophotometer. Each test scan was run from 2000 to 7000 Å to check for eventual leaks outside the passband. The transmission accuracy was kept within ±2% as required in Reference 2-1.

It would be beyond the scope of this report to document the spectral transmittance curves of all 48 flight filters. Therefore, only a typical sample set is shown in Figures 3-13 through 3-25. However, the differences between all individual filters of the same class ID, which are on file at JPL, are rather insignificant. Also, as can be seen from these figures, the wavelength shift under vacuum conditions is very small for all cases.

The filter factors for all filter positions of the flight ISS cameras were calculated at JPL for the JPL light cannons and for a number of celestial bodies as light sources. These important data are documented in Tables 3-5 through 3-8.

[9] Manufactured by Baird-Atomic, Inc., Massachusetts.

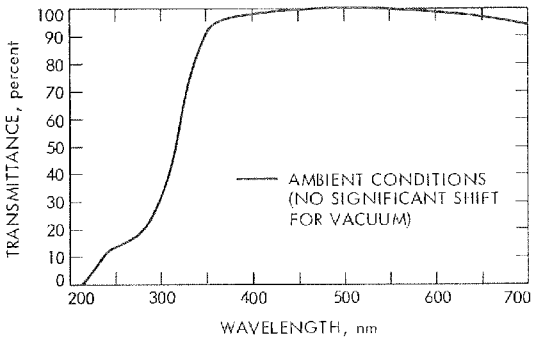

Figure 3-13. Spectral transmittance, clear filter 4BN and 9BW (position narrow-angle 0, 4 and wide-angle 2)

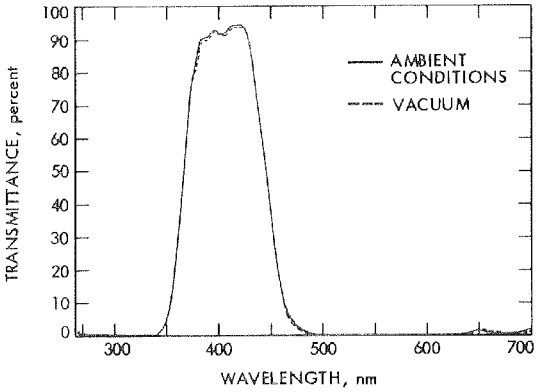

Figure 3-14. Spectral transmittance, violet filter 2AN (position narrow-angle 1)

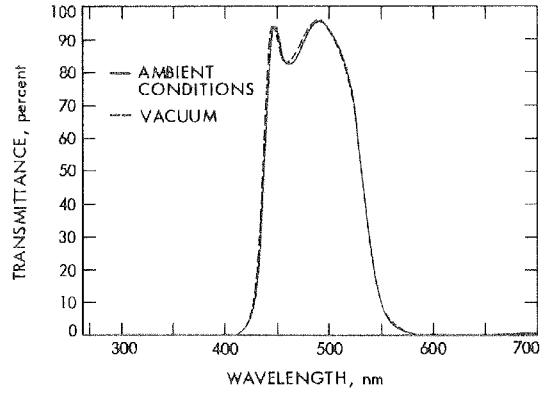

Figure 3-15. Spectral transmittance, blue filter 3AN (position narrow-angle 2)

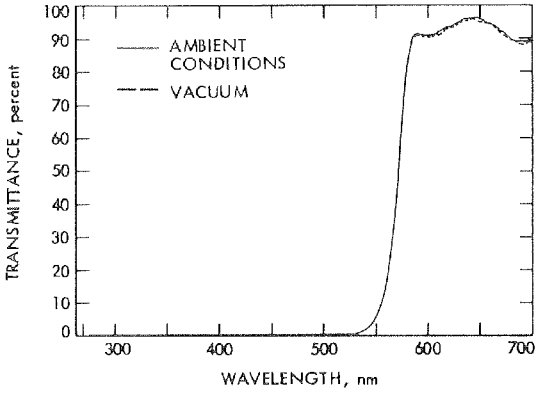

Figure 3-16. Spectral transmittance, orange filter 7BW-thick (position narrow-angle 3)

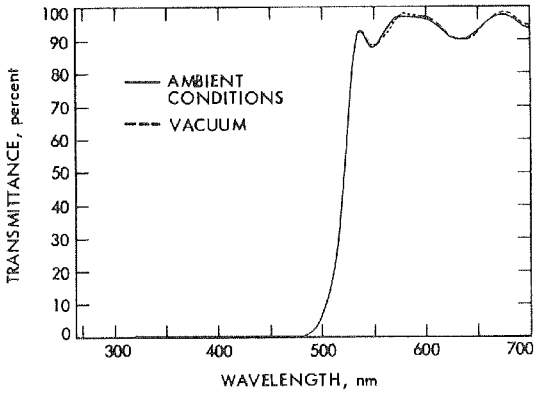

Figure 3-17. Spectral transmittance, green filter 3BN (position narrow-angle 5 and 6)

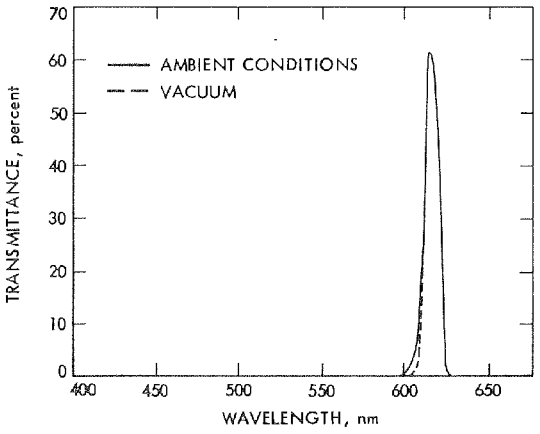

Figure 3-19. Spectral transmittance, methane (6190) filter 2CW (position wide-angle 0)

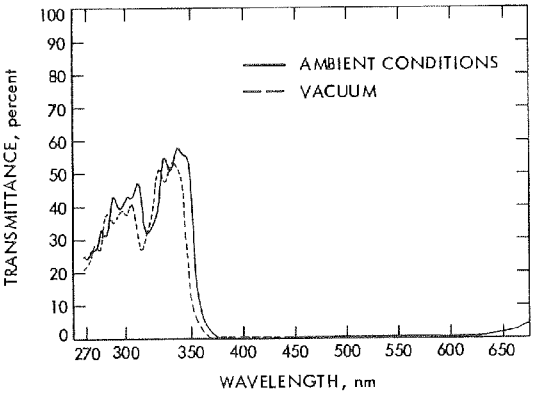

Figure 3-18. Spectral transmittance, ultraviolet filter 1 AN (position narrow-angle 7)

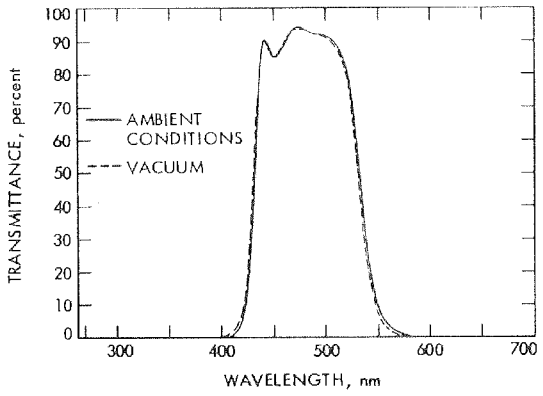

Figure 3-20. Spectral transmittance, blue filter 6AW (position wide-angle 1)

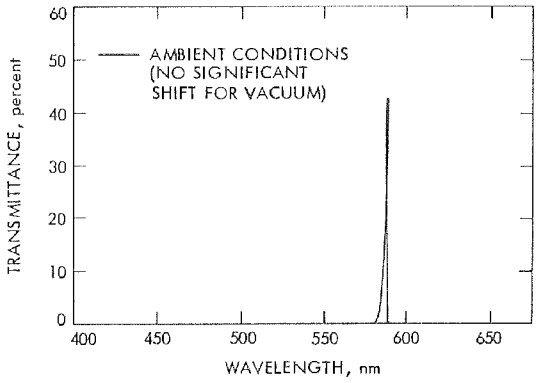

Figure 3-22. Spectral transmittance, sodium-D filter 1CW (position wide-angle 4)

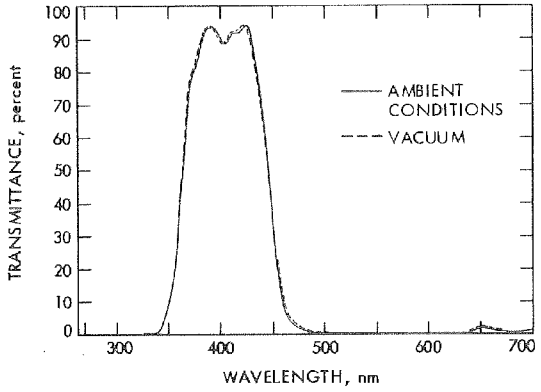

Figure 3-21. Spectral transmittance, violet filter, 4AW (position wide-angle 3)

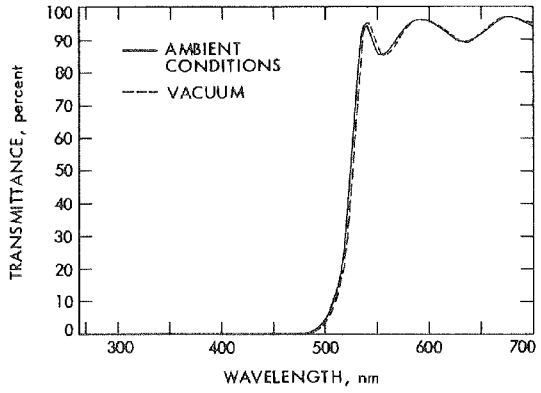

Figure 3-23. Spectral transmittance, green filter 6BW (position wide-angle 5)

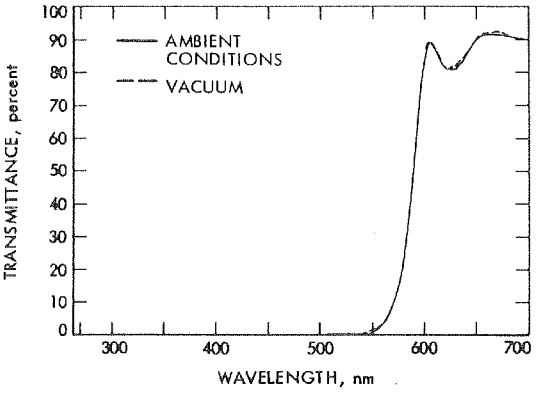

Figure 3-25. Spectral transmittance, orange filter 8BW (position wide-angle 7)

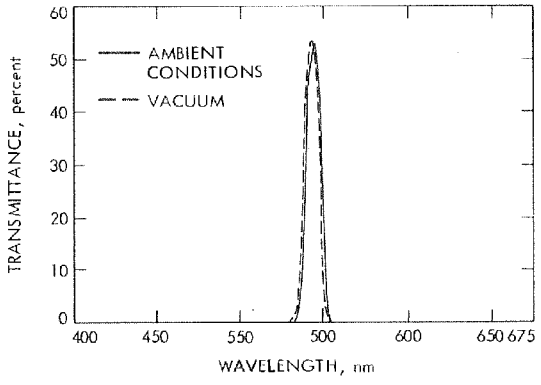

Figure 3-24. Spectral transmittance methane (Uranus) filter 3CW (position wide-angle 6)

Table 3-5. Filter factors, ISS S/N 04

Light source	Filter position							
	0[a]	1	2	3	4[a]	5	6[a]	7
Sun	96	1.84	1.00	3.91	148	3.47	48	14.8
Jupiter		1.87		4.48		3.12		12.8
Saturn		1.96		5.51		2.67		10.6
Moon		1.94		4.68		2.89		11.3
Io		1.87		5.31		2.86		11.7
Europa		1.86		4.39		3.17		13.5
Ganymede		1.85		4.24		3.24		13.6
Callisto		1.86		4.51		3.11		12.9
Amalthea		1.84		3.91		3.47		14.8
Mimas		1.84		3.93		3.46		14.8
Enceladus		1.84		3.93		3.46		14.8
Tethys		1.84		3.93		3.46		14.8
Dione		1.84		3.90		3.49		14.8
Rhea		1.85		4.04		3.37		14.3
Titan		2.03		5.59		2.54		9.89
Hyperion		1.84		3.93		3.46		14.8
Iapetus/dk		1.84		3.96		3.44		14.5
Phoebe		1.84		3.91		3.47		14.8
Rings		1.88		4.76		2.98		12.3
Iapetus/lt		1.84		3.84		3.52		15.0
13-cm L/C		1.79		5.36		3.03		12.0

[a]Filter factors for filters 0, 4, and 6 are only approximate and may have to be verified during the mission.

Table 3-6. Filter factors, ISS S/N 05

Light source	Filter position							
	0	1	2	3	4	5	6	7
Sun	1.00	3.44	2.54	9.92	1.00	4.39	Same as filter 5	39.2
Jupiter		3.96	2.39	8.21		3.73		58.7
Saturn		5.20	2.34	6.53		3.04		59.2
Moon		4.12	2.48	7.41		3.48		50.4
Io		5.02	2.18	6.94		3.16		146.2
Europa		3.93	2.40	8.60		3.81		51.2
Ganymede		3.67	2.43	8.81		3.94		58.5
Callisto		4.12	2.33	8.02		3.63		66.8
Amalthea		3.44	2.54	9.92		4.39		39.2
Mimas		3.46	2.50	9.83		4.34		43.3
Enceladus		3.46	2.50	9.83		4.34		43.3
Tethys		3.46	2.50	9.83		4.34		43.3
Dione		3.43	2.53	9.98		4.41		40.6
Rhea		3.55	2.49	9.46		4.19		44.7
Titan		5.05	2.42	6.10		2.90		77.6
Hyperion		3.46	2.50	9.83		4.34		43.3
Iapetus/dk		3.46	2.53	9.73		4.35		40.7
Phoebe		3.44	2.54	9.92		4.39		39.2
Rings		4.29	2.33	7.62		3.46		71.3
Iapetus/lt		3.40	2.52	10.02		4.43		41.7
30-cm L/C #1		5.19	2.19	6.40		3.04		77

Table 3-7. Filter factors, ISS S/N 06

Light source	Filter position							
	0[a]	1	2	3	4[a]	5	6[a]	7
Sun	85	2.02	1.00	4.86	118	2.54	43	9.48
Jupiter		2.08		5.71		2.33		8.40
Saturn		2.22		7.28		2.06		7.12
Moon		2.18		6.08		2.19		7.50
Io		2.10		6.91		2.18		7.79
Europa		2.06		5.57		2.37		8.81
Ganymede		2.05		5.36		2.41		8.85
Callisto		2.07		5.75		2.33		8.44
Amalthea		2.02		4.86		2.54		9.48
Mimas		2.02		4.90		2.54		9.45
Enceladus		2.02		4.90		2.54		9.45
Tethys		2.02		4.90		2.54		9.45
Dione		2.02		4.86		2.56		9.46
Rhea		2.03		5.07		2.48		9.20
Titan		2.30		7.48		1.98		6.75
Hyperion		2.02		4.90		2.54		9.45
Iapetus/dk		2.02		4.94		2.53		9.29
Phoebe		2.02		4.86		2.54		9.48
Rings		2.10		6.13		2.25		8.08
Iapetus/lt		2.01		4.77		2.58		9.58
13-cm L/C		2.02		6.86		2.27		7.73

[a]Filter factors for filters 0, 4, and 6 are only approximate and may have to be verified during the mission.

Table 3-8. Filter factors, ISS S/N 07

Light source	Filter position							
	0	1	2	3	4	5	6	7
Sun	1.00	3.47	2.52	10.1	1.00	3.91	4.03	40.8
Jupiter		3.99	2.39	8.35		3.34	3.44	61.5
Saturn		5.22	2.35	6.66		2.75	2.83	62.3
Moon		4.17	2.49	7.52		3.13	3.22	52.8
Io		5.02	2.19	7.10		2.85	2.93	154.0
Europa		3.96	2.40	8.77		3.40	3.50	53.6
Ganymede		3.70	2.43	8.97		3.52	3.63	61.2
Callisto		4.14	2.33	8.18		3.26	3.35	70.0
Amalthea		3.47	2.52	10.1		3.91	4.03	40.8
Mimas		3.49	2.49	9.98		3.86	3.98	45.2
Enceladus		3.49	2.49	9.98		3.86	3.98	45.2
Tethys		3.49	2.49	9.98		3.86	3.98	45.2
Dione		3.46	2.51	10.1		3.92	4.04	42.4
Rhea		3.58	2.48	9.61		3.73	3.85	46.7
Titan		5.08	2.43	6.22		2.63	2.70	81.8
Hyperion		3.49	2.49	9.98		3.86	3.98	45.2
Iapetus/dk		3.50	2.52	9.88		3.87	3.99	42.4
Phoebe		3.47	2.52	10.1		3.91	4.03	40.8
Rings		4.31	2.34	7.77		3.11	3.20	74.8
Iapetus/lt		3.43	2.51	10.2		3.93	4.06	43.5
30-cm L/C #1		5.19	2.20	6.59		2.76	2.83	60

C. SHUTTER TIMES

The ISS shutters are of the mechanical focal-plane type with two blades: one blade opens the aperture, and the other blade covers it after the desired exposure interval. The exposure time is controlled by the flight data subsystem (FDS), which provides a separate pulse to start each of the two shutter blades.

Each shutter assembly has a different response to commands because of differing frictional forces and other influences. The actual exposure and shading data were obtained at 35, 25, and -15°C.

A shutter test fixture illuminated five diodes with collimated light for measurements of shutter characteristics. The five diodes were equally spaced at 3.75 mm for wide-angle shutters and 3.15 mm for narrow-angle shutters. The true times obtained for a commanded exposure of 5.0, 12.5, 25.0, 50.0, and 97.5 ms are summarized in Table 3-9. As can be seen, the true shutter times are shorter than the commanded time for all ISS cameras, but what is even more important is that the difference is consistently systematic. These systematic shutter time offsets, listed in Table 3-10, were also verified during radiometric reciprocity calibrations (see Section IV-A-3 for full details).

The shutter shading characteristics are shown in Figures 3-26 through 3-31 for a commanded 12.5-ms exposure. With only one exception, the deviations for all ISS cameras lie within ±0.4 ms, which is excellent. The only exception is ISS camera S/N 07 at 35°C, where the deviation reaches +0.51 and -0.64 ms (Figure 3-31). The accuracy of several repeated measurements was between ±0.01 to ±0.07 ms, i.e., well within the ±1% limit set by Reference 2-1. Only in the case of shutter blade bounce, the accuracy drastically deteriorated up to ±0.8 ms, but this is an unacceptable mode anyway.

Only diodes 2 to 4 lie within the active ISS vidicon format, although the average shutter time is based on all five diodes (four diodes wherever shutter blade bounce is present). The shutter blade bounce for diode 5, which is indicated in Figures 3-26 to 3-29 and 3-31, starts at -5°C or -8°C. No attempt was made to determine how far back this bounce really goes, but it was assumed that it does not reach into the active vidicon format. The results and analysis of the subsystem level radiometric tests indicate that this assumption was justified (see Section IV-A-1); but, to stay on the safe side, freezing operational temperatures should be avoided, if at all possible.

Table 3-11 lists all 24 anticipated operational shutter-time commands that can be used for the ISS cameras. However, during component-level calibrations of the shutters, any shutter time could be commanded. It is obvious that the systematic true shutter time offset (Table 3-10) will affect only the shortest shutter times and will become insignificant for the longer shutter times (see radiometric reciprocity results in Section IV-A-3).

Table 3-9. ISS component-level shutter times

Temperature	True shutter-time, ms	Commanded shutter time, ms					
		ISS S/N 03	ISS S/N 04	ISS S/N 05	ISS S/N 06	ISS S/N 07	ISS S/N 08
		Shutter S/N 07	Shutter S/N 06	Shutter S/N 09	Shutter S/N 12	Shutter S/N 11	Shutter S/N 08
+35°C	5.0	7.06	7.14	5.82	6.81	5.59	6.05
	12.5	14.52	14.63	13.33	14.36	12.58	13.57
	25.0	27.12	27.15	25.90	26.86	25.20	26.04
	50.0	52.08	52.15	50.90	51.93	50.24	51.13
	97.5	99.67	99.66	98.41	99.43	97.74	98.64
+25°C	5.0	7.12	6.66	6.04	6.90	6.33	6.16
	12.5	14.59	14.17	13.59	14.39	13.87	13.67
	25.0	27.10	26.71	26.11	26.88	26.27	26.21
	50.0	52.16	51.78	51.11	51.95	51.40	51.25
	97.5	99.66	99.28	98.57	99.44	98.90	98.75
-15°C	5.0	7.09	Not available	5.91	6.84	6.49	6.12
(All five diodes; includes shutter-blade bounce)	12.5	15.49		14.11	14.95	14.02	14.15
	25.0	27.92		26.66	27.33	26.51	26.31
	50.0	52.92		51.62	52.03	51.60	51.30
	97.5	100.45		99.14	99.63	99.09	98.82
-15°C	5.0	7.09	6.25	5.81	6.84	Not necessary; no shutter-blade bounce	6.02
(Four diodes only; without shutter-blade bounce)	12.5	14.55	13.64	13.48	14.27		13.55
	25.0	27.01	26.19	25.93	26.79		26.15
	50.0	52.00	51.21	50.88	51.81		51.28
	97.5	99.52	98.70	98.40	99.31		98.82

Table 3-10. Systematic ISS true shutter-time offset

Temperature	Systematic true shutter-time offset, ms					
	ISS S/N 03	ISS S/N 04	ISS S/N 05	ISS S/N 06	ISS S/N 07	ISS S/N 08
	Shutter S/N 07	Shutter S/N 06	Shutter S/N 09	Shutter S/N 12	Shutter S/N 11	Shutter S/N 08
+35°C	-2.09 ±0.03	-2.15 ±0.01	-0.87 ±0.02	-1.88 ±0.02	-0.27 ±0.09	1.09 ±0.02
+25°C	-2.13 ±0.01	-1.72 ±0.03	-1.08 ±0.01	-1.91 ±0.01	-1.35 ±0.02	-1.21 ±0.02
-15°C (Includes bounce)	-2.77 ±0.17	Not available	-1.49 ±0.14	-2.16 ±0.11	-1.54 ±0.02	-1.34 ±0.09
-15°C (Without bounce)	-2.03 ±0.02	-1.20 ±0.02	-0.92 ±0.02	-1.80 ±0.01	No bounce	-1.16 ±0.06

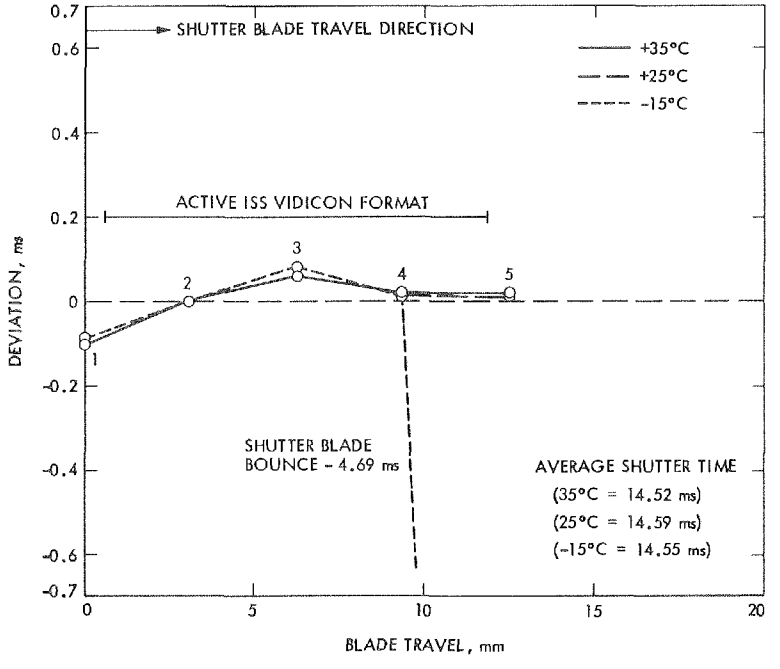

Figure 3-26. ISS S/N 03 (shutter S/N 07) shutter shading

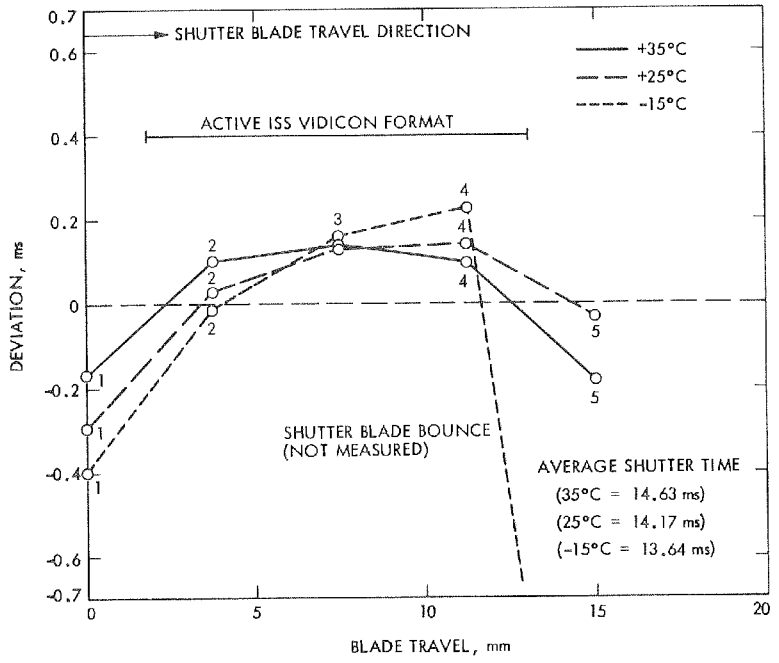

Figure 3-27. ISS S/N 04 (shutter S/N 06) shutter shading

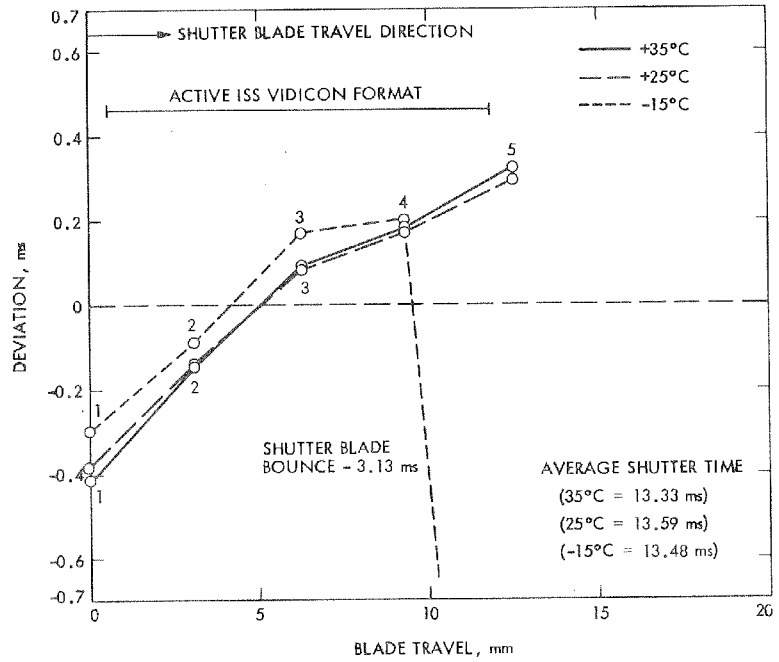

Figure 3-28. ISS S/N 05 (shutter S/N 09) shutter shading

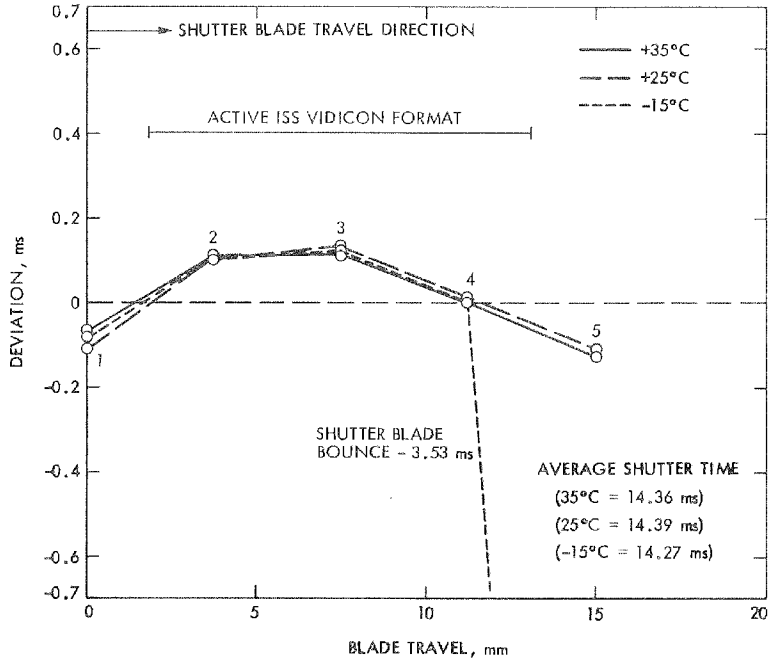

Figure 3-29. ISS S/N 06 (shutter S/N 12) shutter shading

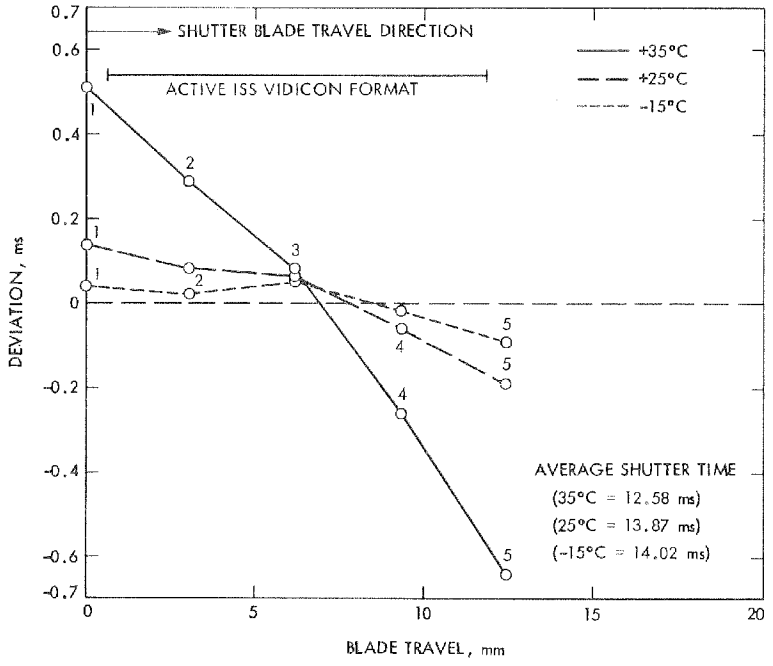

Figure 3-30. ISS S/N 07 (shutter S/N 11) shutter shading

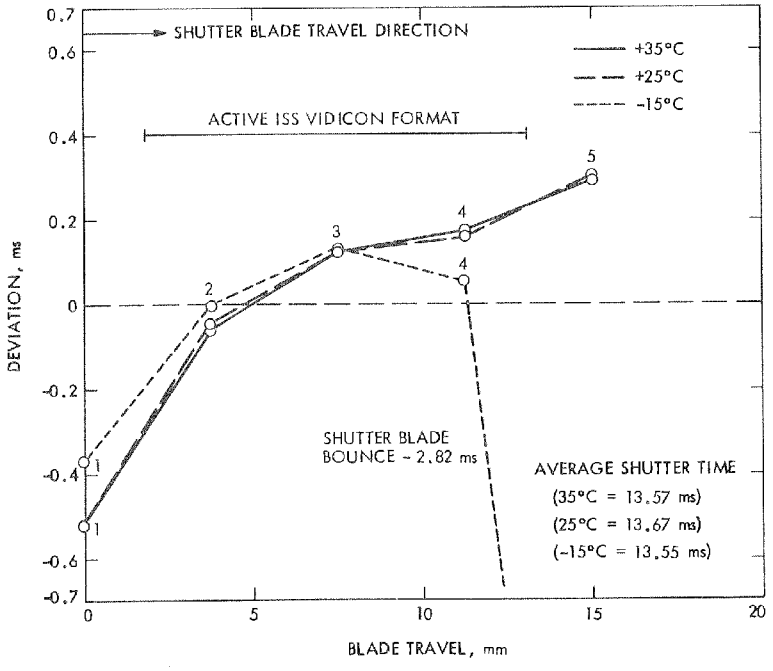

Figure 3-31. ISS S/N 08 (shutter S/N 08) shutter shading

Table 3-11. Operational ISS shutter times

BCE Code number	Command, ms	Shutter time (includes BCE/FDS offset), ms
1	5.0	7.01
2	7.5	9.51
3	12.5	14.51
4	15.0	17.01
5	22.5	24.51
6	30	32.01
7	45	47.01
8	60	62.01
9	90	92.01
10	120	122.01
11	180	182.01
12	240	242.01
13	360	362.01
14	480	482.01
15	720	722.01
16	960	962.01
17	1,440	1,442.01
18	1,920	1,922.01
19	2,880	2,882.01
20	3,840	3,842.01
21	5,760	5,762.01
22	7,680	7,682.01
23	11,520	11,522.01
24	15,360	15,362.01

D. VIDICON

The sensor used in the Voyager-ISS camera system is a 25-mm all-magnet vidicon.[10] The vidicon storage surface (target) is a selenium-sulphur and can store a high resolution (1500 TVL) picture for over 100 s at room temperature.

The active image area on the target is 11.14 x 11.14 mm. Each frame consists of 800 lines with 800 picture elements (pixels) per line, i.e., 1 pixel = 14 μm. One frame requires 48 s for electronic readout. Following readout, light flooding is used to remove any residual image that might remain from the previous frame. At the end of light flooding, 14 erase frames are used to stabilize and prepare the vidicon target for the next exposure sequence. In addition to the normal frame readout of 48 s (1:1), four extended frame-time modes of 2:1, 3:1, 5:1, and 10:1 are available by command. Table 3-12 lists the specific rates and timing intervals for the ISS camera system. Figure 3-32 shows a typical ISS two-camera timing cycle.

1. Spectral Response

The relative spectral response was measured for each flight-quality vidicon. This information was used for tube selection and as a guide to determine which tube was to be installed in the wide-or narrow-angle cameras. The relative spectral response data from each tube was then combined with the other optical component responses to arrive at a complete system spectral response.

Spectral response measurements were made over the wavelength band from 280 to 640 nm by using a monochrometer and a 150-W xenon light source. Constant optical power was supplied to the vidicon over the measurement range by monitoring the flux at the vidicon faceplate with a Hewlett-Packard radiometer. The relative spectral response was then taken as the vidicon output current versus wavelength as shown in Figures 3-33 through 3-38. Measured irradiance uncertainty for the system was 10% and the wavelength uncertainty was ±0.1 nm, which is in compliance with the requirements given in Reference 2-1.

2. Reseau Geometry

Exact knowledge of X-Y coordinates of the vidicon reseau grid is essential for geometric corrections, navigational calculations, and photogrammetric evaluations of Voyager-ISS photography. The reseau grid was also used to determine focal length and field of view.

Both the narrow-angle and wide-angle cameras are equipped with the same type of vidicon; and a typical ISS reseau grid pattern, containing 202 reseau marks, is shown in Figure 3-39. The reseau marks were measured on a Moore universal measuring machine using a 150 x microscope. Both the traditional alignment method and the random

---

[10] Number B41-033, General Electro-dynamics Co.

Table 3-12. ISS specific rates and timing intervals

Parameter	Wide-angle camera	Narrow-angle camera
Effective focal length	200 mm	1500 mm
Focal ratio	f/3.5	f/8.5
Angular field-of-view	56 x 56 mr	7.4 x 7.4 mr
Resolution 10% modulation	At 36 line pair/mm	At 36 line pair/mm
Approximate fastest shutter speed	5 ms	5 ms
Active target raster	11.14 x 11.14 mm	11.14 x 11.14 mm
Raster aspect ratio	1:1	1:1
Pixel aspect ratio	1:1	1:1
Active scan lines per frame	800	800
Active pixels per line	800	800
Frame time	From 48 s (1:1) to 480 s (10:1)	
Bits/picture element	8	8
Number of filters	8	8
Active line time	55.694 ms	55.694 ms
Line synchronization time	From 4.3 ms (1:1) to 604.3 ms (10:1)	
Video base band	7.2 kHz	7.2 kHz
Video sample frequency	14.4 kHz	14.4 kHz
Star detection capability		
Star type:		
KO	6th at ≤5 μrad/s	9th at ≤5 μrad/s
AO	7th at ≤10 μrad/s	9th at ≤10 μrad/s
O	7th at ≤15 μrad/s	9th at ≤15 μrad/s

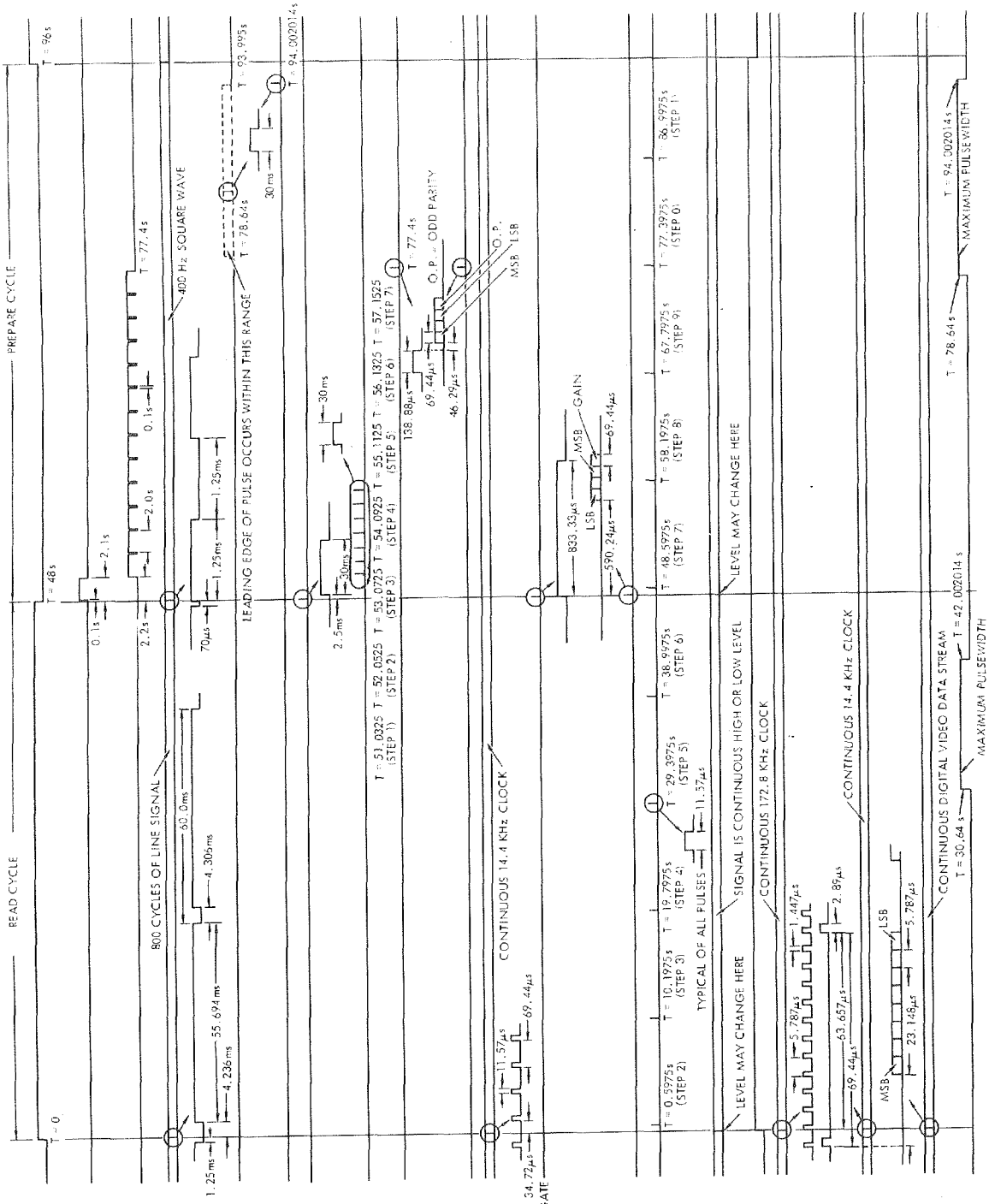

Figure 3-32. ISS timing diagram

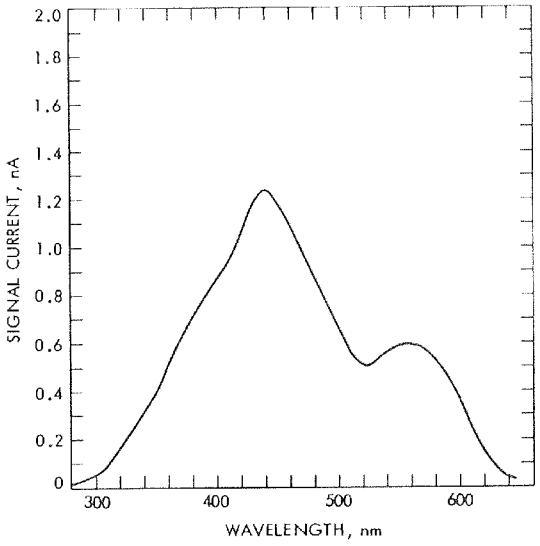

Figure 3-33. Relative spectral response, ISS S/N 03 (vidicon S/N 115 9880)

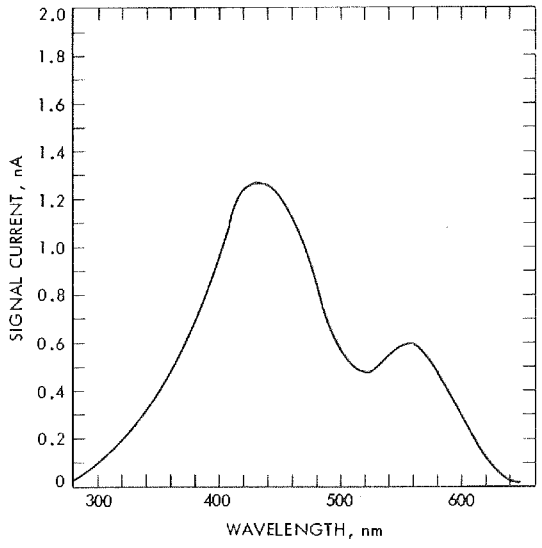

Figure 3-34. Relative spectral response, ISS S/N 04 (vidicon S/N 305 2719)

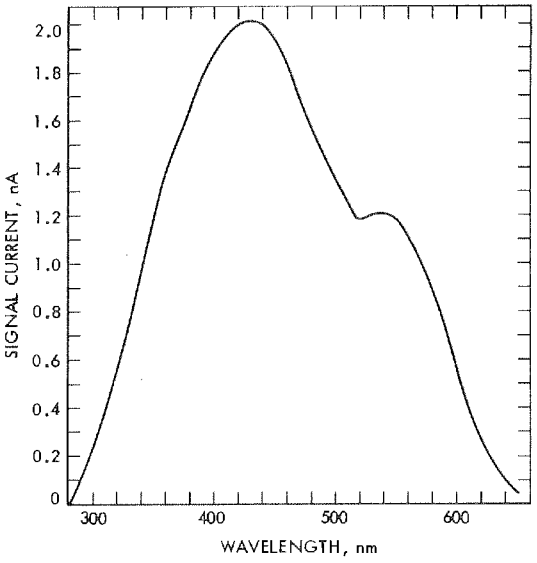

Figure 3-35. Relative spectral response, ISS S/N 05 (vidicon S/N 225 1901)

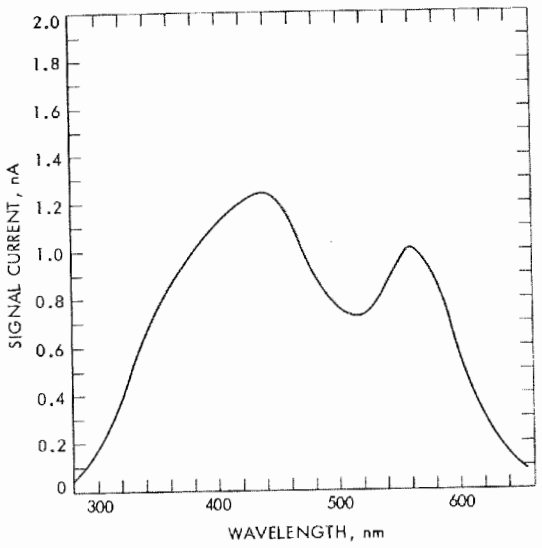

Figure 3-36. Relative spectral response, ISS S/N 06 (vidicon S/N 115 9903)

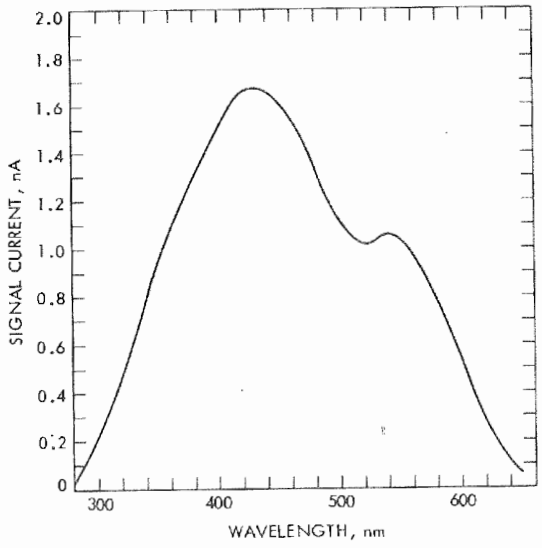

Figure 3-37. Relative spectral response, ISS S/N 07 (vidicon S/N 165 1402

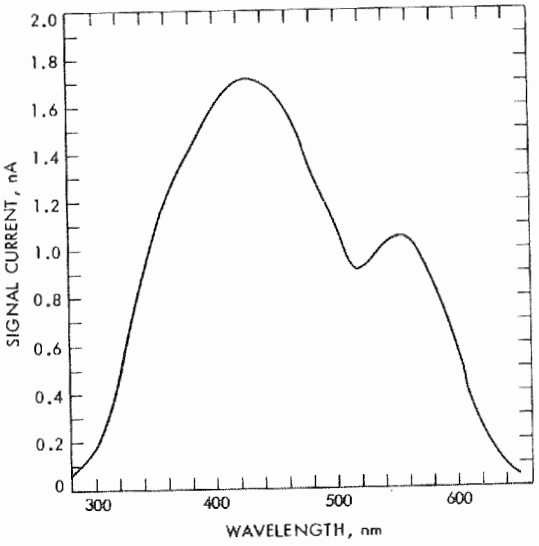

Figure 3-38. Relative spectral response, ISS S/N 08 (vidicon S/N 165 1407

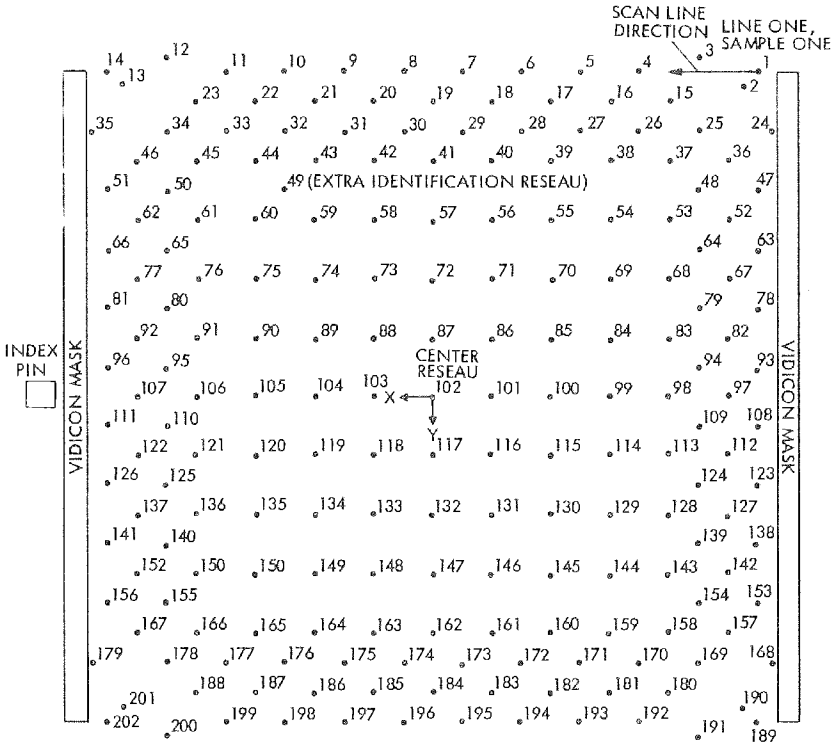

Figure 3-39. Reseau grid of Voyager ISS vidicons (The true reseau marks are square, approximately 0.04 x 0.04 mm)

method were used. The resulting positional accuracy is better than ±0.002 mm, which is very close to the limit of ±0.001 mm set in Reference 2-1.

The reseau marks are approximately square with an average size of 0.040 mm (2.9 pixels), and the great majority of them have sharp edges and corners. The measured coordinates (Tables 3-13 through 3-18) refer to the center of each reseau mark. It should be noted that, on the vidicon faceplate, reseau mark 1 (line one, sample one) appears in the upper right-hand corner, when viewed through the telescope with the camera mounting feet pointing up, but after IPL processing this reseau mark will appear in the usual upper left-hand corner of each photograph, thereby changing the direction of the plus X-axis.

Figures 3-40 through 3-45 show the location of each center reseau mark with respect to the vidicon tube axis. The average outside diameter (OD) of the tube is 26.085 mm.

Table 3-13. Reseau grid coordinates, ISS S/N 03 (vidicon S/N 115 9880), mm

Reseau	X	Y	Reseau	X	Y	Reseau	X	Y
1	-5.597	-5.597	46	5.292	-4.344	91	4.345	-1.085
2	-5.429	-5.431	47	-5.597	-3.801	92	5.292	-1.085
3	-4.887	-5.652	48	-4.887	-3.801	93	-5.597	-0.541
4	-3.801	-5.597	49	2.715	-3.801	94	-4.887	-0.541
5	-2.716	-5.597	50	4.888	-3.801	95	4.888	-0.541
6	-1.629	-5.597	51	5.598	-3.801	96	5.598	-0.541
7	-0.541	-5.597	52	-5.291	-3.257	97	-5.291	0.000
8	0.543	-5.597	53	-4.344	-3.257	98	-4.344	0.000
9	1.629	-5.597	54	-3.260	-3.257	99	-3.260	-0.000
10	2.715	-5.597	55	-2.173	-3.257	100	-2.173	-0.000
11	3.801	-5.597	56	-1.085	-3.257	101	-1.085	-0.000
12	4.888	-5.652	57	0.000	-3.257	102	0.000	0.000
13	5.431	-5.431	58	1.085	-3.257	103	1.085	0.000
14	5.598	-5.597	59	2.172	-3.257	104	2.172	-0.000
15	-4.344	-5.291	60	3.258	-3.257	105	3.258	-0.000
16	-3.260	-5.291	61	4.345	-3.257	106	4.345	-0.000
17	-2.173	-5.291	62	5.292	-3.257	107	5.292	0.000
18	-1.085	-5.291	63	-5.597	-2.716	108	-5.597	0.541
19	0.000	-5.291	64	-4.887	-2.716	109	-4.887	0.541
20	1.085	-5.291	65	4.888	-2.716	110	4.888	0.541
21	2.172	-5.291	66	5.598	-2.716	111	5.598	0.541
22	3.258	-5.291	67	-5.291	-2.172	112	-5.291	1.084
23	4.345	-5.291	68	-4.344	-2.172	113	-4.344	1.084
24	-5.654	-4.887	69	-3.260	-2.172	114	-3.260	1.084
25	-4.887	-4.887	70	-2.173	-2.172	115	-2.173	1.084
26	-3.801	-4.887	71	-1.085	-2.172	116	-1.085	1.084
27	-2.716	-4.887	72	0.000	-2.172	117	0.000	1.084
28	-1.629	-4.887	73	1.085	-2.172	118	1.085	1.084
29	-0.541	-4.887	74	2.172	-2.172	119	2.172	1.084
30	0.543	-4.887	75	3.258	-2.172	120	3.258	1.084
31	1.629	-4.887	76	4.345	-2.172	121	4.345	1.084
32	2.715	-4.887	77	5.292	-2.172	122	5.292	1.084
33	3.801	-4.887	78	-5.597	-1.629	123	-5.597	1.628
34	4.888	-4.887	79	-4.887	-1.629	124	-4.887	1.628
35	5.655	-4.887	80	4.888	-1.629	125	4.888	1.628
36	-5.291	-4.344	81	5.598	-1.629	126	5.598	1.628
37	-4.344	-4.344	82	-5.291	-1.085	127	-5.291	2.171
38	-3.260	-4.344	83	-4.344	-1.085	128	-4.344	2.171
39	-2.173	-4.344	84	-3.260	-1.085	129	-3.260	2.171
40	-1.085	-4.344	85	-2.173	-1.085	130	-2.173	2.171
41	0.000	-4.344	86	-1.085	-1.085	131	-1.085	2.171
42	1.085	-4.344	87	0.000	-1.085	132	0.000	2.171
43	2.172	-4.344	88	1.085	-1.085	133	1.085	2.171
44	3.256	-4.344	89	2.172	-1.085	134	2.172	2.171
45	4.345	-4.344	90	3.258	-1.085	135	3.258	2.171

Table 3-13 (contd)

Reseau	X	Y	Reseau	X	Y	Reseau	X	Y
136	4.345	2.171	158	-4.344	4.345	180	-4.344	5.292
137	5.292	2.171	159	-3.260	4.345	181	-3.260	5.292
138	-5.597	2.714	160	-2.173	4.345	182	-2.173	5.292
139	-4.887	2.714	161	-1.085	4.345	183	-1.085	5.292
140	4.888	2.714	162	0.000	4.345	184	0.000	5.292
141	5.598	2.714	163	1.085	4.345	185	1.085	5.292
142	-5.291	3.257	164	2.172	4.345	186	2.172	5.292
143	-4.344	3.257	165	3.258	4.345	187	3.258	5.292
144	-3.260	3.257	166	4.345	4.345	188	4.345	5.292
145	-2.173	3.257	167	5.292	4.345	189	-5.597	5.598
146	-1.085	3.257	168	-5.654	4.888	190	-5.429	5.430
147	0.000	3.257	169	-4.887	4.888	191	-4.887	5.655
148	1.085	3.257	170	-3.801	4.888	192	-3.801	5.598
149	2.172	3.257	171	-2.716	4.888	193	-2.716	5.598
150	3.258	3.257	172	-1.629	4.888	194	-1.629	5.598
151	4.345	3.257	173	-0.541	4.888	195	-0.541	5.598
152	5.292	3.257	174	0.543	4.888	196	0.543	5.598
153	-5.597	3.801	175	1.629	4.888	197	1.629	5.598
154	-4.887	3.801	176	2.715	4.888	198	2.715	5.598
155	4.888	3.801	177	3.801	4.888	199	3.801	5.598
156	5.598	3.801	178	4.888	4.888	200	4.888	5.655
157	-5.291	4.345	179	5.655	4.888	201	5.431	5.430
						202	5.598	5.598

Table 3-14. Reseau grid coordinates, ISS S/N 04 (vidicon S/N 305 2719), mm

Reseau	X	Y	Reseau	X	Y	Reseau	X	Y
1	-5.597	-5.599	46	5.292	-4.343	91	4.343	-1.086
2	-5.430	-5.430	47	-5.597	-3.801	92	5.292	-1.086
3	-4.887	-5.655	48	-4.887	-3.801	93	-5.598	-0.542
4	-3.802	-5.599	49	2.715	-3.800	94	-4.887	-0.542
5	-2.714	-5.599	50	4.886	-3.800	95	4.886	-0.543
6	-1.629	-5.599	51	5.598	-3.800	96	5.598	-0.543
7	-0.542	-5.599	52	-5.292	-3.258	97	-5.292	-0.000
8	0.543	-5.598	53	-4.344	-3.258	98	-4.344	-0.000
9	1.627	-5.598	54	-3.260	-3.258	99	-3.260	-0.000
10	2.715	-5.598	55	-2.174	-3.258	100	-2.174	-0.000
11	3.798	-5.598	56	-1.087	-3.258	101	-1.087	-0.000
12	4.886	-5.655	57	0.000	-3.258	102	0.000	0.000
13	5.431	-5.429	58	1.084	-3.257	103	1.084	0.000
14	5.598	-5.598	59	2.172	-3.257	104	2.172	0.000
15	-4.343	-5.292	60	3.259	-3.257	105	3.259	0.000
16	-3.259	-5.292	61	4.343	-3.257	106	4.343	0.000
17	-2.173	-5.292	62	5.292	-3.257	107	5.292	0.000
18	-1.087	-5.292	63	-5.597	-2.715	108	-5.598	0.542
19	0.000	-5.291	64	-4.887	-2.715	109	-4.887	0.542
20	1.084	-5.291	65	4.886	-2.714	110	4.886	0.543
21	2.172	-5.291	66	5.598	-2.714	111	5.598	0.543
22	3.259	-5.291	67	-5.292	-2.172	112	-5.292	1.085
23	4.343	-5.291	68	-4.344	-2.172	113	-4.344	1.085
24	-5.654	-4.887	69	-3.260	-2.172	114	-3.260	1.085
25	-4.887	-4.887	70	-2.174	-2.172	115	-2.174	1.085
26	-3.802	-4.887	71	-1.087	-2.172	116	-1.087	1.085
27	-2.714	-4.887	72	0.000	-2.172	117	-0.000	1.086
28	-1.629	-4.887	73	1.084	-2.172	118	1.084	1.086
29	-0.542	-4.887	74	2.172	-2.172	119	2.172	1.086
30	0.543	-4.887	75	3.259	-2.172	120	3.259	1.086
31	1.627	-4.887	76	4.343	-2.172	121	4.343	1.086
32	2.715	-4.887	77	5.292	-2.172	122	5.292	1.086
33	3.798	-4.887	78	-5.597	-1.629	123	-5.599	1.629
34	4.886	-4.887	79	-4.887	-1.629	124	-4.888	1.629
35	5.655	-4.887	80	4.886	-1.629	125	4.886	1.629
36	-5.291	-4.344	81	5.598	-1.629	126	5.598	1.629
37	-4.344	-4.344	82	-5.292	-1.085	127	-5.292	2.172
38	-3.260	-4.344	83	-4.344	-1.085	128	-4.344	2.172
39	-2.174	-4.344	84	-3.260	-1.085	129	-3.260	2.172
40	-1.087	-4.344	85	-2.174	-1.085	130	-2.174	2.172
41	0.000	-4.344	86	-1.087	-1.085	131	-1.087	2.172
42	1.084	-4.343	87	0.000	-1.086	132	-0.000	2.172
43	2.172	-4.343	88	1.084	-1.086	133	1.084	2.172
44	3.259	-4.343	89	2.172	-1.086	134	2.172	2.172
45	4.343	-4.343	90	3.259	-1.086	135	3.259	2.172

Table 3-14 (contd)

Reseau	X	Y	Reseau	X	Y	Reseau	X	Y
136	4.343	2.172	158	-4.344	4.344	180	-4.344	5.292
137	5.292	2.172	159	-3.260	4.344	181	-3.260	5.292
138	-5.599	2.715	160	-2.174	4.344	182	-2.174	5.292
139	-4.888	2.715	161	-1.087	4.344	183	-1.087	5.292
140	4.886	2.714	162	-0.000	4.344	184	-0.000	5.291
141	5.598	2.714	163	1.084	4.343	185	1.084	5.291
142	-5.292	3.258	164	2.172	4.343	186	2.172	5.291
143	-4.344	3.258	165	3.259	4.343	187	3.259	5.291
144	-3.260	3.258	166	4.343	4.343	188	4.343	5.291
145	-2.174	3.258	167	5.292	4.343	189	-5.599	5.598
146	-1.087	3.258	168	-5.656	4.887	190	-5.432	5.429
147	-0.000	3.258	169	-4.888	4.887	191	-4.888	5.655
148	1.084	3.257	170	-3.802	4.887	192	-3.802	5.598
149	2.172	3.257	171	-2.716	4.887	193	-2.716	5.598
150	3.259	3.257	172	-1.631	4.887	194	-1.631	5.598
151	4.343	3.257	173	-0.542	4.887	195	-0.542	5.598
152	5.292	3.257	174	0.543	4.887	196	0.543	5.598
153	-5.599	3.801	175	1.627	4.887	197	1.627	5.598
154	-4.888	3.801	176	2.715	4.887	198	2.715	5.598
155	4.886	3.800	177	3.798	4.887	199	3.798	5.598
156	5.598	3.800	178	4.886	4.887	200	4.886	5.655
157	-5.293	4.344	179	5.655	4.887	201	5.431	5.429
						202	5.598	5.598

Table 3-15. Reseau grid coordinates, ISS S/N 05 (vidicon S/N 225 1901), mm

Reseau	X	Y	Reseau	X	Y	Reseau	X	Y
1	-5.597	-5.595	46	5.291	-4.343	91	4.344	-1.085
2	-5.430	-5.428	47	-5.597	-3.798	92	5.291	-1.085
3	-4.887	-5.652	48	-4.887	-3.798	93	-5.597	-0.541
4	-3.802	-5.595	49	2.714	-3.800	94	-4.887	-0.541
5	-2.714	-5.595	50	4.887	-3.800	95	4.887	-0.543
6	-1.628	-5.595	51	5.598	-3.800	96	5.598	-0.543
7	-0.544	-5.595	52	-5.292	-3.256	97	-5.292	0.002
8	0.543	-5.595	53	-4.344	-3.256	98	-4.344	0.002
9	1.628	-5.595	54	-3.259	-3.256	99	-3.259	0.002
10	2.714	-5.595	55	-2.171	-3.256	100	-2.171	0.000
11	3.891	-5.595	56	-1.085	-3.257	101	-1.085	0.000
12	4.887	-5.652	57	0.000	-3.257	102	0.000	0.000
13	5.430	-5.428	58	1.086	-3.257	103	1.085	0.000
14	5.598	-5.595	59	2.172	-3.257	104	2.172	0.000
15	-4.344	-5.289	60	3.257	-3.257	105	3.257	0.000
16	-3.259	-5.289	61	4.344	-3.257	106	4.344	0.000
17	-2.171	-5.289	62	5.291	-3.257	107	5.291	0.000
18	-1.085	-5.289	63	-5.597	-2.712	108	-5.597	0.543
19	-0.000	-5.289	64	-4.887	-2.712	109	-4.887	0.543
20	1.085	-5.289	65	4.887	-2.714	110	4.887	0.542
21	2.172	-5.289	66	5.598	-2.714	111	5.598	0.542
22	3.257	-5.289	67	-5.292	-2.170	112	-5.292	1.086
23	4.344	-5.289	68	-4.344	-2.170	113	-4.344	1.086
24	-5.555	-4.885	69	-3.259	-2.170	114	-3.259	1.086
25	-4.887	-4.885	70	-2.171	-2.170	115	-2.171	1.086
26	-3.802	-4.885	71	-1.085	-2.172	116	-1.085	1.086
27	-2.714	-4.885	72	0.000	-2.172	117	0.000	1.086
28	-1.528	-4.885	73	1.085	-2.172	118	1.085	1.086
29	-0.544	-4.885	74	2.172	-2.172	119	2.172	1.086
30	0.543	-4.885	75	3.257	-2.172	120	3.257	1.086
31	1.628	-4.885	76	4.344	-2.172	121	4.344	1.086
32	2.714	-4.885	77	5.291	-2.172	122	5.291	1.086
33	3.891	-4.885	78	-5.597	-1.628	123	-5.597	1.630
34	4.887	-4.886	79	-4.887	-1.628	124	-4.887	1.630
35	5.654	-4.886	80	4.887	-1.629	125	4.887	1.630
36	-5.292	-4.341	81	5.598	-1.629	126	5.598	1.630
37	-4.344	-4.341	82	-5.292	-1.083	127	-5.292	2.173
38	-3.259	-4.341	83	-4.344	-1.083	128	-4.344	2.173
39	-2.171	-4.341	84	-3.259	-1.084	129	-3.259	2.173
40	-1.085	-4.341	85	-2.171	-1.084	130	-2.171	2.173
41	0.000	-4.343	86	-1.086	-1.085	131	-1.086	2.173
42	1.085	-4.343	87	0.000	-1.085	132	0.000	2.173
43	2.172	-4.343	88	1.086	-1.085	133	1.086	2.173
44	3.257	-4.343	89	2.172	-1.085	134	2.172	2.173
45	4.344	-4.343	90	3.257	-1.085	135	3.257	2.173

Table 3-15 (contd)

Reseau	X	Y	Reseau	X	Y	Reseau	X	Y
136	4.344	2.173	158	-4.344	4.345	180	-4.344	5.292
137	5.291	2.173	159	-3.259	4.345	181	-3.259	5.292
138	-5.597	2.716	160	-2.171	4.345	182	-2.171	5.292
139	-4.887	2.716	161	-1.086	4.345	183	-1.085	5.292
140	4.887	2.716	162	0.000	4.345	184	0.000	5.292
141	5.598	2.716	163	1.086	4.345	185	1.086	5.292
142	-5.292	3.259	164	2.172	4.345	186	2.172	5.292
143	-4.344	3.259	165	3.257	4.345	187	3.257	5.292
144	-3.259	3.259	166	4.344	4.345	188	4.344	5.292
145	-2.171	3.259	167	5.291	4.345	189	-5.597	5.599
146	-1.085	3.259	168	-5.555	4.889	190	-5.430	5.432
147	0.000	3.259	169	-4.887	4.889	191	-4.887	5.656
148	1.085	3.259	170	-3.802	4.889	192	-3.802	5.599
149	2.172	3.259	171	-2.714	4.889	193	-2.714	5.599
150	3.257	3.259	172	-1.628	4.889	194	-1.628	5.599
151	4.344	3.259	173	-0.544	4.889	195	-0.544	5.599
152	5.291	3.259	174	0.543	4.889	196	0.543	5.599
153	-5.597	3.802	175	1.628	4.889	197	1.628	5.599
154	-4.887	3.802	176	2.714	4.889	198	2.714	5.599
155	4.887	3.802	177	3.801	4.889	199	3.801	5.599
156	5.598	3.802	178	4.887	4.889	200	4.887	5.656
157	-5.292	4.345	179	5.554	4.889	201	5.430	5.432
						202	5.598	5.599

Table 3-16. Reseau grid coordinates, ISS S/N 06 (vidicon S/N 115 9903), mm

Reseau	X	Y	Reseau	X	Y	Reseau	X	Y
1	-5.596	-5.596	46	5.291	-4.343	91	4.343	-1.087
2	-5.429	-5.429	47	-5.596	-3.800	92	5.291	-1.087
3	-4.886	-5.653	48	-4.886	-3.800	93	-5.597	-0.542
4	-3.801	-5.596	49	2.715	-3.800	94	-4.884	-0.542
5	-2.715	-5.596	50	4.889	-3.801	95	4.889	-0.543
6	-1.627	-5.596	51	5.600	-3.801	96	5.600	-0.543
7	-0.542	-5.596	52	-5.290	-3.257	97	-5.290	-0.000
8	0.543	-5.596	53	-4.344	-3.257	98	-4.344	-0.000
9	1.627	-5.596	54	-3.256	-3.257	99	-3.256	-0.000
10	2.715	-5.596	55	-2.171	-3.257	100	-2.171	0.000
11	3.801	-5.596	56	-1.086	-3.257	101	-1.086	0.000
12	4.887	-5.653	57	0.000	-3.257	102	0.000	0.000
13	5.431	-5.429	58	1.087	-3.257	103	1.087	0.000
14	5.598	-5.596	59	2.171	-3.257	104	2.171	0.000
15	-4.344	-5.290	60	3.256	-3.257	105	3.256	0.000
16	-3.256	-5.290	61	4.342	-3.257	106	4.343	0.000
17	-2.171	-5.290	62	5.291	-3.257	107	5.291	-0.000
18	-1.086	-5.290	63	-5.596	-2.715	108	-5.597	0.539
19	0.000	-5.290	64	-4.886	-2.715	109	-4.884	0.544
20	1.087	-5.290	65	4.889	-2.716	110	4.889	0.541
21	2.171	-5.290	66	5.600	-2.716	111	5.600	0.541
22	3.256	-5.290	67	-5.290	-2.172	112	-5.290	1.086
23	4.342	-5.290	68	-4.344	-2.172	113	-4.344	1.086
24	-5.652	-4.885	69	-3.256	-2.172	114	-3.256	1.086
25	-4.886	-4.885	70	-2.171	-2.172	115	-2.171	1.086
26	-3.801	-4.885	71	-1.086	-2.172	116	-1.086	1.086
27	-2.715	-4.885	72	0.000	-2.172	117	0.000	1.086
28	-1.627	-4.885	73	1.087	-2.172	118	1.087	1.086
29	-0.542	-4.885	74	2.171	-2.172	119	2.171	1.086
30	0.543	-4.885	75	3.256	-2.172	120	3.256	1.084
31	1.627	-4.885	76	4.343	-2.173	121	4.343	1.084
32	2.715	-4.885	77	5.291	-2.173	122	5.291	1.084
33	3.801	-4.886	78	-5.597	-1.630	123	-5.597	1.628
34	4.887	-4.886	79	-4.886	-1.630	124	-4.884	1.628
35	5.655	-4.886	80	4.889	-1.630	125	4.889	1.628
36	-5.290	-4.342	81	5.600	-1.630	126	5.600	1.628
37	-4.344	-4.342	82	-5.290	-1.087	127	-5.290	2.172
38	-3.256	-4.343	83	-4.344	-1.087	128	-4.344	2.172
39	-2.171	-4.343	84	-3.256	-1.087	129	-3.256	2.172
40	-1.086	-4.343	85	-2.171	-1.086	130	-2.171	2.172
41	0.000	-4.343	86	-1.086	-1.086	131	-1.086	2.172
42	1.087	-4.343	87	0.000	-1.087	132	0.000	2.172
43	2.171	-4.343	88	1.087	-1.087	133	1.087	2.172
44	3.256	-4.343	89	2.171	-1.087	134	2.171	2.172
45	4.342	-4.343	90	3.256	-1.087	135	3.256	2.172

Table 3-16 (contd)

Reseau	X	Y	Reseau	X	Y	Reseau	X	Y
136	4.343	2.170	158	-4.344	4.343	180	-4.344	5.291
137	5.291	2.170	159	-3.256	4.343	181	-3.256	5.291
138	-5.597	2.714	160	-2.171	4.345	182	-2.171	5.291
139	-4.884	2.714	161	-1.086	4.345	183	-1.086	5.291
140	4.889	2.714	162	0.000	4.345	184	-0.000	5.291
141	5.600	2.714	163	1.087	4.345	185	1.087	5.291
142	-5.290	3.258	164	2.171	4.345	186	2.171	5.291
143	-4.344	3.258	165	3.256	4.345	187	3.256	5.291
144	-3.256	3.258	166	4.342	4.345	188	4.342	5.291
145	-2.171	3.258	167	5.291	4.345	189	-5.597	5.598
146	-1.086	3.258	168	-5.652	4.887	190	-5.429	5.429
147	-0.000	3.258	169	-4.886	4.887	191	-4.886	5.654
148	1.087	3.258	170	-3.801	4.887	192	-3.801	5.598
149	2.171	3.258	171	-2.715	4.887	193	-2.715	5.598
150	3.256	3.258	172	-1.627	4.887	194	-1.627	5.598
151	4.342	3.257	173	-0.542	4.887	195	-0.542	5.598
152	5.291	3.257	174	0.543	4.887	196	0.543	5.598
153	-5.597	3.799	175	1.627	4.887	197	1.627	5.598
154	-4.884	3.799	176	2.715	4.887	198	2.715	5.598
155	4.887	3.799	177	3.801	4.887	199	3.801	5.598
156	5.600	3.799	178	4.887	4.887	200	4.887	5.654
157	-5.290	4.343	179	5.655	4.887	201	5.431	5.429
						202	5.599	5.598

Table 3-17. Reseau grid coordinates, ISS S/N 07 (vidicon S/N 165 1402), mm

Reseau	X	Y	Reseau	X	Y	Reseau	X	Y
1	-5.597	-5.597	46	5.290	-4.343	91	4.344	-1.086
2	-5.430	-5.428	47	-5.597	-3.800	92	5.290	-1.086
3	-4.886	-5.654	48	-4.886	-3.800	93	-5.597	-0.542
4	-3.802	-5.597	49	2.713	-3.800	94	-4.886	-0.542
5	-2.714	-5.597	50	4.887	-3.800	95	4.887	-0.542
6	-1.629	-5.597	51	5.599	-3.800	96	5.599	-0.542
7	-0.542	-5.597	52	-5.291	-3.257	97	-5.291	-0.000
8	0.542	-5.597	53	-4.346	-3.257	98	-4.346	-0.000
9	1.627	-5.597	54	-3.258	-3.257	99	-3.258	-0.000
10	2.713	-5.597	55	-2.171	-3.257	100	-2.171	-0.000
11	3.800	-5.597	56	-1.086	-3.257	101	-1.086	-0.000
12	4.887	-5.654	57	0.000	-3.257	102	0.000	0.000
13	5.431	-5.428	58	1.085	-3.257	103	1.085	0.000
14	5.599	-5.597	59	2.171	-3.257	104	2.171	0.000
15	-4.346	-5.290	60	3.257	-3.257	105	3.257	0.000
16	-3.258	-5.290	61	4.344	-3.257	106	4.344	-0.000
17	-2.171	-5.290	62	5.290	-3.257	107	5.290	0.000
18	-1.086	-5.290	63	-5.597	-2.712	108	-5.597	0.542
19	0.000	-5.290	64	-4.886	-2.712	109	-4.886	0.542
20	1.085	-5.290	65	4.887	-2.712	110	4.887	0.542
21	2.171	-5.290	66	5.599	-2.712	111	5.599	0.542
22	3.257	-5.290	67	-5.291	-2.172	112	-5.291	1.086
23	4.344	-5.290	68	-4.346	-2.172	113	-4.346	1.086
24	-5.654	-4.886	69	-3.258	-2.172	114	-3.258	1.086
25	-4.886	-4.886	70	-2.171	-2.172	115	-2.171	1.086
26	-3.802	-4.886	71	-1.086	-2.172	116	-1.086	1.086
27	-2.714	-4.886	72	0.000	-2.172	117	-0.000	1.086
28	-1.629	-4.886	73	1.085	-2.172	118	1.085	1.086
29	-0.542	-4.886	74	2.171	-2.172	119	2.171	1.086
30	0.542	-4.886	75	3.257	-2.172	120	3.257	1.086
31	1.627	-4.886	76	4.344	-2.172	121	4.344	1.086
32	2.713	-4.886	77	5.290	-2.172	122	5.290	1.086
33	3.800	-4.886	78	-5.597	-1.629	123	-5.597	1.630
34	4.887	-4.886	79	-4.886	-1.629	124	-4.886	1.630
35	5.655	-4.886	80	4.887	-1.629	125	4.887	1.630
36	-5.291	-4.343	81	5.599	-1.629	126	5.599	1.630
37	-4.346	-4.343	82	-5.291	-1.086	127	-5.291	2.172
38	-3.258	-4.343	83	-4.346	-1.086	128	-4.346	2.172
39	-2.171	-4.343	84	-3.258	-1.086	129	-3.258	2.172
40	-1.086	-4.343	85	-2.171	-1.086	130	-2.171	2.172
41	0.000	-4.343	86	-1.086	-1.086	131	-1.086	2.172
42	1.085	-4.343	87	0.000	-1.086	132	0.000	2.172
43	2.171	-4.343	88	1.085	-1.086	133	1.085	2.172
44	3.257	-4.343	89	2.171	-1.086	134	2.171	2.172
45	4.344	-4.343	90	3.257	-1.086	135	3.257	2.172

Table 3-17 (contd)

Reseau	X	Y	Reseau	X	Y	Reseau	X	Y
136	4.344	2.172	158	-4.346	4.344	180	-4.346	5.291
137	5.290	2.172	159	-3.258	4.344	181	-3.258	5.291
138	-5.597	2.715	160	-2.171	4.344	182	-2.171	5.291
139	-4.886	2.715	161	-1.086	4.344	183	-1.086	5.291
140	4.887	2.715	162	0.000	4.344	184	0.000	5.291
141	5.599	2.715	163	1.085	4.344	185	1.085	5.291
142	-5.291	3.258	164	2.171	4.344	186	2.171	5.291
143	-4.346	3.258	165	3.257	4.344	187	3.257	5.291
144	-3.258	3.258	166	4.344	4.344	188	4.344	5.291
145	-2.171	3.258	167	5.290	4.344	189	-5.597	5.598
146	-1.086	3.258	168	-5.654	4.888	190	-5.430	5.430
147	0.000	3.258	169	-4.886	4.888	191	-4.886	5.656
148	1.085	3.258	170	-3.802	4.888	192	-3.802	5.598
149	2.171	3.258	171	-2.714	4.888	193	-2.714	5.598
150	3.257	3.258	172	-1.629	4.888	194	-1.629	5.598
151	4.344	3.258	173	-0.542	4.888	195	-0.542	5.598
152	5.290	3.258	174	0.542	4.888	196	0.542	5.598
153	-5.597	3.800	175	1.627	4.888	197	1.627	5.598
154	-4.886	3.800	176	2.713	4.888	198	2.713	5.598
155	4.887	3.800	177	3.800	4.888	199	3.800	5.598
156	5.599	3.800	178	4.887	4.888	200	4.887	5.656
157	-5.291	4.344	179	5.655	4.888	201	5.431	5.430
						202	5.599	5.598

Table 3-18. Reseau grid coordinates, ISS S/N 08 (vidicon S/N 165 1407), mm

Reseau	X	Y	Reseau	X	Y	Reseau	X	Y
1	-5.596	-5.596	46	5.292	-4.343	91	4.344	-1.086
2	-5.429	-5.428	47	-5.596	-3.800	92	5.292	-1.086
3	-4.886	-5.654	48	-4.886	-3.800	93	-5.596	-0.543
4	-3.799	-5.596	49	2.715	-3.800	94	-4.886	-0.543
5	-2.713	-5.596	50	4.888	-3.800	95	4.888	-0.543
6	-1.626	-5.596	51	5.599	-3.800	96	5.599	-0.543
7	-0.541	-5.596	52	-5.290	-3.257	97	-5.290	-0.000
8	0.544	-5.596	53	-4.344	-3.257	98	-4.344	-0.000
9	1.629	-5.596	54	-3.258	-3.257	99	-3.258	-0.000
10	2.715	-5.596	55	-2.170	-3.257	100	-2.170	-0.000
11	3.801	-5.596	56	-1.085	-3.257	101	-1.085	-0.000
12	4.888	-5.654	57	0.000	-3.257	102	0.000	0.000
13	5.431	-5.428	58	1.087	-3.257	103	1.087	0.000
14	5.599	-5.596	59	2.172	-3.257	104	2.172	0.000
15	-4.344	-5.289	60	3.259	-3.257	105	3.259	-0.000
16	-3.258	-5.289	61	4.344	-3.257	106	4.344	0.000
17	-2.170	-5.289	62	5.292	-3.257	107	5.292	0.000
18	-1.085	-5.289	63	-5.596	-2.715	108	-5.596	0.542
19	0.000	-5.289	64	-4.886	-2.715	109	-4.886	0.542
20	1.087	-5.289	65	4.888	-2.715	110	4.888	0.542
21	2.172	-5.289	66	5.599	-2.715	111	5.599	0.542
22	3.259	-5.289	67	-5.290	-2.172	112	-5.290	1.085
23	4.344	-5.289	68	-4.344	-2.172	113	-4.344	1.085
24	-5.652	-4.885	69	-3.258	-2.172	114	-3.258	1.085
25	-4.886	-4.885	70	-2.170	-2.172	115	-2.170	1.085
26	-3.799	-4.885	71	-1.085	-2.172	116	-1.085	1.085
27	-2.713	-4.885	72	0.000	-2.172	117	-0.000	1.085
28	-1.626	-4.885	73	1.087	-2.172	118	1.087	1.085
29	-0.541	-4.885	74	2.172	-2.172	119	2.172	1.085
30	0.544	-4.885	75	3.259	-2.172	120	3.259	1.085
31	1.629	-4.885	76	4.344	-2.172	121	4.344	1.085
32	2.715	-4.885	77	5.292	-2.172	122	5.292	1.085
33	3.801	-4.885	78	-5.596	-1.629	123	-5.596	1.629
34	4.888	-4.885	79	-4.886	-1.629	124	-4.886	1.629
35	5.655	-4.885	80	4.888	-1.629	125	4.888	1.629
36	-5.290	-4.343	81	5.999	-1.629	126	5.599	1.629
37	-4.344	-4.343	82	-5.290	-1.086	127	-5.290	2.172
38	-3.258	-4.343	83	-4.344	-1.086	128	-4.344	2.172
39	-2.170	-4.343	84	-3.258	-1.086	129	-3.258	2.172
40	-1.085	-4.343	85	-2.170	-1.086	130	-2.170	2.172
41	0.000	-4.343	86	-1.085	-1.086	131	-1.085	2.172
42	1.087	-4.343	87	0.000	-1.086	132	-0.000	2.172
43	2.172	-4.343	88	1.087	-1.086	133	1.087	2.172
44	3.259	-4.343	89	2.172	-1.086	134	2.172	2.172
45	4.344	-4.343	90	3.259	-1.086	135	3.259	2.172

Table 3-18 (contd)

Reseau	X	Y	Reseau	X	Y	Reseau	X	Y
136	4.344	2.172	158	-4.344	4.345	180	-4.344	5.291
137	5.292	2.172	159	-3.258	4.345	181	-3.258	5.291
138	-5.596	2.714	160	-2.170	4.345	182	-2.170	5.291
139	-4.886	2.714	161	-1.085	4.345	183	-1.085	5.291
140	4.888	2.714	162	0.000	4.345	184	-0.000	5.291
141	5.599	2.714	163	1.087	4.345	185	1.087	5.291
142	-5.290	3.257	164	2.172	4.345	186	2.172	5.291
143	-4.344	3.257	165	3.259	4.345	187	3.259	5.291
144	-3.258	3.257	166	4.344	4.345	188	4.344	5.291
145	-2.170	3.257	167	5.292	4.345	189	-5.596	5.597
146	-1.085	3.257	168	-5.652	4.887	190	-5.429	5.429
147	0.000	3.257	169	-4.886	4.887	191	-4.886	5.655
148	1.087	3.257	170	-3.799	4.887	192	-3.799	5.597
149	2.172	3.257	171	-2.714	4.887	193	-2.714	5.597
150	3.259	3.257	172	-1.628	4.887	194	-1.628	5.597
151	4.344	3.257	173	-0.542	4.887	195	-0.542	5.597
152	5.292	3.257	174	0.542	4.887	196	0.542	5.597
153	-5.596	3.801	175	1.629	4.887	197	1.629	5.597
154	-4.886	3.801	176	2.715	4.887	198	2.715	5.597
155	4.888	3.801	177	3.801	4.887	199	3.801	5.597
156	5.599	3.801	178	4.888	4.887	200	4.888	5.655
157	-5.290	4.345	179	5.655	4.887	201	5.431	5.429
						202	5.599	5.597

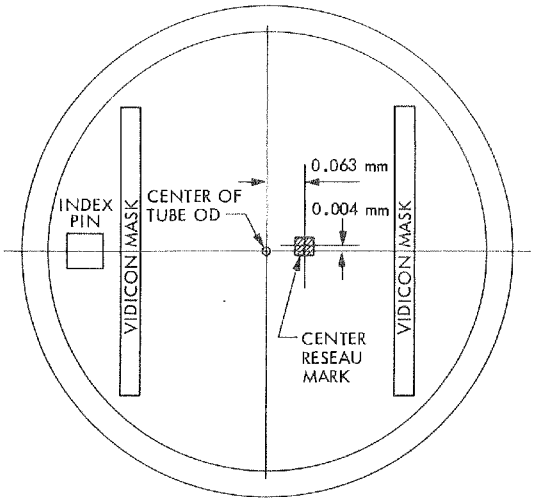

Figure 3-40. Vidicon tube geometry, ISS S/N 03 (vidicon S/N 115 9880)

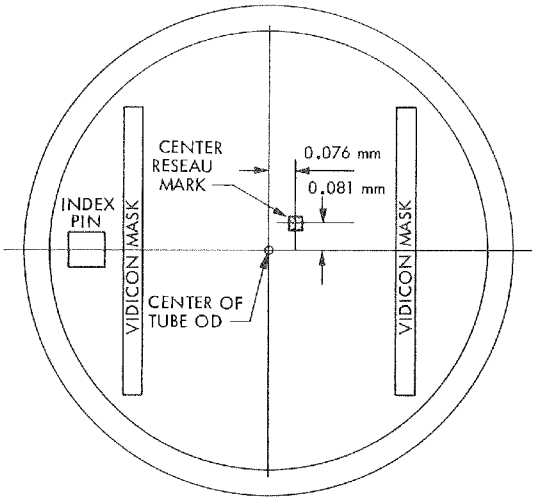

Figure 3-41. Vidicon tube geometry, ISS S/N 04 (vidicon S/N 305 2719)

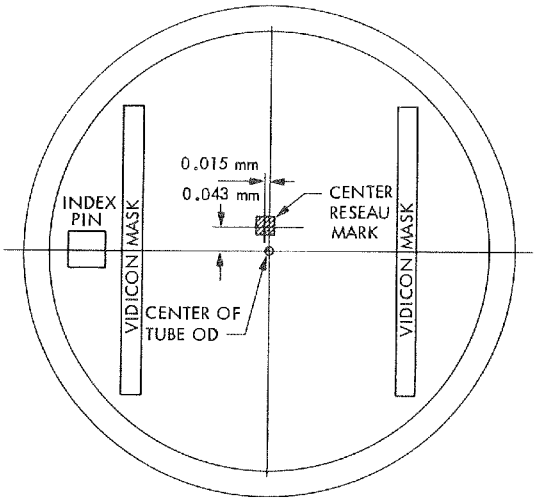

Figure 3-42. Vidicon tube geometry, ISS S/N 05 (vidicon S/N 225 1901)

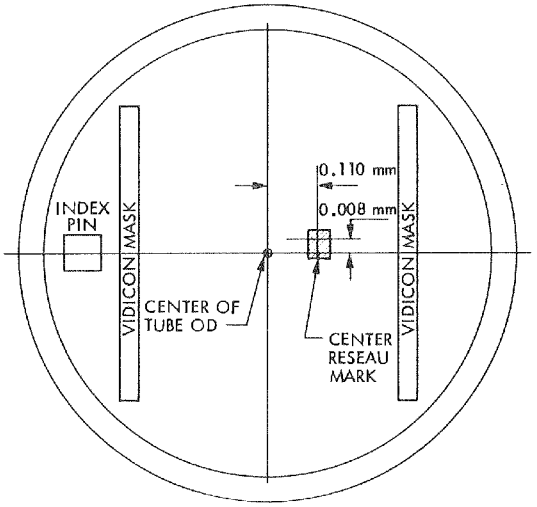

Figure 3-43. Vidicon tube geometry, ISS S/N 06 (vidicon S/N 115 9903)

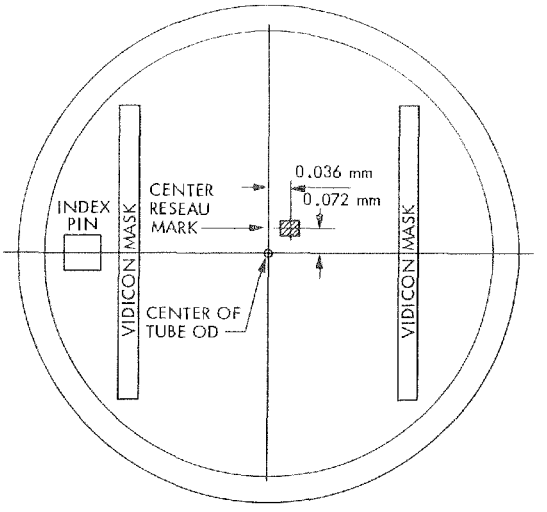

Figure 3-44. Vidicon tube geometry, ISS S/N 07 (vidicon S/N 165 1402)

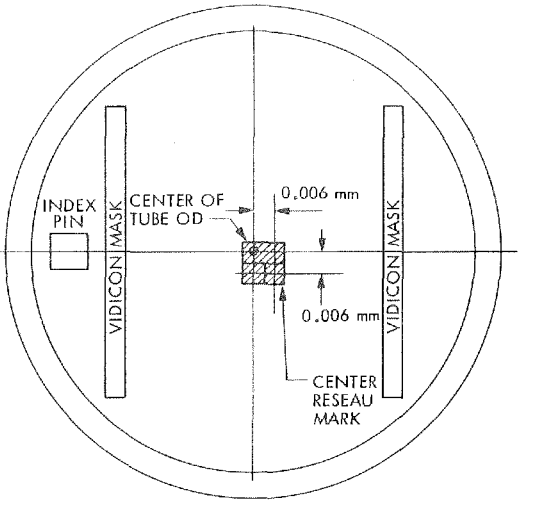

Figure 3-45. Vidicon tube geometry, ISS S/N 08 (vidicon S/N 165 1407)

3. Light Transfer Curves

The light transfer curves of the ISS flight cameras are shown in Figures 3-46 through 3-51. The target operating point was selected to minimize the temperature dependence of the light transfer characteristic. The system offset adjustment is set with the target of the vidicon at -15°C to allow a linear transfer characteristic without the lens/vidicon heaters. The resultant operating point exhibits a gamma of 1.00 ±0.02, thus allowing a large brightness dynamic range. The 8-bit encoding of video data provides 256 signal levels between black and white saturation. Because the vidicon has a dynamic range that exceeds 256:1, white saturation is electronic and not limited by the vidicon.

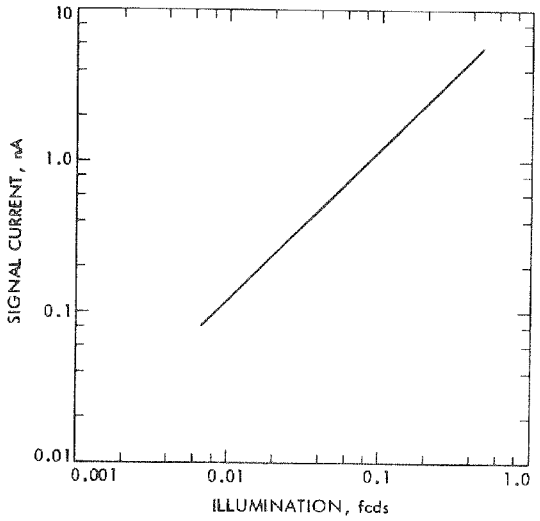

Figure 3-46. Light transfer curve, ISS S/N 03 (vidicon S/N 115 9880)

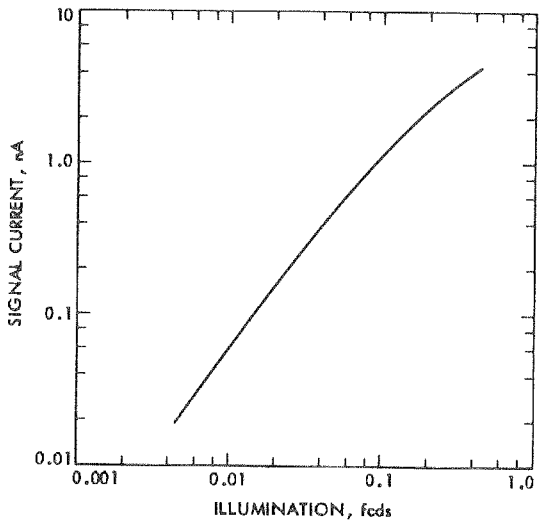

Figure 3-47. Light transfer curve, ISS S/N 04 (vidicon S/N 305 2719)

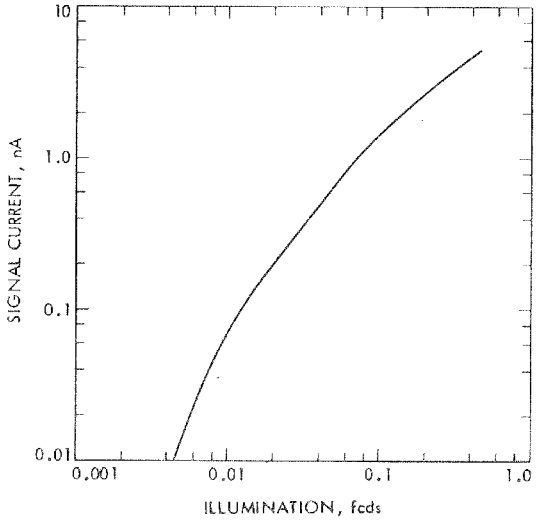

Figure 3-48. Light transfer curve, ISS S/N 05 (vidicon S/N 225 1901)

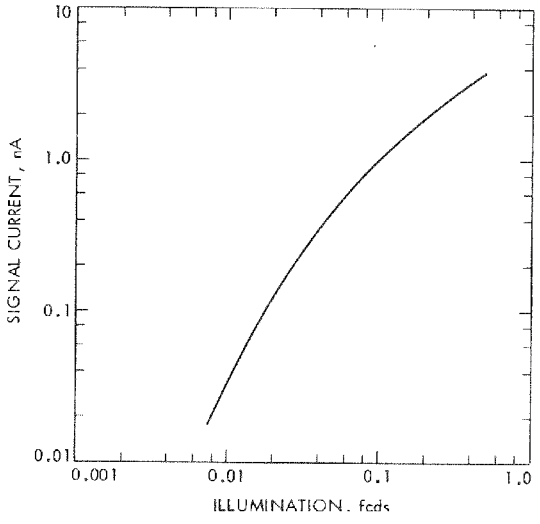

Figure 3-49. Light transfer curve, ISS S/N 06 (vidicon S/N 115 9903)

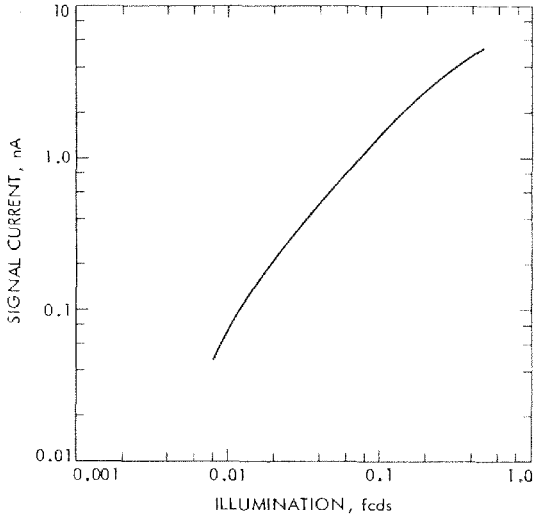

Figure 3-50. Light transfer curve, ISS S/N 07 (vidicon S/N 165 1402)

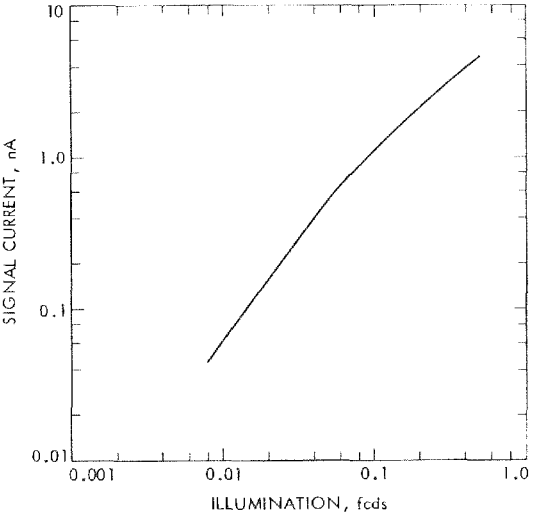

Figure 3-51. Light transfer curve, ISS S/N 08 (vidicon S/N 165 1407)

REFERENCES

3-1. M. Benesh and M. Morrill, MVM'73 TV Subsystem, Calibration Report, JPL Document 615-148, July 1975.

3-2. MJS77-ISS Flight Equipment, Detail Specification for Narrow-Angle Optical System, JPL Specification No. ES510993, 19 November 1975.

3-3. MJS77-ISS Flight Equipment, Detail Specification for Wide-Angle Optical System, JPL Specification No. ES509965, 19 November 1975.

3-4. ISS-MJS77 Flight Equipment, Design Requirements For Narrow-Angle Optical Subsystem, JPL MJS77-2036-1, 14 August 1974.

3-5. ISS-MJS77 Flight Equipment, Design Requirements For Wide-Angle Optical Subsystem, JPL MJS77-2036-2, 14 August 1974.

SECTION IV

SUBSYSTEM CALIBRATIONS

The ISS subsystem-level calibrations were designed to:

(a) Supplement and integrate the component-level calibration data discussed in Section III.

(b) Establish the standard performance characteristics of the ISS cameras.

(c) Aid instrument parametric adjustment during flight operations.

(d) Enable construction of decalibration data files, which will be used by IPL for data reduction during the mission.

(e) Enable interpretation and analysis of the acquired flight data by the Voyager science team members and other users.

The subsystem-level calibrations were performed in the JPL optical tunnel and in the JPL thermal-vacuum chamber. The environmental conditions and camera setup are described in Section II-E.

No support equipment, particularly the BCE (Section II-A) and the light cannons (Section II-B), was used without an appropriate warmup period, and no radiometric calibrations were started, unless the vidicons were first saturated and then stabilized for at least 15 frames. The light cannons were calibrated and operated as described in Section II-B-3, and all outside lights were turned off during the calibrations to prevent unwanted glare. All calibrations were recorded on magnetic tapes, which are stored at IPL together with their accompanying log sheets.

All radiometric data contained in this document have been corrected for both the long-term and short-term brightness drift of the light cannons (see Section II-B-3); and the shading offset corrections for the narrow-angle camera field-of-view (annulus) have been included, as described in Section II-B-2. However, to make a meaningful comparison of the thermal-vacuum and bench-calibration results, adjustments for the spectral transmission loss of the chamber window will have to be included (see Figure 2-33 and Table 2-5 in Section II-E). These corrections will be automatically incorporated in the final IPL decalibration program.

The ISS cameras can be operated in the following modes:

(a) Low or high gain.

(b) Automatic light flooding on or off.

(c) Scan rate 1:1, 2:1, 3:1, 5:1, or 10:1.

(d) Simultaneous exposures.

(e) In-flight calibration lamps.

(f) Long exposures.

(g) Eight filter positions.

(h) Edit mode 3/4, 1/2, 1/3, 1/5, and 1/10.

With the exception of the long-exposure mode and the edit mode, all these modes were tested and calibrated, and the results obtained are described in this section.

The long-exposure mode was not included in the calibration requirements because it would be prohibitively time-consuming and, moreover, it will be used only for a few special applications, such as taking pictures of the dark side of the planet and sodium-D filter photography.

The edit mode did not require any special calibrations at all because it consists of segments of regular full frames and therefore does not affect the radiometric, geometric, or optical characteristics of the ISS images.

The light-flood-off mode is not considered for the Voyager mission at all, but it was tested as part of the beam bending (Section IV-B-4) and star simulation (Section IV-C-2) calibrations.

To avoid any misunderstandings, the reader should assume that all tests and calibrations were performed on the optical bench in the following modes, unless specifically mentioned otherwise:

(a) Low gain.

(b) Automatic light flooding on.

(c) Scan rate, 1:1.

(d) Normal exposure.

(e) Clear filter.

Reference is often made to subareas 1 to 5 of the ISS images. These subareas are explained in Section IV-A-1-a, and the user should become familiar with them.

A. RADIOMETRIC CALIBRATIONS

The MJS 1977-ISS calibration requirement document (Reference 2-1) calls specifically for calibrations to be performed in radiometric units (W/cm^2-ster). However, because of the limitations of the available hardware, as well as for other technical reasons, it was necessary to use the photometric units (fL and fLs), the same as for all previous flight projects. This discrepancy was resolved by defining and calculating the conversion factors from the photometric to the required radiometric units.

Let us assume that a frame was taken of an object with a particular filter and exposure time. The number of fLs corresponding to each output DN per pixel of the frame can be found via the light-transfer function curve for that filter.

A conversion factor has been calculated for each filter position from available component calibration data, which transforms the fLs per pixel to the radiance of the object per pixel averaged over the spectral response of the system.

If

N_λ = radiance of object for a particular pixel (W/cm^2-ster-nm)

T_λ = spectral transmission of the optics (range from 0 to 1)

F_λ = spectral transmission of the filter (range from 0 to 1)

S_λ = relative vidicon spectral response (normalized at 555 nm)

Δt = exposure time of the frame (s)

fLs = foot-Lambert-seconds per pixel

f/# = focal ratio of the ISS camera (3.5 for wide-angle and 8.5 for narrow-angle cameras)

ξ = conversion factor (W-sec/cm^2-fLs)

then

$$\int_{280nm}^{650nm} N\lambda T\lambda F\lambda S\lambda d\lambda = \frac{\xi \times fLs}{\Delta t \frac{\pi}{4(f/\#)^2}} \quad (W/cm^2\text{-ster}) \qquad (1)$$

It should be noted that the relative vidicon response curve is determined to only two significant figures, which is the limiting accuracy of the radiometric decalibrations.

Table 4-1 lists the conversion factors, ξ, which have been calculated for each filter position of the flight ISS cameras. Inasmuch as all mission planning and data processing will be done in radiometric units, the conversion factors have become an integral part of the IPL decalibration files and will be used consistently throughout the mission.

Application of the conversion factors is a complicated and complex process; therefore, to avoid any misunderstanding or confusion, the following should be noted:

(a) The f/# of the proper optics and the exposure time in seconds of the particular frame under consideration must be used.

(b) $\pi/4(f/\#)^2$ has units of steradians, which introduces these units into Eq. (1).

(c) N_λ is integrated over λ. Let us assume that the relative spectral shape of N_λ is the same as the relative spectral shape n_λ of the Sun, normalized at λ = 555 nm. Also, let N_0 be defined as the absolute radiance of the object at the same wavelength. Then:

$$N_\lambda = N_0 \cdot n_\lambda \tag{2}$$

Table 4-1. Conversion factors ξ from photometric to radiometric units

ISS S/N	Conversion factors ξ (W-s/cm^2-fLs)							
	Filter position							
	0	1	2	3	4	5	6	7
04	N.A.	1.17E-8	2.09E-8	3.89E-9	N.A.	6.90E-9	N.A.	1.73E-9
05	3.31E-9	6.38E-10	1.52E-9	5.19E-10	3.31E-9	1.09E-9	1.09E-9	1.36E-11
06	N.A.	1.53E-8	3.12E-8	4.58E-9	N.A.	2.11E-8	N.A.	4.07E-9
07	3.27E-9	6.30E-10	1.49E-9	4.96E-10	3.27E-9	1.18E-9	1.15E-9	1.27E-11

Equation (2) can be solved as follows:

$$\int_{280}^{650} N_\lambda T_\lambda F_\lambda S_\lambda d\lambda = N_0 \int_{280}^{650} n_\lambda T_\lambda F_\lambda S_\lambda d\lambda$$

$$\therefore N_0 = \frac{\frac{\xi \cdot fLs}{650}}{\Delta t \frac{\pi}{4(f/\#)^2} \int_{280}^{650} n_\lambda T_\lambda F_\lambda S_\lambda d\lambda} \quad (W/cm^2\text{-ster-nm})$$

where $\int_{280}^{650} n_\lambda T_\lambda F_\lambda S_\lambda d\lambda$ has been calculated for each camera and filter position in the nm units.

Let $$K_S = \frac{\frac{\xi}{650}}{\frac{\pi}{4(f/\#)^2} \int_{280}^{650} n_\lambda T_\lambda F_\lambda S_\lambda d\lambda} \quad (W\text{-}s/cm^2\text{-ster-nm-fLs})$$

$$\therefore N_0 = K_S \frac{fLS}{\Delta t} \quad (W/cm^2\text{-ster-nm}) \quad \text{at } \lambda = 555 \text{ nm} \qquad (3)$$

where

K_S = solar conversion factors listed in Table 4-2

fLs = number of fLs per pixel obtained from the calibrated light transfer curves as a function of the raw DN output

Δt = exposure time in seconds

The value of N_0 calculated from Eq. (3) can now be substituted into Eq. (2) to get the final desired value of N_λ.

Table 4-2. Solar conversion factors K_s

ISS S/N	Solar conversion factors K_s (W-s/cm^2-ster-nm-fLs) at λ = 555 nm							
	Filter position							
	0	1	2	3	4	5	6	7
04	N.A.	8.75E-9	8.48E-9	6.17E-9	N.A.	9.65E-9	N.A.	1.04E-8
05	6.94E-9	4.50E-9	7.92E-9	1.04E-8	6.94E-9	9.78E-9	9.78E-9	1.09E-9
06	N.A.	8.81E-9	8.81E-9	6.29E-9	N.A.	1.52E-8	N.A.	1.05E-8
07	6.88E-9	4.60E-9	7.92E-9	1.05E-8	6.88E-9	9.70E-9	9.75E-9	1.09E-9

1. Flat-Field Light Transfer

The purpose of the light-transfer function and shading calibrations is to determine the sensitivity of the ISS cameras, the linearity of their response and their shading characteristics as a function of the exposure level in different operational modes and under various environmental conditions.

a. Vidicon Spatial Sensitivity. The sensitivity of the ISS vidicons at each pixel can be examined by taking a set of flat-field images starting with dark current and increasing the brightness until saturation is reached.

Because of limited capacity of the magnetic tapes, a set of 10 images was typically exposed; i.e., dark current plus nine levels equally spaced between the dark current and saturation. The variable shutter method was used; the brightness of the light cannon was kept constant while the shutter time was gradually increased until the sequence was completed.

The function so derived is referred to as the light-transfer function and provides sufficient information to determine the radiometric response of the ISS cameras over the spectral bandpass of the filter being used.

This function, although available at each pixel for decalibration, is frequently displayed by averaging over five 100 x 100 pixel areas of the vidicon. Figure 4-1 shows the five selected subareas which were used for the purpose of this report.

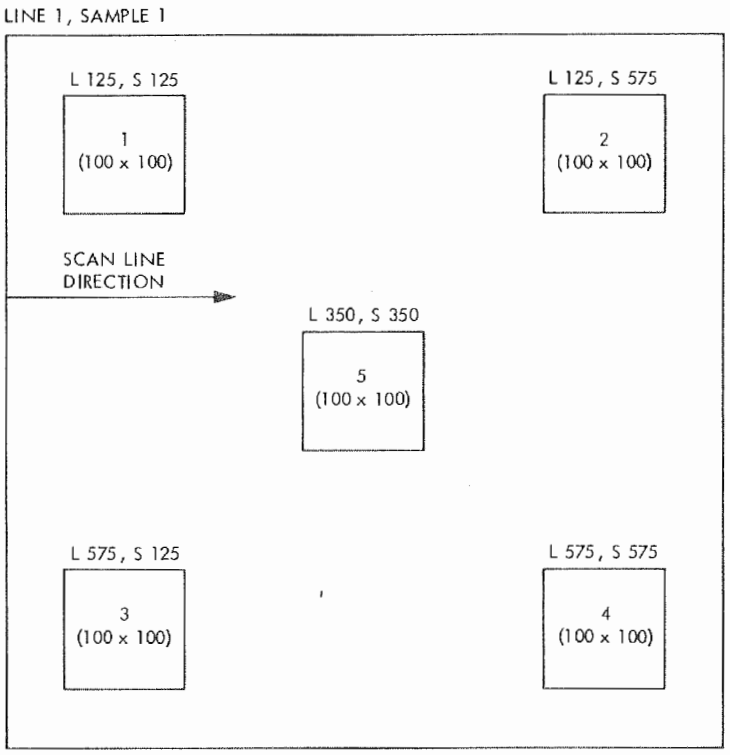

Figure 4-1. Subareas 1 to 5 of ISS vidicons used for light-transfer function analysis

Figures 4-2 to 4-5 show plots of the clear-filter light-transfer functions of the flight ISS cameras. Vidicon shading and spatial sensitivity are evident by the differences between the functions for the five subareas of the same vidicon.

The spatial sensitivity of the ISS vidicons can also be displayed by fitting a linear curve through a series of selected images and creating a picture of the slope of this curve.

Figures 4-6 to 4-9 illustrate a dark-current image and three flat-field images of ISS S/N 07. Each flat field is dominated by the shape of the dark current, which in turn is dependent upon gain and readout time.

Figure 4-10 shows the gain map, which indicates higher sensitivity toward the top of the frame in a generally radial manner. Figure 4-11 shows a dark-current image created by extrapolating each linear function back to zero exposure. If the function were linear, then the created synthetic dark-current image should closely approximate the true dark current, and the ratio of the two images should be 1, or 100 in this case, since the data have been scaled. The accuracy of this

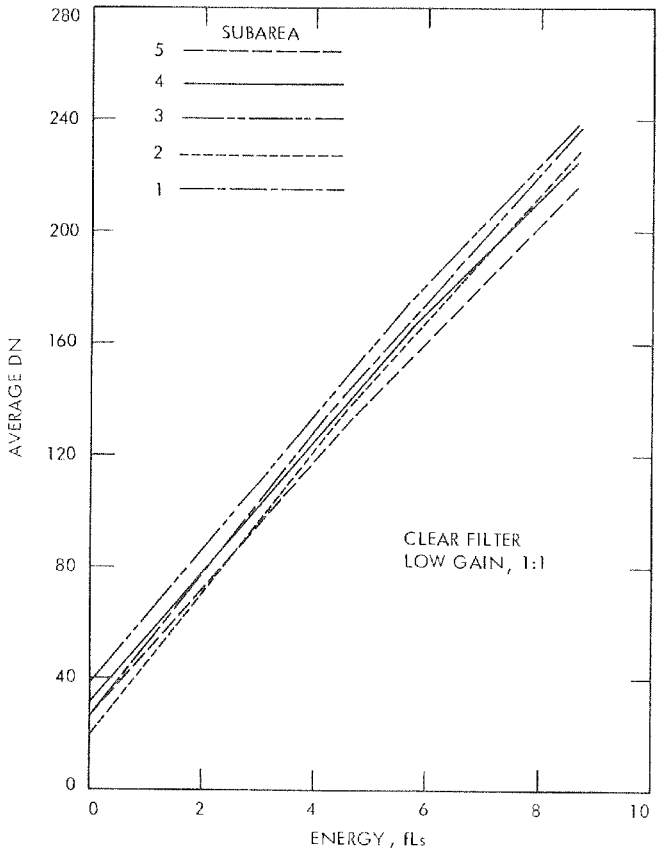

Figure 4-2. Light-transfer function, ISS S/N 04

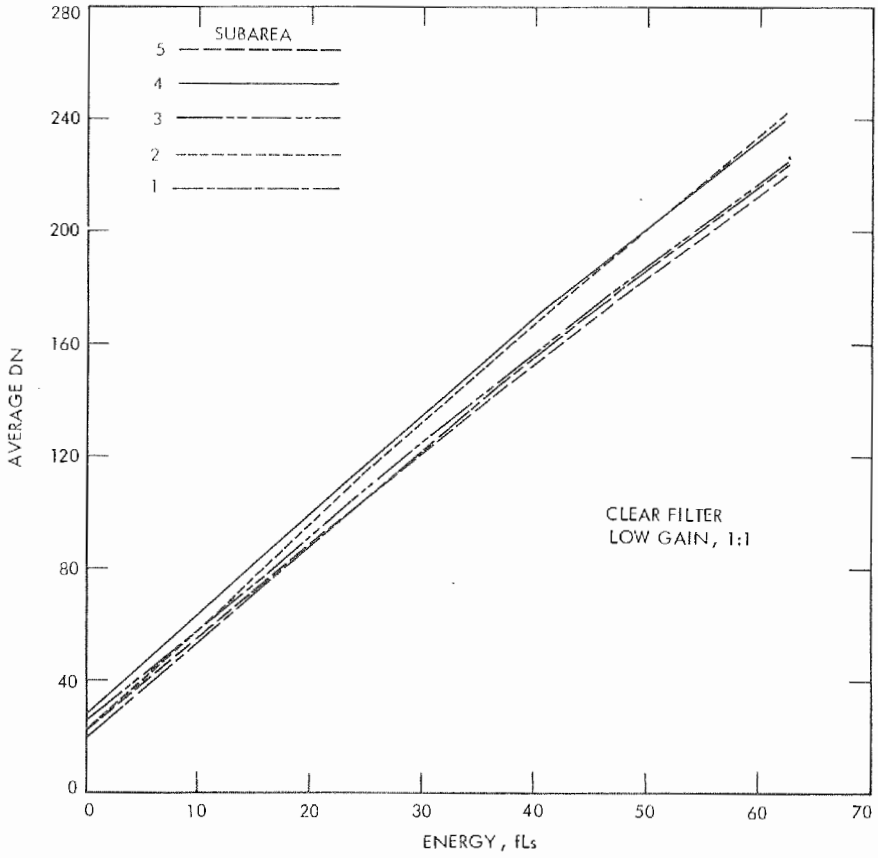

Figure 4-3. Light-transfer function, ISS S/N 05

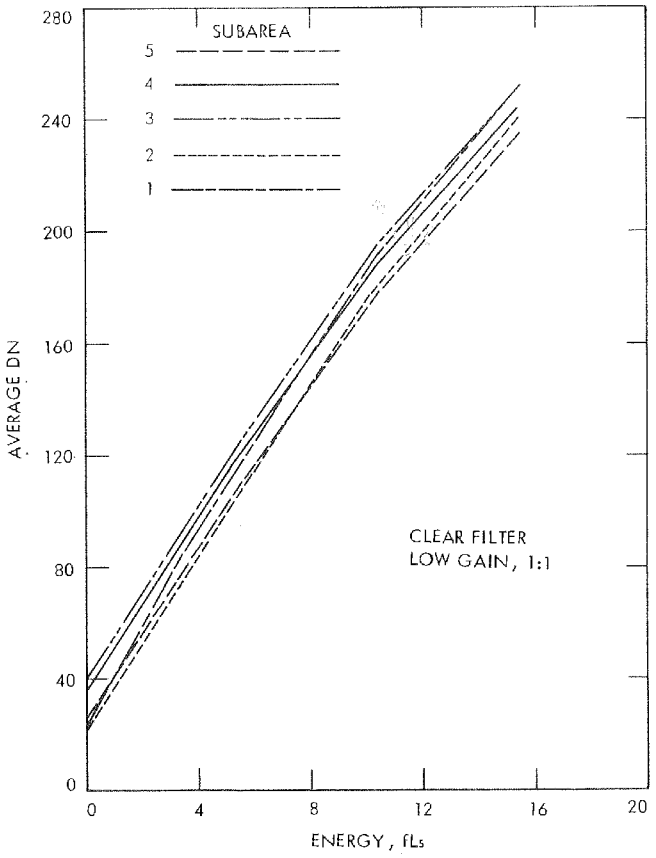

Figure 4-4. Light-transfer function, ISS S/N 06

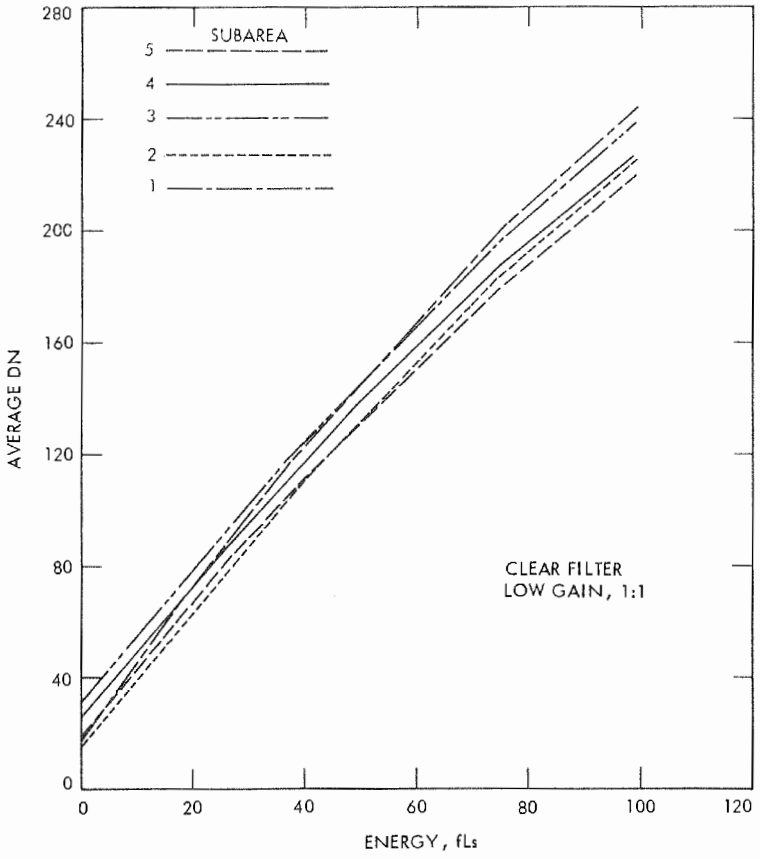

Figure 4-5. Light-transfer function, ISS S/N 07

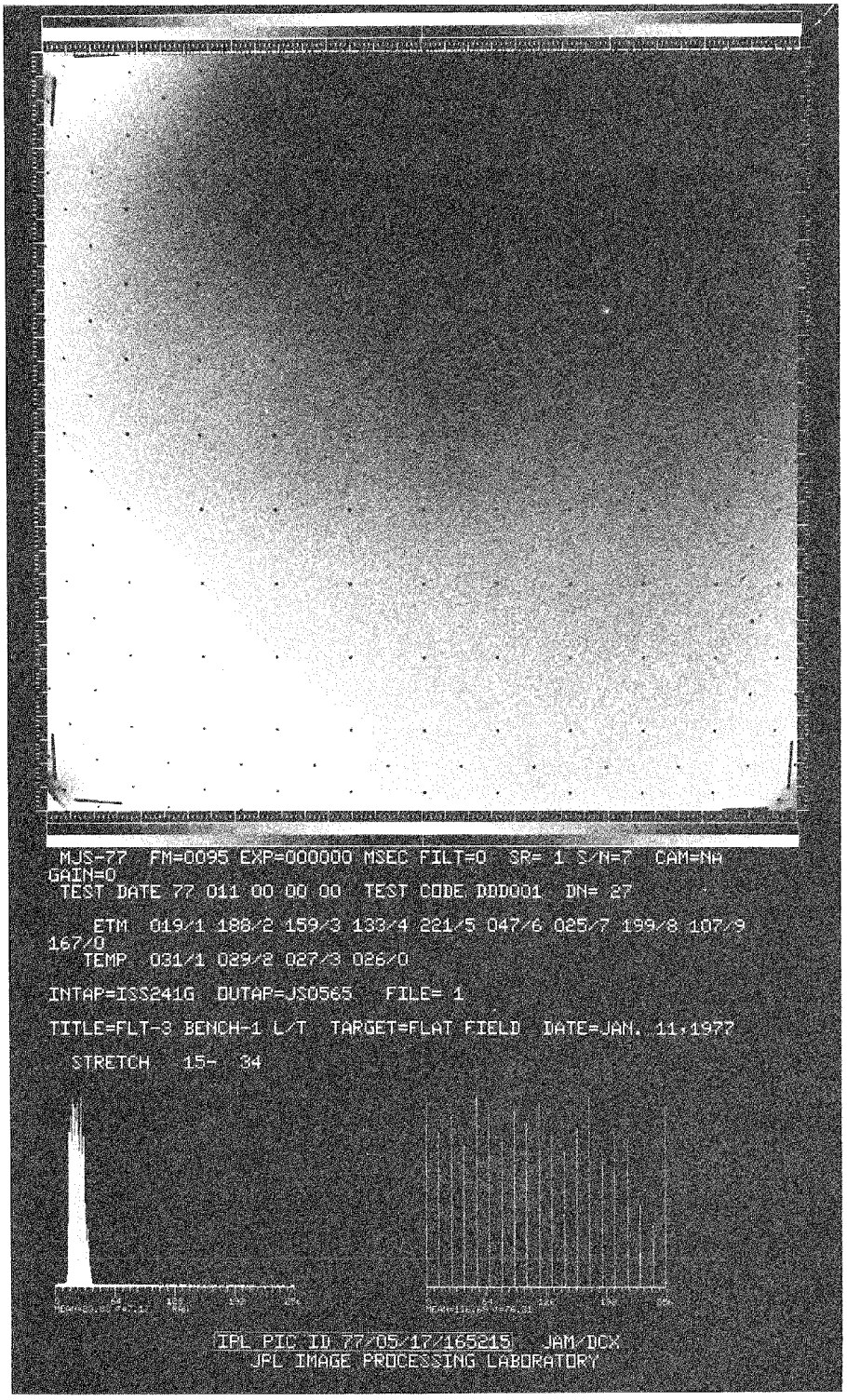

Figure 4-6. Dark-current image, ISS S/N 07

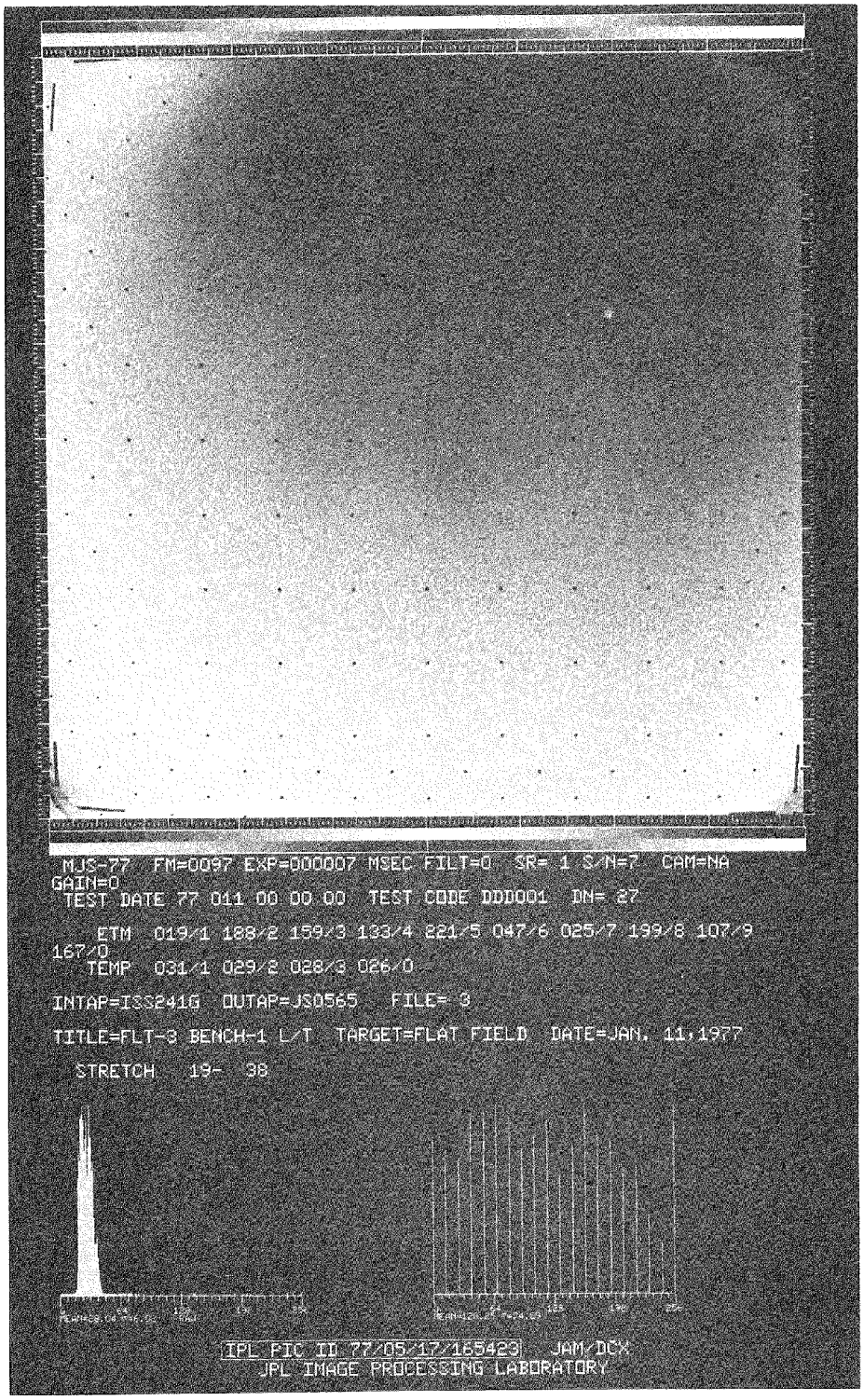

Figure 4-7. Flat-field image (7.5 ms), ISS S/N 07

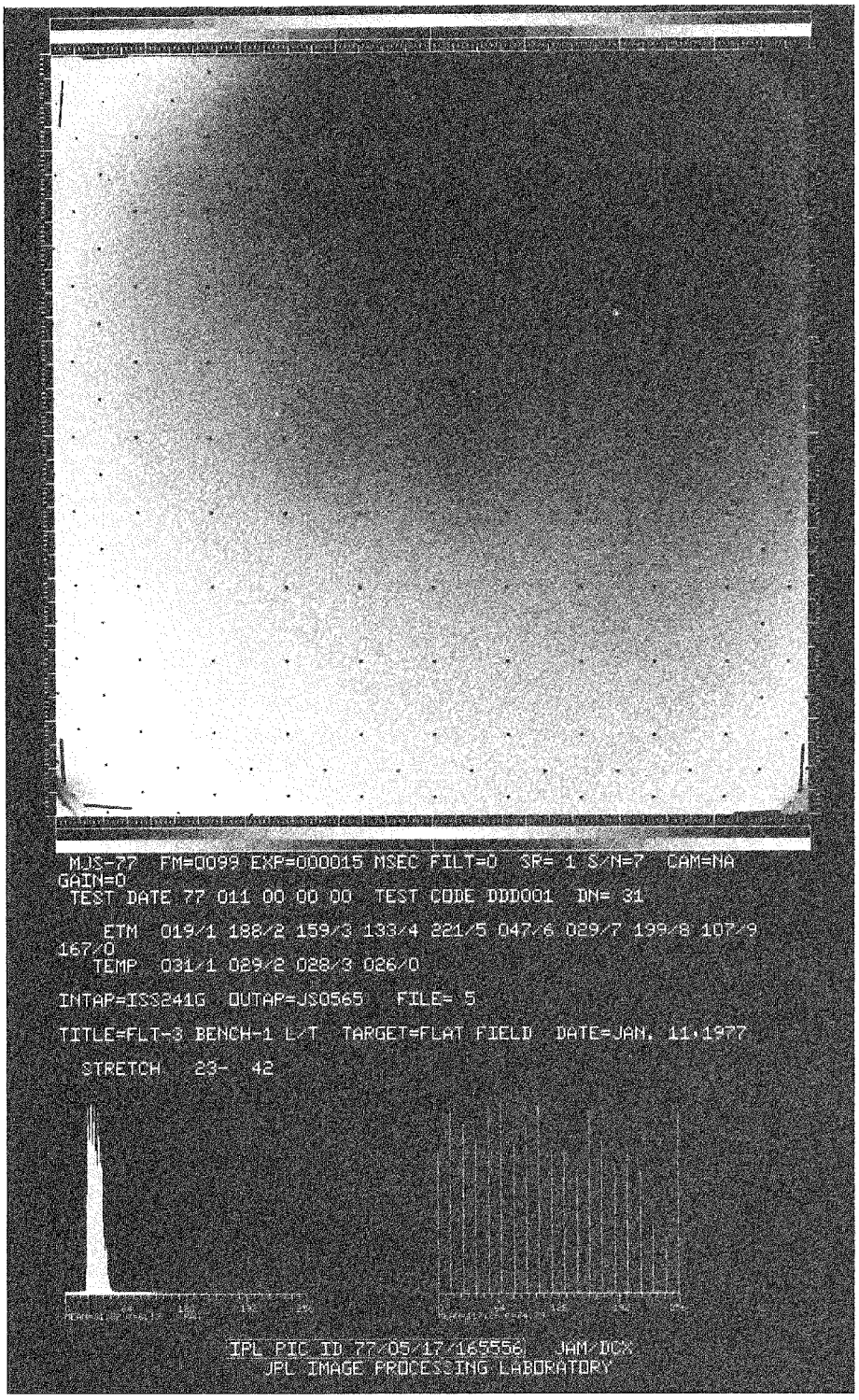

Figure 4-8. Flat-field image (15 ms), ISS S/N 07

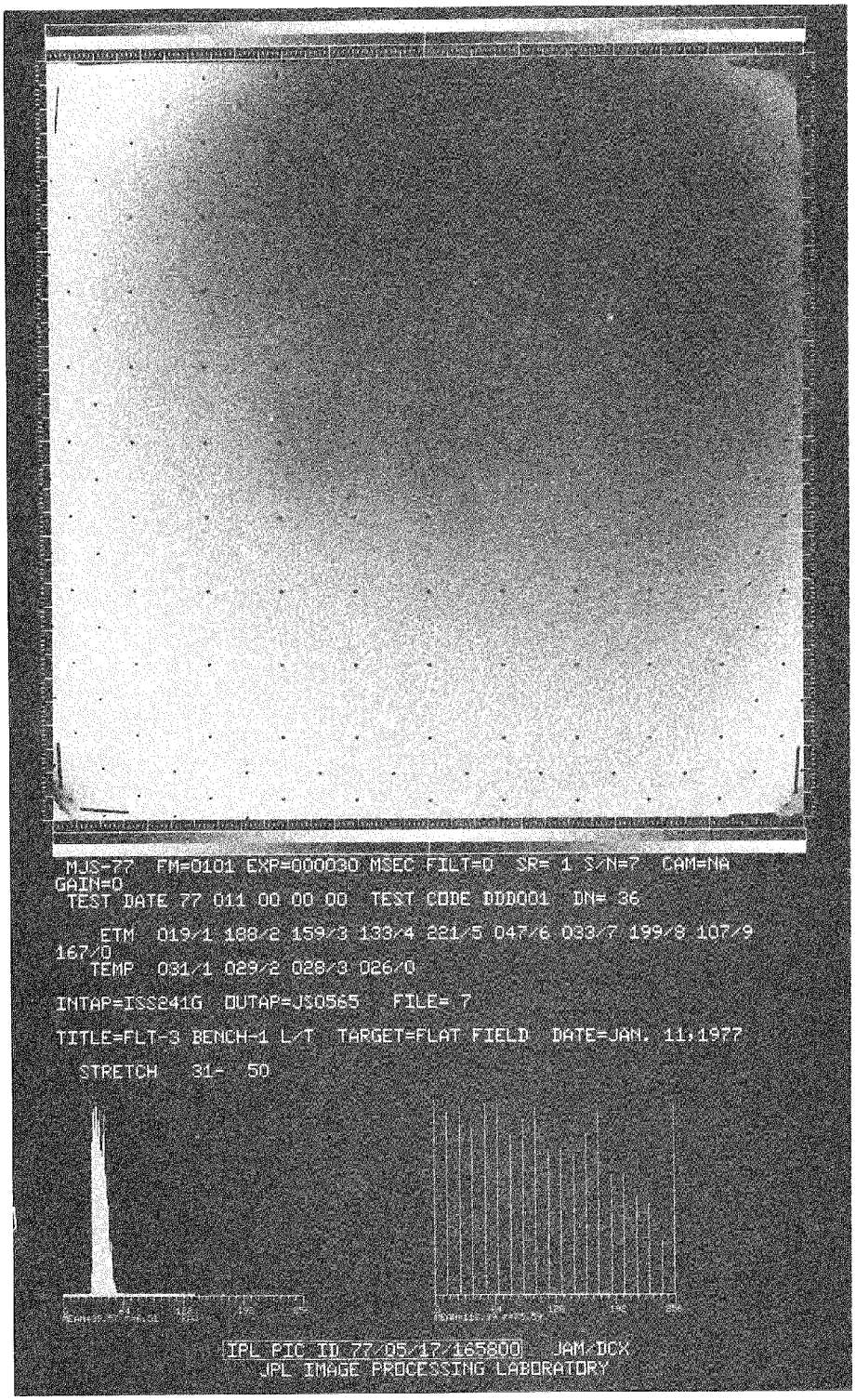

Figure 4-9. Flat-field image (30 ms), ISS S/N 07

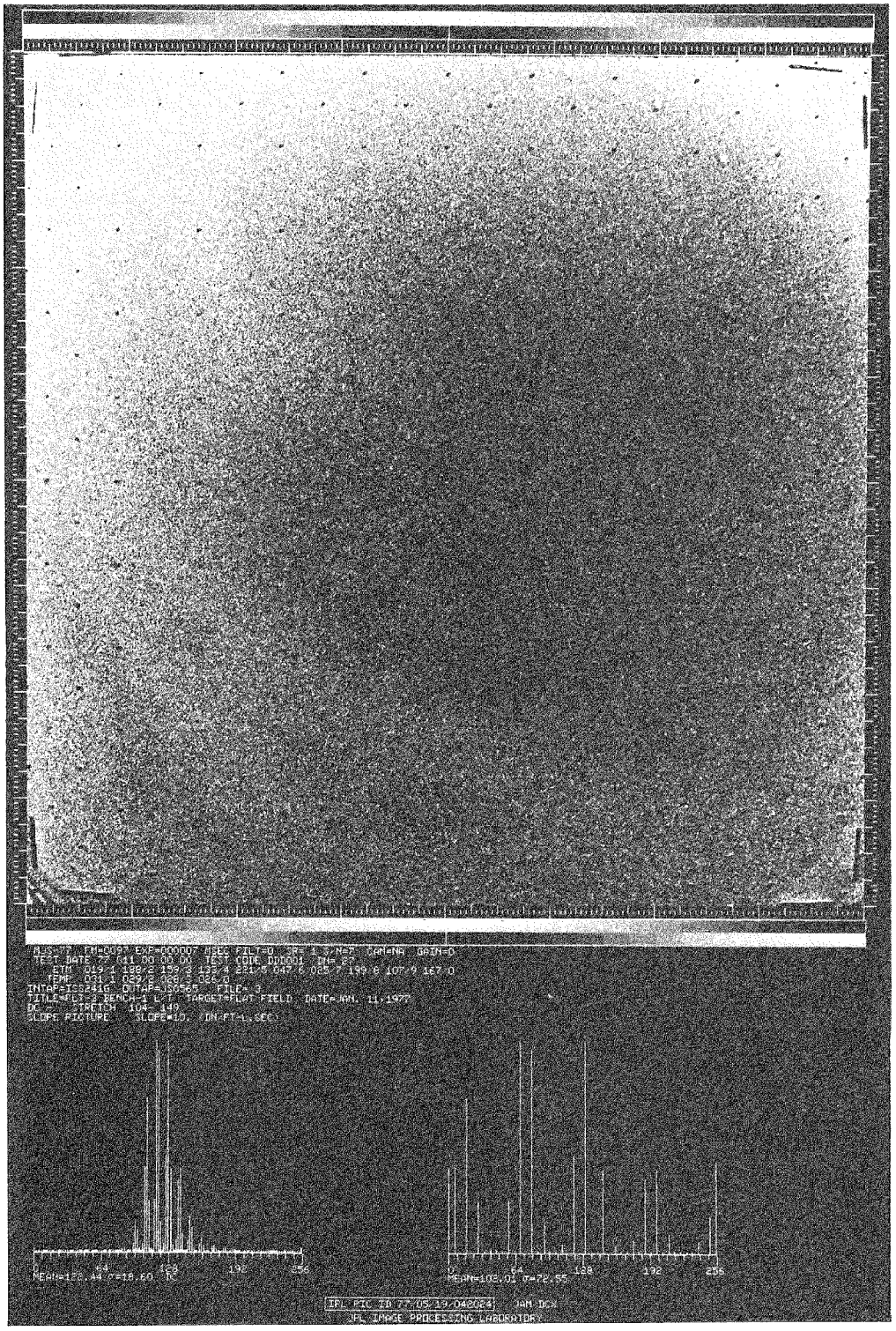

Figure 4-10. Gain-map image, ISS S/N 07

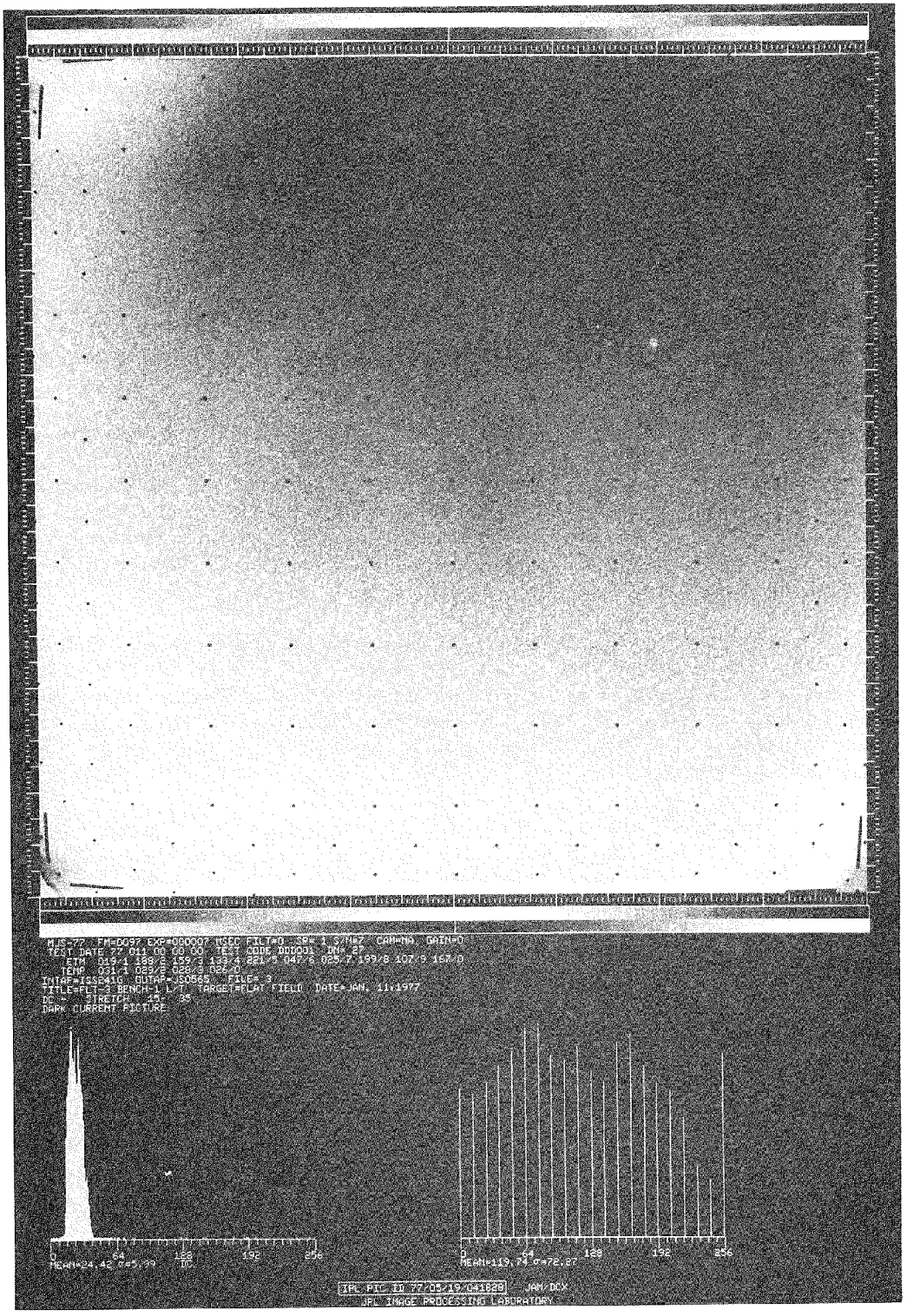

Figure 4-11. Created synthetic dark-current image, ISS S/N 07

dark current is seen in Figure 4-12, which is a contrast-enhanced ratio of the true dark current to the synthetic current. The histogram of the ratioed image, third from the left below the image, has a mean DN = 97.23; i.e., within ±3% of the true linearity of the light transfer-function.

It would be prohibitively expensive and beyond the scope of this report to document the light transfer-functions of all spectral filters of the flight ISS cameras. However, all these cases were extensively calibrated and analyzed, and the obtained results were included in the ISS decalibration files. Therefore, only the most important and pertinent spectral filter data were included in this document, such as in Section II-B (filter spectral transmittance and filter factors), Section IV-A-1-b (spatial color sensitivity) and Section IV-A-6 (color reconstruction).

The required accuracy of the light-transfer functions (see Reference 2-1) was ±5% of half-scale signal averaged over any randomly selected area of 10 contiguous pixels. This requirement was consistently met for all ISS flight cameras. The radiance of the used light cannons was supposed to be ±5% or better of the level to produce a half-scale signal. This criterion was also met, as is apparent from the detailed discussion in Section II-B.

b. Spatial Color Sensitivity. ISS wide-angle camera S/N 06 and narrow-angle camera S/N 07 were selected to illustrate the representative spatial dependence of color sensitivity. Images were chosen in two different colors (clear and another spectral filter), which had similar histograms. Dark currents were removed from each frame, and the ratios determined.

Figures 4-13 to 4-19 show the ratios of the contrast-enhanced images of ISS S/N 06; and Figures 4-20 to 4-26, those of ISS S/N 07. Each figure is clearly marked to indicate which filter combination was used. The spatial dependence of color sensitivity can be expressed by the following formula:

$$R = \frac{A - B}{C - D}$$

where

R = ratio of image

A = "other" spectral filter image

B = dark current of A

C = clear filter image

D = dark current of C

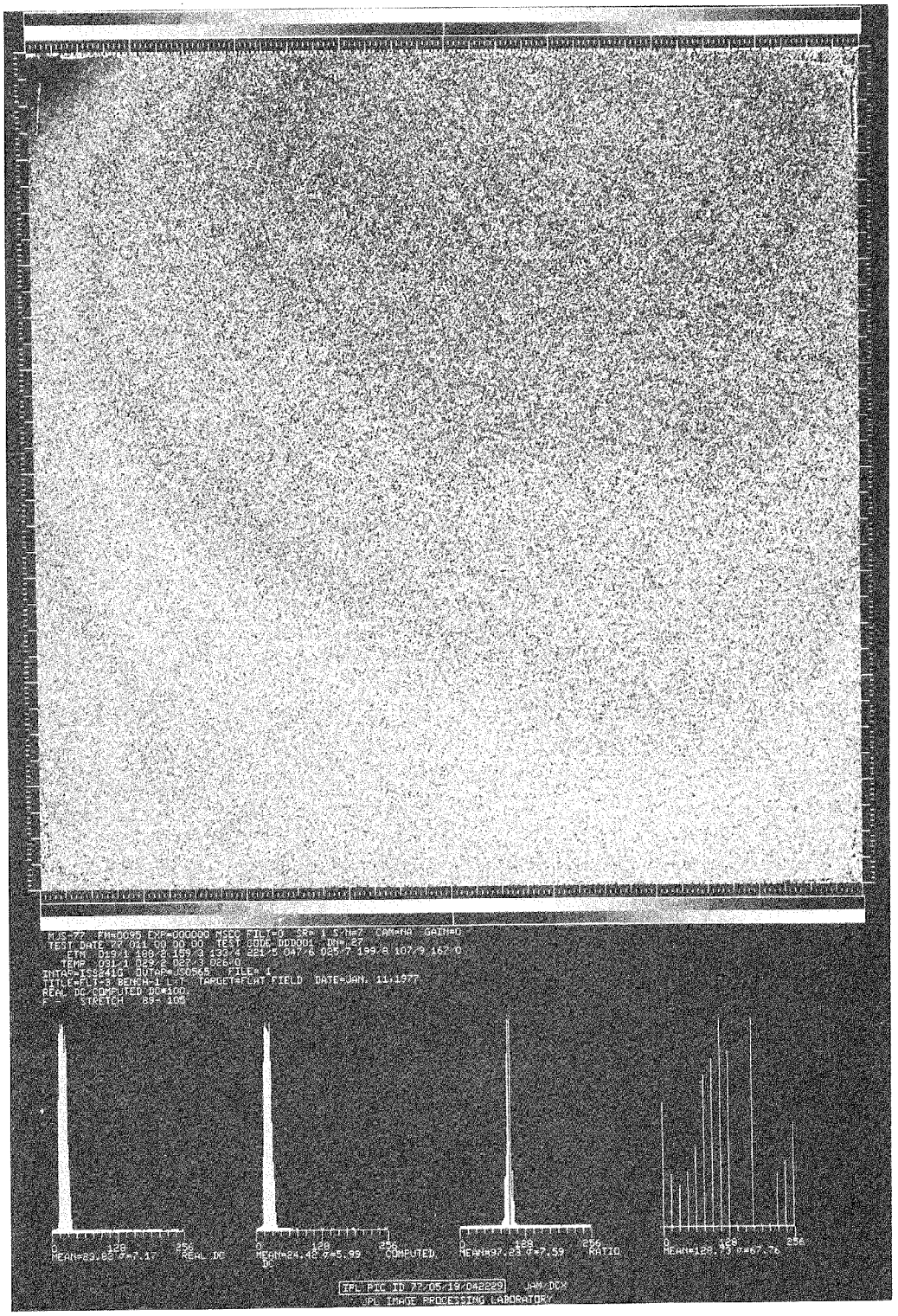

Figure 4-12. Ratio of dark-current image, ISS S/N 07

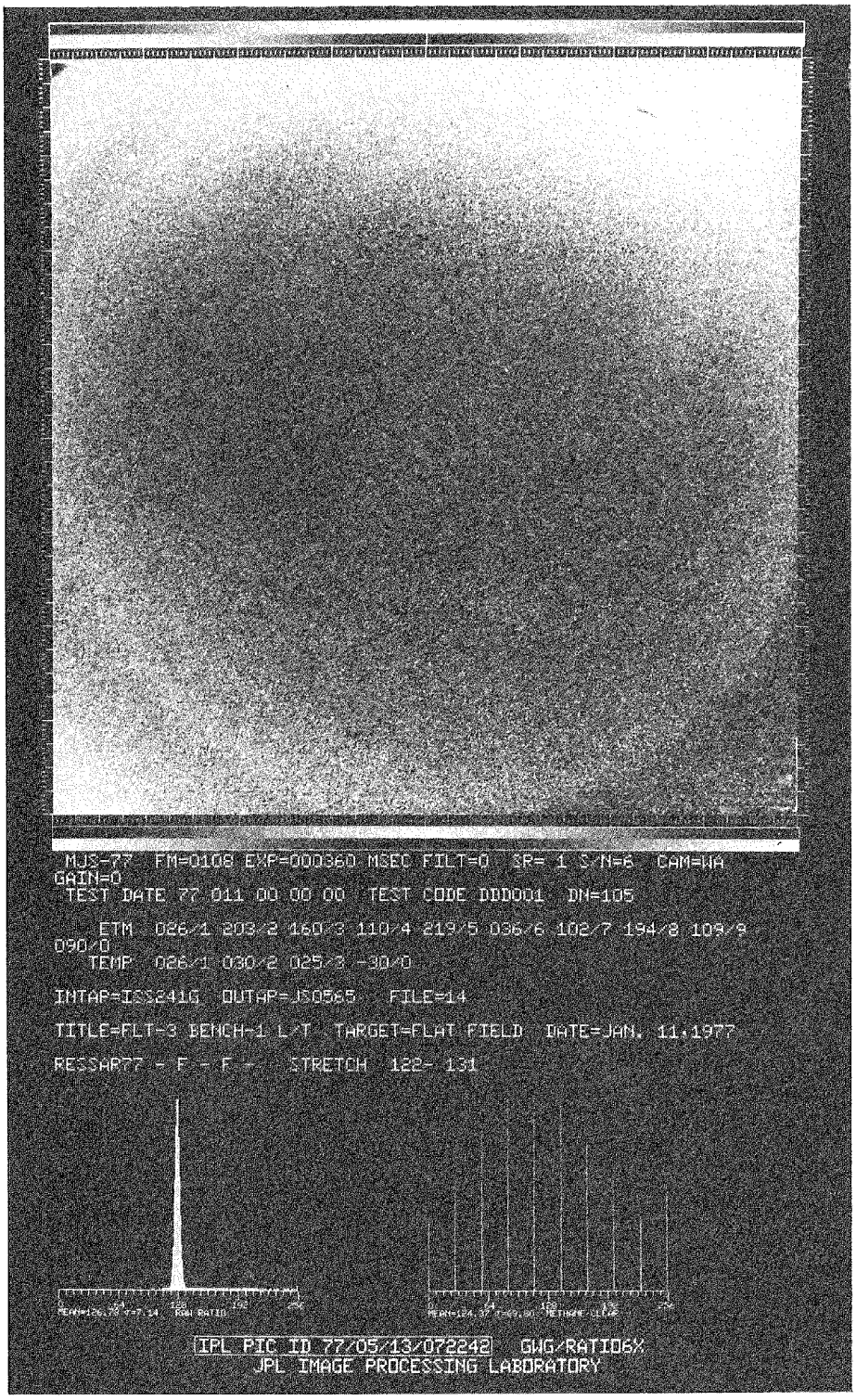

Figure 4-13. Ratio of image, ISS S/N 06: methane 6190 versus clear filter

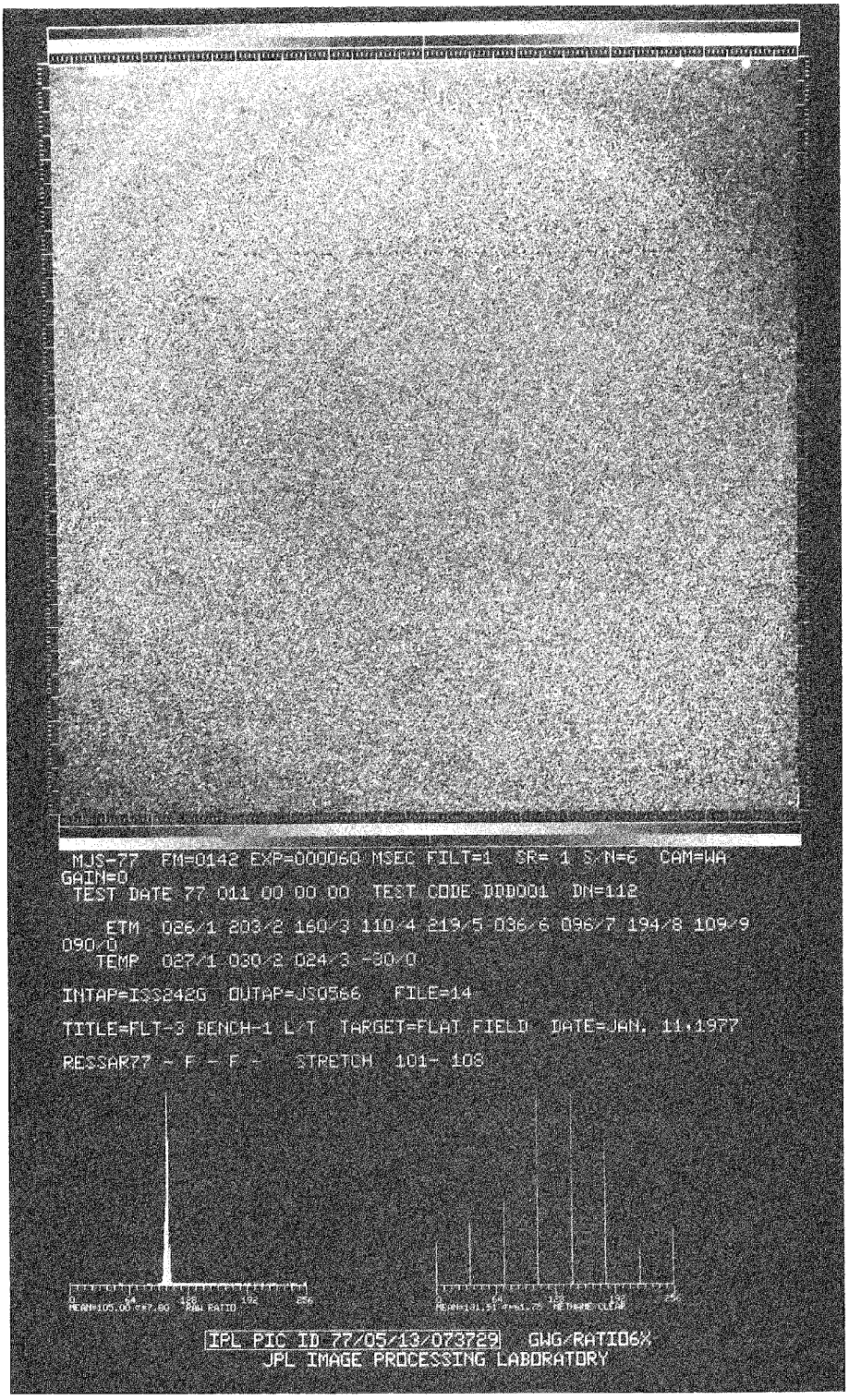

Figure 4-14. Ratio of image, ISS S/N 06: blue versus clear filter

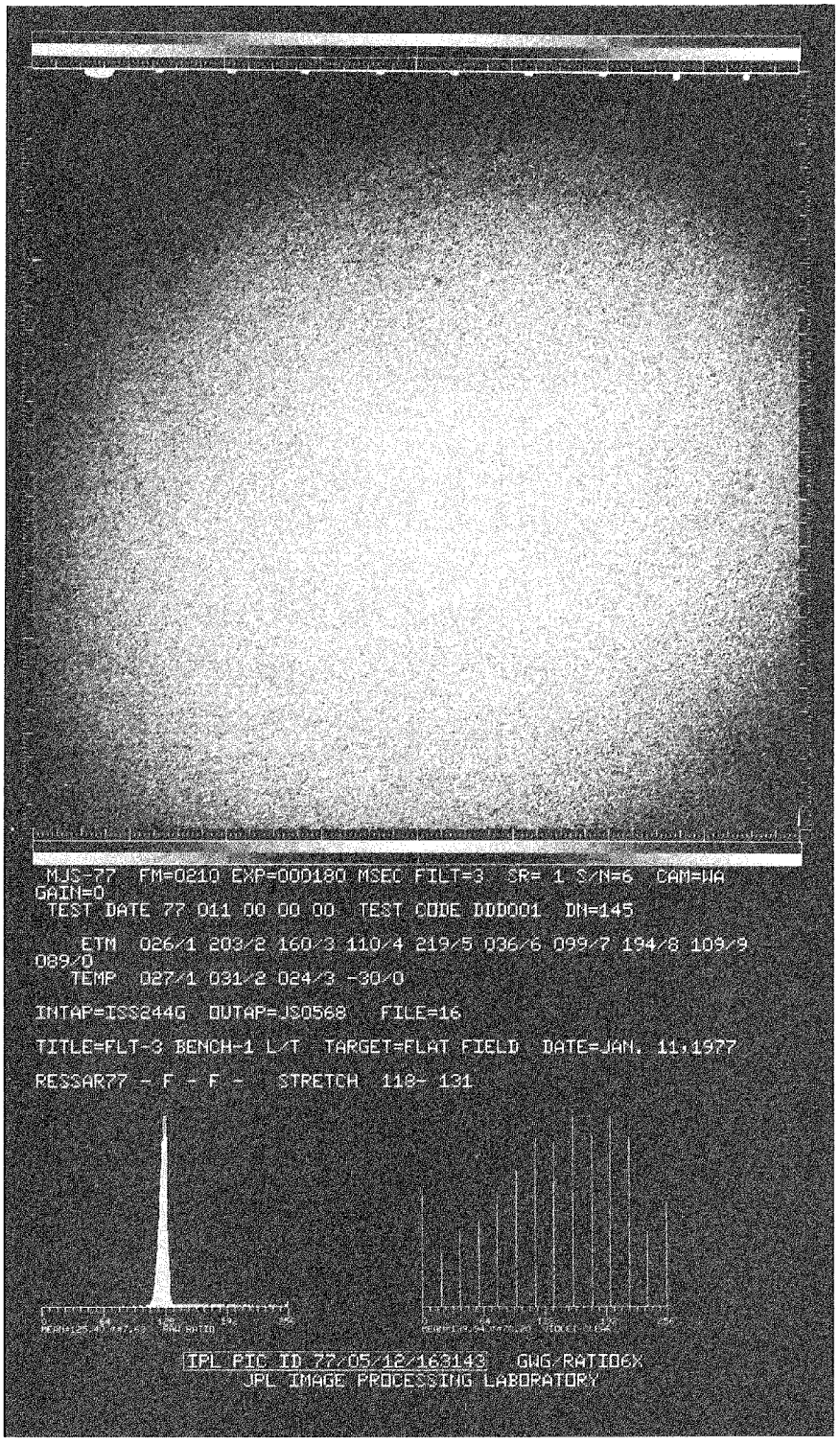

Figure 4-15. Ratio of image, ISS S/N 06: violet versus clear filter

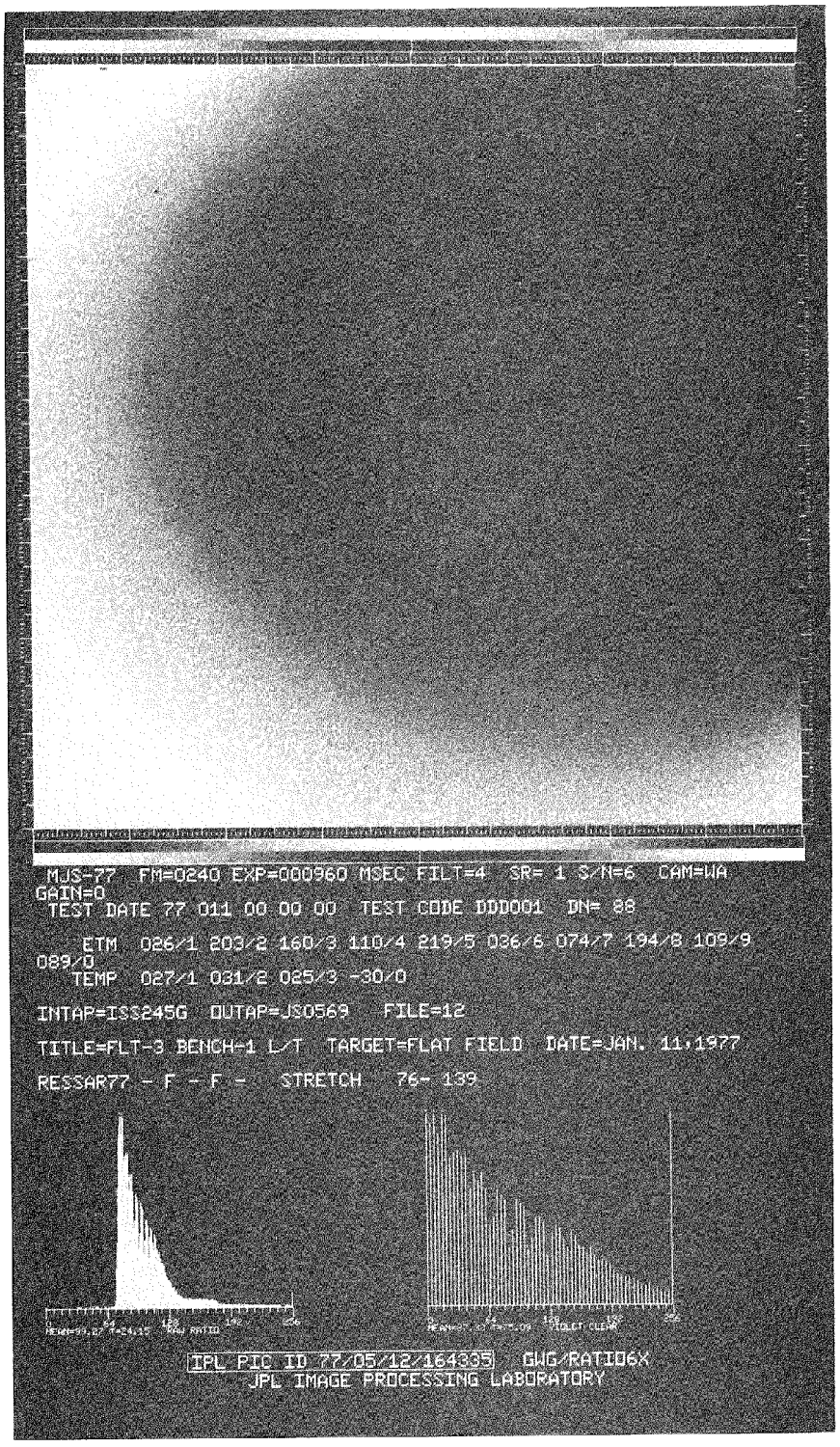

Figure 4-16. Ratio of image, ISS S/N 06: sodium-D versus clear filter

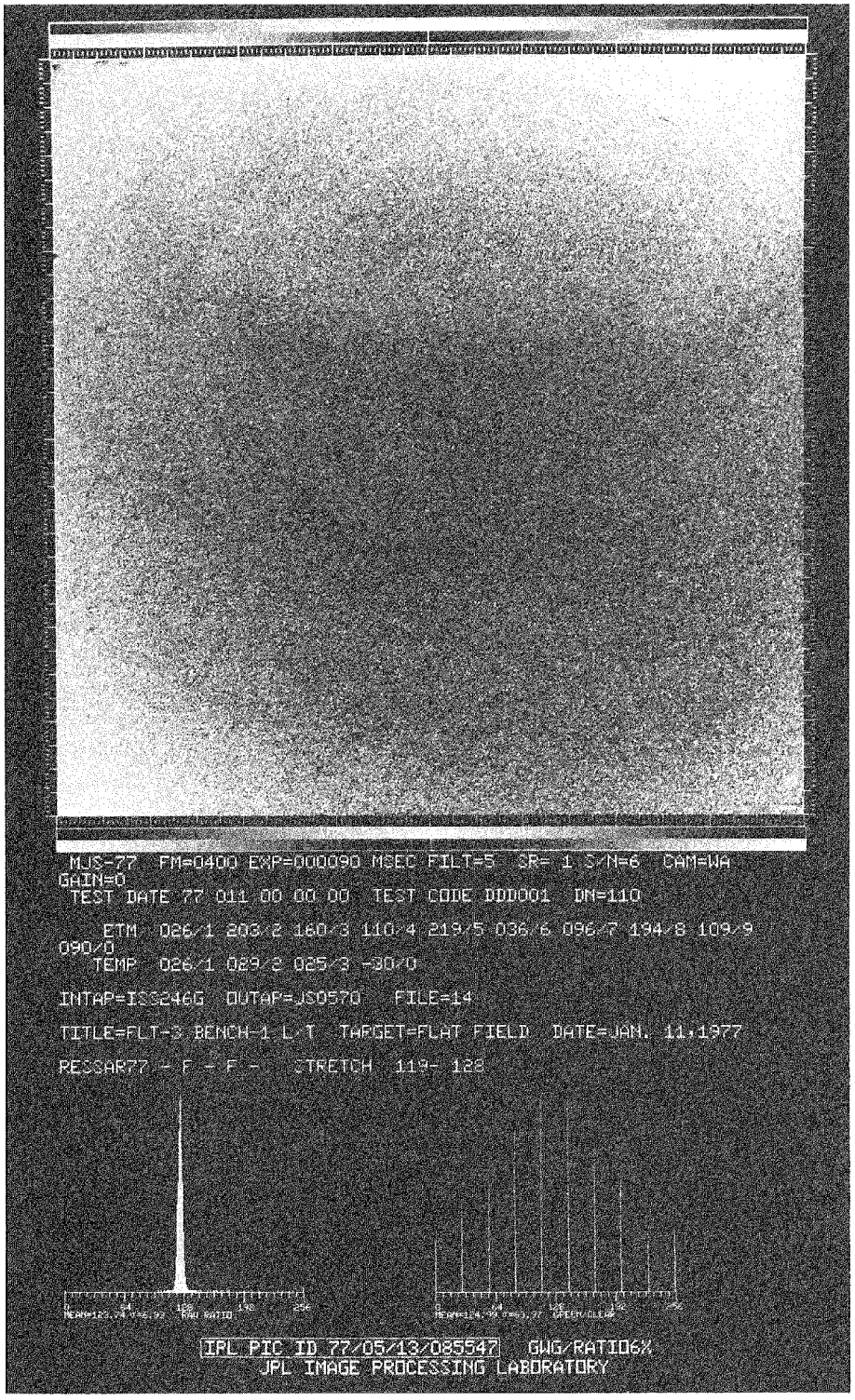

Figure 4-17. Ratio of image, ISS S/N 06: green versus clear filter

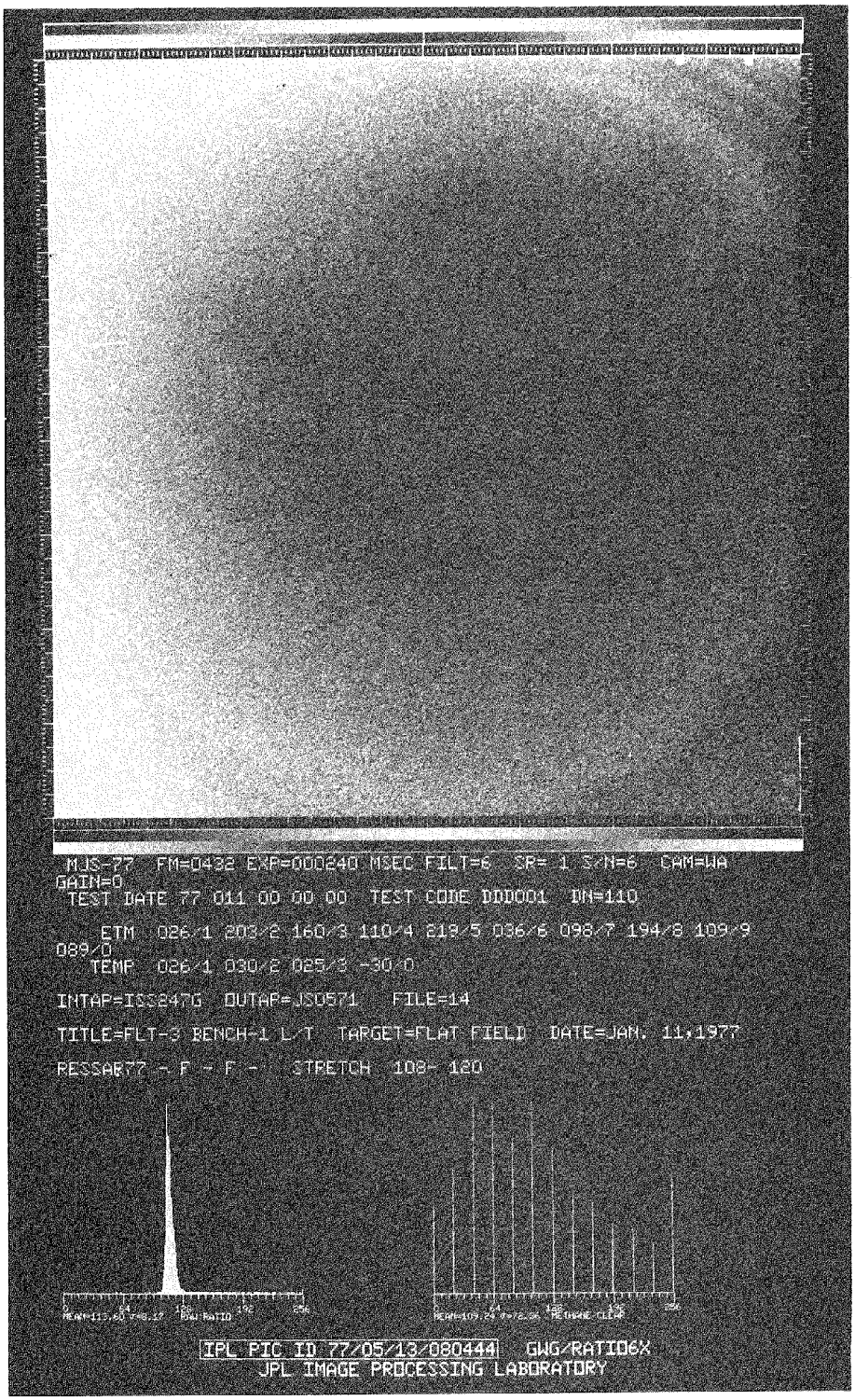

Figure 4-18. Ratio of image, ISS S/N 06: methane (Uranus) versus clear filter

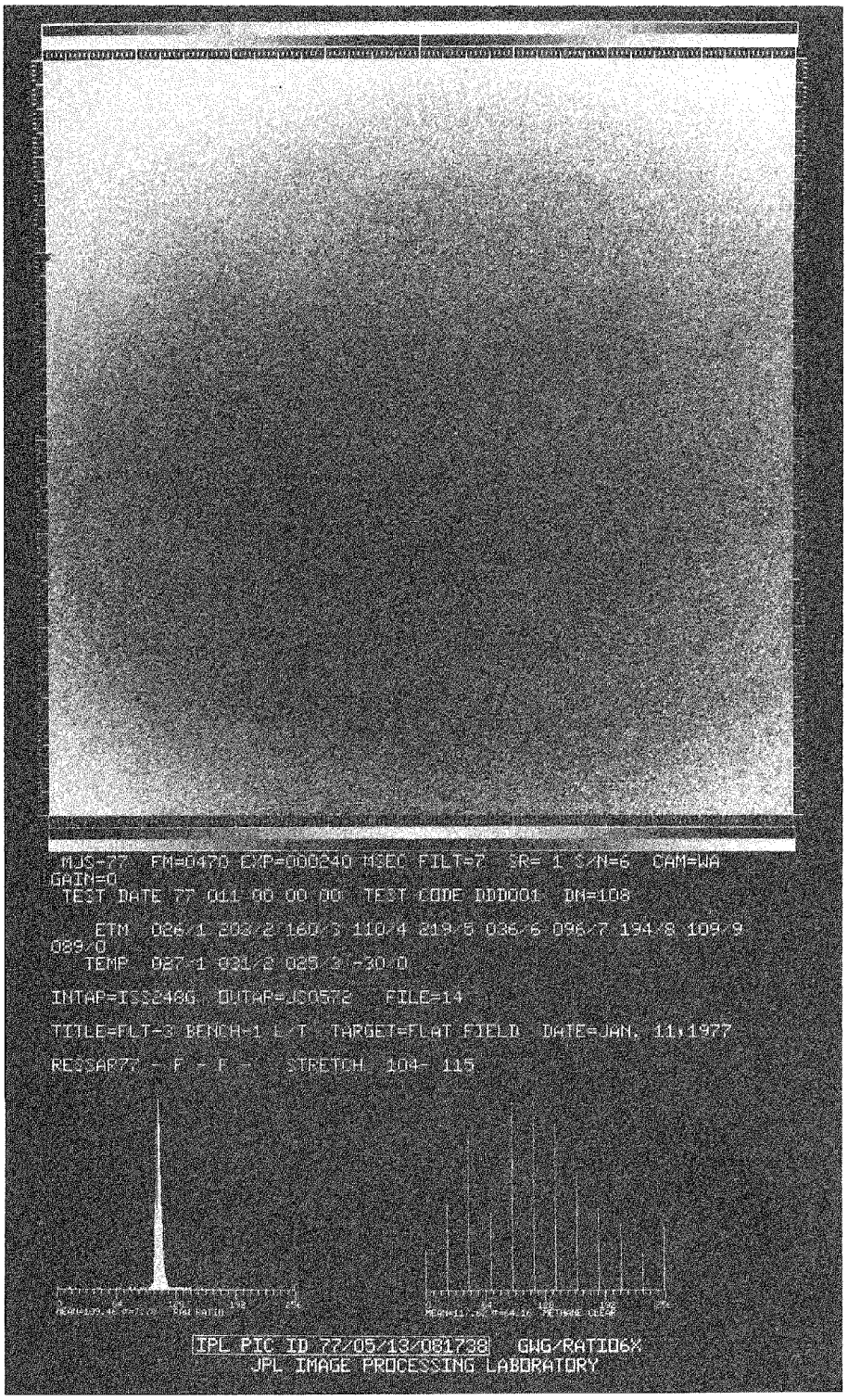

Figure 4-19. Ratio of image, ISS S/N 06: orange versus clear filter

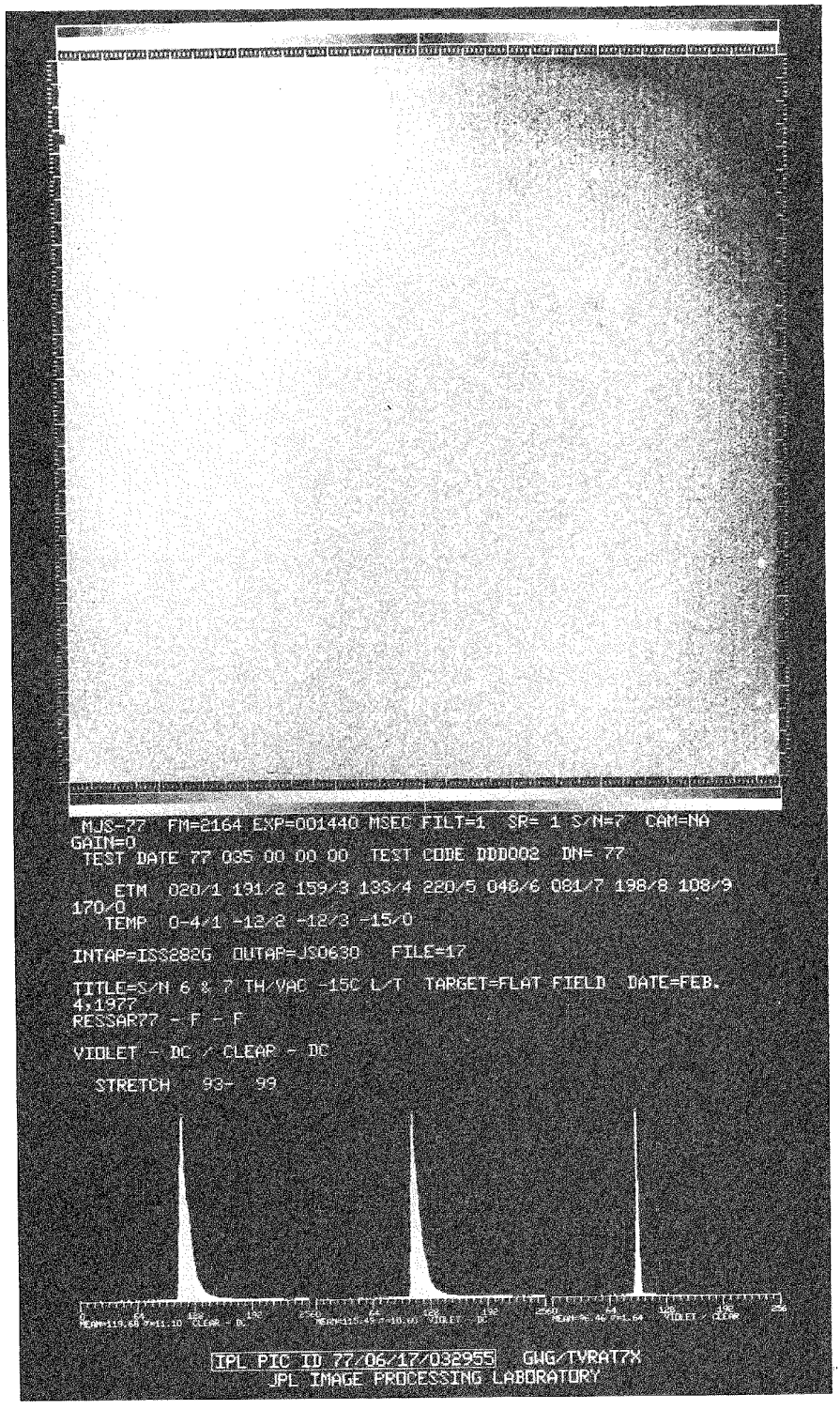

Figure 4-20. Ratio of image, ISS S/N 07: violet versus clear filter

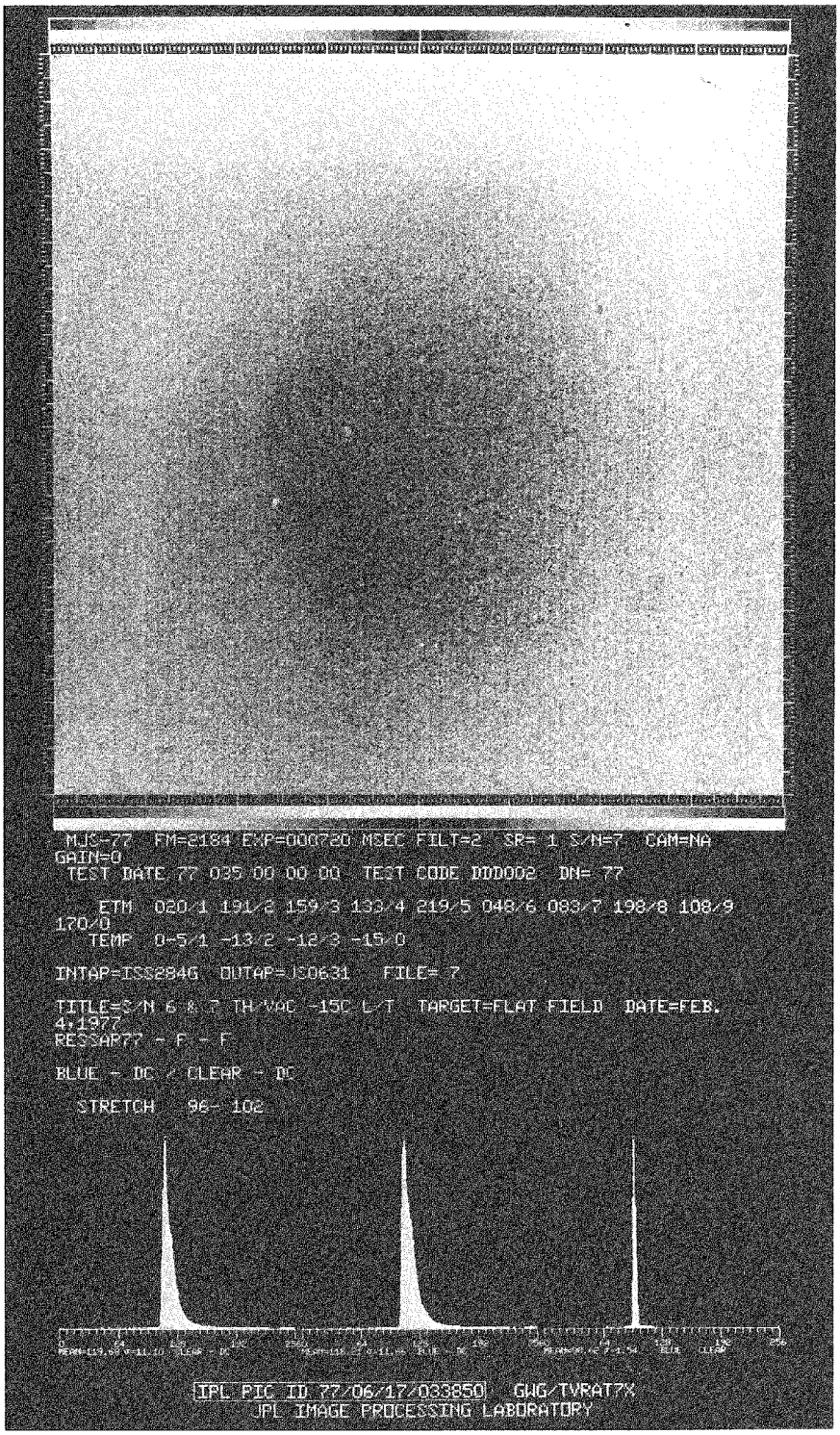

Figure 4-21. Ratio of image, ISS S/N 07: blue versus clear filter

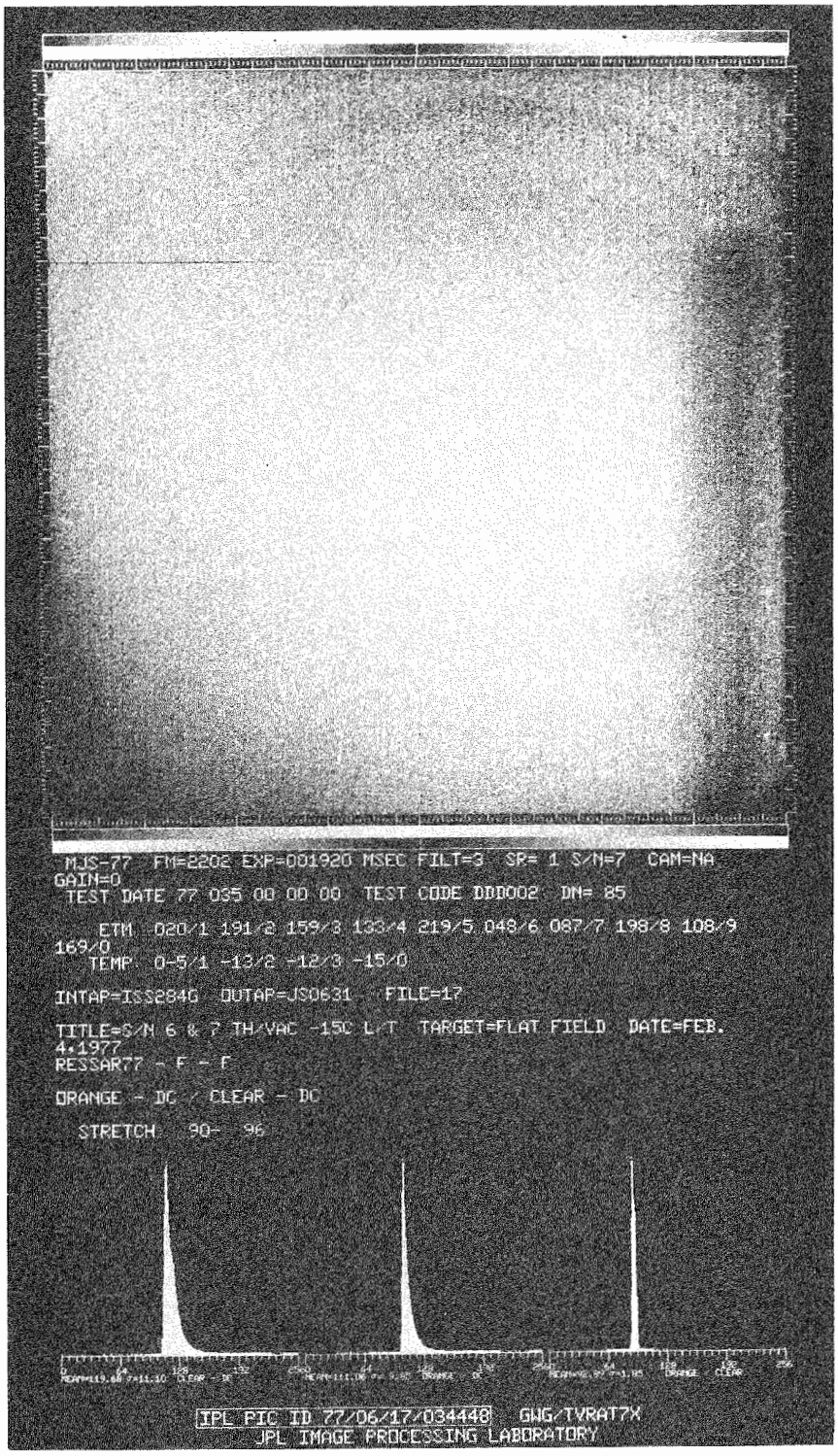

Figure 4-22. Ratio of image, ISS S/N 07: orange versus clear filter

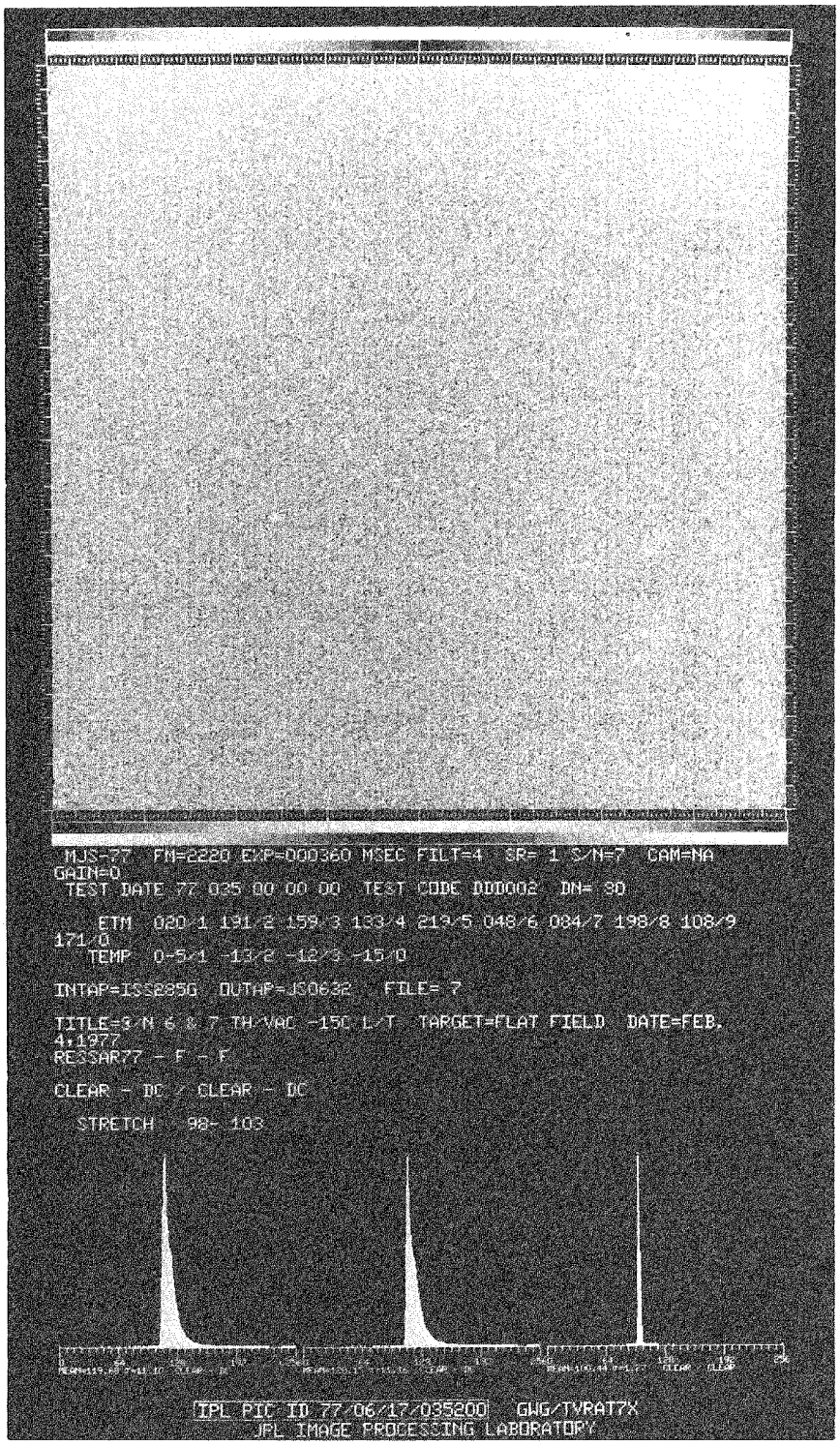

Figure 4-23. Ratio of image, ISS S/N 07: clear versus clear filter

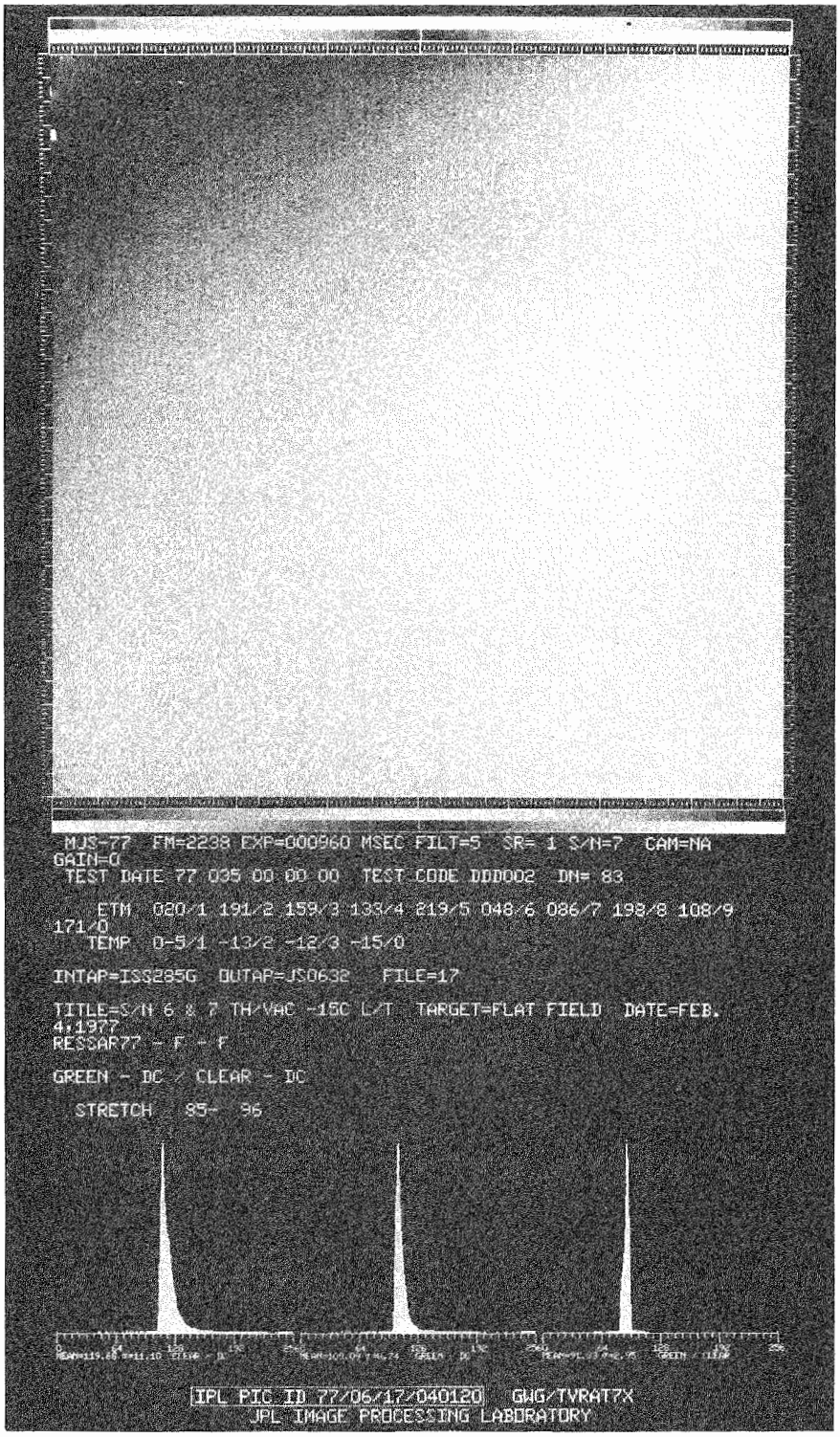

Figure 4-24. Ratio of image, ISS S/N 07: green (position 5) versus clear filter

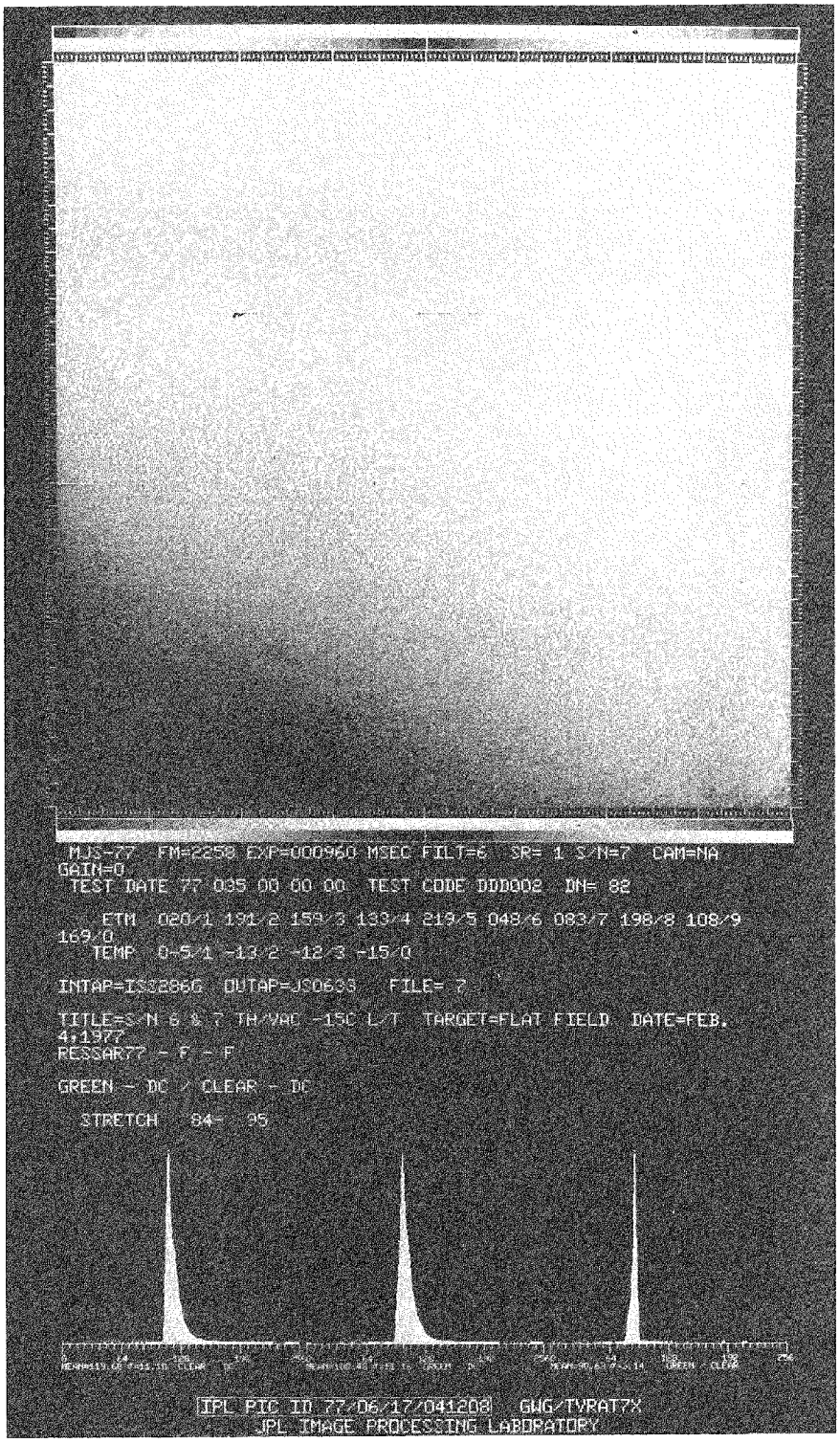

Figure 4-25. Ratio of image, ISS S/N 07: green (position 6) versus clear filter

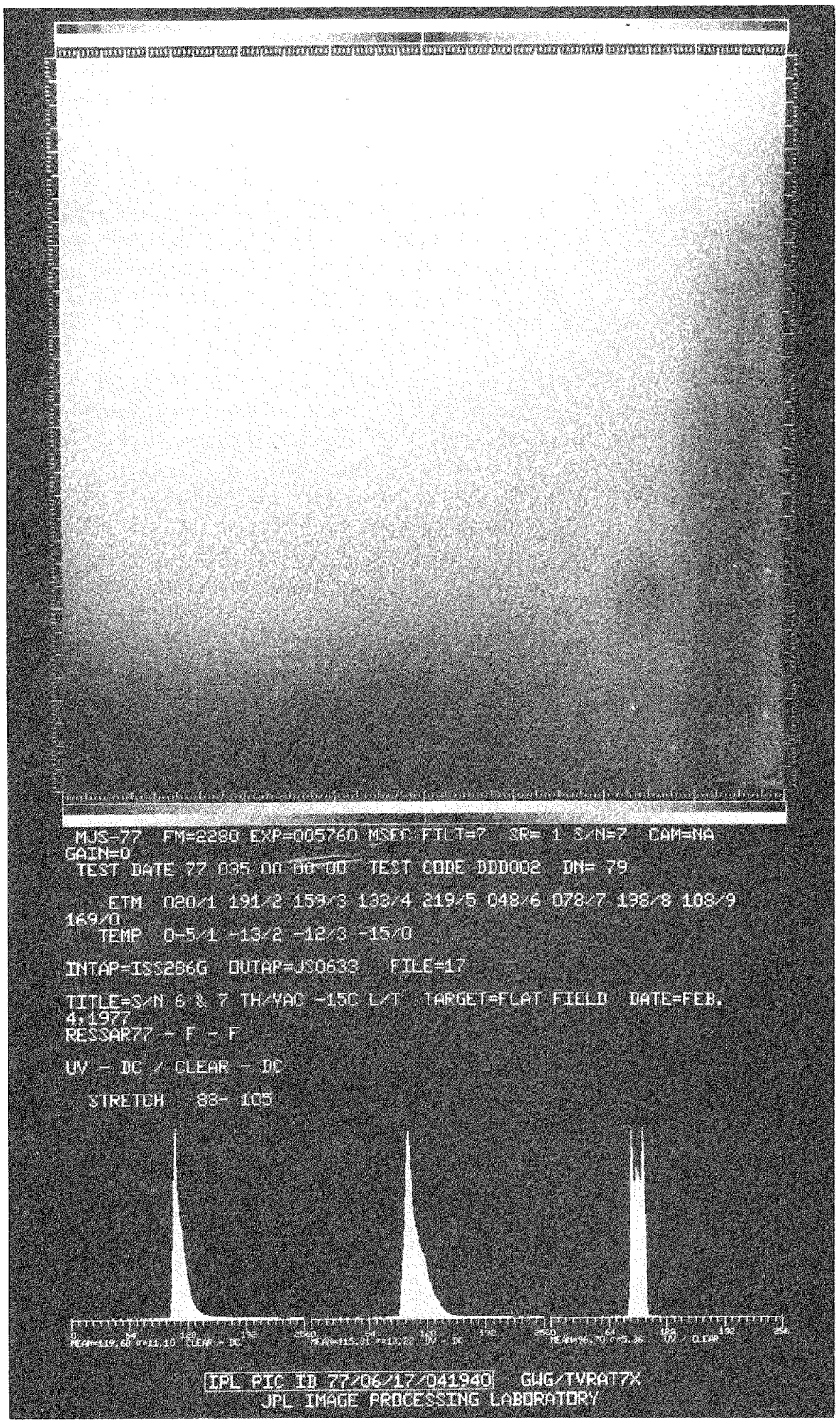

Figure 4-26. Ratio of image, ISS S/N 07: ultraviolet versus clear filter

If the relative response of each pixel were the same, the ratio would be equal for each pixel, which was not the case. Global variations were present in each combination, except where another clear filter was used. This indicates a slight but definite spatial color dependence.

It is not clear from Figures 4-13 to 4-26 whether the dependence is due to the vidicon, or whether the filters have varying transmissions. In the latter case, the ratios would be independent of light level; and this has been observed to be the case for all flight cameras. Moreover, vidicons have not shown scale variations of this magnitude in the past, so that it is easier to believe that they are due to the spectral filters rather than to the vidicons.

The color sensitivity is sufficient to require a separate decalibration file for each spectral filter, which has been done, but not gross enough to cause concern about the quality of the image itself.

c. Temperature Dependence. The ISS vidicon response is temperature-dependent. This dependence is a function of gain and dark current, both of which are proportional with temperature (vidicon temperature was used for the purpose of this analysis).

Figures 4-27(a) to (f) show this effect. A functional relation of the form below is a good model for temperature variations over the operating range of the ISS cameras:

$$(DN_{T_2} - DC_{T_2})k = DN_{T_1} - DC_{T_1} \qquad (4)$$

where

DN_{T_2} and DN_{T_1} = data numbers at temperatures T_2 and T_1

DC_{T_2} and DC_{T_1} = dark currents at temperatures T_2 and T_1

k = proportionality constant

When the DNs are near zero, the difference is due primarily to dark currents, whereas, at high DNs, it is due mostly to gain. If entirely ignored, a temperature difference of 25°C could cause an error in the estimate of object radiance by 20% at mid scale.

Figure 4-28 shows four light-transfer curves for subarea 5 of the ISS S/N 05 camera in the clear filter position and low-gain state. They were measured at three different temperatures (+26°C, +5°C and -7°C) in the thermal-vacuum chamber and at room temperature (+22°C) on the optical bench in the JPL optical tunnel. The comparison of these

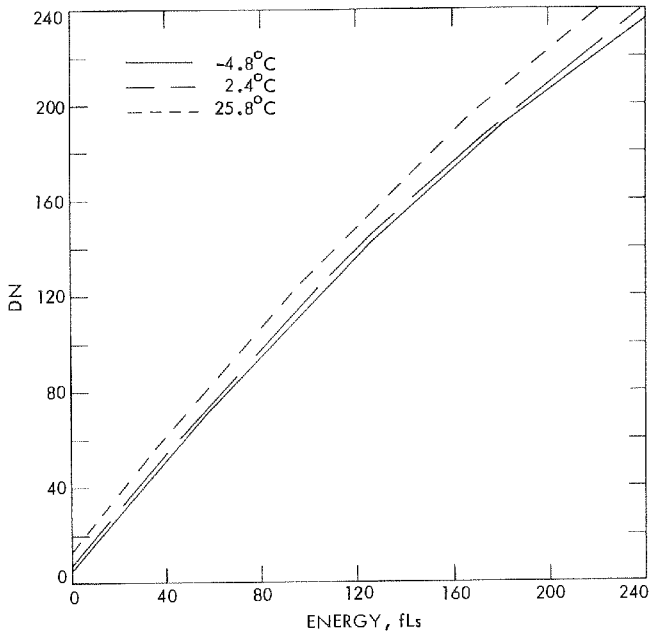

(a) ISS S/N 03

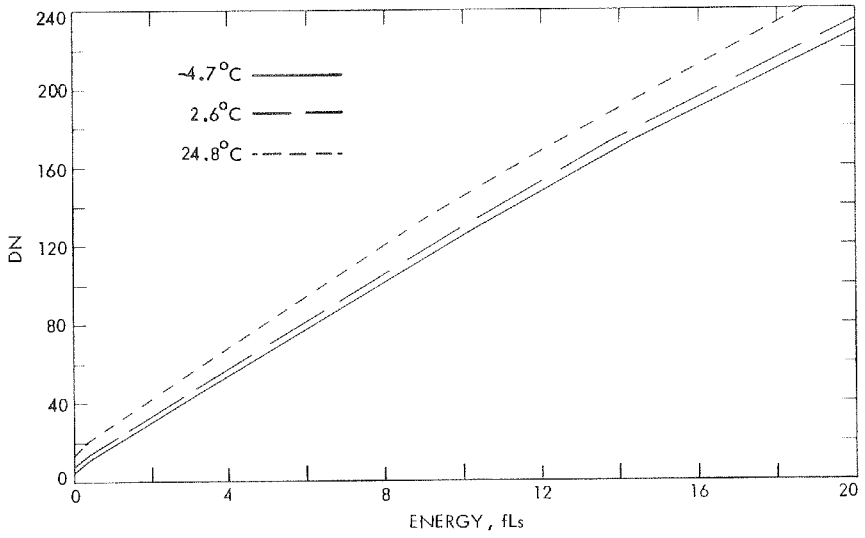

(b) ISS S/N 04

Figure 4-27. Temperature dependence of vidicon response (clear filter, 1:1, low gain): ISS S/N 03 to 08

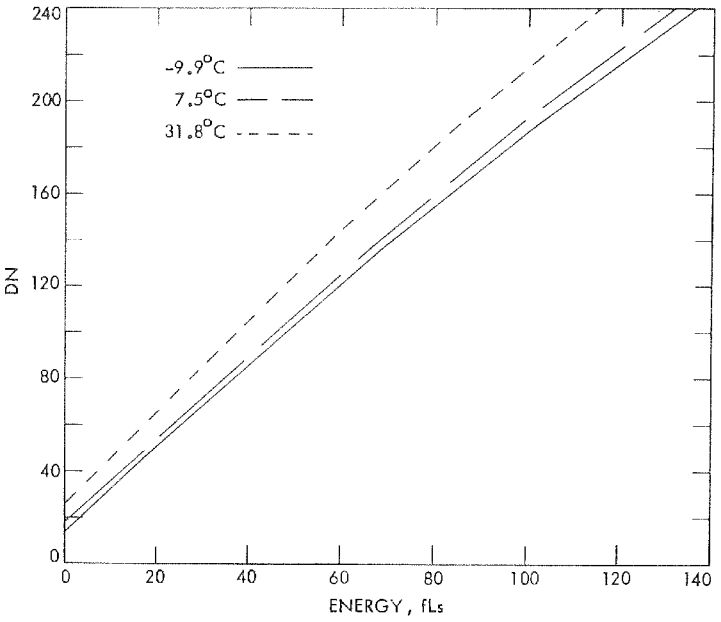

(c) ISS S/N 05

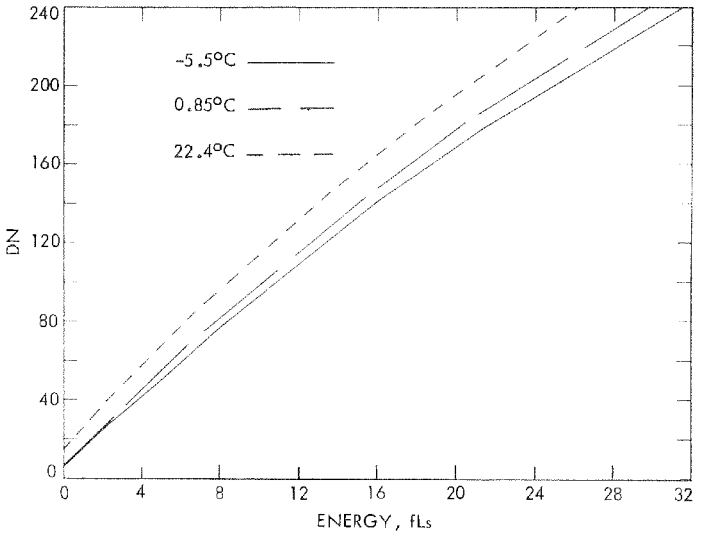

(d) ISS S/N 06

Figure 4-27 (contd)

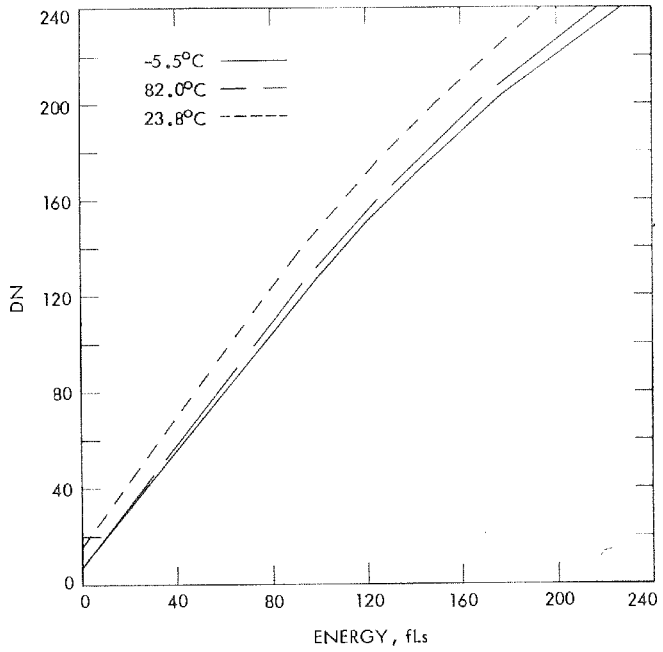

(e) ISS S/N 07

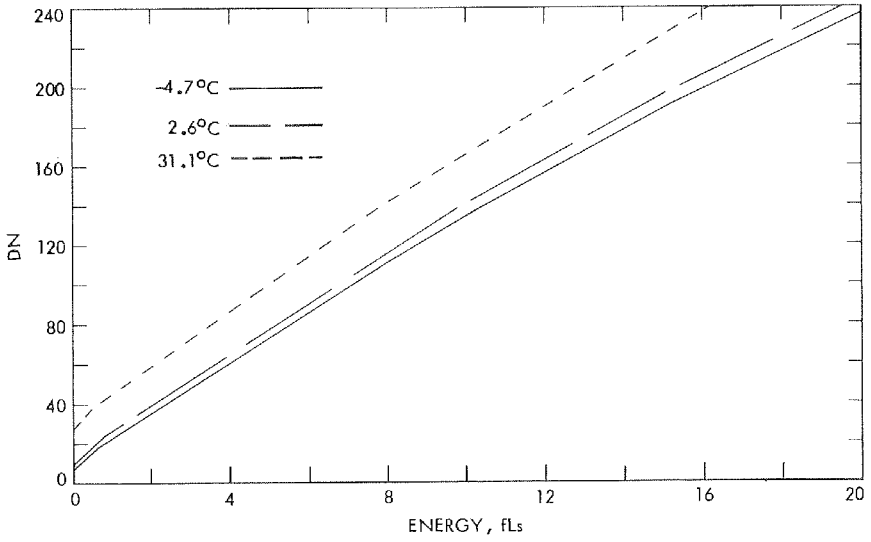

(f) ISS S/N 08

Figure 4-27 (contd)

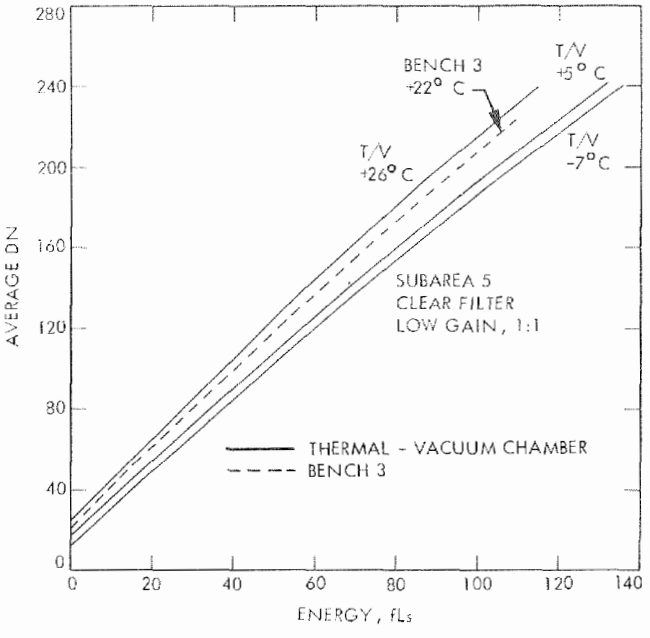

Figure 4-28. Comparison of thermal-vacuum chamber and bench light-transfer curves, ISS S/N 05

curves was made possible by applying the spectral transmittance data of the thermal-vacuum chamber quartz window[11] (see Section II-E for further details). Figure 4-28 can also be used to demonstrate how Eq. (4) may be utilized.

First, it is necessary to determine the proportionality constant k. The following values were derived at 40 fLs:

$$DC_{-7} = 13 \qquad DN_{-7} = 85$$

$$DC_{+26} = 26 \qquad DN_{+26} = 105$$

Hence

$$k = \frac{85 - 13}{105 - 26} = 0.911$$

[11] See "Thermal-Vacuum Chamber Window Filter Factors" by J. Mosher, JPL IOM 324-IPL/SIPG-77/234, November 2, 1977.

To predict the value of DN_{-7} at 100 fLs, one can obtain the following relation

$$(215 - 26) \times 0.911 = DN_{-7} - 13$$

$$DN_{-7} = 185.2$$

This agrees very well with the plotted data, but a more useful application would be to predict the light-transfer function for an uncalibrated temperature. Although +5°C was calibrated, it is used here for illustration.

At 100 fLs, the predicted value for +5°C is

$$DN_{+5} = (215 - 26) \times 0.911 + 19 = 191.2$$

Similarly, at 20 fLs,

$$DN_{+5} = (65 - 26) \times 0.911 + 19 = 54.5$$

Both of these values agree remarkably with the actual test results in Figure 4-28.

d. Gain Dependence. Two possible gain states are built into the ISS vidicon support electronics: the low-gain state and the high-gain state. The high-gain state is obtained by amplifying the signal as it is read out from the vidicon in the normal low-gain condition.

The data numbers received at low gain (DN_0) and at high gain (DN_1) can be modelled as:

$$DN_0 = S - K \tag{5}$$

$$DN_1 = gS - K \tag{6}$$

where

S = vidicon signal output

g = amplifying constant

K = additive constant

Equations (5) and (6) can be combined to give relation (7) between the two gain states:

$$DN_1 = g\ DN_0 + (g-1)\ K \qquad (7)$$

It should also be noted that the DNs include the dark-current pedestal. The constants g and K are listed in Table 4-3 for the ISS flight cameras. The gain dependence itself is shown in Figure 4-29 for ISS S/N 03 to 08.

It is evident from the nature of the system that random noise is also amplified by approximately the same ratio, although the quantization noise is not. This peculiarity should be taken into account before applications of the high-gain state are considered during the mission.

e. Scan-Rate Dependence. The ISS vidicons can, for relatively short time periods, act as storage devices for imaging data. This capability is used to minimize the need for the spacecraft recorder, as long as the time required to store the image is $\leq$ 480 s.

The vidicons can operate at five different readout (scan) rates, namely 1:1, 2:1, 3:1, 5:1, and 10:1. Each particular scan state determines the frame time during which the vidicon is read out. For example, 1:1 is the ISS readout time of 48 s, whereas 10:1 is the longest frame time, 480 s. Provided there is no temporal degradation of the image itself, non-unity scan rates will generally be characterized only by an increase in dark-current level.

The light-transfer curves in Figure 4-30 show clearly that dark current is the principal cause of differences between the different scan rates. Note that once the appropriate dark-current pedestal is removed, the light-transfer functions very closely overlay each other. The apparent compression at the upper end of the functions can be partially explained as being caused by the nonlinearity of the ISSs at higher DNs. However, empirical results indicate a small temporal effect as well.

Table 4-3. High-gain constants, g and K, ISS S/N 04 to 07

ISS S/N	g	K
04	4.04	-2.94
05	4.24	2.42
06	3.94	4.26
07	3.92	4.85

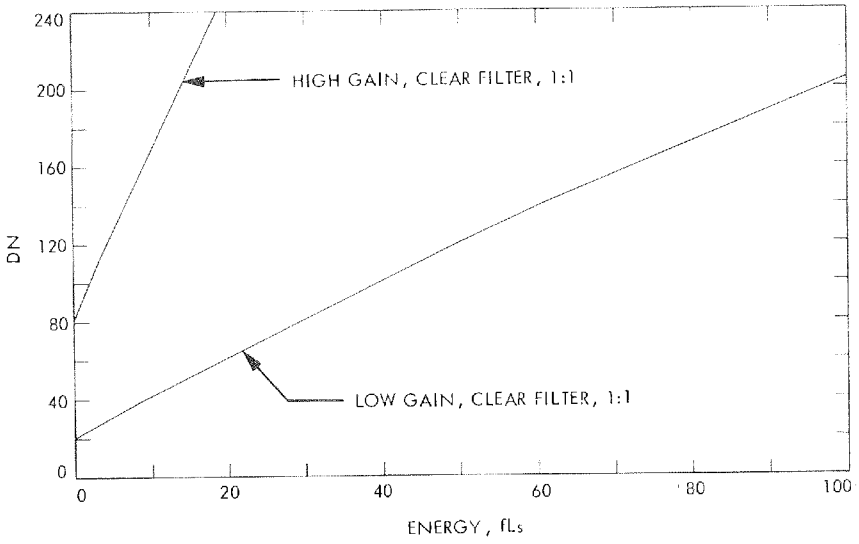

(a) ISS S/N 03

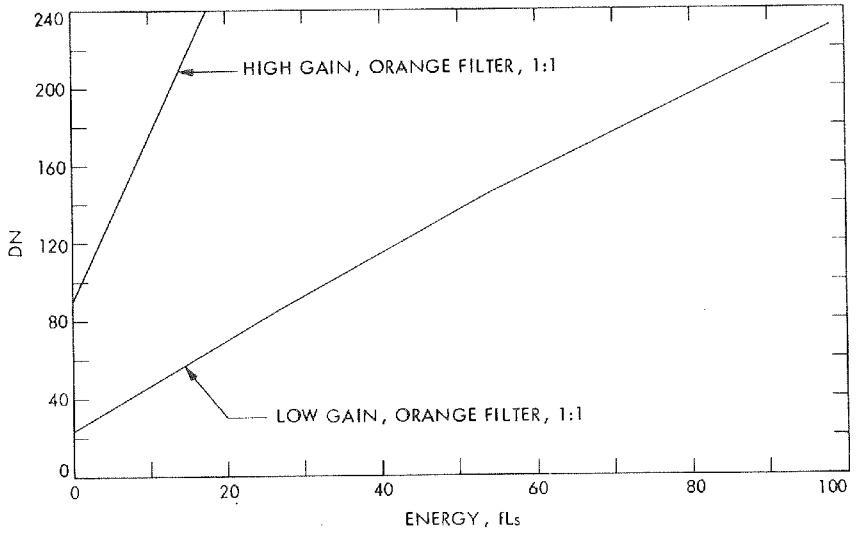

(b) ISS S/N 04

Figure 4-29. High-gain dependence, ISS S/N 03 to 08

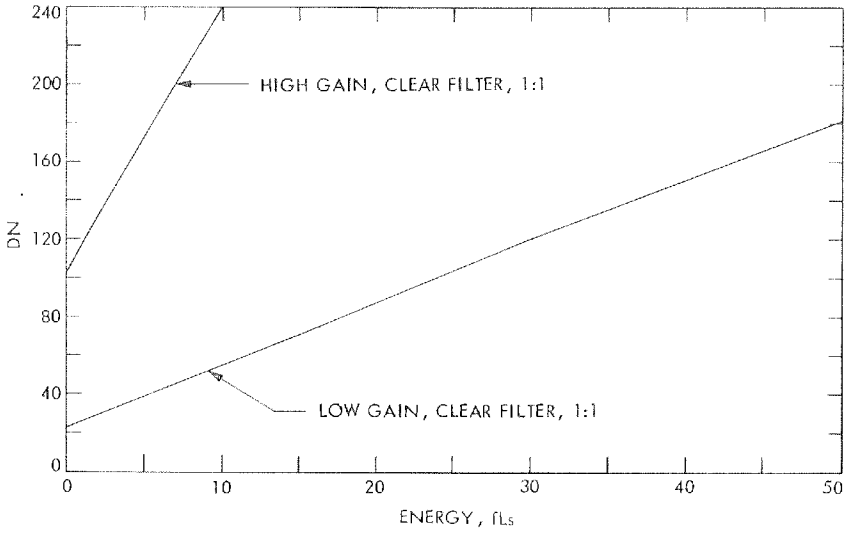

(c) ISS S/N 05

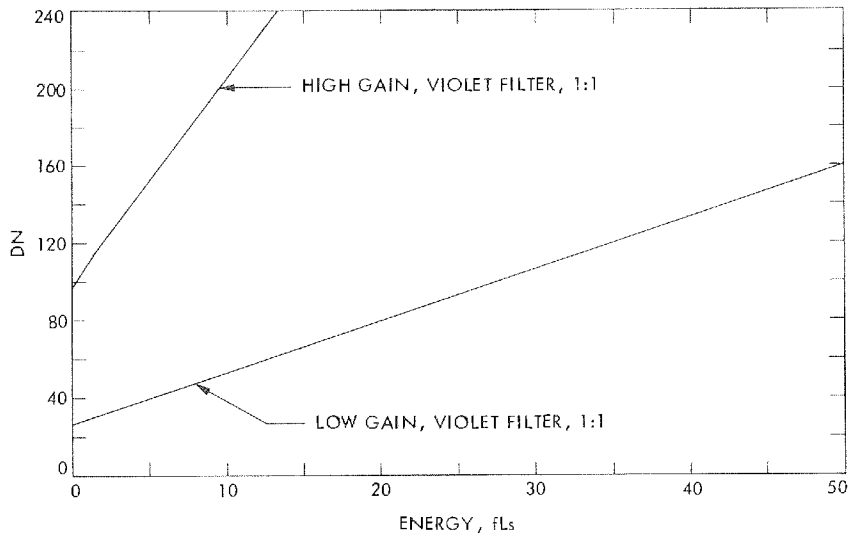

(d) ISS S/N 06

Figure 4-29 (contd)

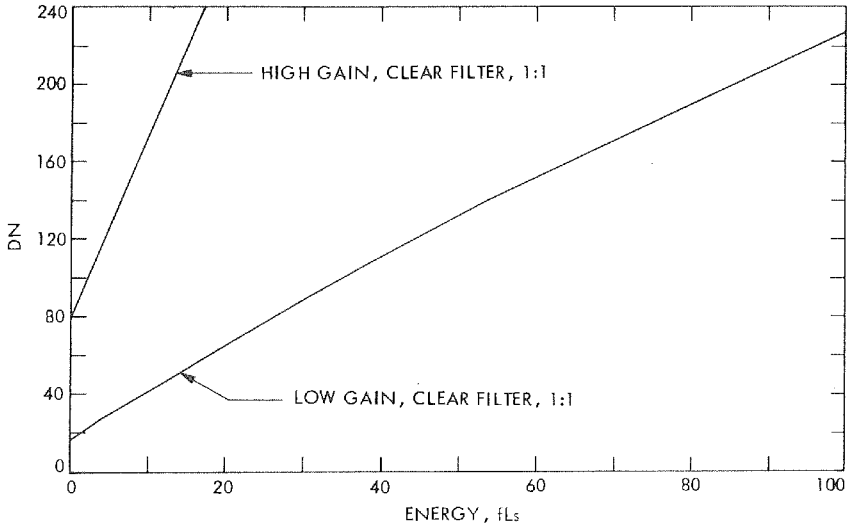

(e) ISS S/N 07

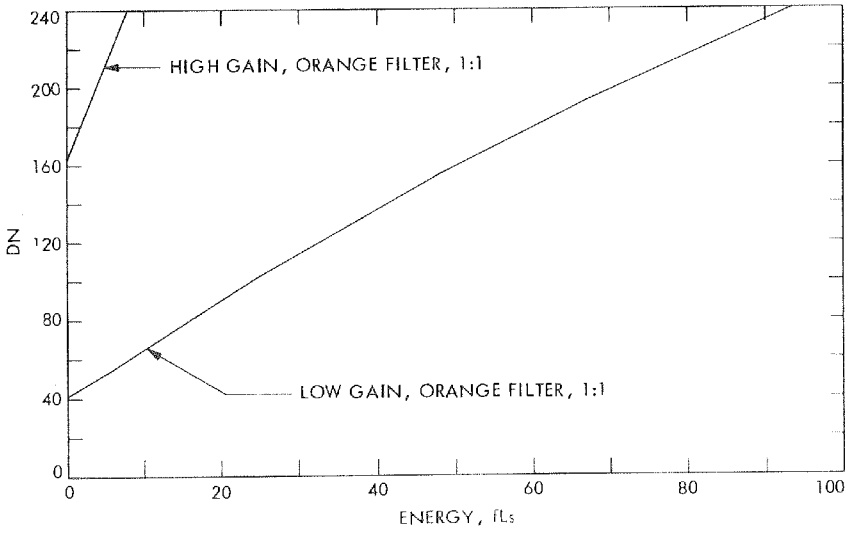

(f) ISS S/N 08

Figure 4-29 (contd)

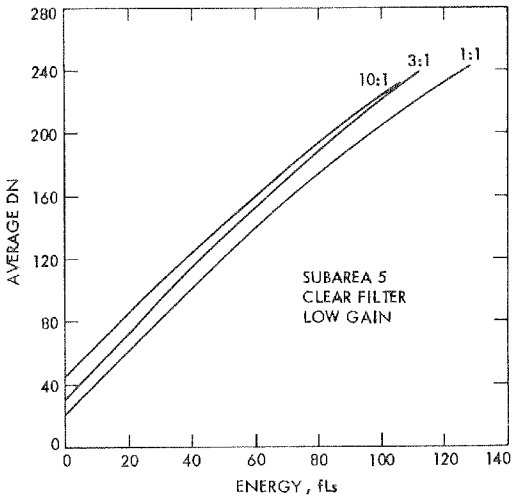

(a) ISS S/N 03

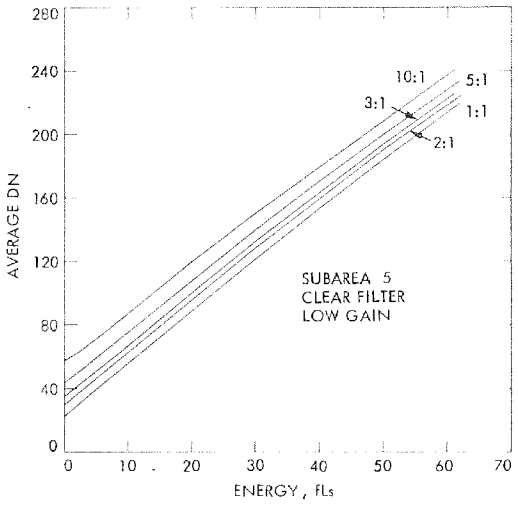

(c) ISS S/N 05

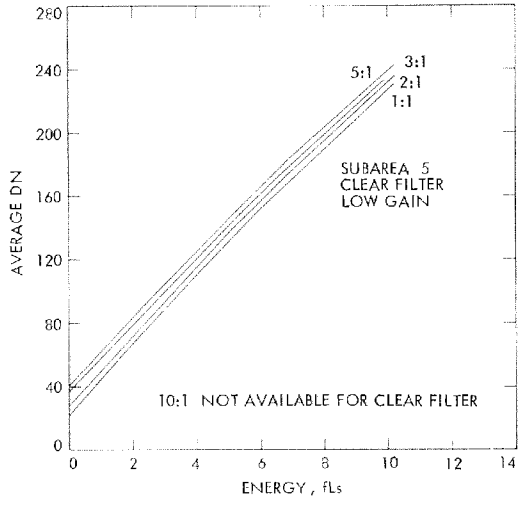

(b) ISS S/N 04

Figure 4-30. Scan rate dependence, ISS S/N 03 to 08

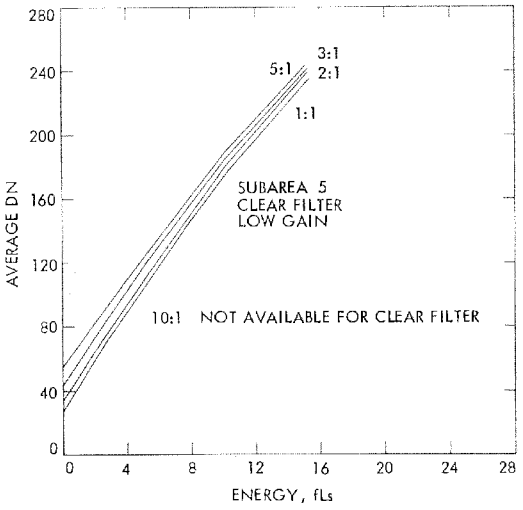

(d) ISS S/N 06

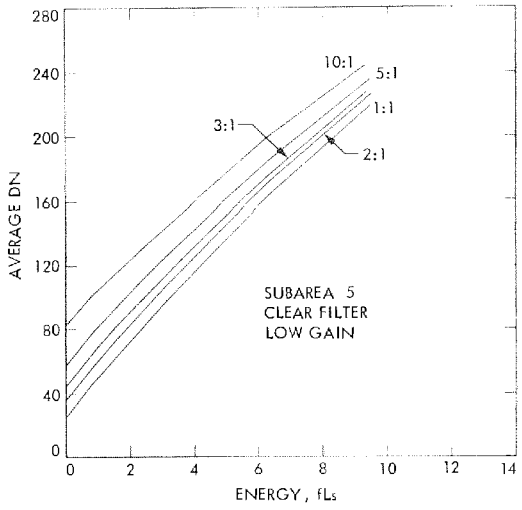

(f) ISS S/N 08

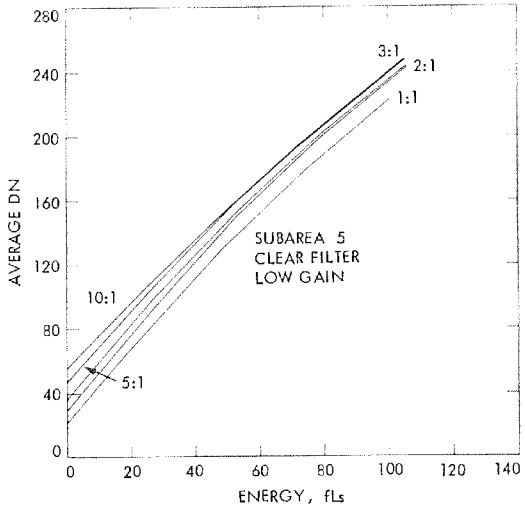

(e) ISS S/N 07

Figure 4-30 (contd)

A linear expression that provides an adequate model is:

$$DN_1 - DC_1 = a(DN_N - DC_N)\,\ell + b(DN_N - DC_N)$$

where

DN_1, DN_N = data numbers at scan rate 1:1 and N:1

DC_1, DC_N = dark current at scan rate 1:1 and N:1

a, b = multiplicative constants (typically $a \approx 10^{-4}$ and $b \approx 1$)

ℓ = picture line number

Adequate earth-based data are available to characterize the response of the ISS vidicons for different scan rates, so that there is no specific requirement to provide a formula such as the one above. However, should the system response change significantly from the earth-based calibrations during the mission, there are no direct ways at present to recalibrate the ISS cameras for other than the 1:1 scan rate. In this situation, a formula such as the one above would have to be used.

2. Light Leaks

The purpose of the light leak test was to measure the amount of light reaching the vidicon faceplate through a fully assembled camera, when the shutter was closed. The light leak test was performed for all ISS cameras on the Askania optical bench in the JPL optical tunnel.

The on-axis light leak was tested with the light cannon pointing directly into the telescope along its optical axis. The 30-cm light cannon No. 1 was used for the narrow-angle cameras; the 13-cm light cannon, for the wide-angle cameras; and the brightness was at least 7,000 fL. The off-axis test utilized multiple 500-W floodlights straddling the mounting surface between the telescope and the camera head.

The following procedure, which is described in detail in Reference 4-1, was designed for the test:

(a) Light flood on, high-gain state, shutter inhibited: stabilize the dark-current video signal for at least 15 frames.

(b) Record a dark-current frame with the camera fully covered and all lights out.

(c) Record a dark-current frame with the camera uncovered and fully illuminated (either on-axis or off-axis).

(d) Repeat step (b).

It is obvious that any difference in video level output between the illuminated and non-illuminated frames, which represent the dark-current reference pedestal, would indicate the presence of a light leak.

The obtained dark-current frames were processed by IPL for five 100 x 100 pixel areas, as explained in Figure 4-1, and Table 4-4 describes the corresponding light leaks as percentage of the dark-current reference pedestal. The requirement in Reference 2-1 for light leak detectablity of ±0.1% of the dark current turned out to be unrealistic because the standard error of IPL processing may be as high as ±6% (especially in areas 1 and 2) and the dark current itself may fluctuate up to ±2% between Steps (2) and (4).

However, as can be seen from Table 4-4, the differences between the illuminated and non-illuminated frames lie well within ±2%; and it can therefore be safely concluded that the ISS cameras are free from any detectable light leak. It should also be realized that the tests were performed in the high-gain state and that the light-source levels were deliberately very high (approximately 7,000 fL, which is at least 10 times the maximum amount of light that can be expected during the mission). This means that, in the low-gain state and under normal operational conditions, the light leak will be practically zero, or rather within the dark-current fluctuations.

Table 4-4. Light leak of ISS cameras

ISS S/N	Mode	Light Leak, % of D/C reference pedestal				
		Area 1	Area 2	Area 3	Area 4	Area 5
03	On-line	100.3	100.2	100.1	100.0	100.2
	Off-line	99.9	99.9	99.8	99.8	99.9
04	On-line	101.5	101.4	100.9	100.9	100.6
	Off-line	99.8	99.8	99.8	99.8	99.8
05	On-line	100.1	100.1	99.9	100.0	100.1
	Off-line	99.4	99.6	99.4	99.5	99.5
06	On-line	101.7	101.3	100.4	100.3	100.9
	Off-line	100.0	99.9	99.9	99.9	99.8
07	On-line	100.1	100.1	100.0	100.0	100.1
	Off-line	99.9	100.0	99.9	99.9	99.9
08	On-line	101.2	101.0	100.3	100.2	100.7
	Off-line	99.7	99.7	99.7	99.7	99.7

3. Reciprocity

Reciprocity of the ISS cameras can be defined as a measure of their radiometric consistency; i.e., a fully reciprocal system produces a constant video-signal output when the exposure, which is a function of the changing scene brightness and shutter time, remains constant.

Reciprocity tests were performed for all ISS cameras during bench calibrations. The cameras were mounted on the Askania optical bench, the 30-cm light cannon No. 1 was used for flat-field illumination of the narrow-angle cameras, and the 13-cm light cannon for the wide-angle cameras. The light cannons were carefully calibrated and operated as explained in Section II-B-3, particular attention being given to the elimination of the Veeder-root-scale backlash.

The effect of a shutter-time offset would be strongest for the shortest shutter times, gradually becoming insignificant for longer shutter times. Therefore, only shutter times from 5 to 120 ms were tested, while the light-cannon brightness was changed from 2400 to 100 fL. Each test was run both in the ascending and descending mode, and the exposure was recorded on a magnetic tape for IPL image processing.

In previous projects, the light-cannon brightness was taken for granted and the obtained video signal output was plotted against the shutter-time values, which is an acceptable approach to reciprocity data analysis. However, the light-cannon brightness does vary slightly because of short-term drift and graphical interpolation inaccuracies (see Section II-B-3). Therefore, a new, more accurate method was designed and used for the ISS cameras.

The true light-cannon brightness was determined by exact numerical interpolation and drift correction, and then the exposure was calculated as a product of the brightness and shutter time. It is obvious that, for a fully reciprocal system, the video signal/exposure ratio (DN/fLs) would be constant. In Figures 4-31 (a) to (f), this ratio was plotted for the component-level offsets (see Section III-C), and then an optimum curve was calculated based on subsystem-level reciprocity data.

It should be noted that the component shutter-time offsets differ in absolute values from the offsets described in Section II-C because both the BCE and the FDS have a built-in +2.0-ms offset to minimize the anticipated negative true shutter-time offsets. Therefore, the shutter-time offsets in Figures 4-31 (a) to (f) and in Tables 4-5 and 4-6 are residual offsets which should be added to the shutter-time commands (Table 3-11) to obtain the true shutter time.

With one exception, the results obtained are excellent (the seeming non-linearity of the curves is due to the deliberately exaggerated vertical scale). The subsystem-level reciprocity tests have confirmed the component calibration conclusions that each shutter has a systematic negative offset, which should be considered. If this is done, the reciprocity of ISS cameras is outstanding. However, the

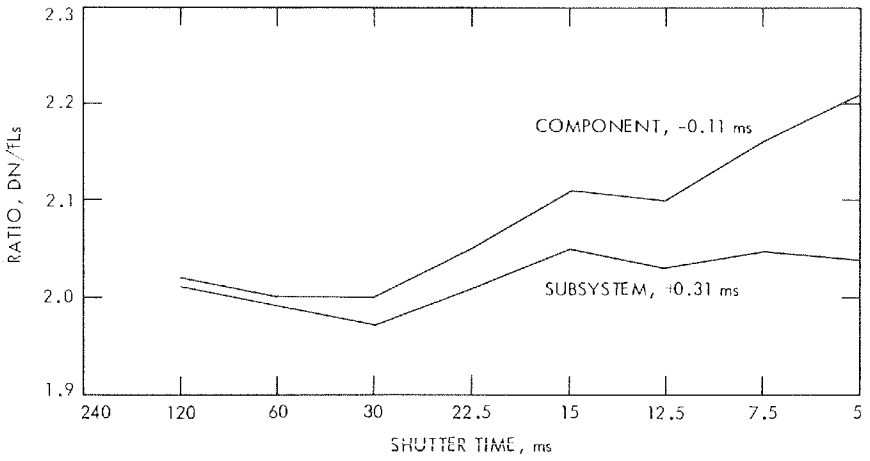

(a) ISS S/N 03

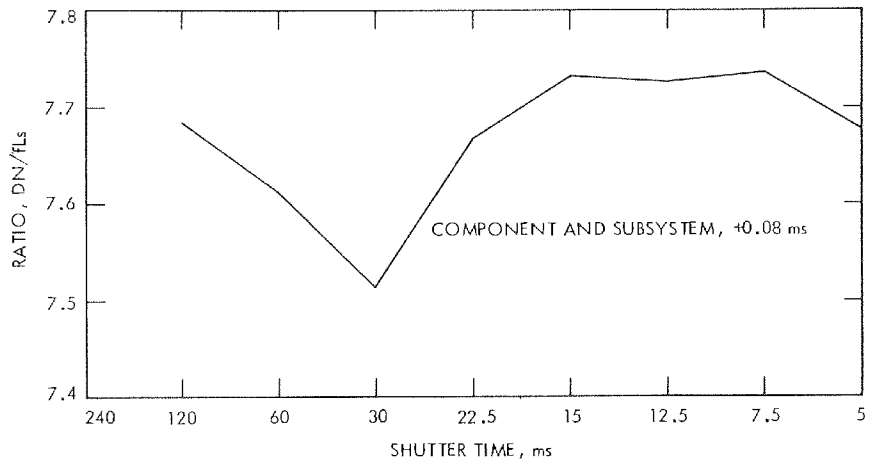

(b) ISS S/N 04

Figure 4-31. Reciprocity, ISS S/N 03 to 08

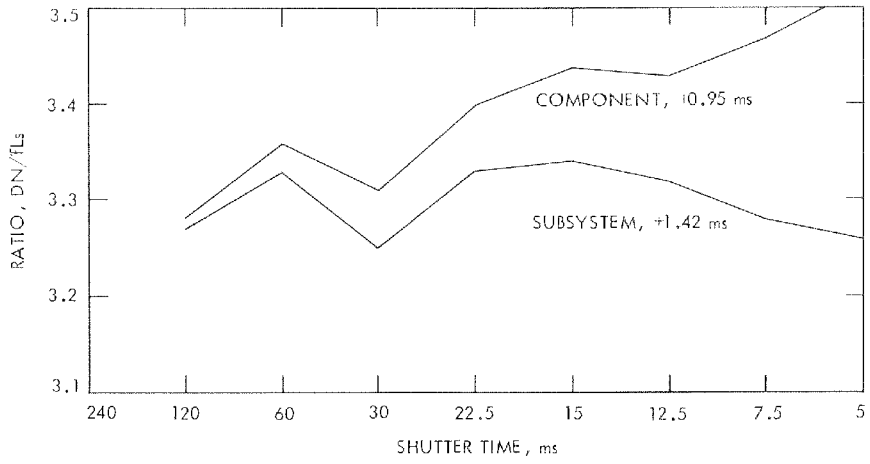

(c) ISS S/N 05

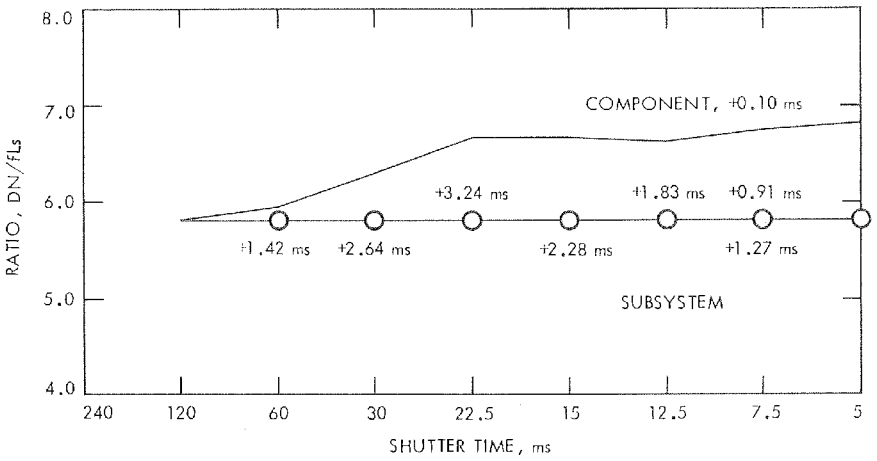

(d) ISS S/N 06

Figure 4-31 (contd)

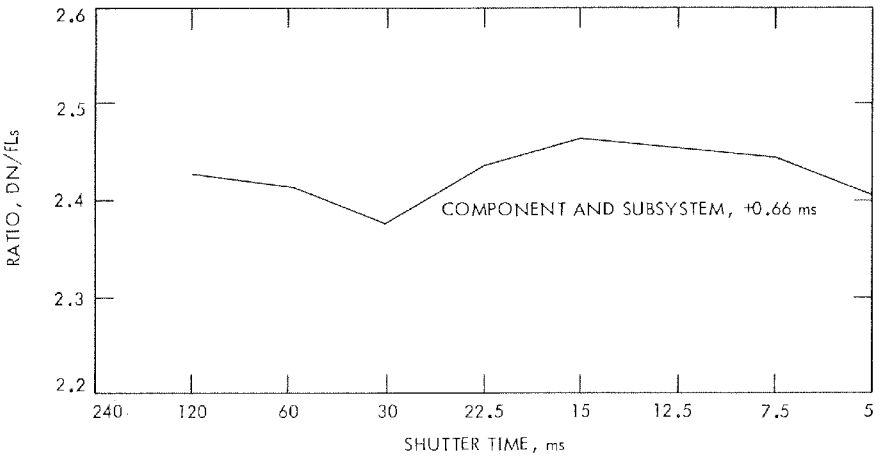

(e) ISS S/N 07

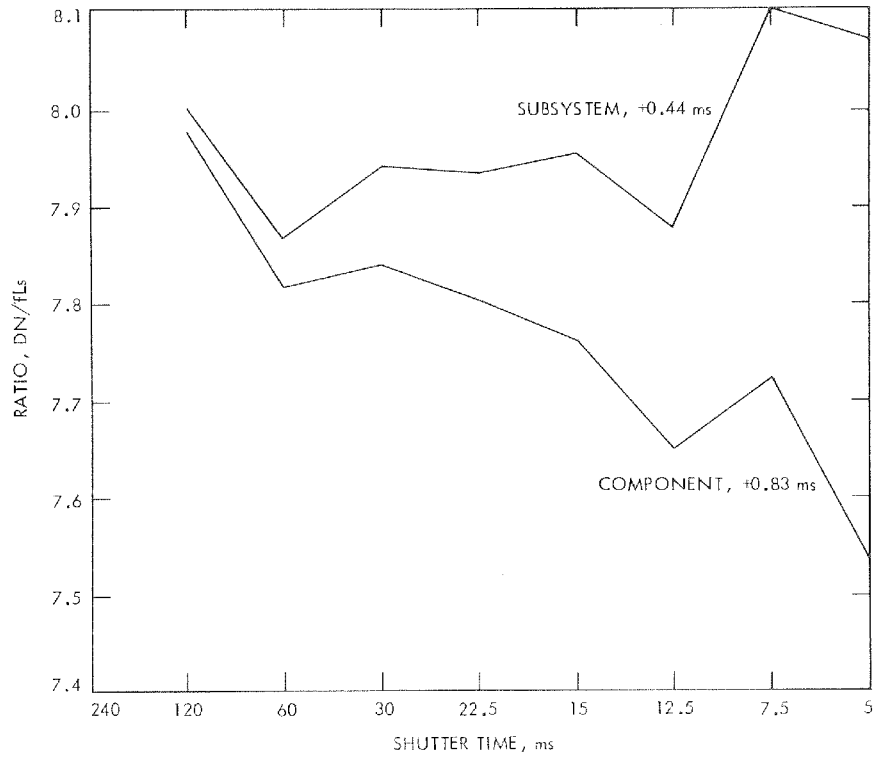

(f) ISS S/N 08

Figure 4-31 (contd)

Table 4-5. Comparison of ISS true shutter-time offsets

ISS S/N	Shutter S/N	Temperature, C°	True shutter time offset with respect to normal command (includes BCE/FDS offset), ms		
			Component calibration	Reciprocity (subsystem) calibration	Average
03	07	+28	-0.11 ±0.02	+0.31 ±0.02	+0.10 ±0.21
04	06	+30	+0.08 ±0.02	+0.08 ±0.02	+0.08 ±0.02
05	09	+26	+0.95 ±0.01	+1.42 ±0.05	+1.18 ±0.23
06	12	+25	+0.10 ±0.01	Poor reciprocity	
07	11	+25	+0.66 ±0.02	+0.66 ±0.06	+0.66 ±0.04
08	08	+27	+0.83 ±0.02	+0.44 ±0.01	+0.64 ±0.19

Table 4-6. True shutter-time offsets, ISS S/N 06

ISS S/N	Shutter S/N	Temperature, °C	Normal command, ms	True shutter time offset (includes BCE/FDS offset), ms	
				Component calibration	Reciprocity (subsystem) calibration
06	12	+25	5	+0.10 ±0.01	+0.91 ±0.04
			7.5	+0.10 ±0.01	+1.27 ±0.04
			12.5	+0.10 ±0.01	+1.83 ±0.05
			15	+0.10 ±0.01	+2.28 ±0.05
			22.5	+0.10 ±0.01	+3.24 ±0.13
			30	+0.10 ±0.01	+2.64 ±0.04
			60	+0.10 ±0.01	+1.42 ±0.10
			120	+0.10 ±0.01	+0.10 ±0.04

shutter-time commands may be considered acceptable for most practical purposes, because of the built-in +2.0-ms offset.

The component-level shutter-time offsets and the reciprocity subsystem-level offsets are compared in Table 4-5. Their differences can be considered as random differences resulting from general inaccuracies of the entire bench calibration environment and input. As can be seen, the measuring accuracy of individual offsets was kept well within the ±5% shutter-time requirement (see Reference 2-1).

The only exception is ISS S/N 06, which has a rather poor reciprocity, as documented in Figure 4-31 (d) and Table 4-6. These results are based on three independent tests performed over a period of time, and in each case the offsets were almost identical. This means that, in this particular case, the offsets are different for each shutter time, and they definitely should be used for all shutter times below 120 ms.

Knowledge of shutter-time offsets is important for analyses of calibration data. The offsets will also be used by IPL for ISS camera products decalibration, definitely for shutter times from 5 to 60 ms. However, new offset values will have to be determined as part of the in-flight calibrations because the shutter performance may be different in vacuum under flight conditions, where the influence of the earth's gravitational environment is not present.

No reciprocity tests were performed in the thermal-vacuum chamber, but the analysis of the light-transfer curves indicates that the shutter-blade bounce, which usually occurs during freezing temperatures, does not reach into the active vidicon format (see Sections III-C and IV-A-1). However, to be safe, operational temperatures below -5°C should be avoided, if at all possible.

4. Dark-Current Buildup (Simulation of Simultaneous Exposures)

A new feature of the ISS cameras is that it is possible to shutter both the wide- and narrow-angle cameras simultaneously. Once this occurs, the narrow-angle image is read out in a normal manner, but the wide-angle image is temporarily stored on the vidicon during the narrow-angle image readout time; i.e., the wide-angle image is read out only after the narrow-angle camera readout is completed.

If, for example, the ISS is in the 10:1 scan rate mode, the frame readout time for the narrow-angle camera is 480 s; and the wide-angle image is retained on the vidicon during this time, which results in a significant dark-current buildup. After that, it is read out in the next 480 s.

It should be noted, however, that, for the ISS bench calibrations, the BCE did not have the capability to command the narrow-angle/wide-angle camera simultaneous exposures, but it could simulate the vidicon image storage of the wide-angle camera, which is the same thing for all practical purposes.

Because of extensive calibrations required for the other camera modes, it was not possible to completely characterize the light-transfer functions for the wide-angle cameras in their simultaneous exposure mode. However, there is nothing unusual about this mode for the narrow-angle cameras, whose response is therefore characterized by the other radiometric calibrations described in this report.

It is believed that a good approximation to the light-transfer function of the wide-angle cameras in their simultaneous exposure mode will be their standard flat-field light-transfer function with a different dark current or offset; namely, the one determined from their dark-current buildup calibrations. However, it should be pointed out that simultaneous exposures in the high-gain state are not feasible for scan rates 3:1 and above because, in this case, dark-current buildup itself approaches the saturation level or goes even beyond it. This is true for any normal operational temperature.

Figures 4-32 to 4-37 show the ratio of a normal dark-current image against its comparable dark-current image in the simultaneous exposure mode for ISS S/N 04 (2:1 low gain and 5:1 low gain) and ISS S/N 06 (1:1 low gain, 1:1 high gain, 3:1 low gain, and 10:1 low gain). The histograms across the bottom of the image from left to right are the normal-mode dark current, the simultaneous-exposure dark current, and the ratio of these two modes.

Note the lack of shading across the image. This lack would indicate that there is nothing unusual happening in the wide-angle camera simultaneous exposure mode. The shading down the image is probably caused by normal dark-current buildup which is present in any mode. Unfortunately, these results are not conclusive because at present there is no direct way to determine whether or not this simple combination of the regular calibrated data with different dark currents will suffice. This method, however, will be verified during in-flight calibrations.

5. In-Flight Calibration Lamps

Two direct tools are provided aboard the Voyager spacecraft to determine the radiometric characteristics of the ISS cameras during the mission. They are the calibration plaque (see Section IV-A-8) and the in-flight calibration lamps, which are discussed in this section.

The location and configuration of the in-flight calibration lamps in the ISS camera was briefly described in Section III. The lamps themselves are tiny Carley 5-V lamps (type 715 AS 15, 0.115 A), which were exposed to extensive electron radiation tests before their installation in the cameras (the radiation varied from 1.0×10^{12} to 1.4×10^{13} electrons/cm^2). The tests have proved that the Carley lamps are very suitable for in-flight calibration purposes because the electron radiation did not result in any measurable deterioration of their spectral characteristics (a typical spectral irradiance curve of a Carley lamp is shown in Figure 4-38).

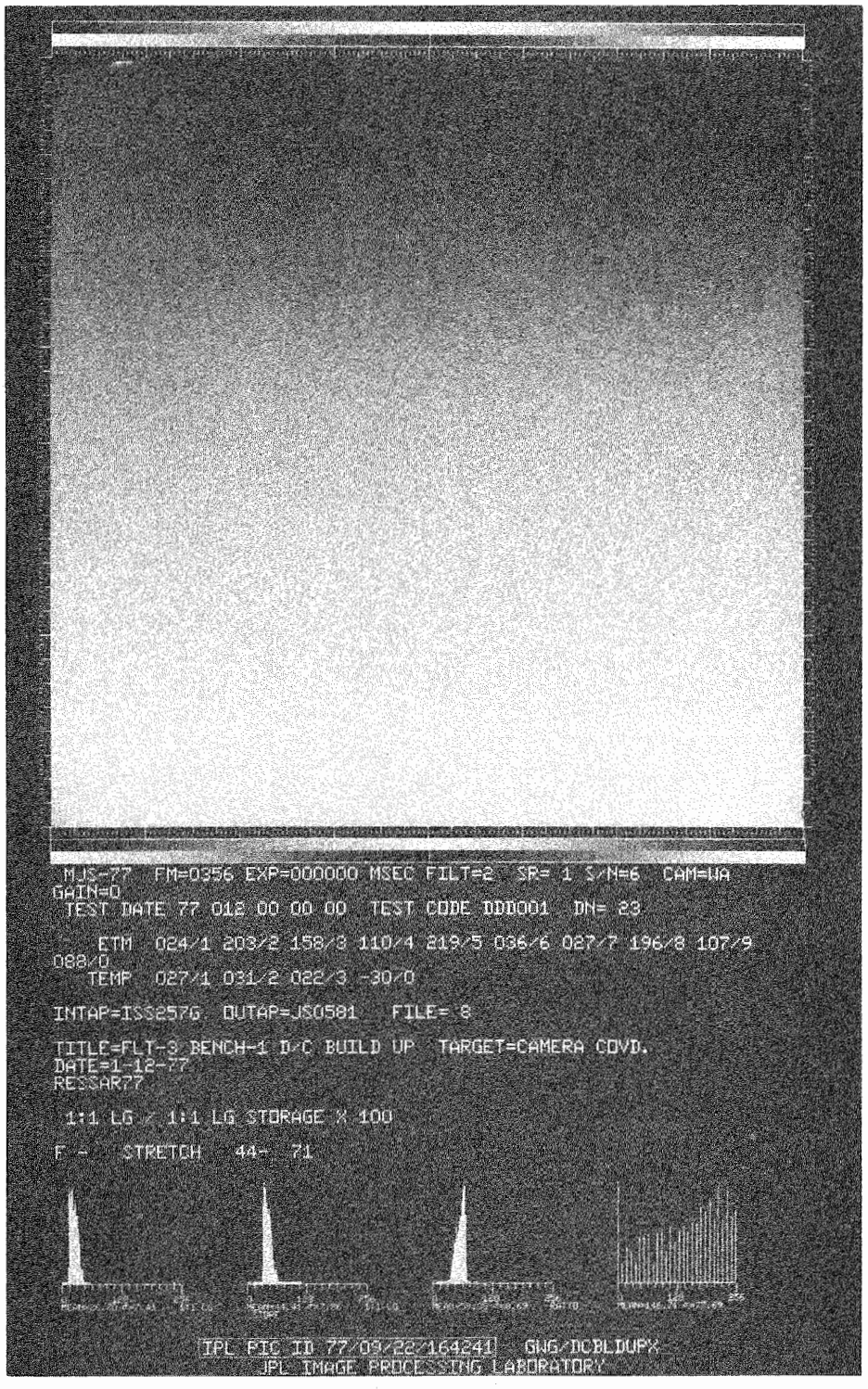

Figure 4-32. Ratio of simultaneous exposure image (scan rate 1:1, low gain), ISS S/N 06

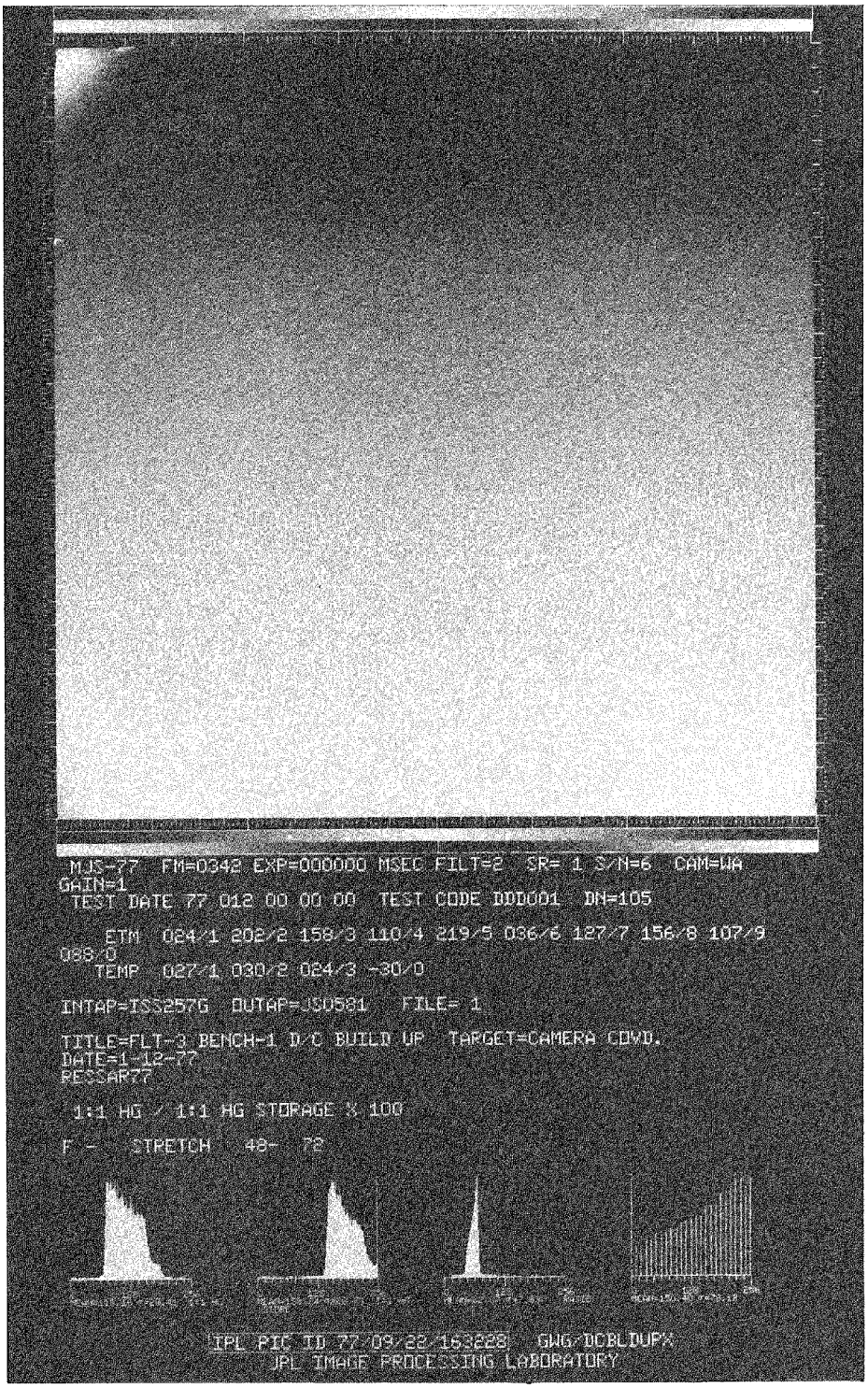

Figure 4-33. Ratio of simultaneous exposure image (scan rate 1:1, high gain), ISS S/N 06

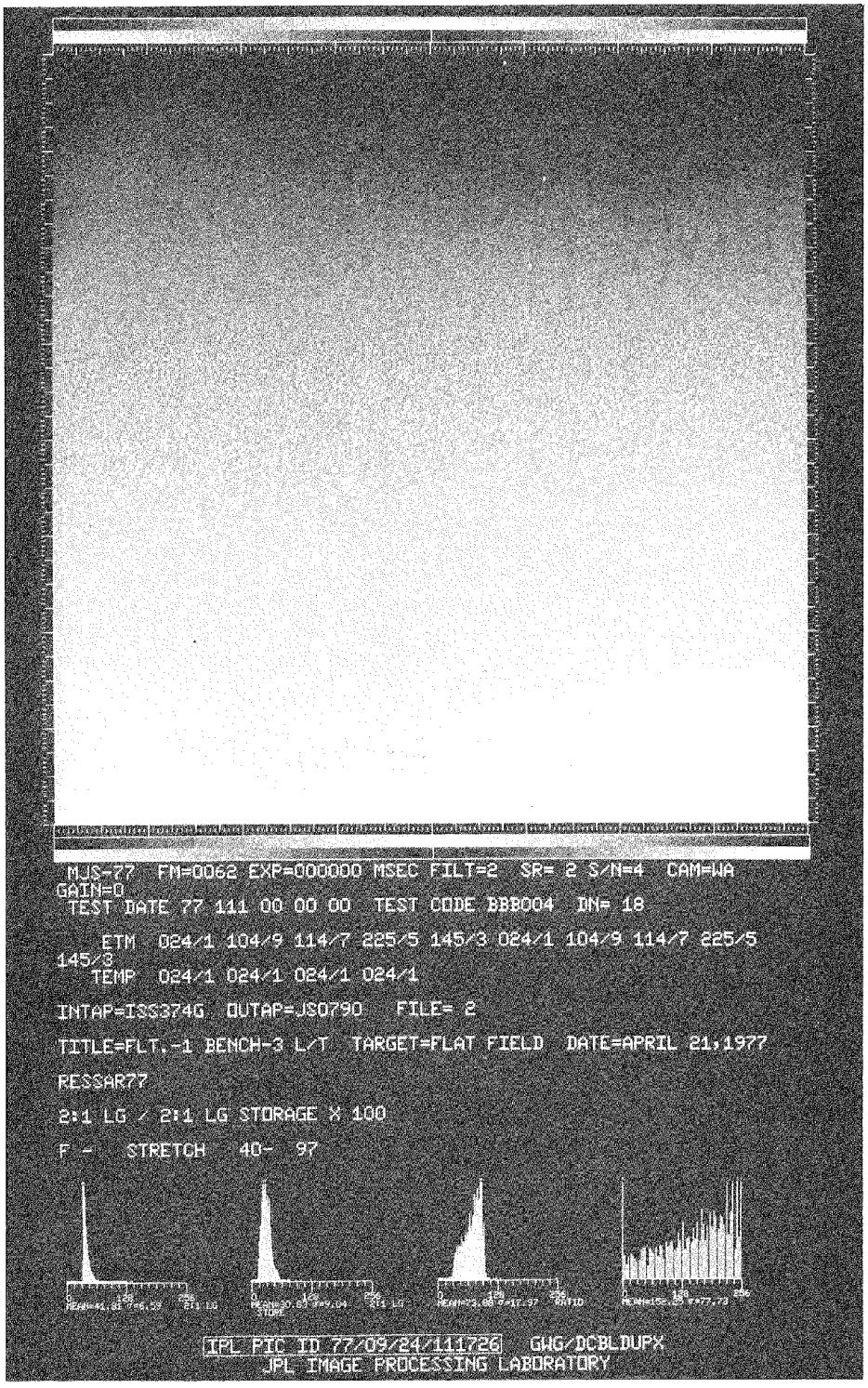

Figure 4-34. Ratio of simultaneous exposure image (scan rate 2:1, low gain), ISS S/N 04

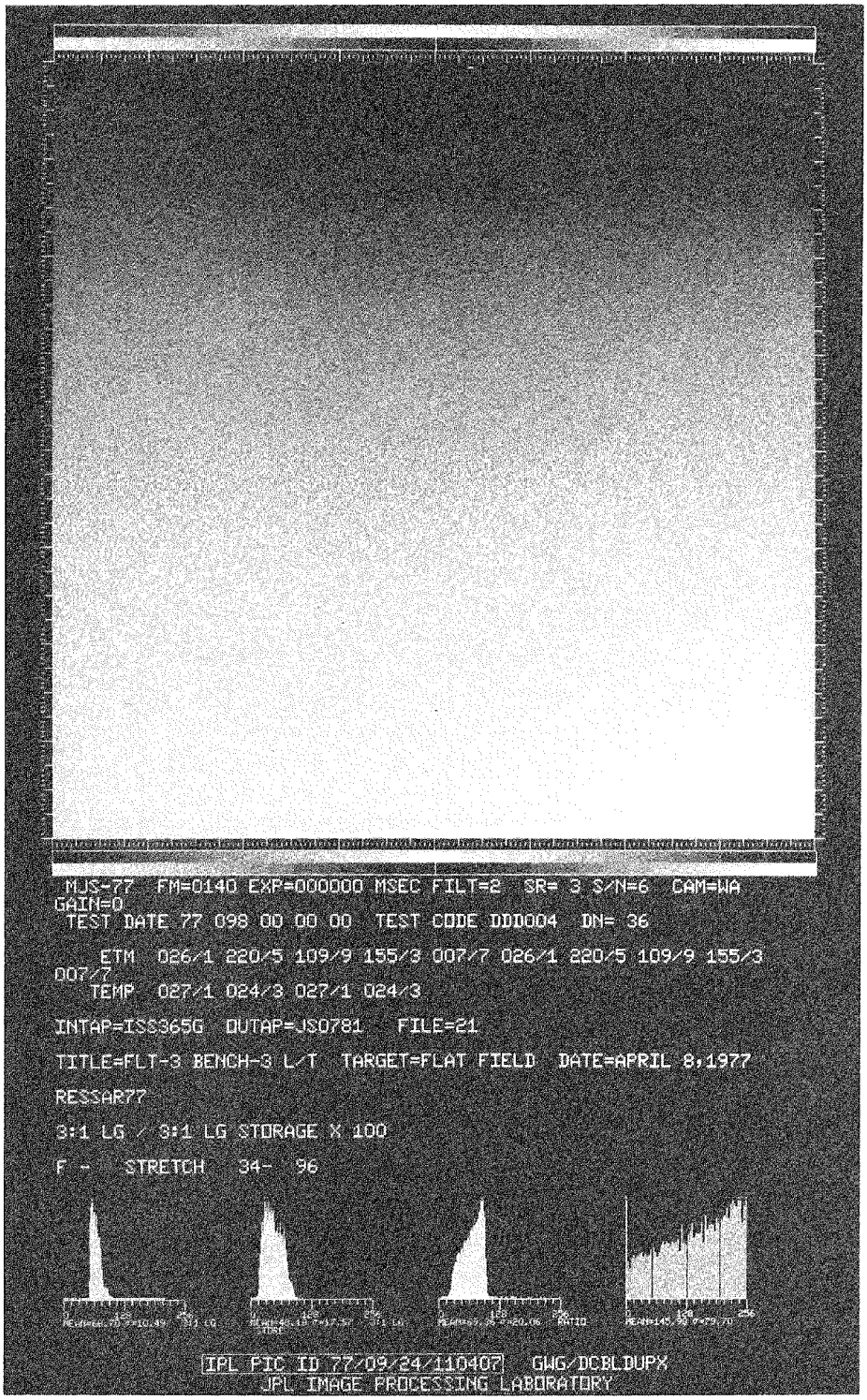

Figure 4-35. Ratio of simultaneous exposure image (scan rate 3:1, low gain), ISS S/N 06

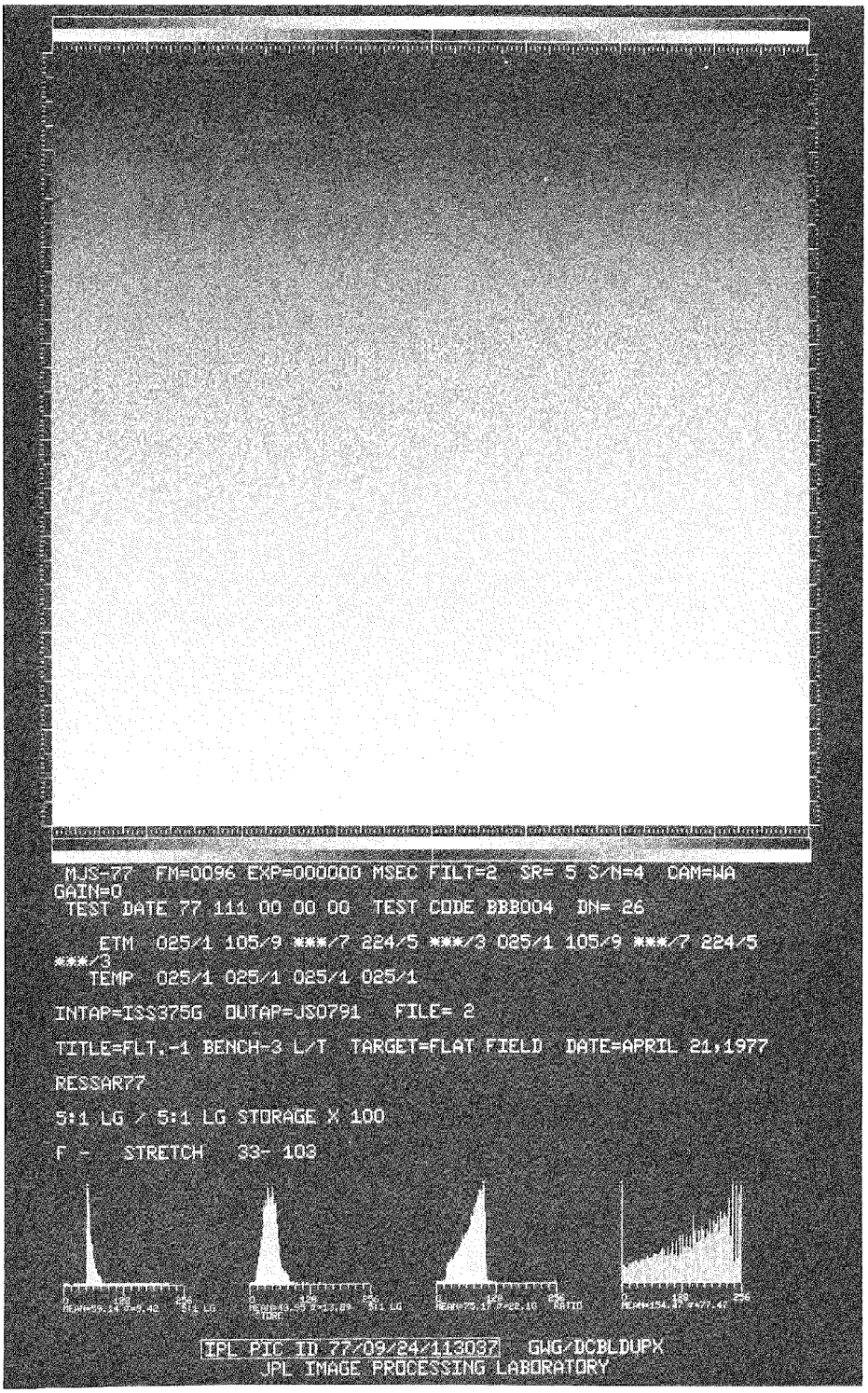

Figure 4-36. Ratio of simultaneous exposure image (scan rate 5:1, low gain), ISS S/N 04

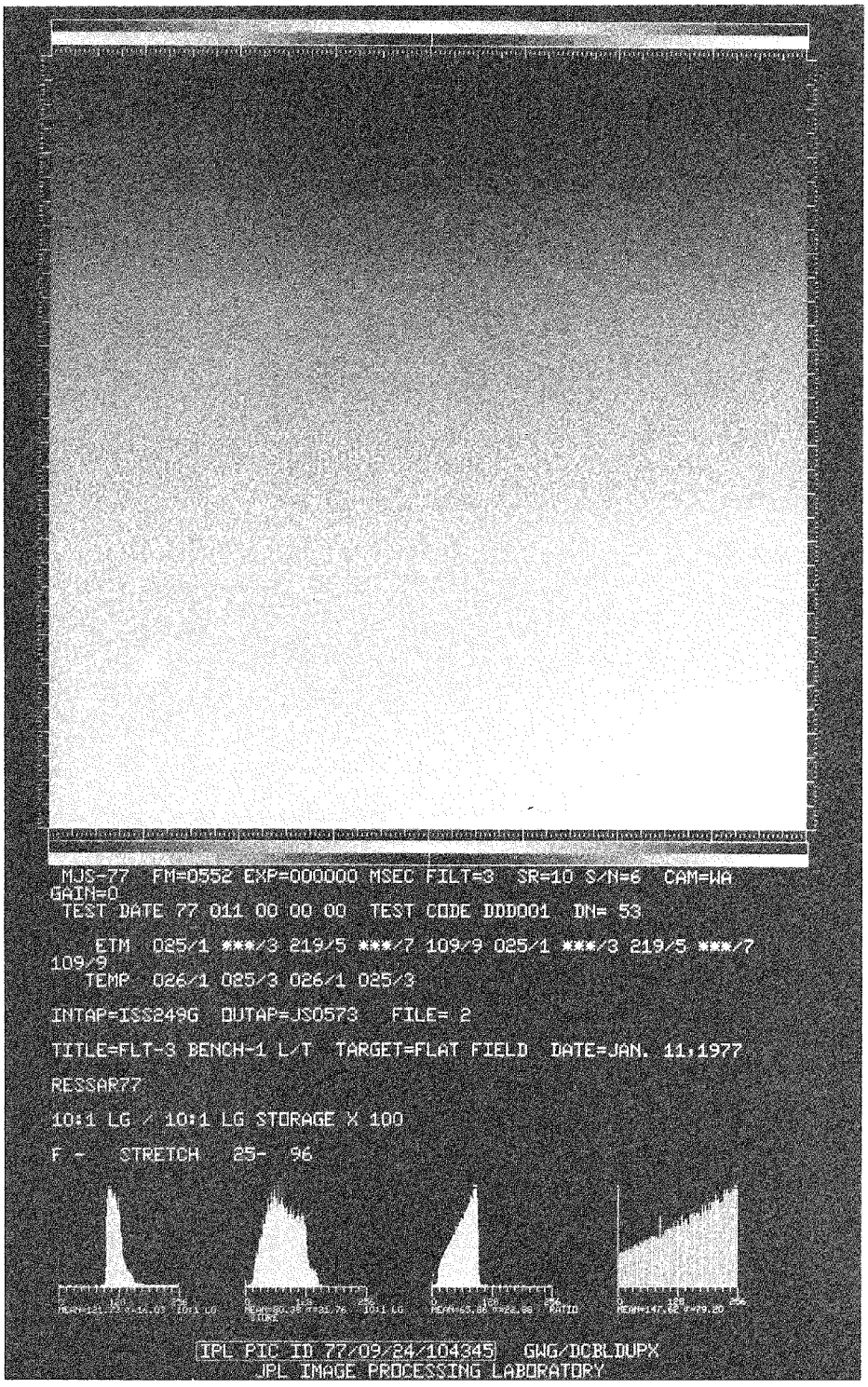

Figure 4-37. Ratio of simultaneous exposure image (scan rate 10:1, low gain), ISS S/N 06

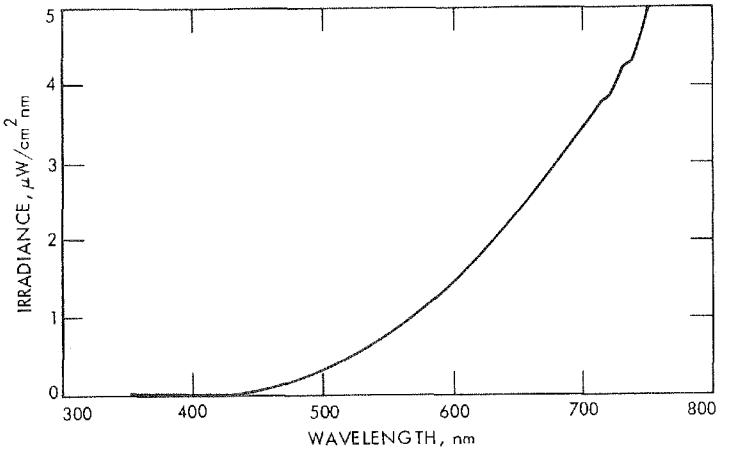

Figure 4-38. Spectral characteristics of a typical Carley 5-V in-flight calibration lamp

It should be noted that the in-flight calibration lamps can be operated in two different modes:

(a) The "vary shutter time" mode, wherein the lamps are lighted for the duration of the frame and the shutter regulates the exposure time the same as for any other regular frame.

(b) The "vary bulb on-time" mode, wherein the shutter stays open and the lamps flash for the commanded time interval.

Figures 4-39 (a) to (f) and 4-40 (a) to (f) show typical samples of ISS S/N 03 to 08 images taken through the clear filter with the in-flight calibration lamps used in both modes. Unfortunately, the reflections and mottling, which are typical, preclude the possibility of using the lamps to directly generate light-transfer functions to be used by the IPL for decalibration purposes.

Figure 4-41 (a) to (f) is the ISS S/N 03 to 08 light transfer-curves of subarea 5 using the clear filter in both modes. These figures shed additional light on the possible use of these lamps for in-flight calibrations. Note the relative smoothness of the data; the reflections and mottling are not at all apparent here. Therefore, this tool will prove useful in determining the relative response of the vidicon, since average response is adequate for this purpose. It should also be noted that only a relative response function is possible because the lamps themselves are not calibrated.

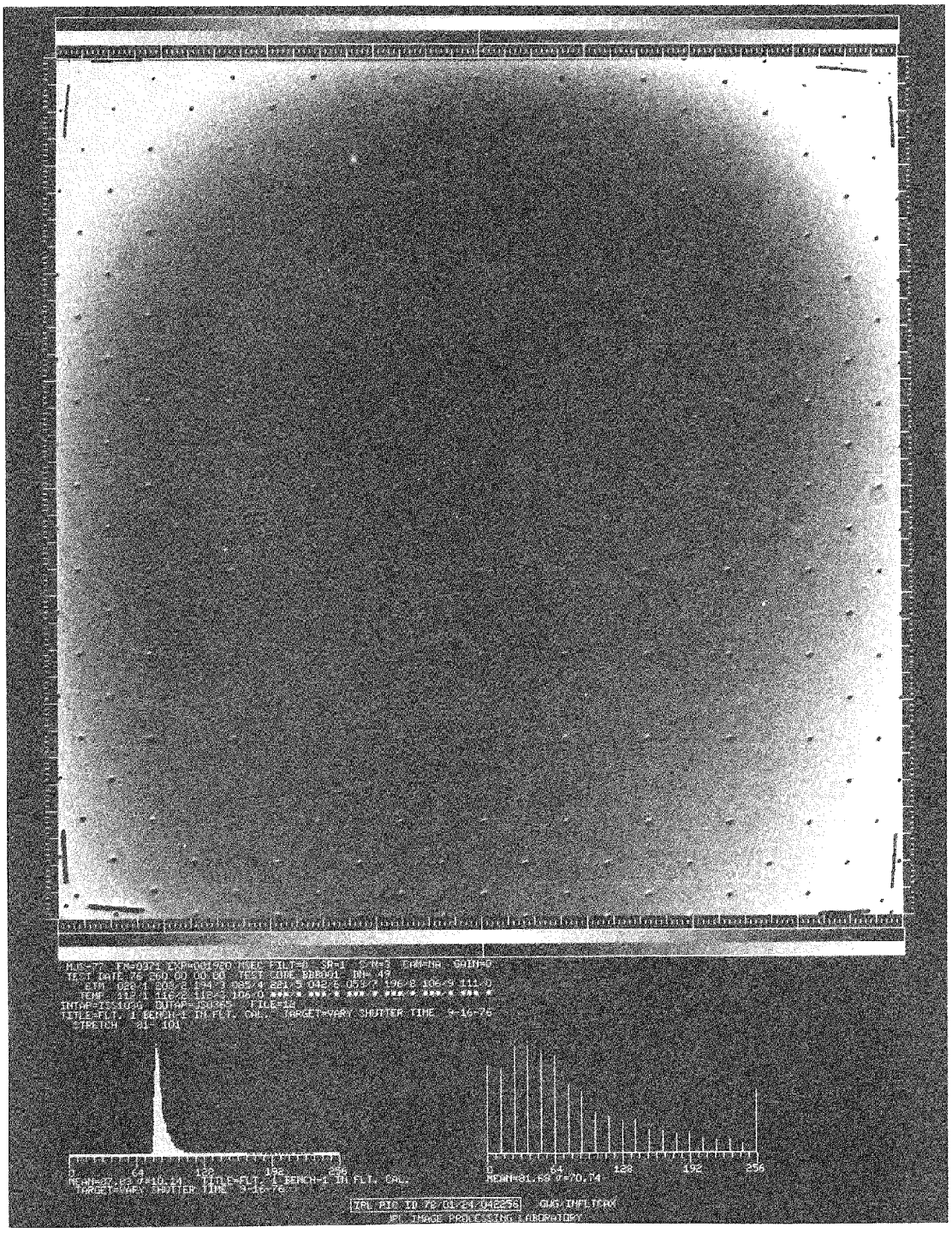

(a) ISS S/N 03

Figure 4-39. Clear filter images using in-flight calibration lamps in mode 1 (vary shutter), ISS S/N 03 to 08

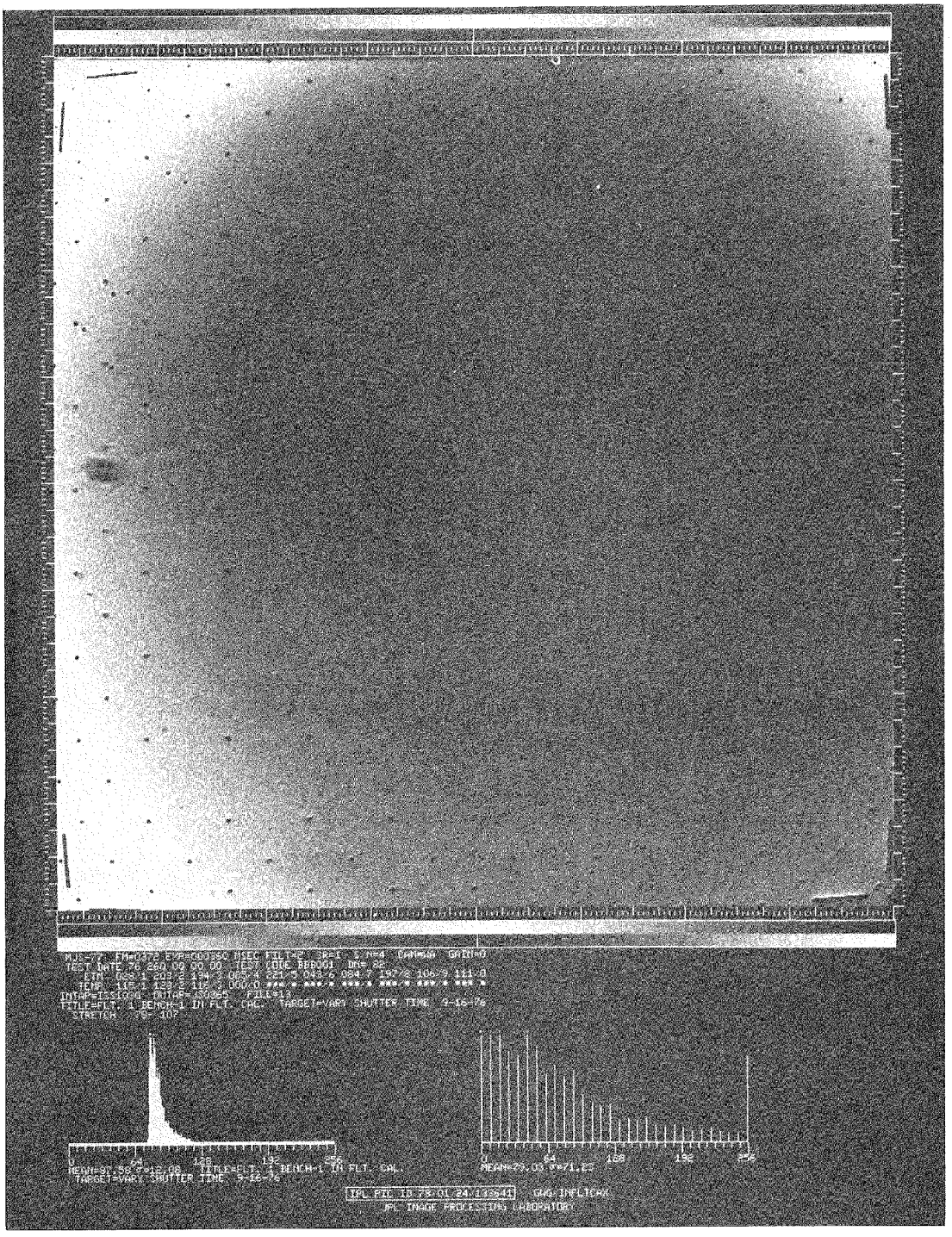

(b) ISS S/N 04

Figure 4-39 (contd)

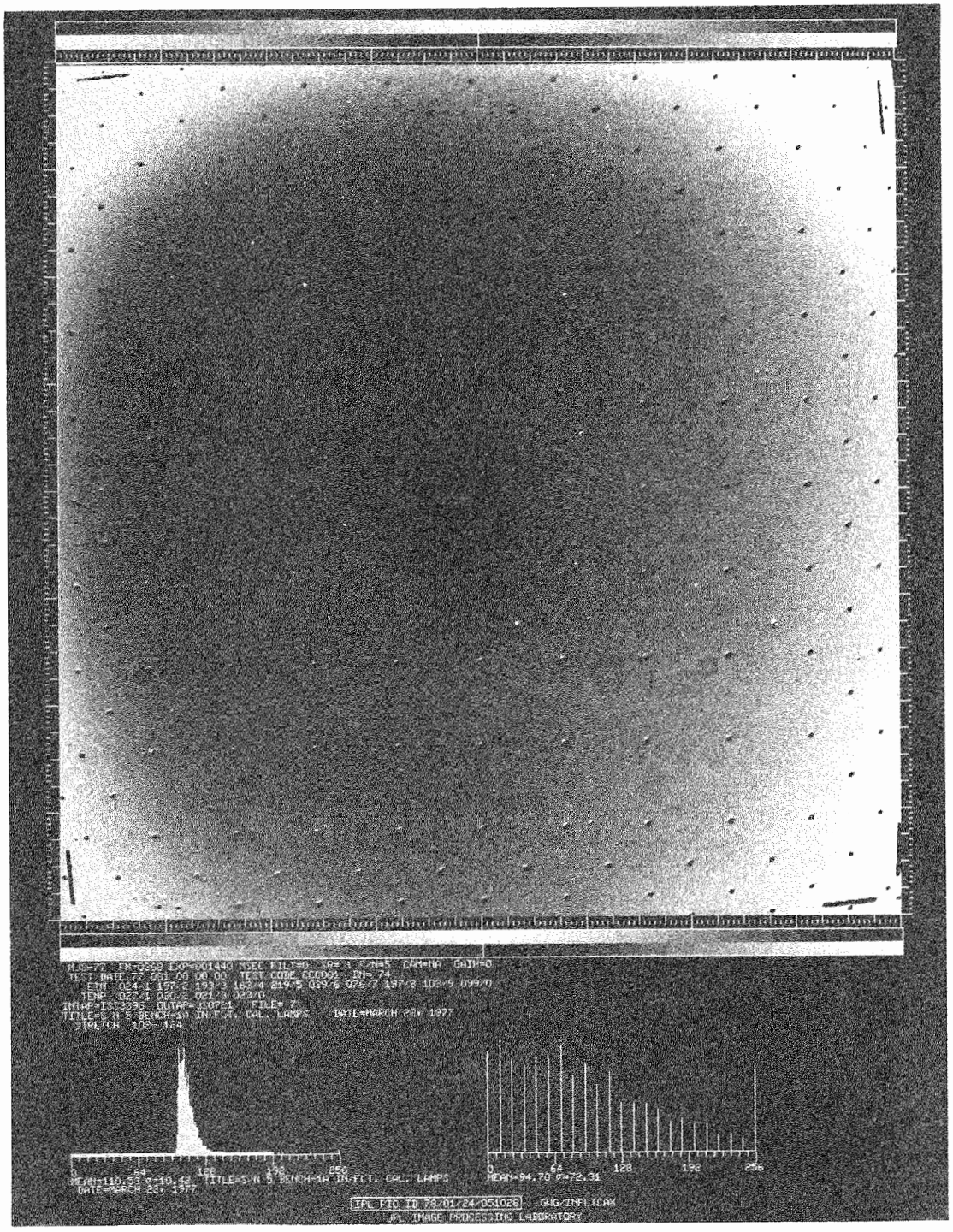

(c) ISS S/N 05

Figure 4-39 (contd)

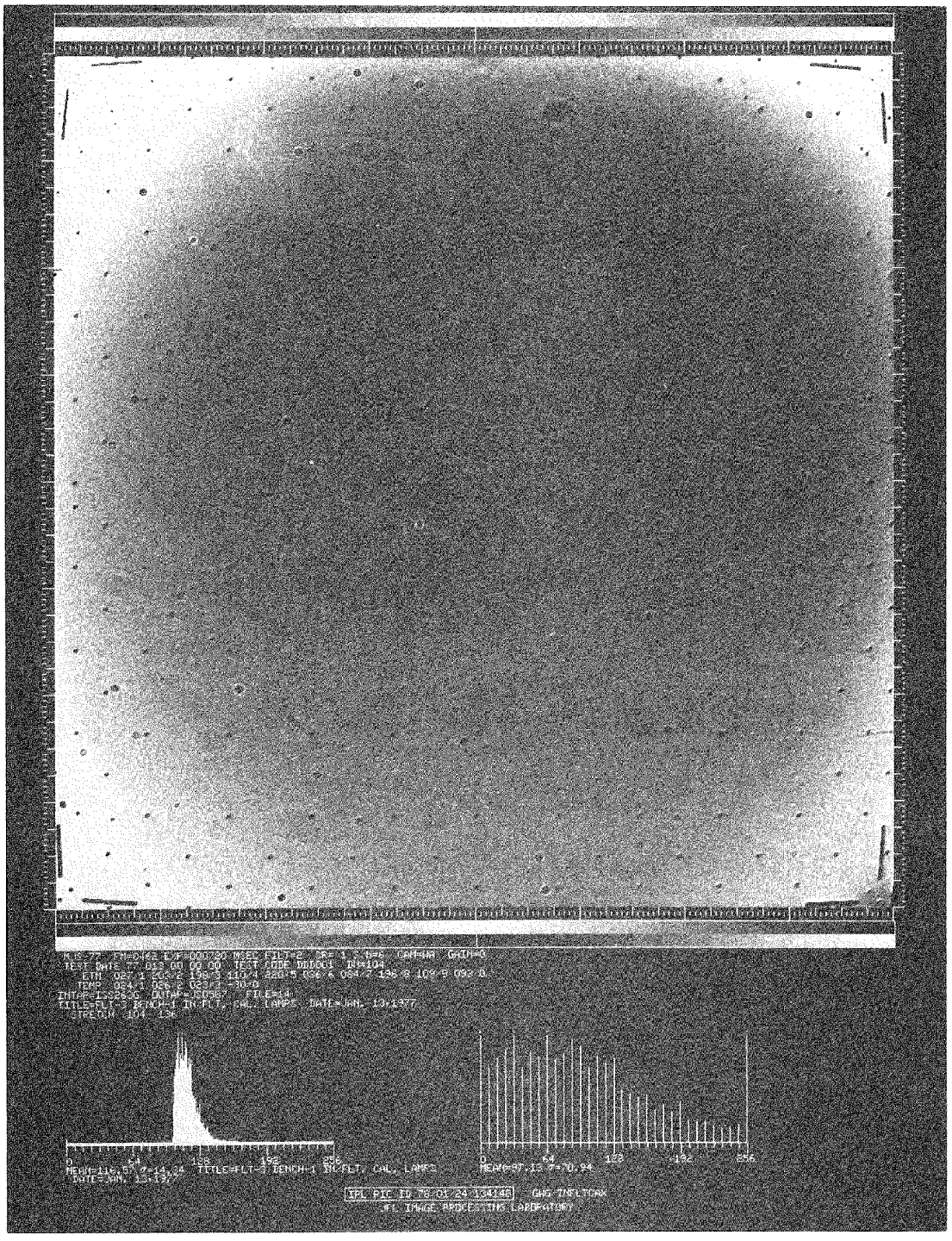

(d) ISS S/N 06

Figure 4-39 (contd)

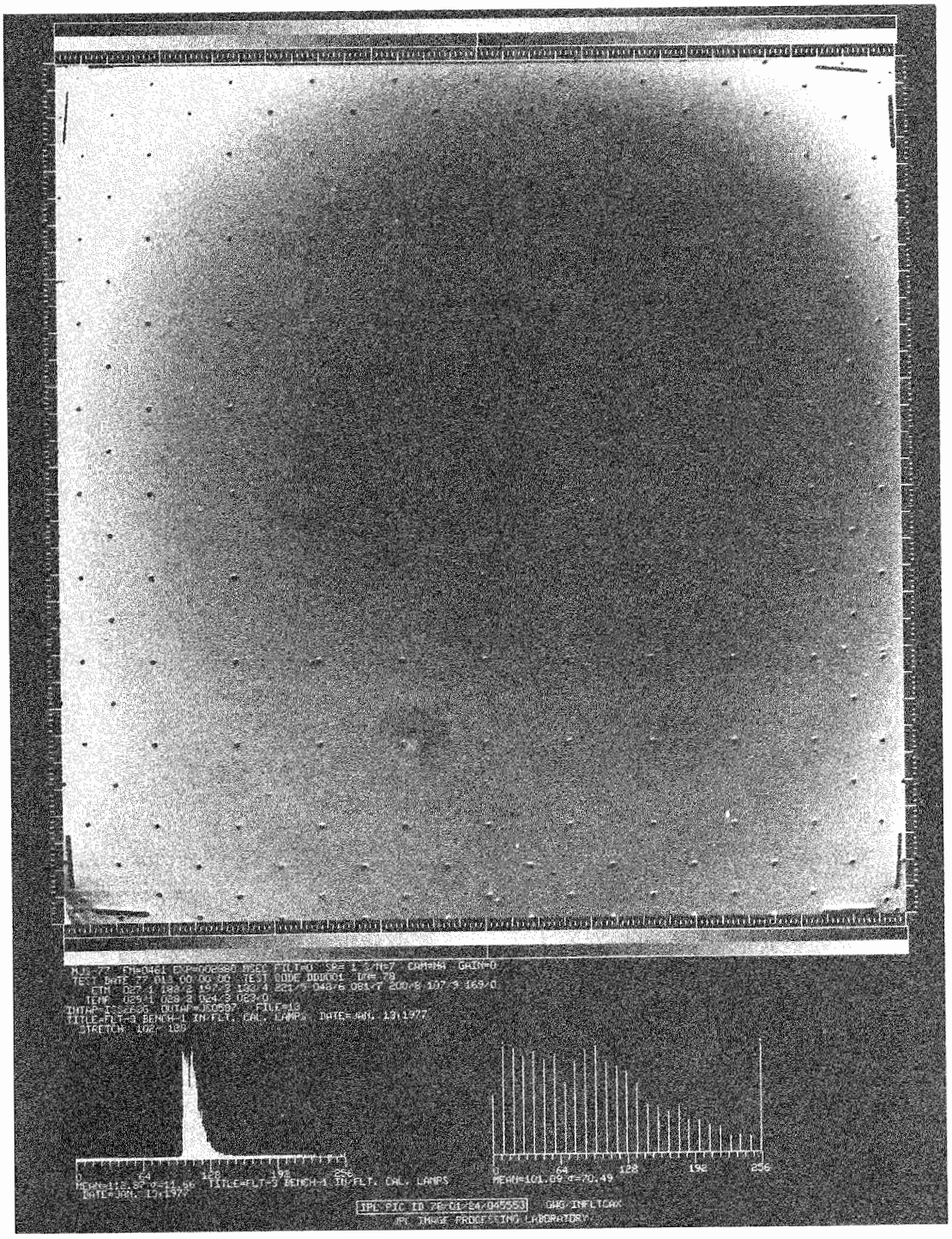

(e) ISS S/N 07

Figure 4-39 (contd)

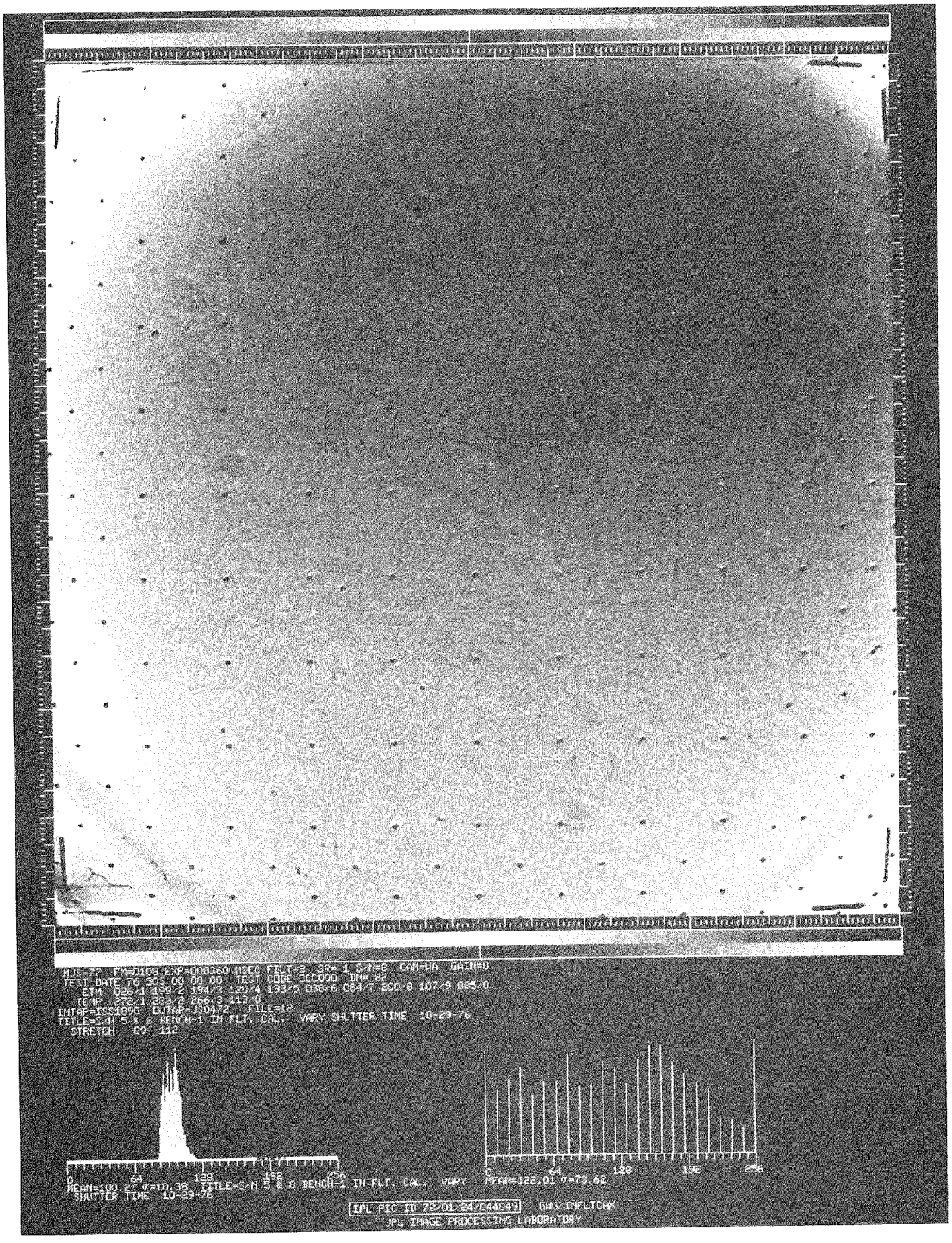

(f) ISS S/N 08

Figure 4-39 (contd)

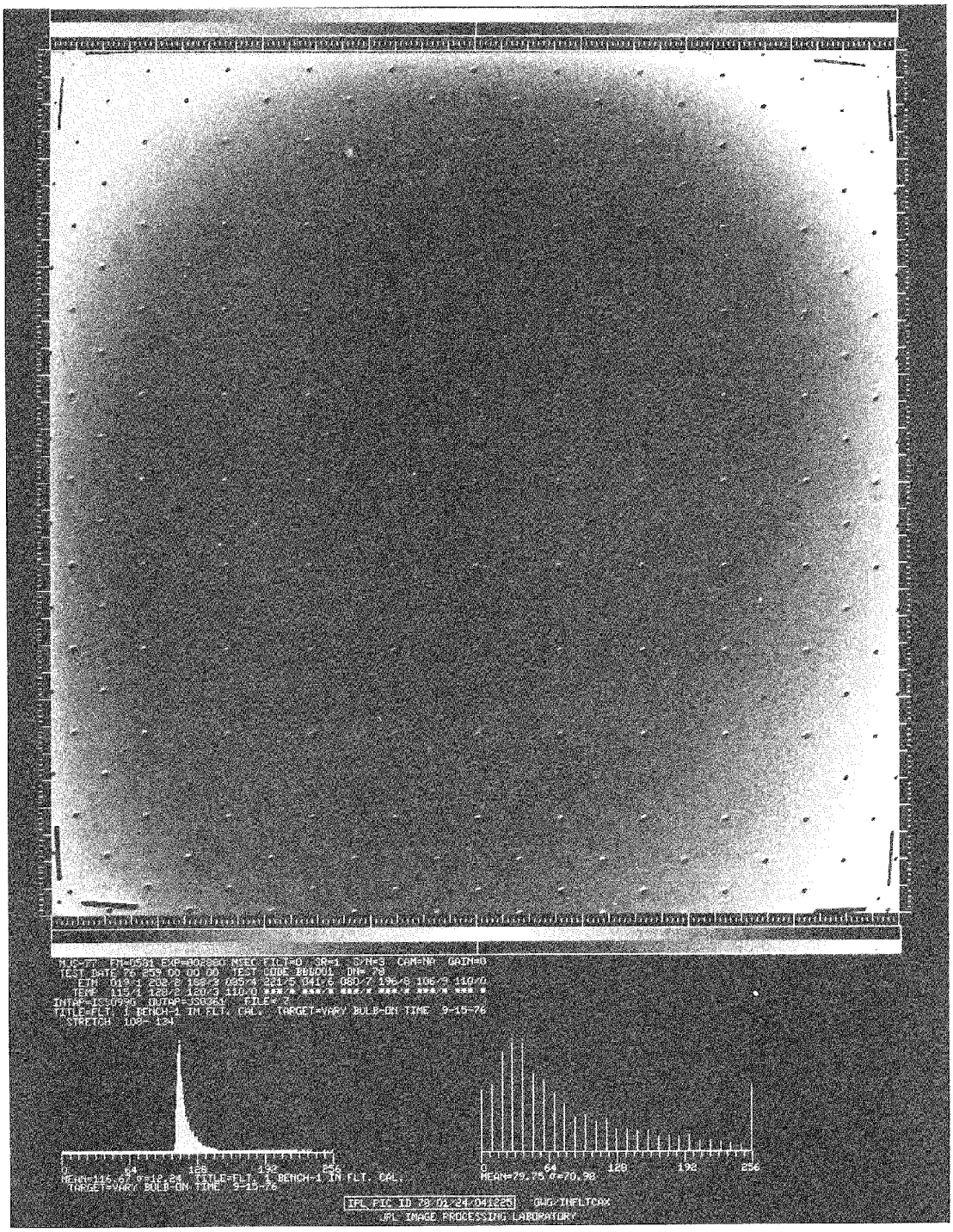

(a) ISS S/N 03

Figure 4-40. Clear filter images using in-flight calibration lamps in mode 2 (vary bulbs), ISS S/N 03 to 08

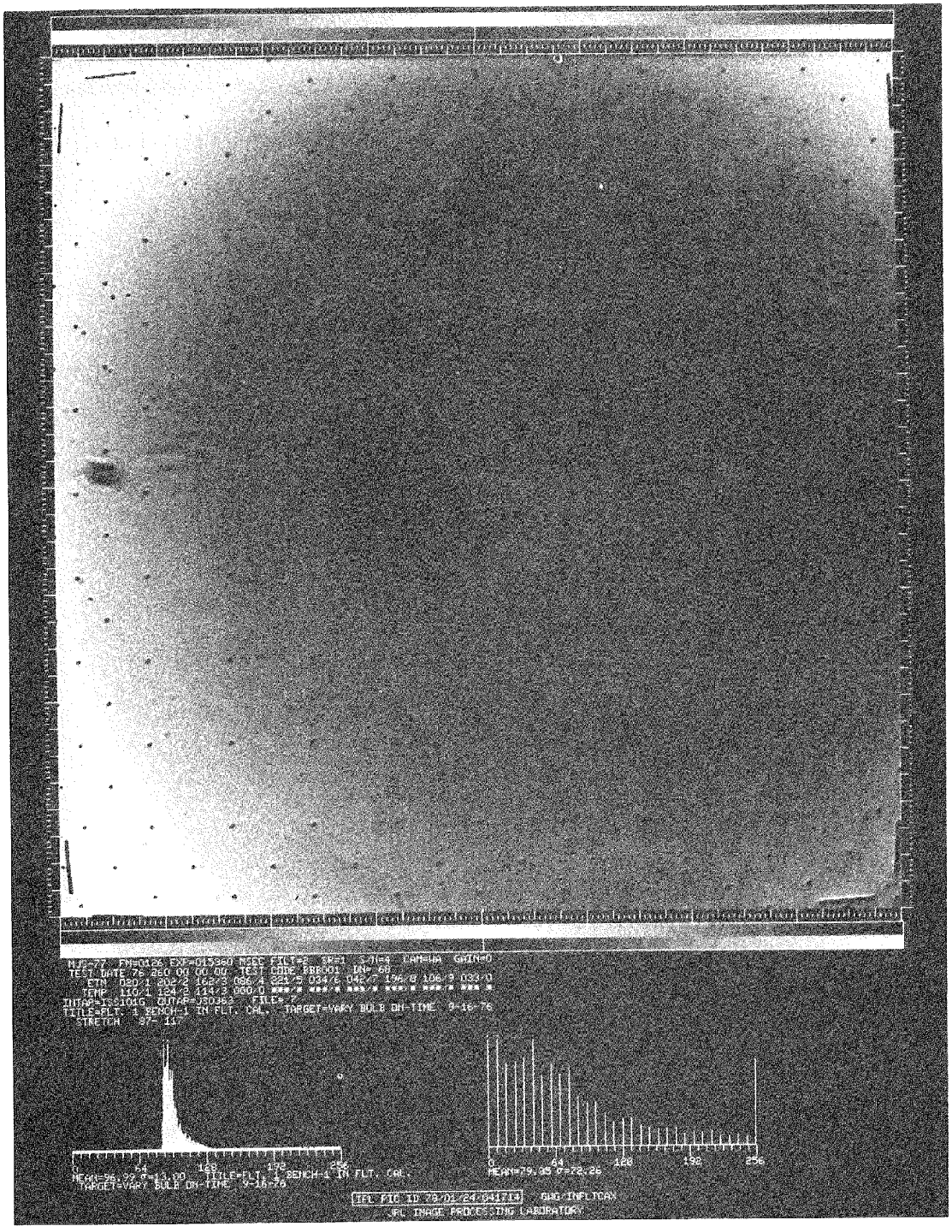

(b) ISS S/N 04

Figure 4-40 (contd)

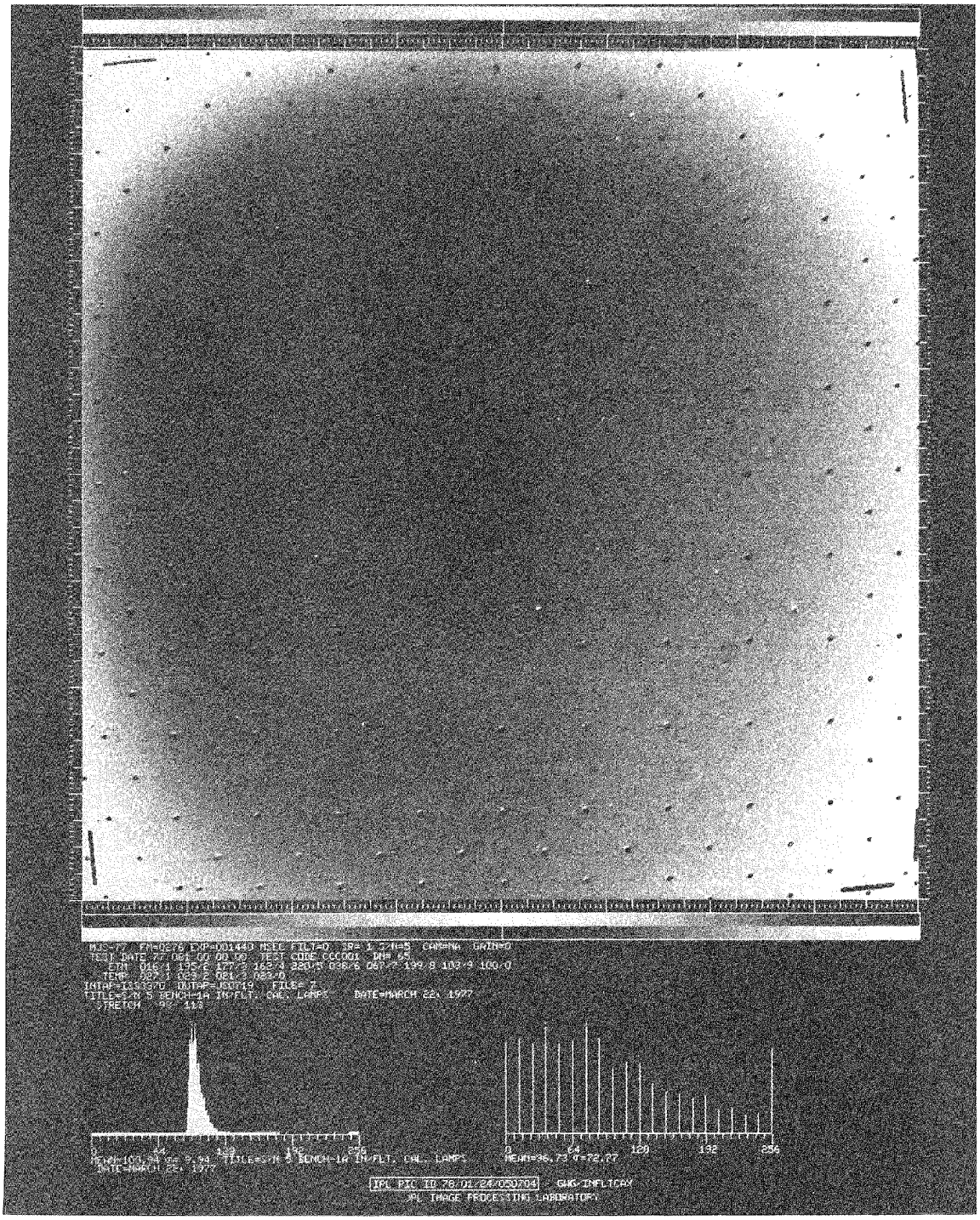

(c) ISS S/N 05

Figure 4-40 (contd)

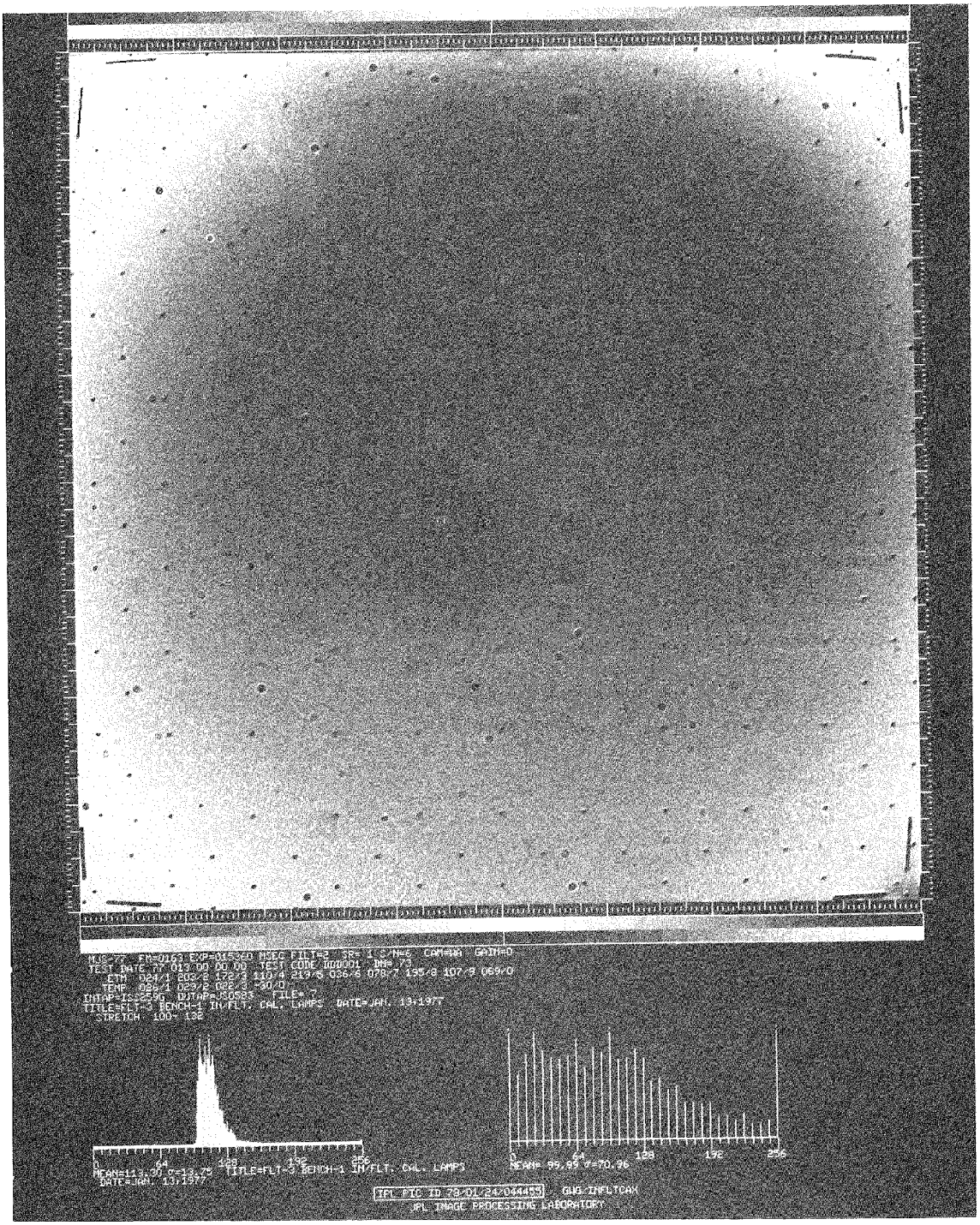

(d) ISS S/N 06

Figure 4-40 (contd)

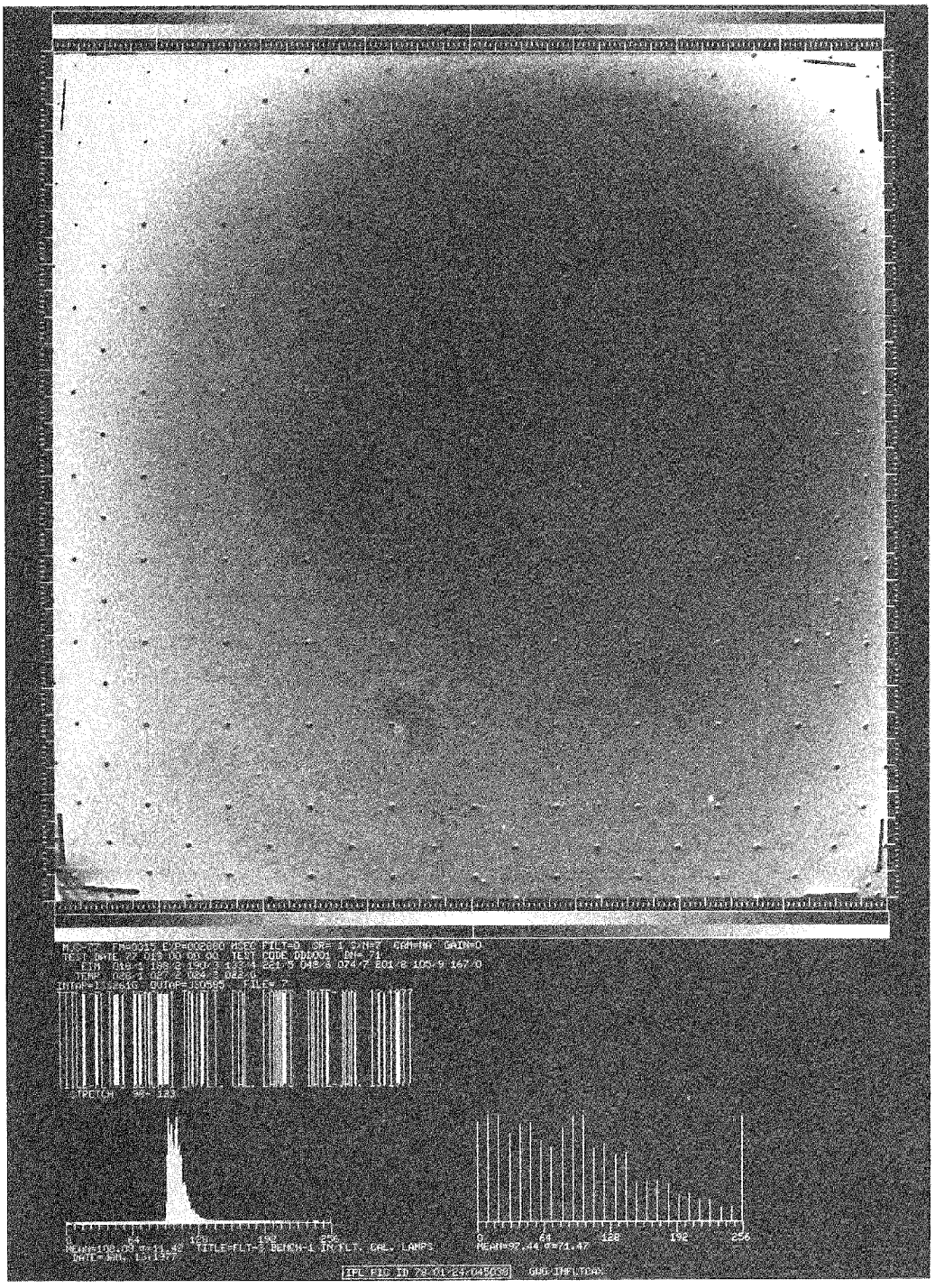

(e) ISS S/N 07

Figure 4-40 (contd)

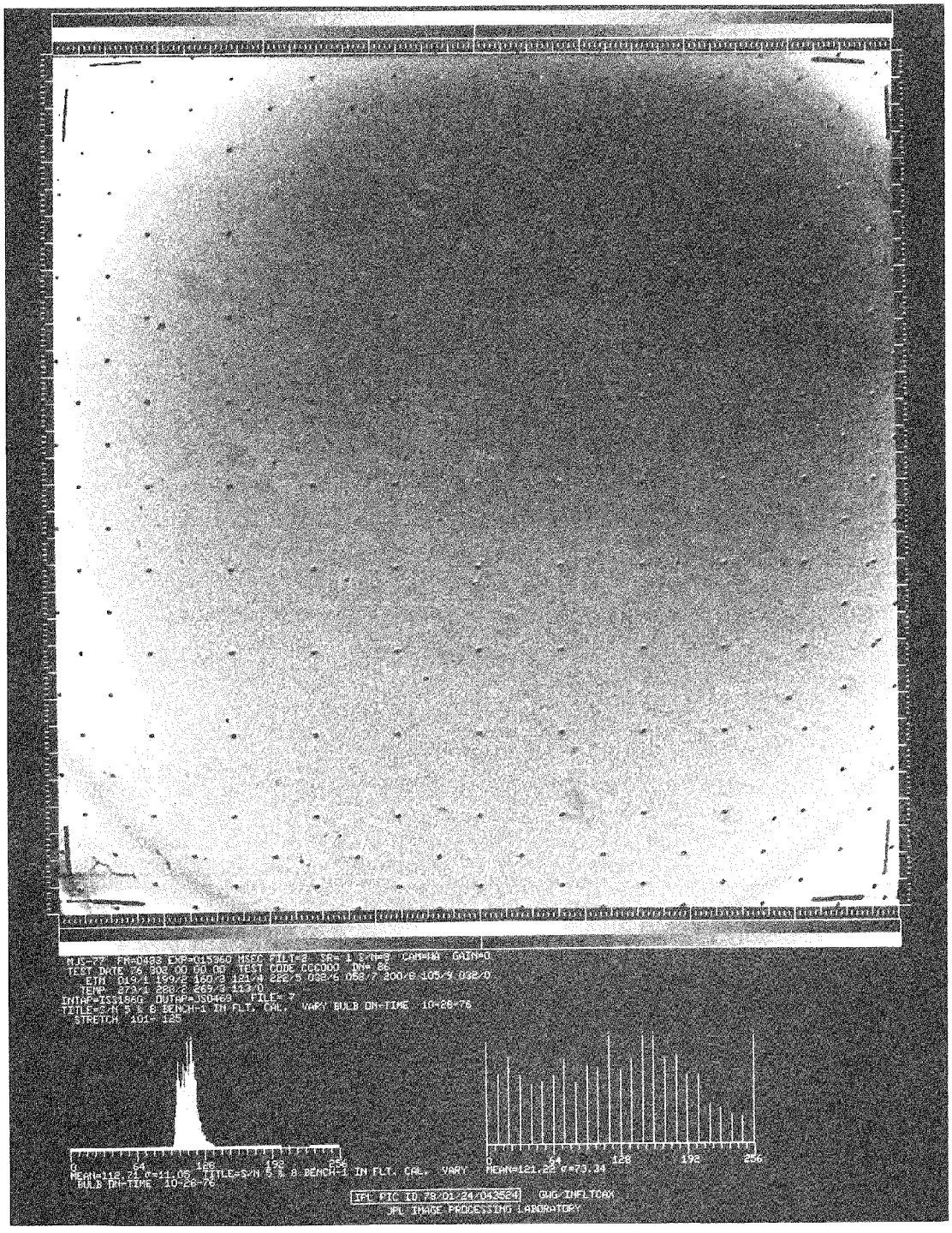

(f) ISS S/N 08

Figure 4-40 (contd)

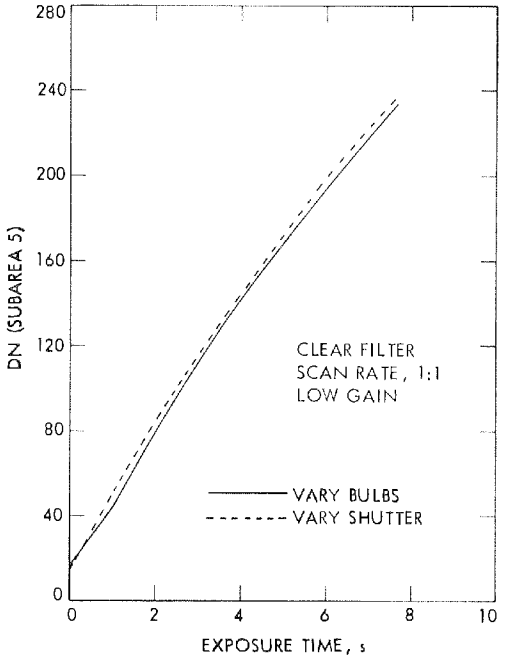

(a) ISS S/N 03

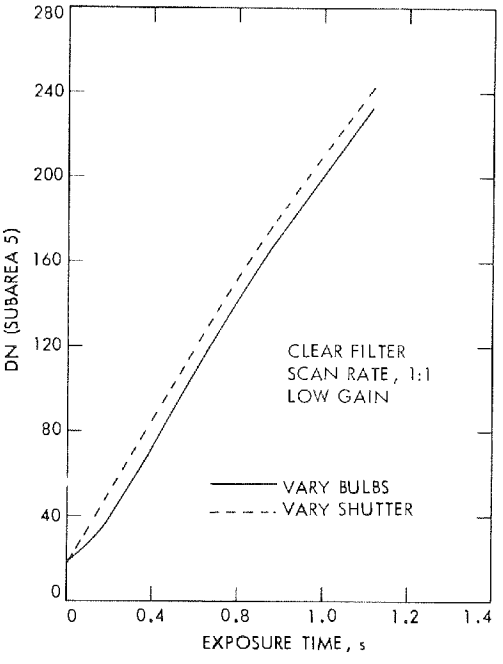

(b) ISS S/N 04

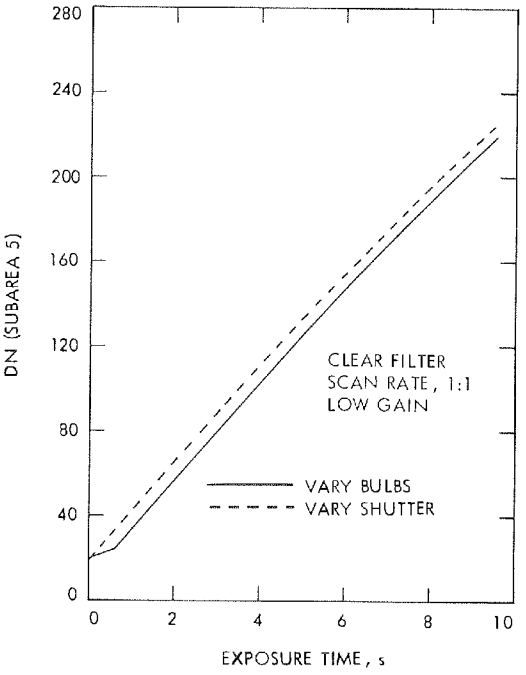

(c) ISS S/N 05

Figure 4-41. Light-transfer curves, in-flight calibration lamps, ISS S/N 03 to 08

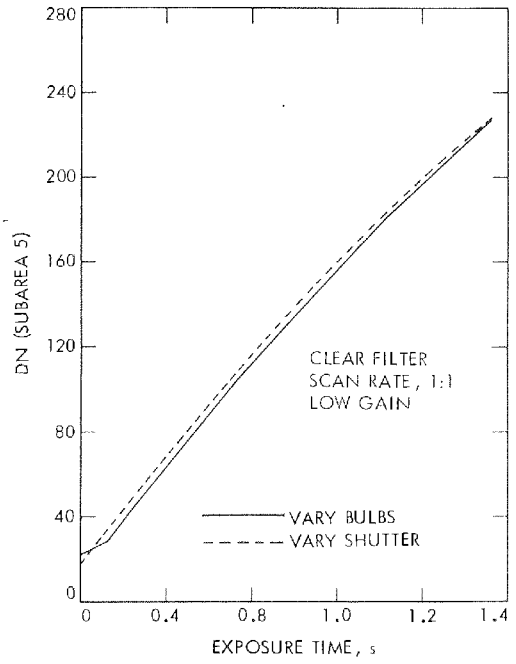

(d) ISS S/N 06

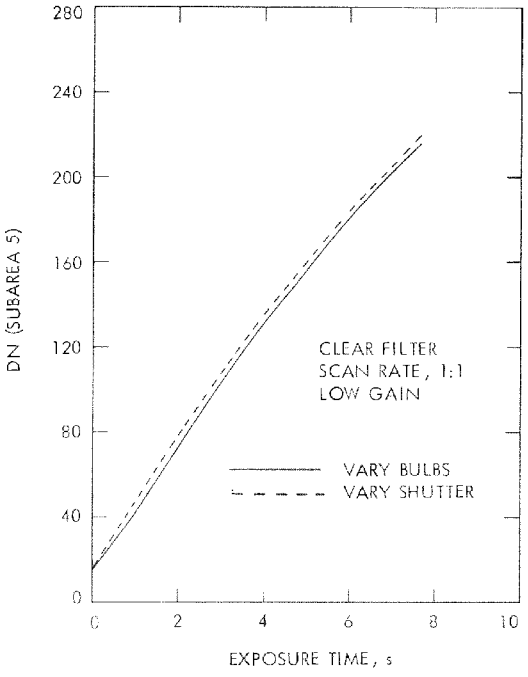

(e) ISS S/N 07

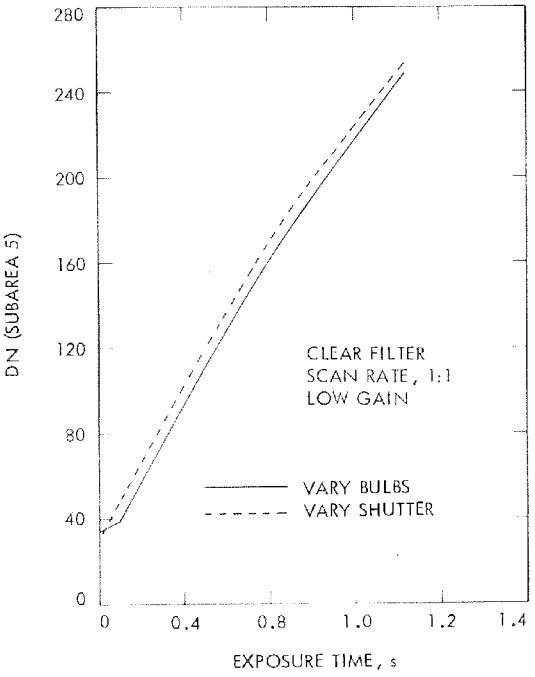

(f) ISS S/N 08

Figure 4-41 (contd)

Comparison of the two modes of operation of the in-flight calibration lamps makes it possible to check for shutter or vidicon malfunctions. The lamps, in fact, were used to pinpoint the failure of ISS S/N 08 vidicon during ETR calibrations at Cape Canaveral, Florida. As a result of this failure, the camera was replaced by ISS S/N 04 shortly before the launch (see Section V-A).

In summary, the calibration activities indicate that the in-flight calibration lamps can not be used directly to determine light-transfer curves for decalibrations. However, they will be used to monitor the relative response of the vidicon and to check for hardware malfunctions. In any case, they are the only source common to both the pre-launch and post-launch imaging, thus providing a direct means of before- and after-launch performance comparison. The calibration plaque, described in Section IV-A-8, does not fully qualify in this respect because not all flight cameras were calibrated during bench calibrations. Further, the plaque was illuminated with a light cannon, whereas, in flight, the Sun will be the light source.

6. Color Reconstruction

This section[1] contains a brief review of the concepts of tristimulus values and chromaticity coordinates, which are used extensively in colorimetry and which characterize the color properties of the Voyager ISS cameras. For a more complete discussion of colorimetry, see Reference 4-2.

Because color reconstruction of Voyager images is a complex problem, it is beyond the scope of this document to explore it in depth. However, it is worthwhile to review the elements which influence and limit the reconstruction.

The Voyager ISS cameras are not particularly sensitive in the red portion of the spectrum. In fact, they can not see colors redder than those normally considered by the human eye to be orange ($\sim$650 nm).

The spectral filters in the ISS, which are best suited for practical colorimetry, are broad band; this means that certain wavelengths, although detectable, can not be distinguished and must be approximated as the dominant wavelength of a given spectral filter.

[1] This section is based on a JPL data analysis. See information provided by J. Mosher in "Color Calibration for Voyager," JPL IOM 324-IPL/SIPG-77/208, 29 September 1977, and in "Revised Color Measurements for Voyager," JPL IOM 324-IPL/SIPG-77/249, 2 December 1977.

There is also a need to be concerned about the color film recorder itself. The recorder also will have problems similar to those discussed above, and it is quite possible that it may be less well calibrated. Possibly the most important problem is the implicit assumption that the radiometric characteristics of the ISS cameras are known, and, although the cameras are calibrated carefully, the inevitable error sources are sufficient to cause concern.

Color can be quantified in two closely related ways. The first way is by specifying the tristimulus values X, Y, and Z. Roughly speaking, the X tristimulus value is related to the amount of red light in a color; Y is the photopic curve and is related to the amount of green light; and Z is the amount of blue light. The X, Y, and Z values are found by numerically summing at 10-nm intervals the product of the illuminating light, the spectral reflectance or transmittance of the sample under study, and each of the three special color matching functions used in colorimetry. For the Voyager cameras, the spectral transmittance of the sample was assumed to be the product of the spectral transmittance of the filter, F_λ, the spectral transmittance of the optics, T_λ, and the spectral response of the vidicon, S_λ. Thus,

$$X = k \sum_\lambda \bar{x} N_\lambda T_\lambda S_\lambda F_\lambda$$

$$Y = k \sum_\lambda \bar{y} N_\lambda T_\lambda S_\lambda F_\lambda$$

$$Z = k \sum_\lambda \bar{z} N_\lambda T_\lambda S_\lambda F_\lambda$$

where

$\bar{x}$, $\bar{y}$, $\bar{z}$ are the color matching functions

N_λ is the illuminating source

k is a normalizing factor defined as $k = 100/\Sigma_\lambda N_\lambda \bar{y}_\lambda$

The summations were done at 10-nm intervals from 380 nm, where the color matching functions begin to be nonzero, to 650 nm, where the vidicon response goes to zero.

The second way color can be quantified is by calculating chromaticity coordinates x, y, and z. These are related to the tristimulus values by

$$x = \frac{X}{X + Y + Z}$$

$$y = \frac{Y}{X + Y + Z}$$

$$z = \frac{Z}{X + Y + Z}$$

Chromaticity coordinates are the quantities plotted for each camera in Figures 4-42 and 4-43. These plots are called the CIE 1931 (x, y)-chromaticity diagrams. Table 4-7 gives the tristimulus value and chromaticity coordinates for ISS S/N 03 to 08 using the xenon illuminant. Data for the wide-angle camera filter positions 0, 4, 6 are limited because detailed and highly accurate spectral transmittance curves are not available for these filters (see Section III-B). Information on narrow-angle camera filter position 7 has been omitted because tristimulus values in the ultraviolet are not defined.

Table 4-8 gives the tristimulus value and chromaticity coordinates for ISS S/N 03 to 08 using the D_{55} illuminant, a light source similar to the Sun.

Use of this information is difficult and complex for reasons mentioned above. However, it is possible to make some general statements about the colors that may be reconstructible.

If a triangle is constructed between the red, green, and blue spectral filters for, say, ISS S/N 07 (see Figure 4-43), the color space within this triangle represents those colors which colorimetry predicts can be reconstructed. The average color of most objects of interest to Voyager lies within this triangle, although, of course, there are also extremes that lie outside.

Colors which lie outside this triangle may or may not be detectable. For example, colors around 700 nm will not be detectable and hence are treated as having zero intensity. However, some other wavelengths may still be detected and approximately reconstructed. The quality of the approximation will depend upon how close and where the chromaticity coordinate to be reconstructed is in relation to the color triangle.

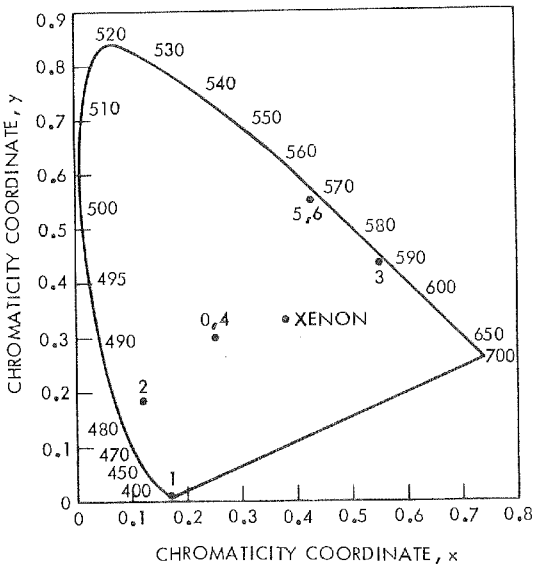

(a) ISS S/N 03

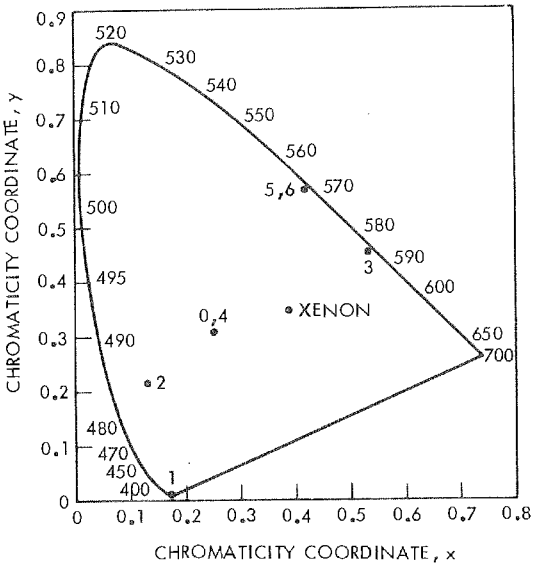

(c) ISS S/N 05

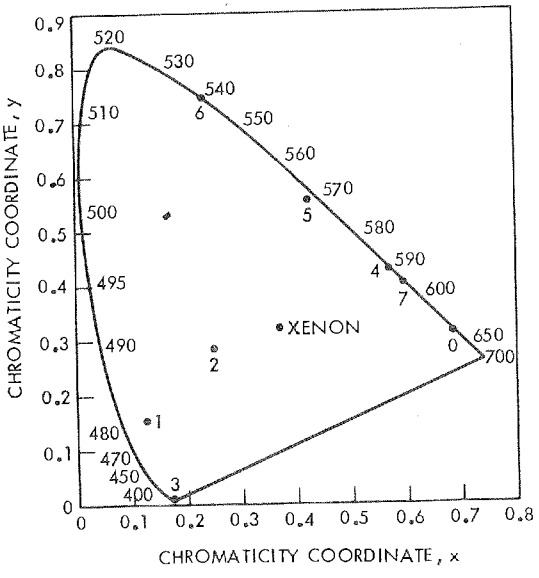

(b) ISS S/N 04

Figure 4-42. Chromaticity diagram (Xenon illuminant), ISS S/N 03 to 08

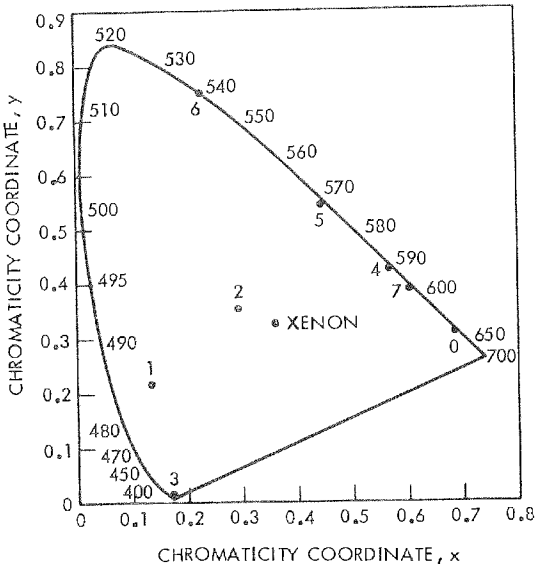

(d) ISS S/N 06

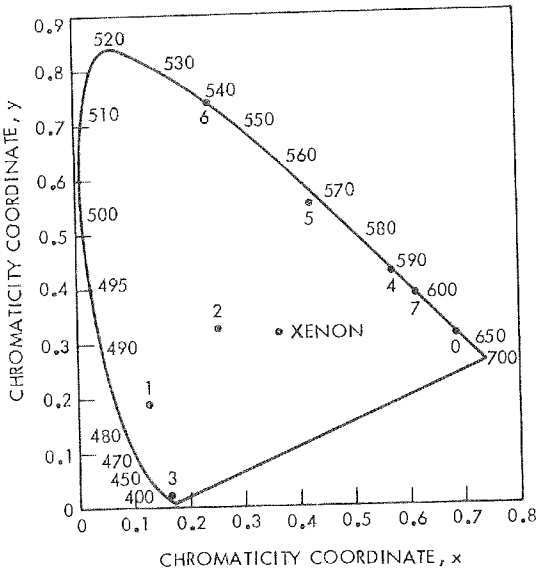

(f) ISS S/N 08

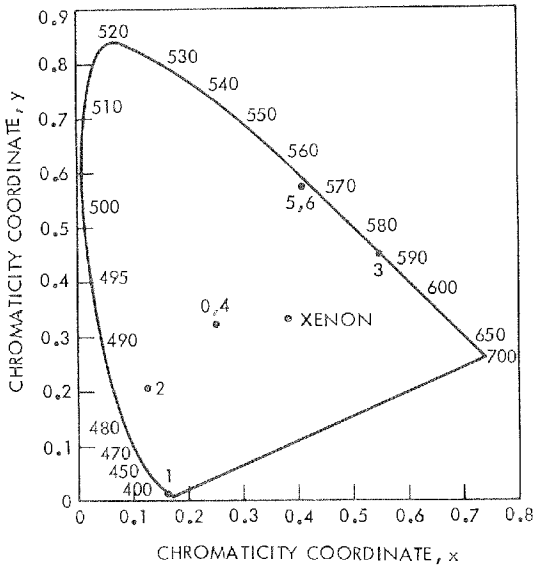

(e) ISS S/N 07

Figure 4-42 (contd)

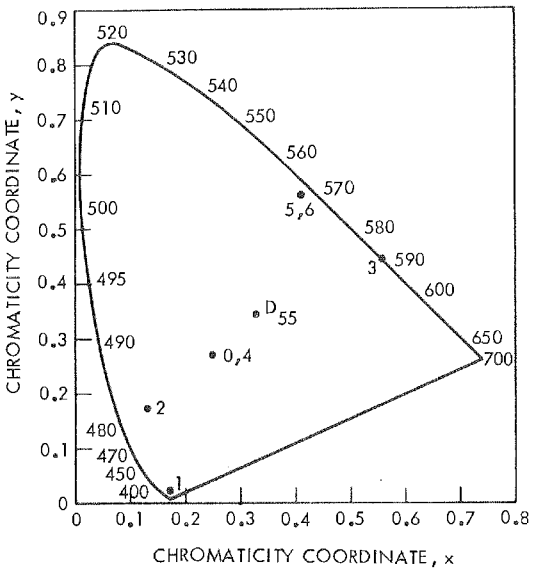

(a) ISS S/N 03

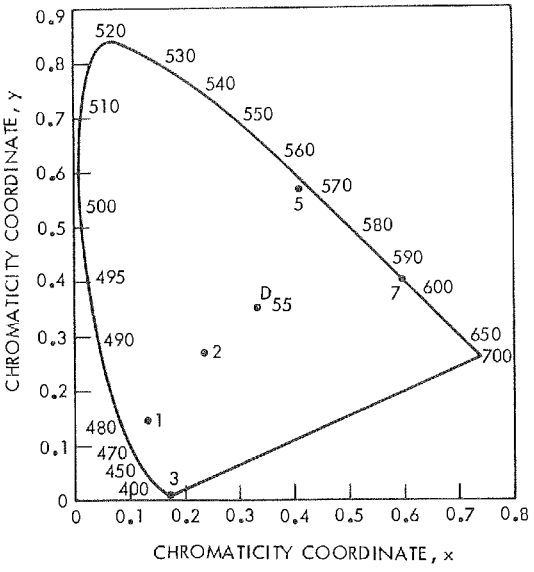

(c) ISS S/N 05

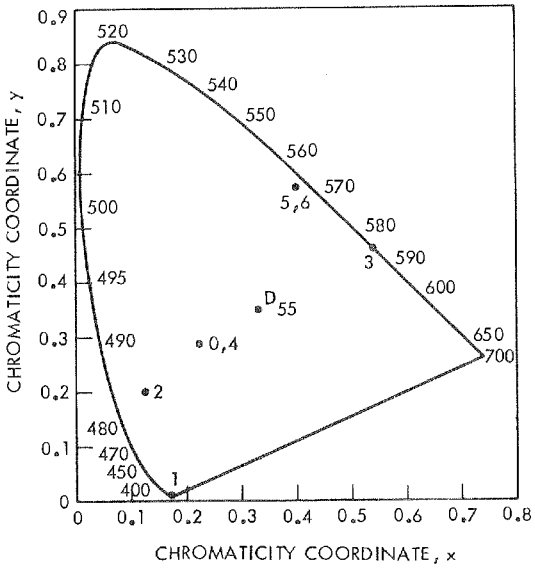

(b) ISS S/N 04

Figure 4-43. Chromaticity diagram (D_{55} illuminant), ISS S/N 03 to 08

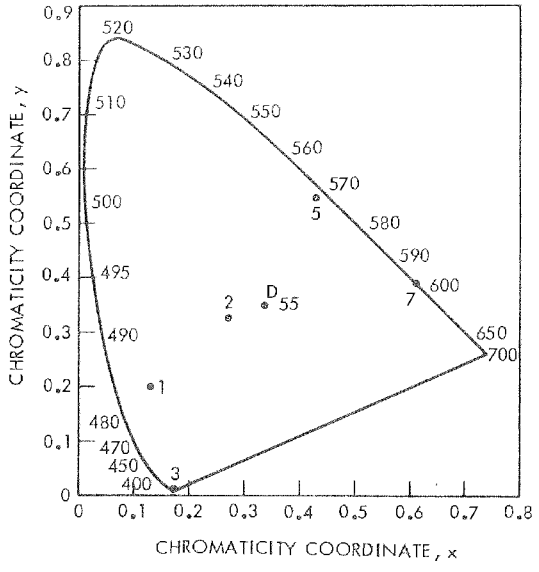

(d) ISS S/N 06

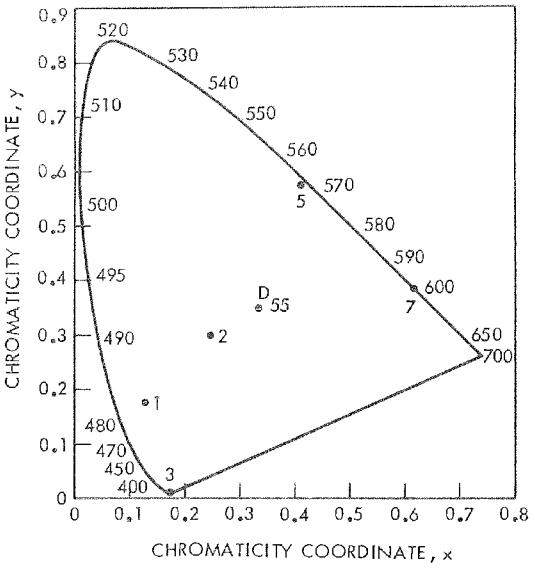

(f) ISS S/N 08

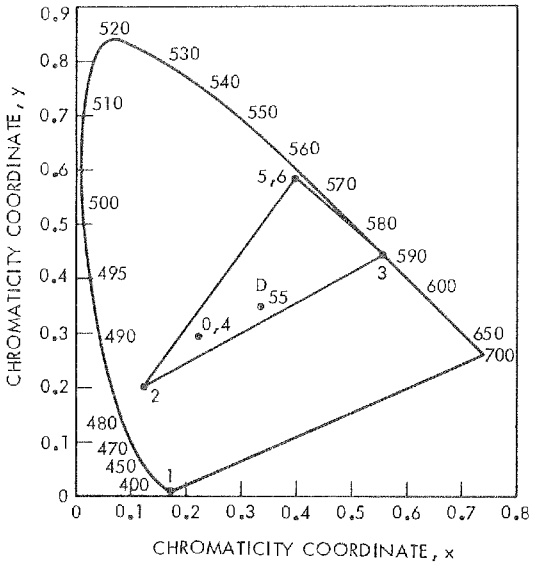

(e) ISS S/N 07

Figure 4-43 (contd)

Table 4-7. Tristimulus values and chromaticity coordinates (Xenon illuminant), ISS S/N 03 to 08

S/N	FP	X	Y	Z	x	y	z
03	0	15.255	17.796	26.146	0.25770	0.30062	0.44167
	1	1.5118	0.10795	7.5983	0.16400	0.01171	0.82428
	2	3.7759	5.2770	19.738	0.13114	0.18328	0.68556
	3	6.8313	5.5029	0.012206	0.55330	0.44571	0.00098862
	4	15.255	17.796	26.146	0.25770	0.30062	0.44167
	5	10.251	13.261	0.27711	0.43091	0.55744	0.011648
	6	10.153	13.043	0.26799	0.43269	0.55588	0.011421
	7			Not available			
04	0		Not available		0.6892	0.3106	0.0002
	1	5.9731	7.2363	31.601	0.13329	0.16148	0.70521
	2	20.887	24.391	38.441	0.24949	0.29134	0.45916
	3	2.6348	0.20501	13.344	0.16280	0.012667	0.82453
	4		Not available		0.5691	0.4302	0.0007
	5	13.354	17.719	0.35650	0.42489	0.56376	0.011342
	6		Not available		0.2368	0.7483	0.0149
	7	5.0991	3.4342	0.0053763	0.59717	0.40219	0.00062963
05	0	18.225	23.376	32.499	0.24594	0.31547	0.43858
	1	1.7160	0.11145	8.5745	0.16497	0.010714	0.82431
	2	4.5603	7.5996	23.756	0.12697	0.21159	0.66143
	3	8.0832	6.8694	0.018435	0.53992	0.45884	0.0012314
	4	18.225	23.376	32.499	0.24594	0.31547	0.43858
	5	12.089	16.343	0.32342	0.42041	0.56834	0.011246
	6	12.089	16.343	0.32342	0.42041	0.56834	0.011246
	7			Not available			
06	0		Not available		0.6892	0.3106	0.0002
	1	7.5507	11.995	36.484	0.13476	0.21408	0.65115
	2	36.532	43.829	43.994	0.29377	0.35245	0.35377
	3	3.0437	0.24791	15.468	0.16224	0.013215	0.82454
	4		Not available		0.5691	0.4302	0.0007
	5	27.430	33.928	0.53995	0.44290	0.54836	0.0087269
	6		Not available		0.2368	0.7483	0.0149
	7	11.370	7.2635	0.010104	0.60987	0.38958	0.00054195

Table 4-7 (contd)

S/N	FP	X	Y	Z	x	y	z
07	0	18.386	23.508	31.551	0.25034	0.32007	0.42959
	1	1.8203	0.12645	9.1316	0.16431	0.011414	0.82427
	2	4.4738	7.4172	23.375	0.12685	0.21032	0.66282
	3	7.8786	6.4007	0.015934	0.55113	0.44775	0.0011146
	4	18.386	23.508	31.551	0.25034	0.32007	0.42959
	5	12.477	17.520	0.43778	0.40995	0.57566	0.014383
	6	12.450	17.204	0.36581	0.41473	0.57308	0.012185
	7			Not available			
08	0		Not available		0.6892	0.3106	0.0002
	1	6.6584	9.8551	34.950	0.12938	0.19149	0.67912
	2	24.437	33.820	42.080	0.26551	0.32727	0.40721
	3	3.1483	0.28491	16.118	0.16102	0.014572	0.82440
	4		Not available		0.5691	0.4302	0.0007
	5	19.287	25.806	0.62653	0.42186	0.56444	0.013703
	6		Not available		0.2368	0.7483	0.0149
	7	6.5312	4.0948	0.0056029	0.61432	0.38515	0.000527

Table 4-8. Tristimulus values and chromaticity coordinates (D_{55} illuminant), ISS S/N 03 to 08

S/N	FP	X	Y	Z	x	y	z
03	0	15.78	18.23	31.89	0.239	0.277	0.484
	1	1.97	0.13	9.91	0.164	0.012	0.824
	2	4.54	5.87	23.85	0.132	0.171	0.696
	3	6.26	5.11	0.01	0.550	0.449	0.001
	4	15.78	18.23	31.89	0.239	0.277	0.484
	5	9.73	13.19	0.30	0.419	0.568	0.013
	6	9.63	12.96	0.29	0.421	0.566	0.013
	7			Not available			
04	0		Not available		0.689	0.311	0.000
	1	6.94	7.68	35.98	0.137	0.152	0.711
	2	21.74	25.04	46.73	0.233	0.268	0.500
	3	3.43	0.26	17.38	0.163	0.012	0.825
	4		Not available		0.569	0.430	0.001
	5	12.71	17.67	0.39	0.413	0.574	0.013
	6		Not available		0.237	0.748	0.015
	7	4.63	3.14	0.005	0.595	0.404	0.001
05	0	18.96	24.17	39.55	0.229	0.292	0.478
	1	2.24	0.14	11.21	0.165	0.011	0.824
	2	5.43	8.45	28.50	0.128	0.199	0.672
	3	7.44	6.43	0.02	0.536	0.463	0.001
	4	18.96	24.17	39.55	0.229	0.292	0.478
	5	11.53	16.34	0.35	0.409	0.579	0.013
	6	11.53	16.34	0.35	0.409	0.579	0.013
	7			Not available			
06	0		Not available		0.689	0.311	0.000
	1	8.95	13.25	43.88	0.135	0.201	0.664
	2	36.71	44.50	53.35	0.273	0.331	0.396
	3	3.97	0.32	20.13	0.162	0.013	0.825
	4		Not available		0.569	0.430	0.001
	5	25.93	33.61	0.58	0.431	0.559	0.010
	6		Not available		0.237	0.748	0.015
	7	10.28	6.61	0.01	0.608	0.391	0.001

Table 4-8 (contd)

S/N	FP	X	Y	Z	x	y	z
07	0	19.05	24.28	38.33	0.233	0.297	0.469
	1	2.38	0.16	11.92	0.164	0.011	0.824
	2	5.32	8.24	28.00	0.128	0.198	0.674
	3	7.32	5.97	0.02	0.547	0.451	0.001
	4	19.05	24.28	38.33	0.233	0.297	0.469
	5	11.91	17.61	0.48	0.397	0.587	0.016
	6	11.89	17.25	0.40	0.402	0.584	0.014
	7			Not available			
08	0		Not available		0.689	0.311	0.000
	1	7.97	10.96	42.00	0.131	0.180	0.689
	2	28.06	34.66	50.97	0.247	0.305	0.448
	3	4.08	0.35	20.86	0.161	0.014	0.825
	4		Not available		0.569	0.430	0.001
	5	18.34	25.78	0.69	0.409	0.575	0.015
	6		Not available		0.237	0.748	0.015
	7	5.92	3.73	0.01	0.613	0.386	0.001

7. Noise Characteristics and Power Spectra

This section describes the noise characteristics of the Voyager Imaging Subsystem (ISS). The techniques used are based on Fourier analysis.[12] Although the two-dimensional Fourier transform is the primary tool, one-dimensional spectral plots are included to help in the data interpretation.

The procedures discussed below provide a RMS measure (without vidicon shading), of the total, random, and periodic noise signals. There are a number of possible error sources, and they are mentioned in the body of the discussion. However, these errors tend to increase the RMS noise measurements; therefore, the numbers provided may be assumed to be upper bounds.

The following 256 x 256 areas were selected for analysis:

(1) S/N 01 and 02, starting line 70, starting sample 70.

(2) S/N 03 to 08, starting line 125, starting sample 125.

After the reseaus are removed (Figure 4-44), an unshading filter is applied in the spatial domain (Figure 4-45). The RMS is computed in the appropriate area (see above) in the resultant image to provide a measure of the total noise signal.

The Fourier transform is then taken of this unshaded image according to the formula

$$G_{jk} = \frac{1}{256} \sum_{\ell=0}^{255} \sum_{s=0}^{255} dn_{\ell,s} \, e^{\frac{2\pi i}{256}(j\ell - ks)}$$

$$j,k = 0,\ldots,255$$

A background amplitude value (A) is computed from frequencies around the noise spike and each frequency in the noise spike is multiplicatively suppressed with the relation

$$F_{jk} = G_{jk} \cdot \left(\frac{A}{|G_{jk}|} \right)^2$$

[12] Fundamentals are described by J. Seidman in "MM '71 TVS Noise Analysis," JPL IOM 324-IPL/70-263, April 16, 1970 and in "MM '71 TVS Calibration - Noise Analysis," JPL IOM 324-IPL/70-508, September 3, 1970.

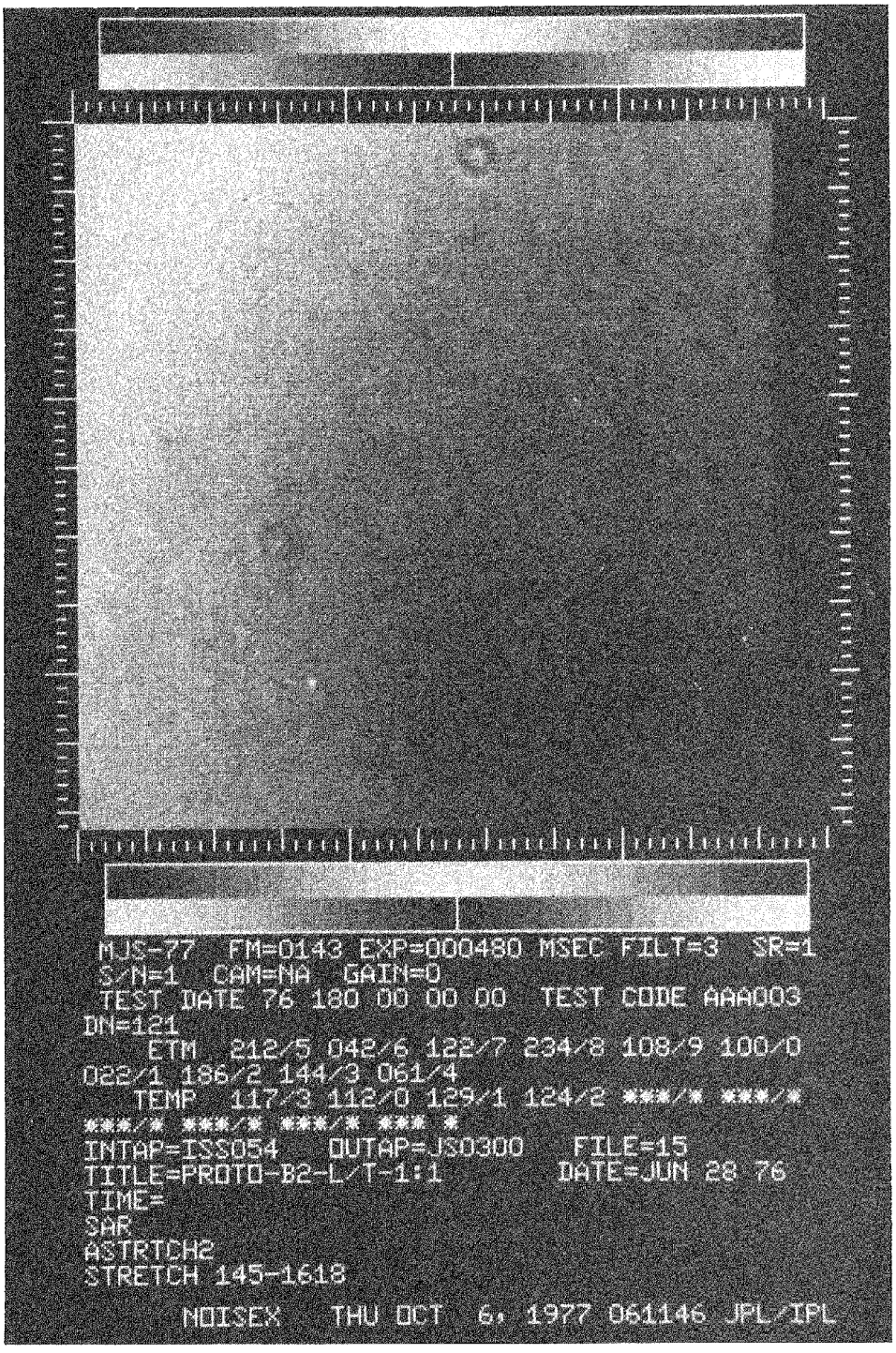

(a) ISS S/N 01

Figure 4-44. Image of flat field without reseaus, ISS S/N 01 to 08

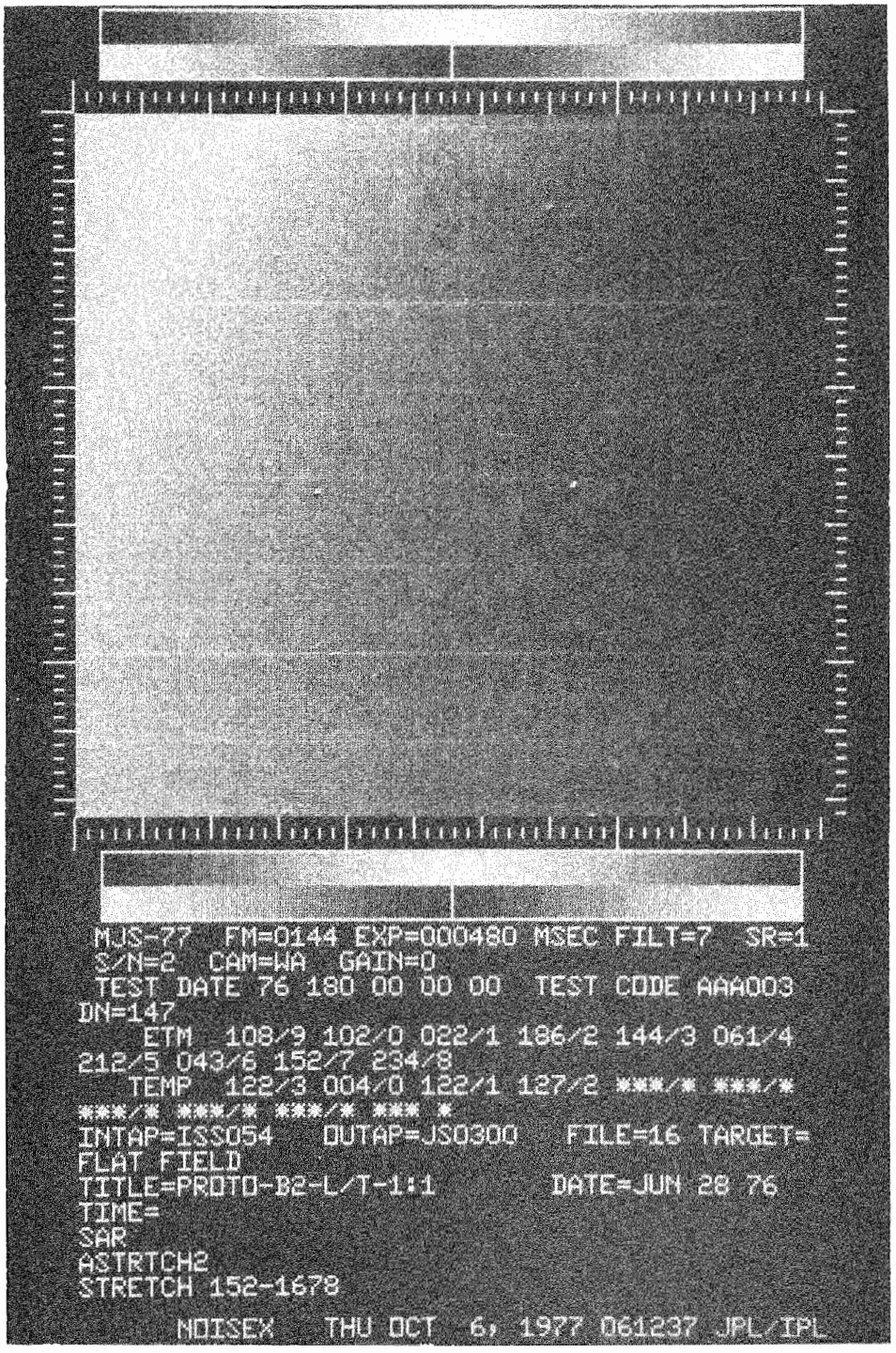

(b) ISS S/N 02

Figure 4-44 (contd)

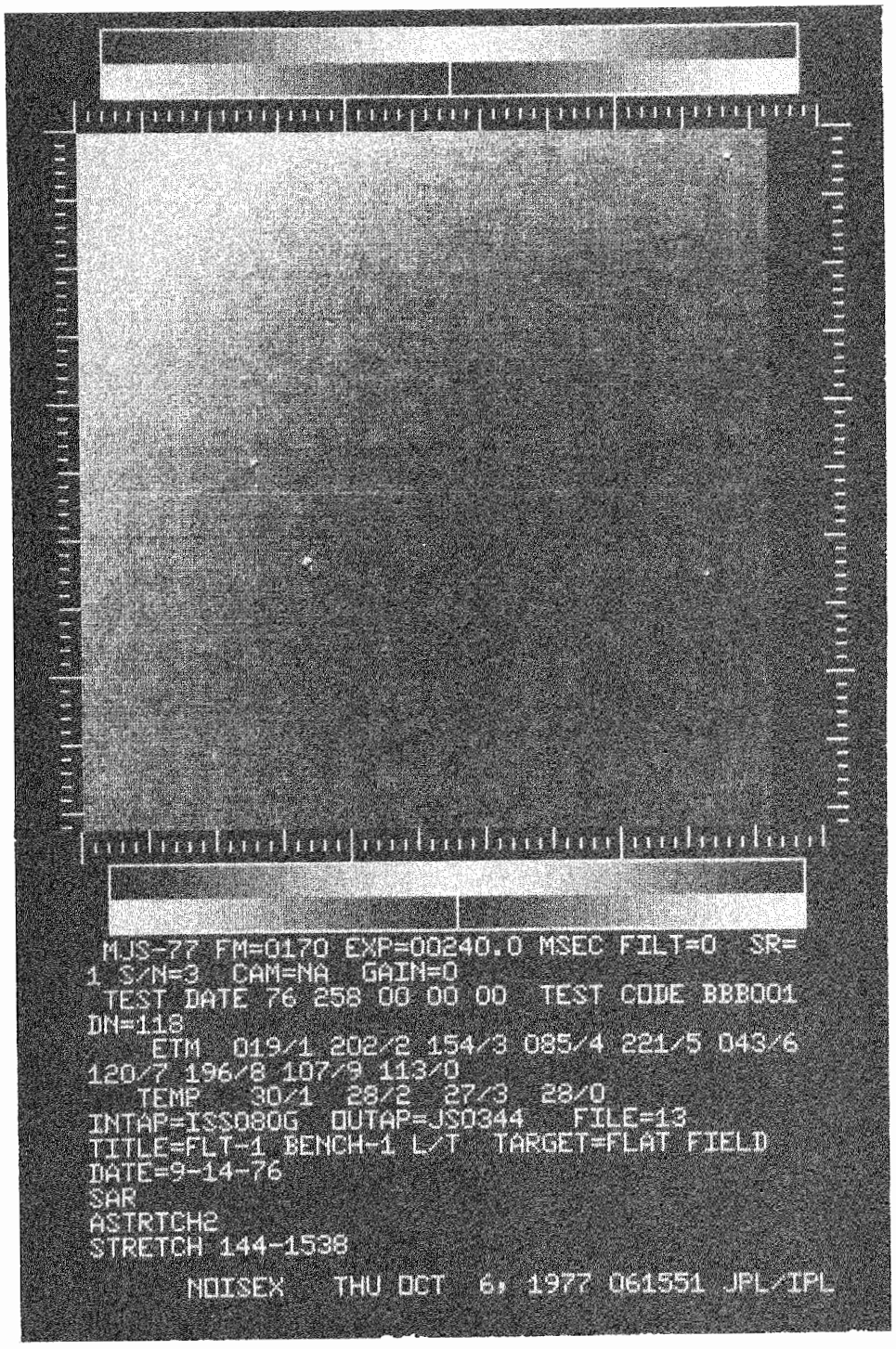

(c) ISS S/N 03

Figure 4-44 (contd)

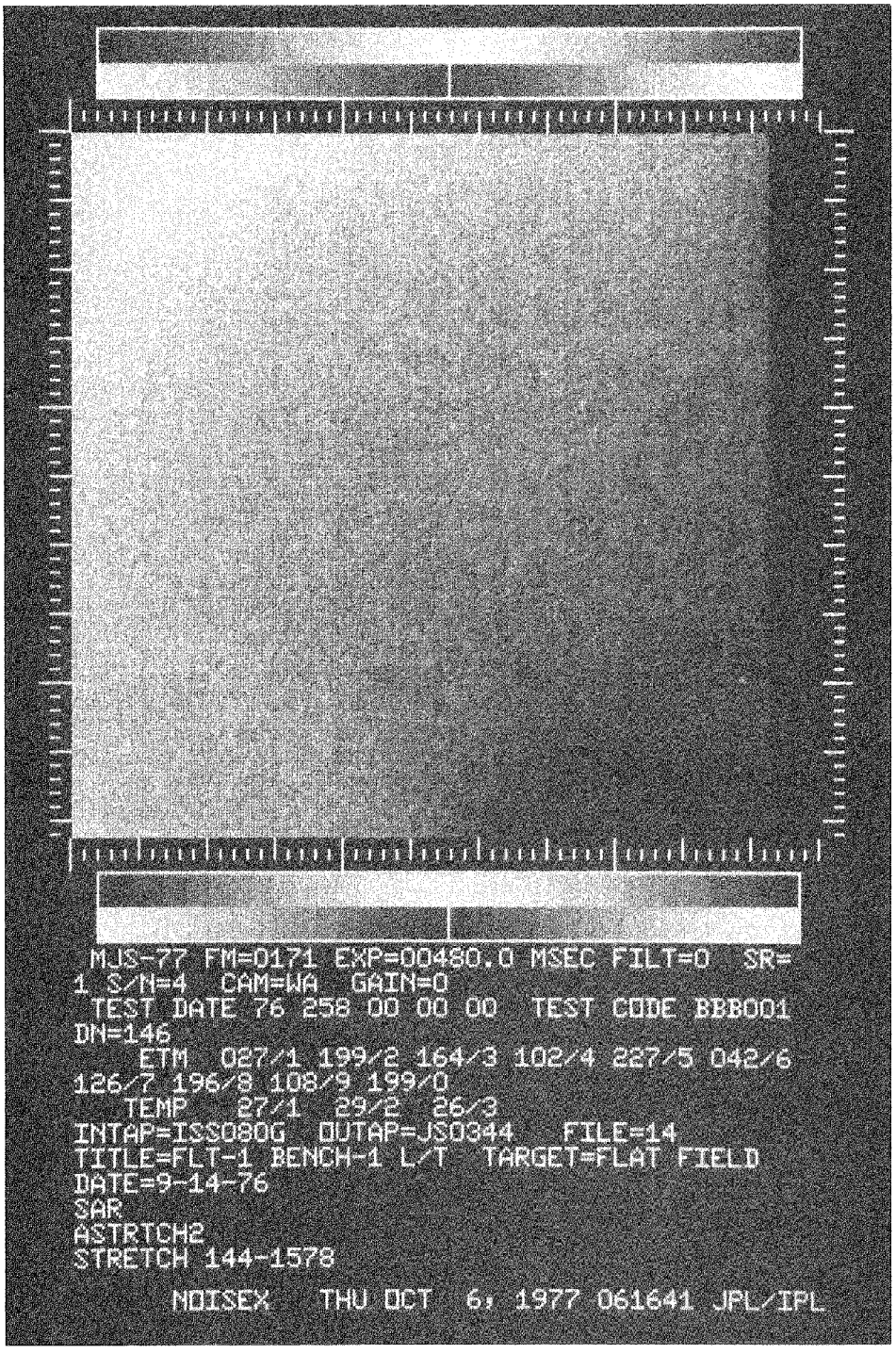

(d) ISS S/N 04

Figure 4-44 (contd)

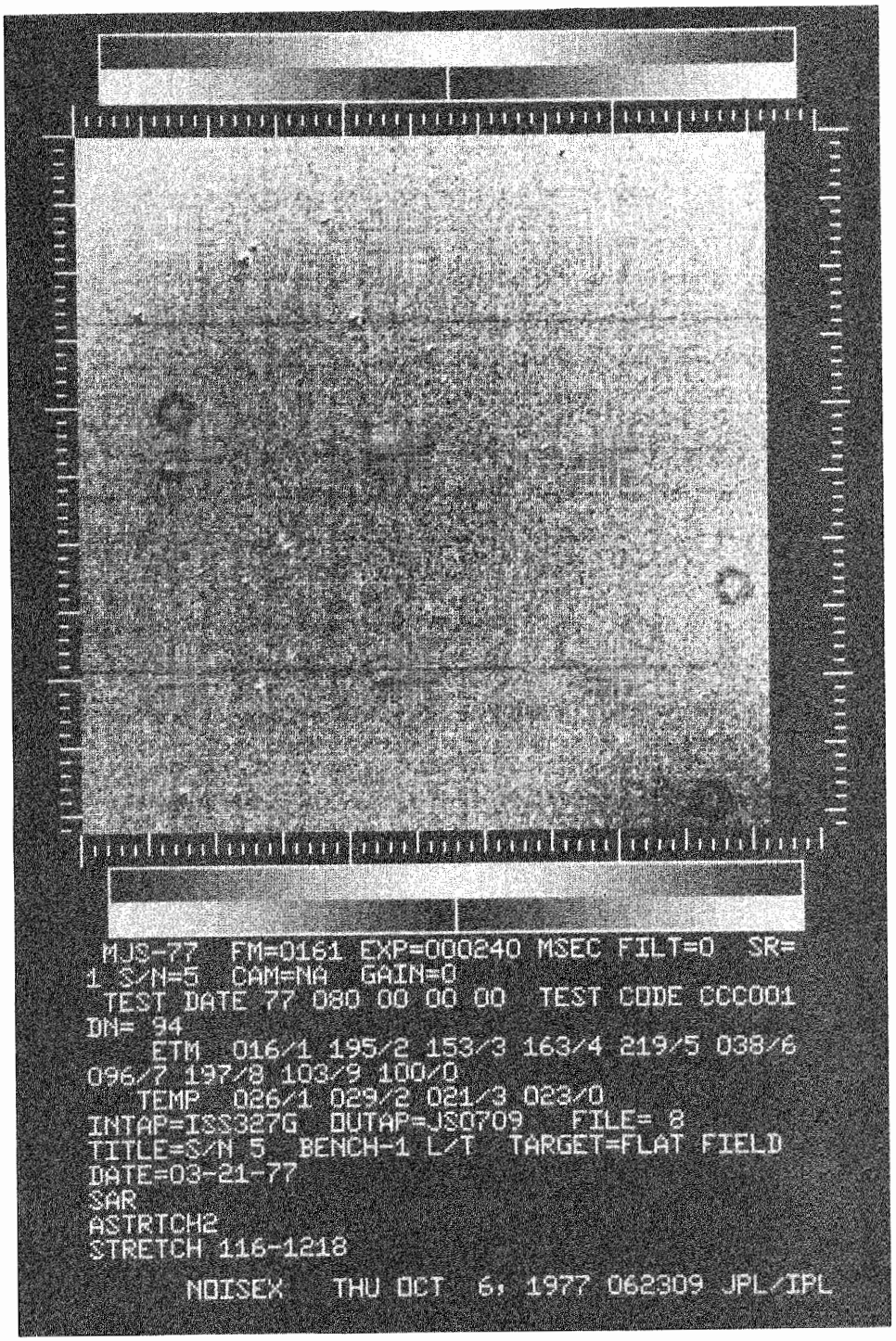

(e) ISS S/N 05

Figure 4-44 (contd)

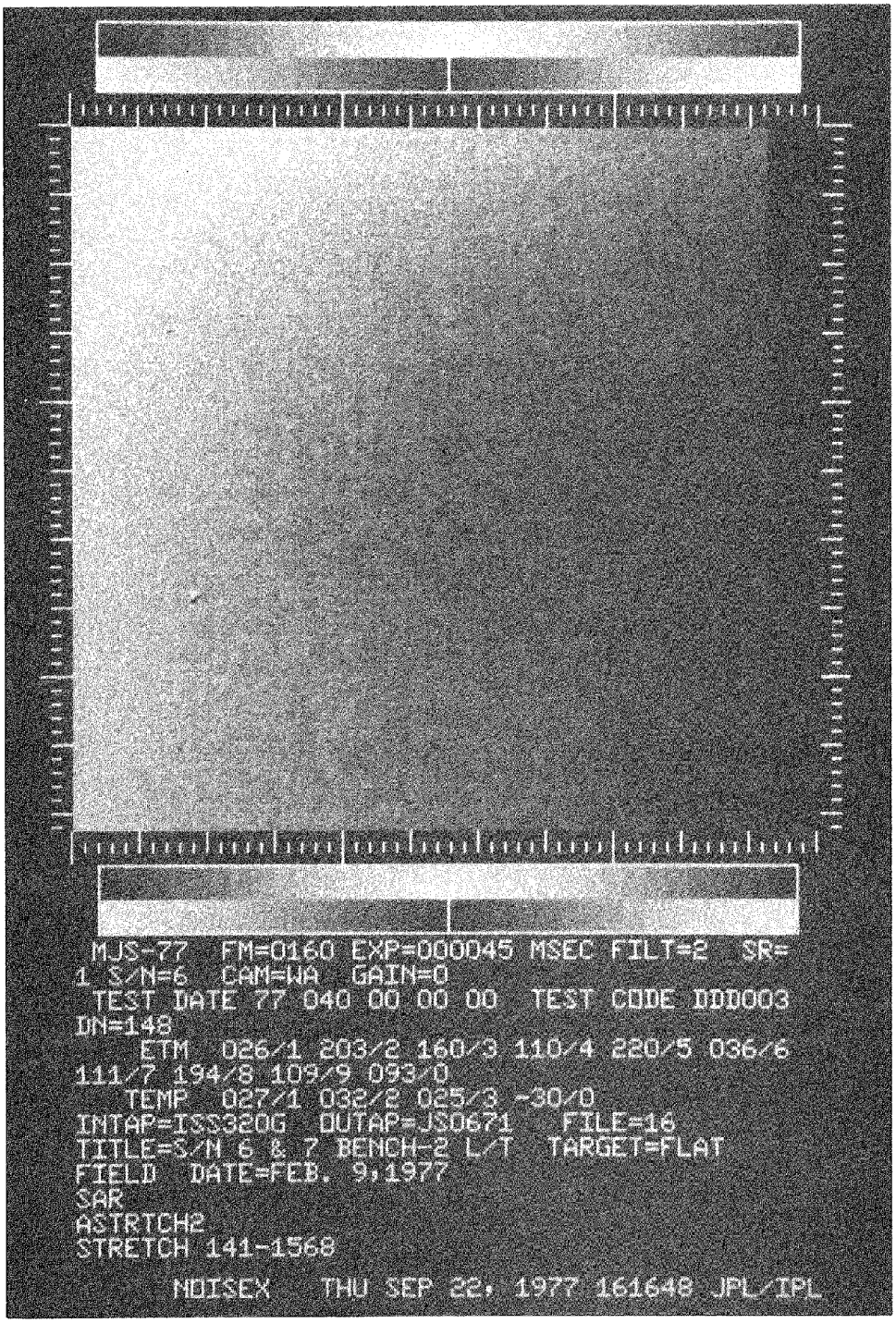

(f) ISS S/N 06

Figure 4-44 (contd)

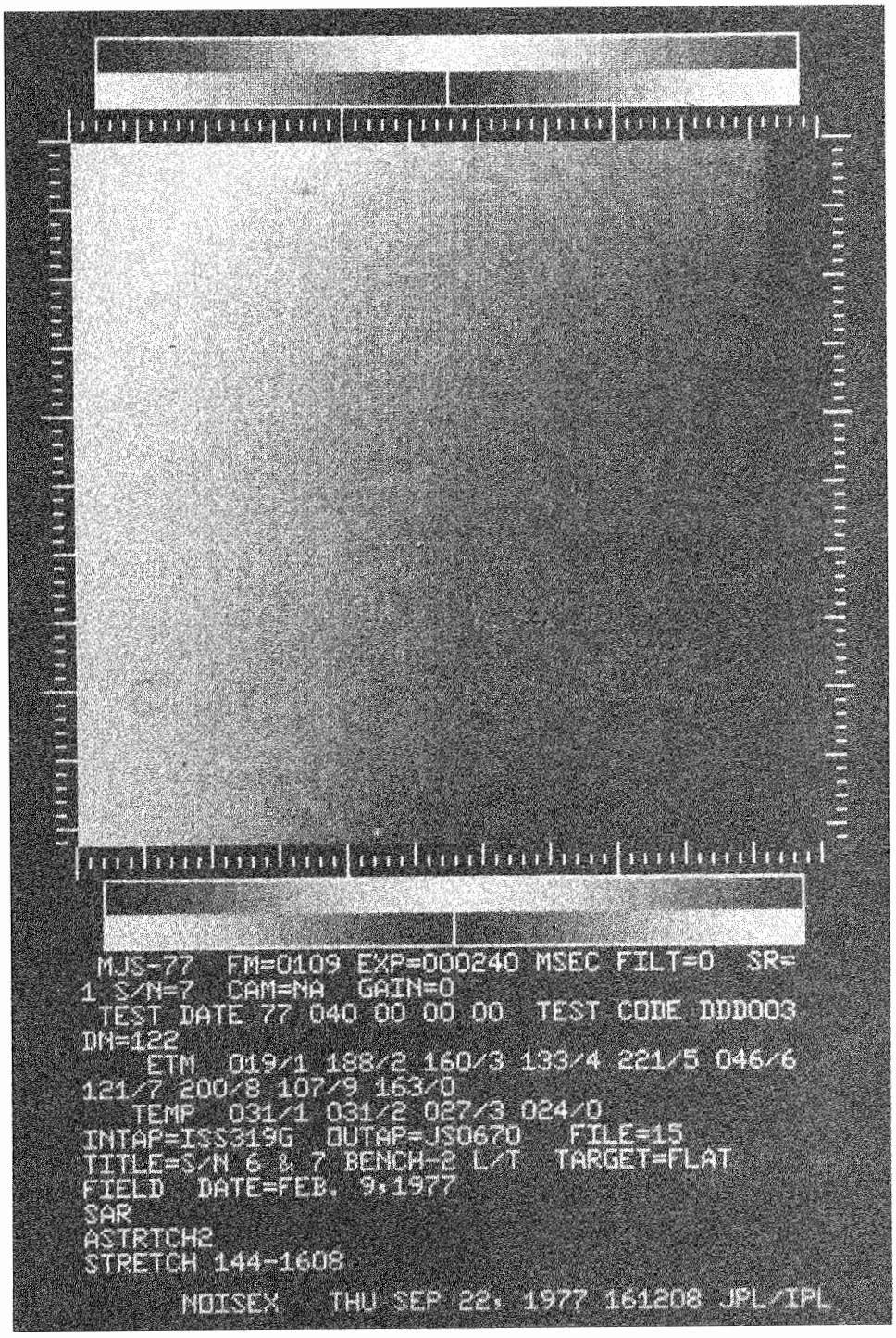

(g) ISS S/N 07

Figure 4-44 (contd)

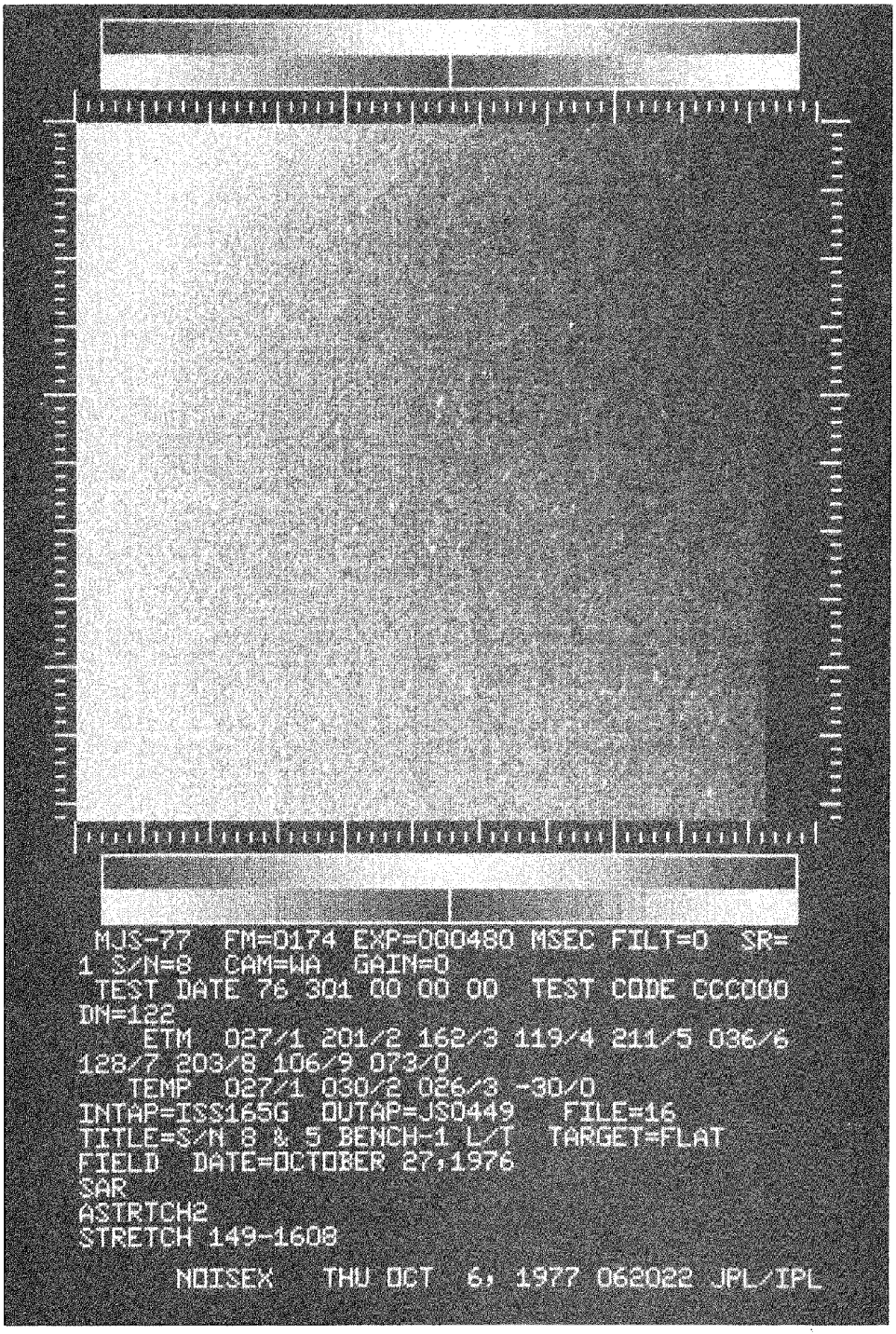

(h) ISS S/N 08

Figure 4-44 (contd)

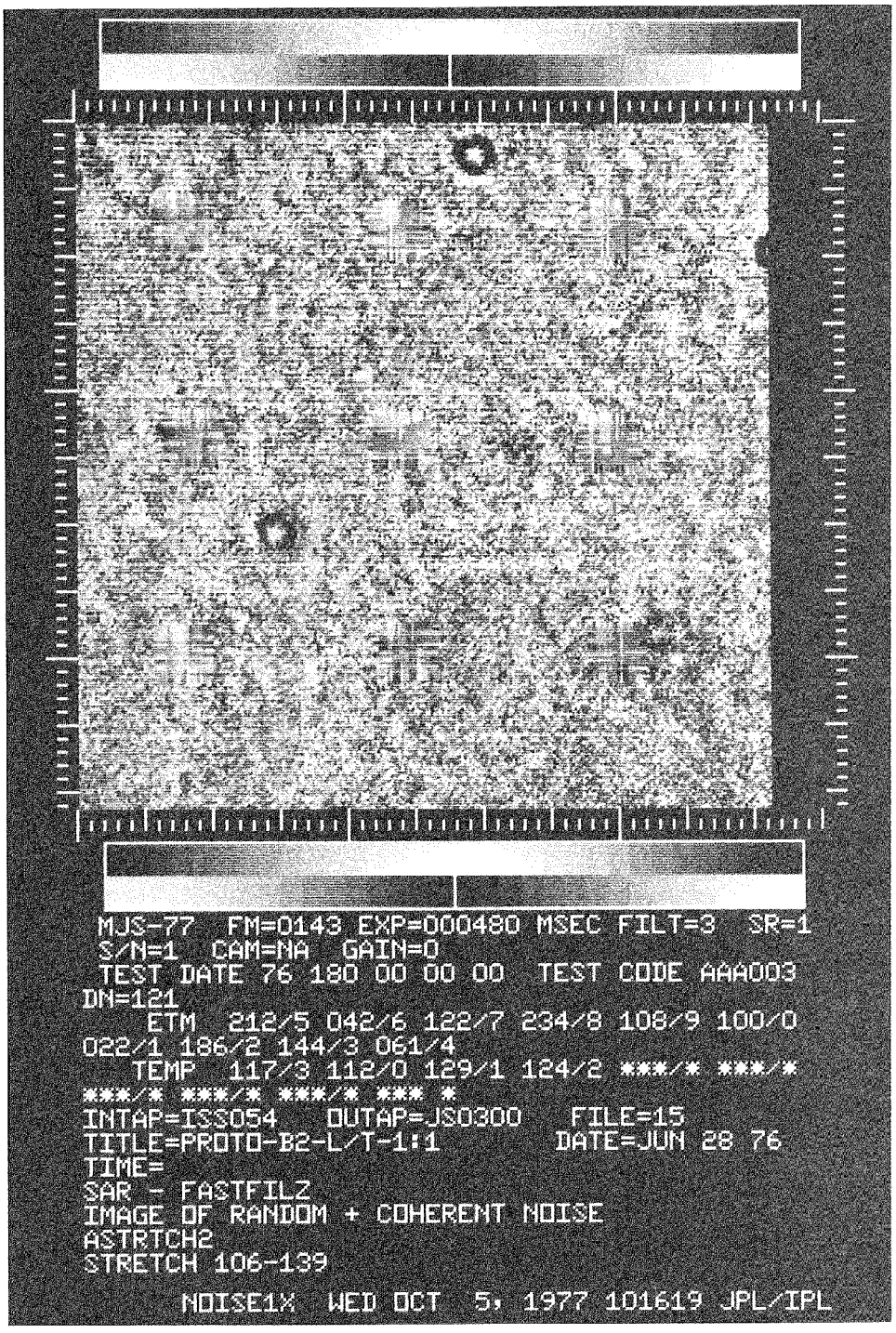

(a) ISS S/N 01

Figure 4-45. Image of flat field after vidicon shading removal, ISS S/N 01 to 08

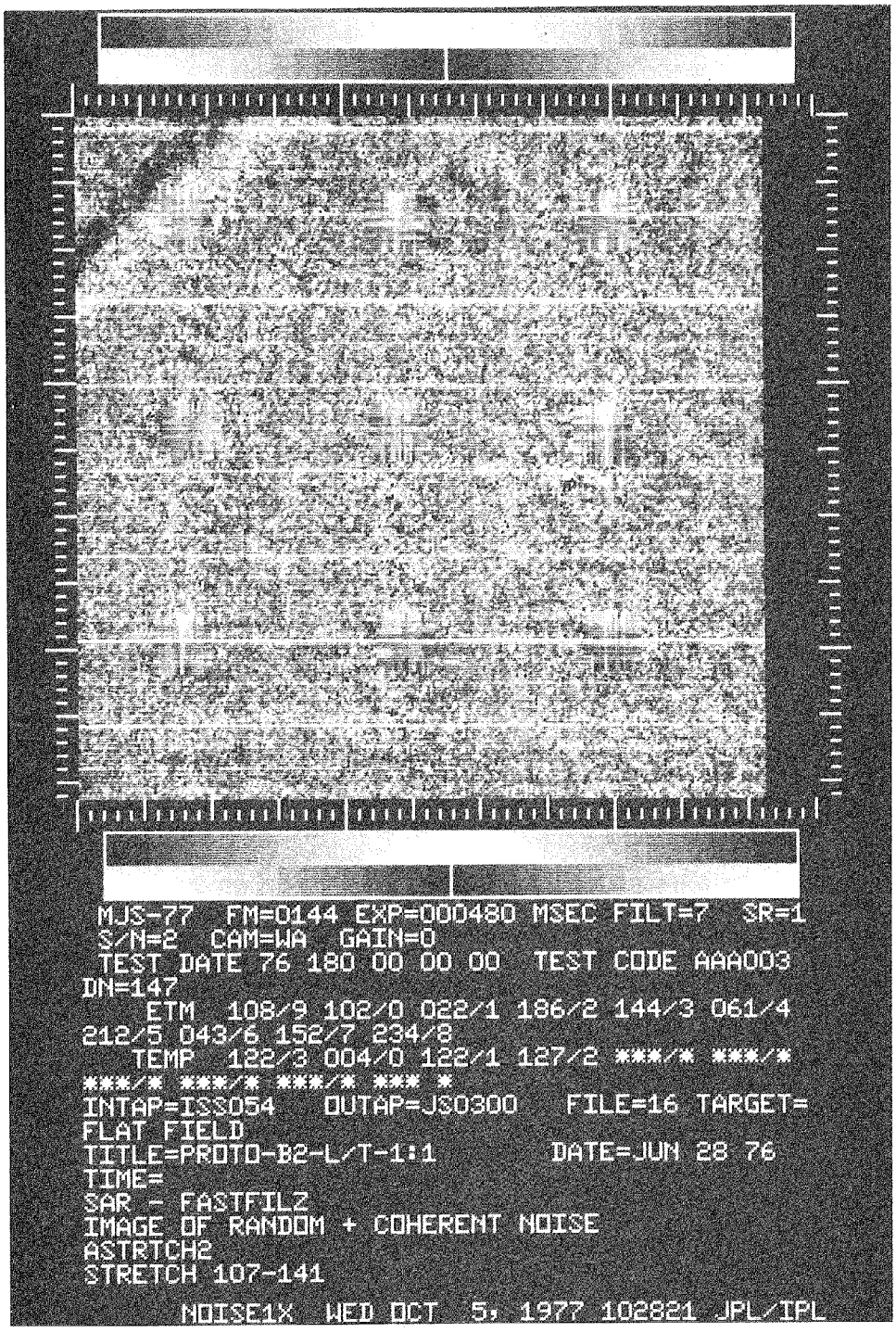

(b) ISS S/N 02

Figure 4-45 (contd)

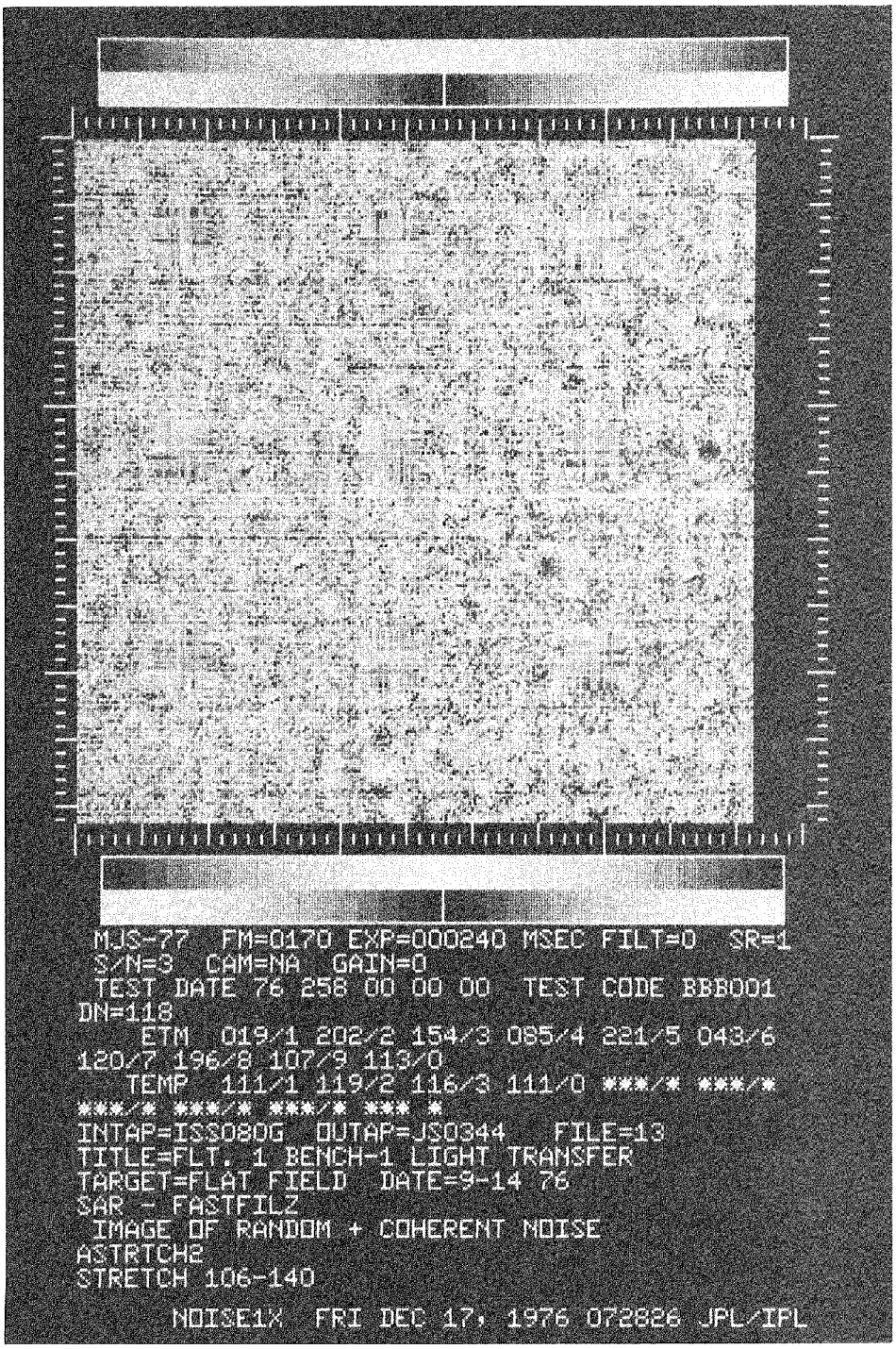

(c) ISS S/N 03

Figure 4-45 (contd)

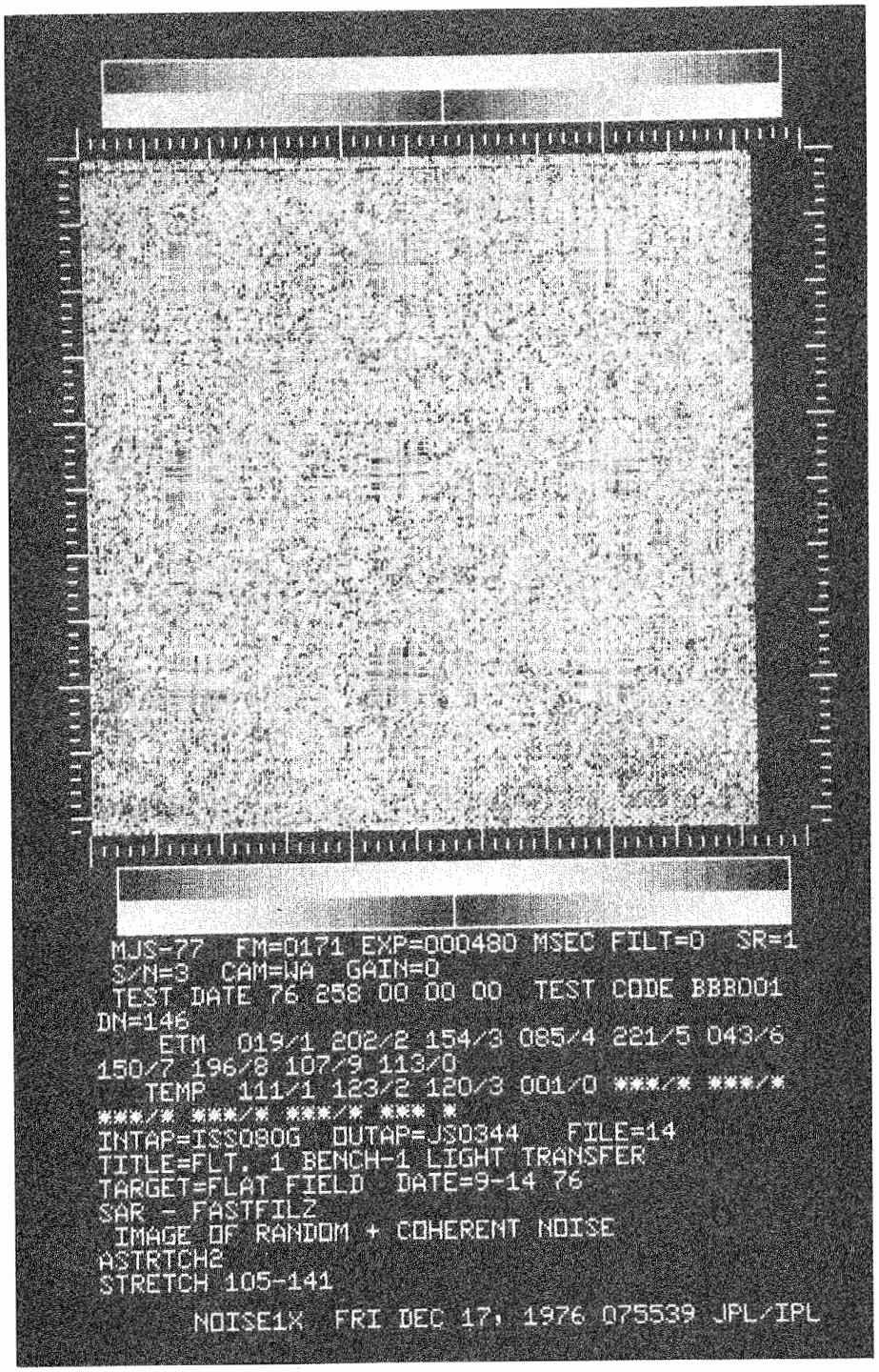

(d) ISS S/N 04

Figure 4-45 (contd)

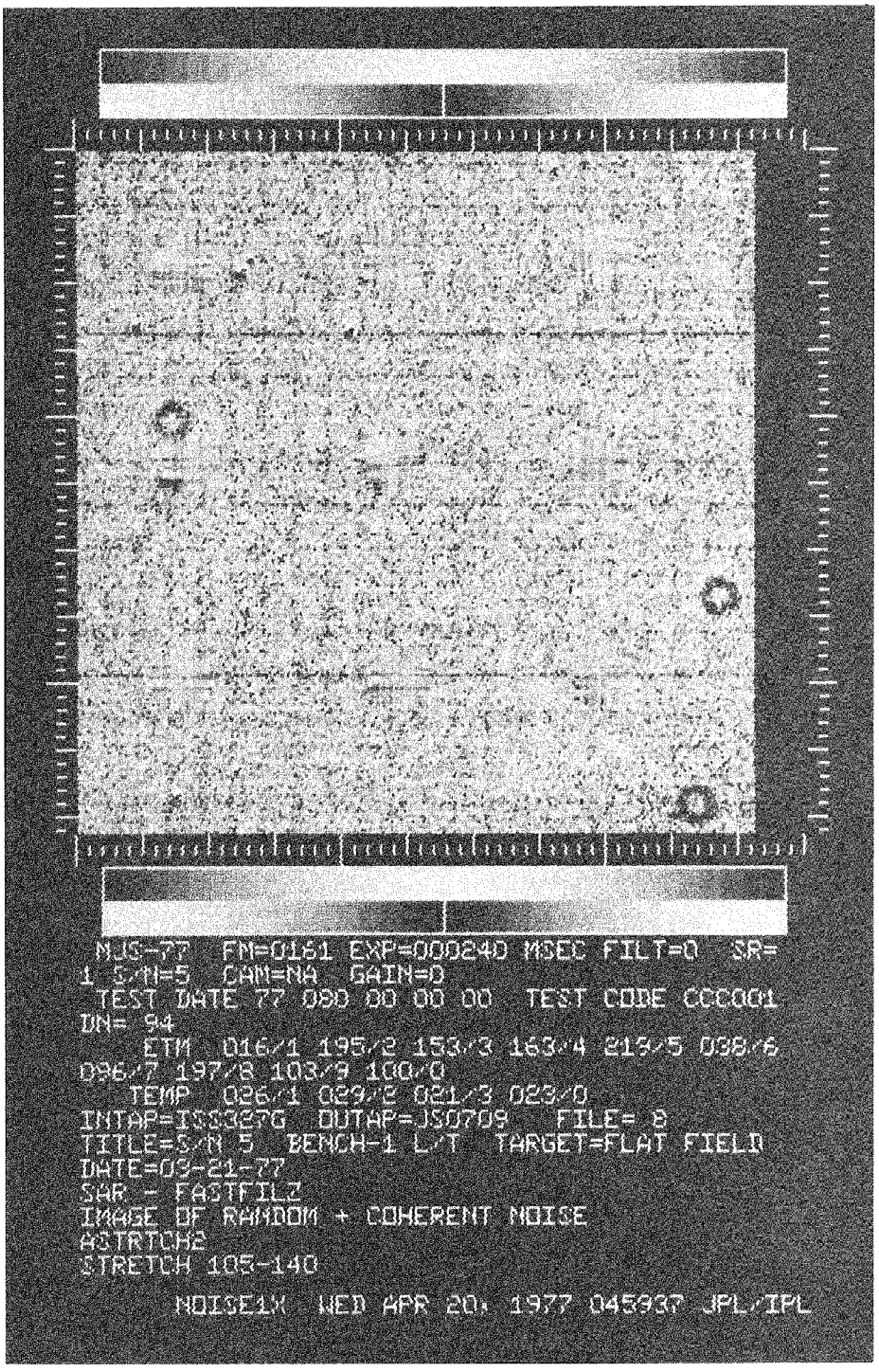

(e) ISS S/N 05

Figure 4-45 (contd)

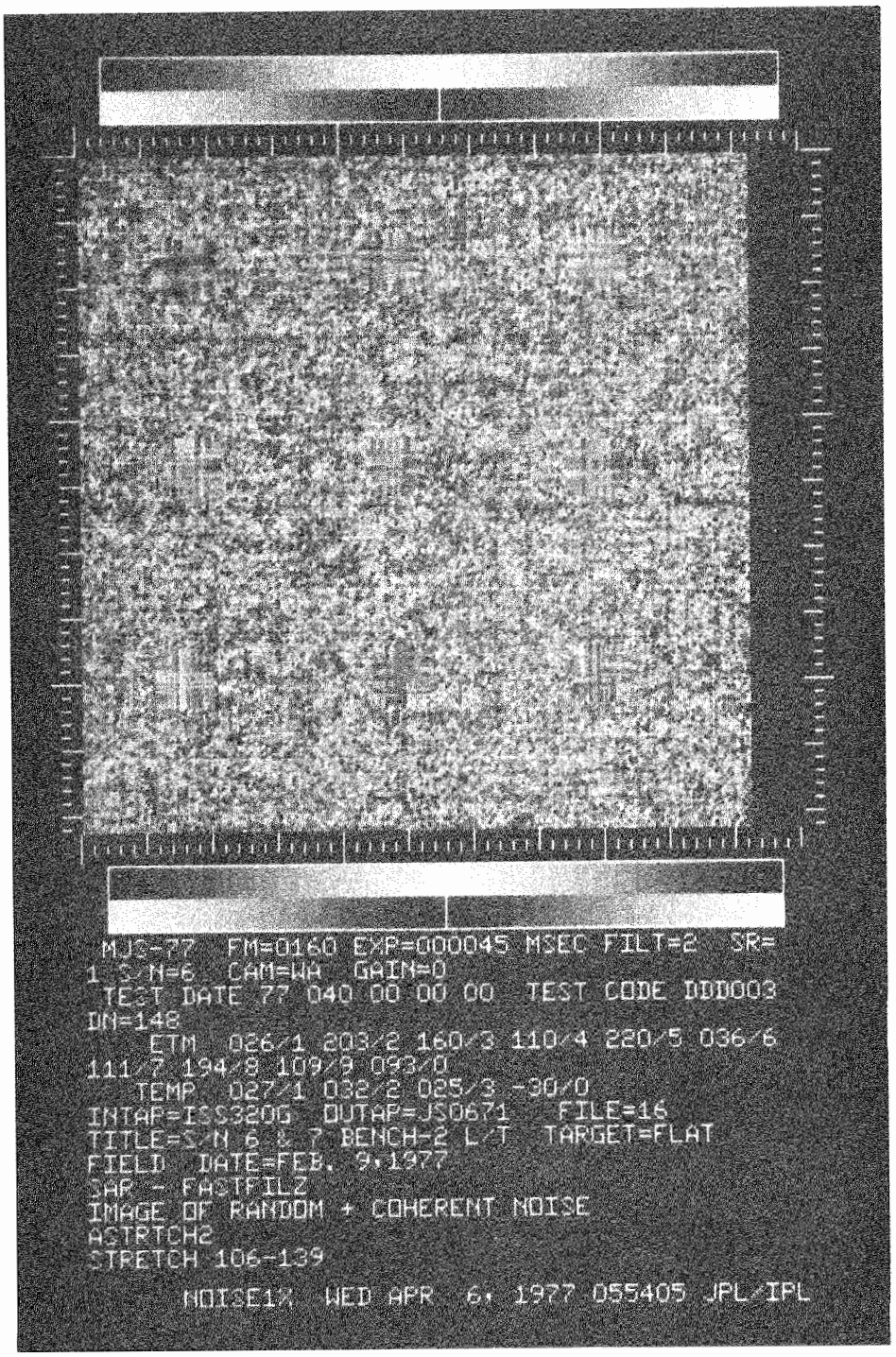

(f) ISS S/N 06

Figure 4-45 (contd)

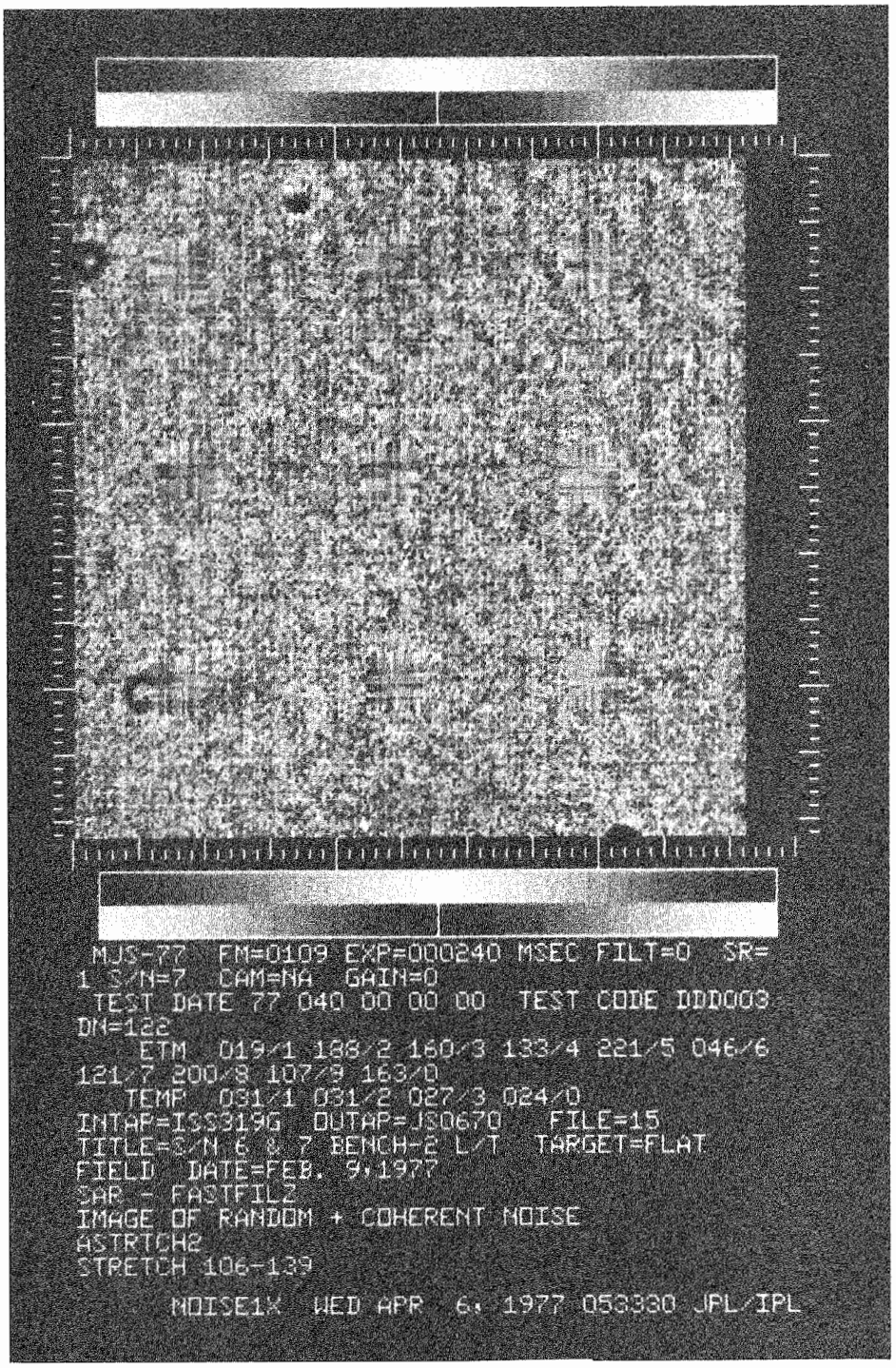

(g) ISS S/N 07

Figure 4-45 (contd)

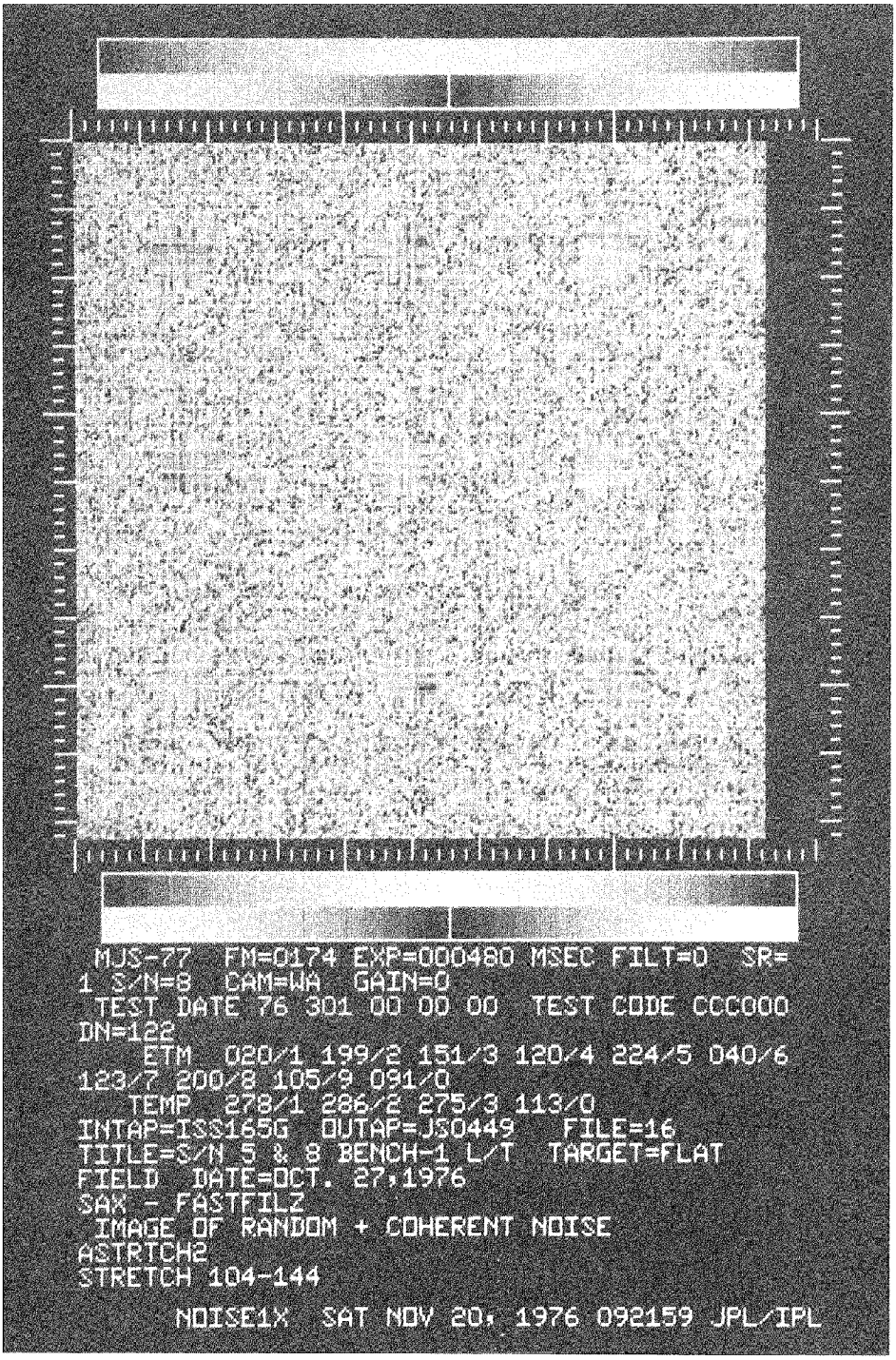

(h) ISS S/N 08

Figure 4-45 (contd)

If F_{jk} is the resultant transform, then the inverse transform is taken as follows:

$$dn'_{\ell s} = \frac{1}{256} \sum_{s=0}^{255} \sum_{k=0}^{255} F_{jk}\, e^{\frac{2\pi i}{256}(ks - j\ell)}$$

$$\ell, s = 0, \ldots, 255$$

where $(dn'_{\ell,s})$ is the resultant periodic noise-free image (Figure 4-46). The RMS measure from this result provides an upper bound of the random noise signal in the ISS. Any blemishes in the areas selected for analysis, as well as the quantization noise signal, will contribute to this result. The areas selected appear to have some blemishes, but the quantization noise level is small so that it is probably more appropriate simply to refer to this signal as the measure of nonperiodic noise. It is also likely that not all vidicon shading has been removed, although this effect is negligible.

The difference between $(dn_{\ell,s})$, the unshaded image, and $(dn'_{\ell,s})$, the nonperiodic noise image, yields an image from which the RMS measure of the periodic noise can be computed (Figure 4-47). A number of possible error sources exist; for example, incomplete reseau removal (since reseaus are spatially coherent); but this would be obvious and results indicate that this is no problem.

One-dimensional amplitude spectra are included in both line and sample directions.[13] Generally, it is possible to get a feel for the relative amplitudes of the periodic noise signals, as well as for the frequencies at which they occur, from these plots (Figures 4-48 and 4-49).

At least two (generally, three) images from the following light-transfer sequences were used for analysis for each of the cameras (the in-flight analysis used one star-field image:

(1) Bench 1 Calibration

  (a) Low-gain state

  (b) High-gain state

[13] Note that the abscissa scales in the line and sample plots differ.

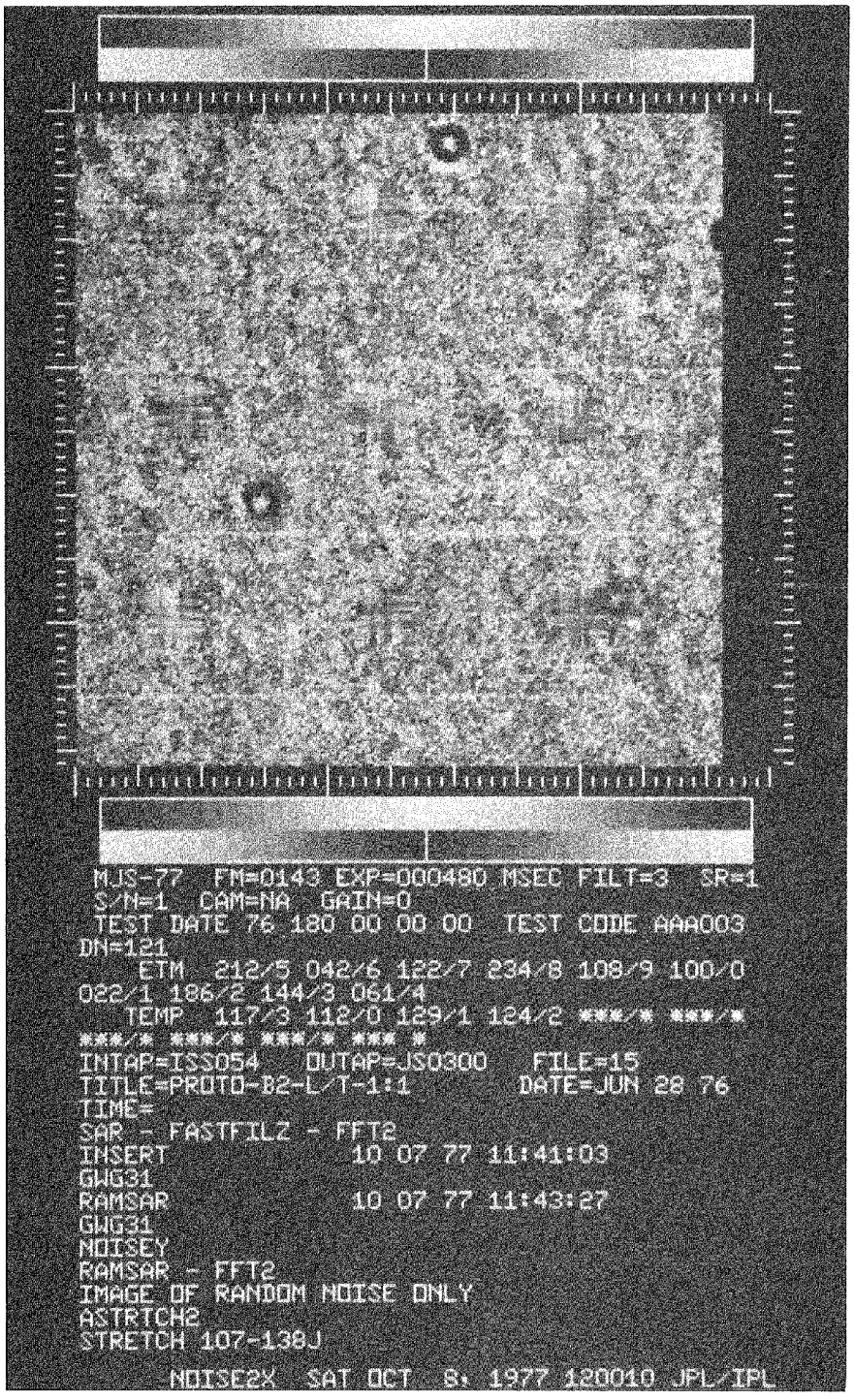

(a) ISS S/N 01

Figure 4-46. Periodic noise-free image, ISS S/N 01 to 08

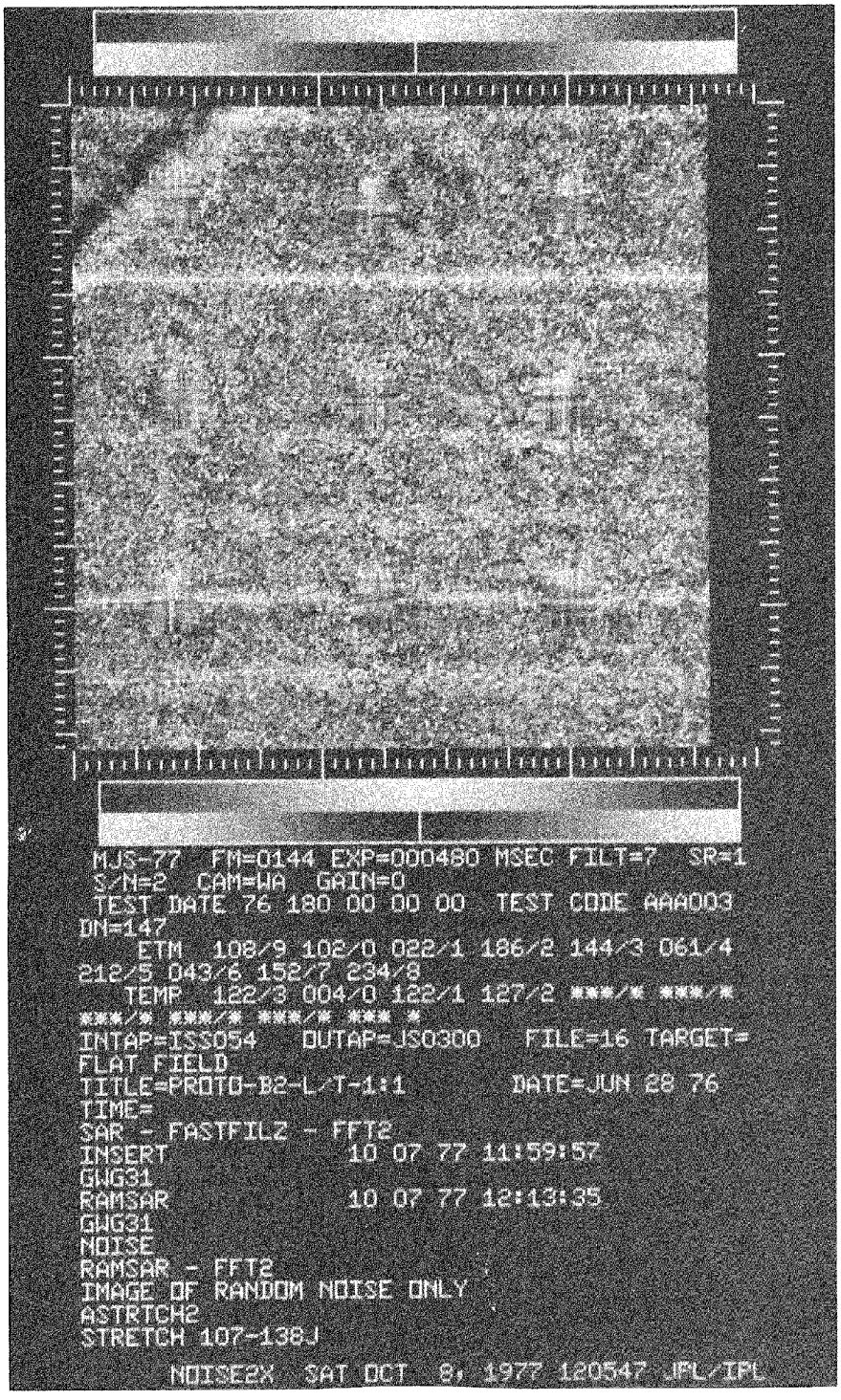

(b) ISS S/N 02

Figure 4-46 (contd)

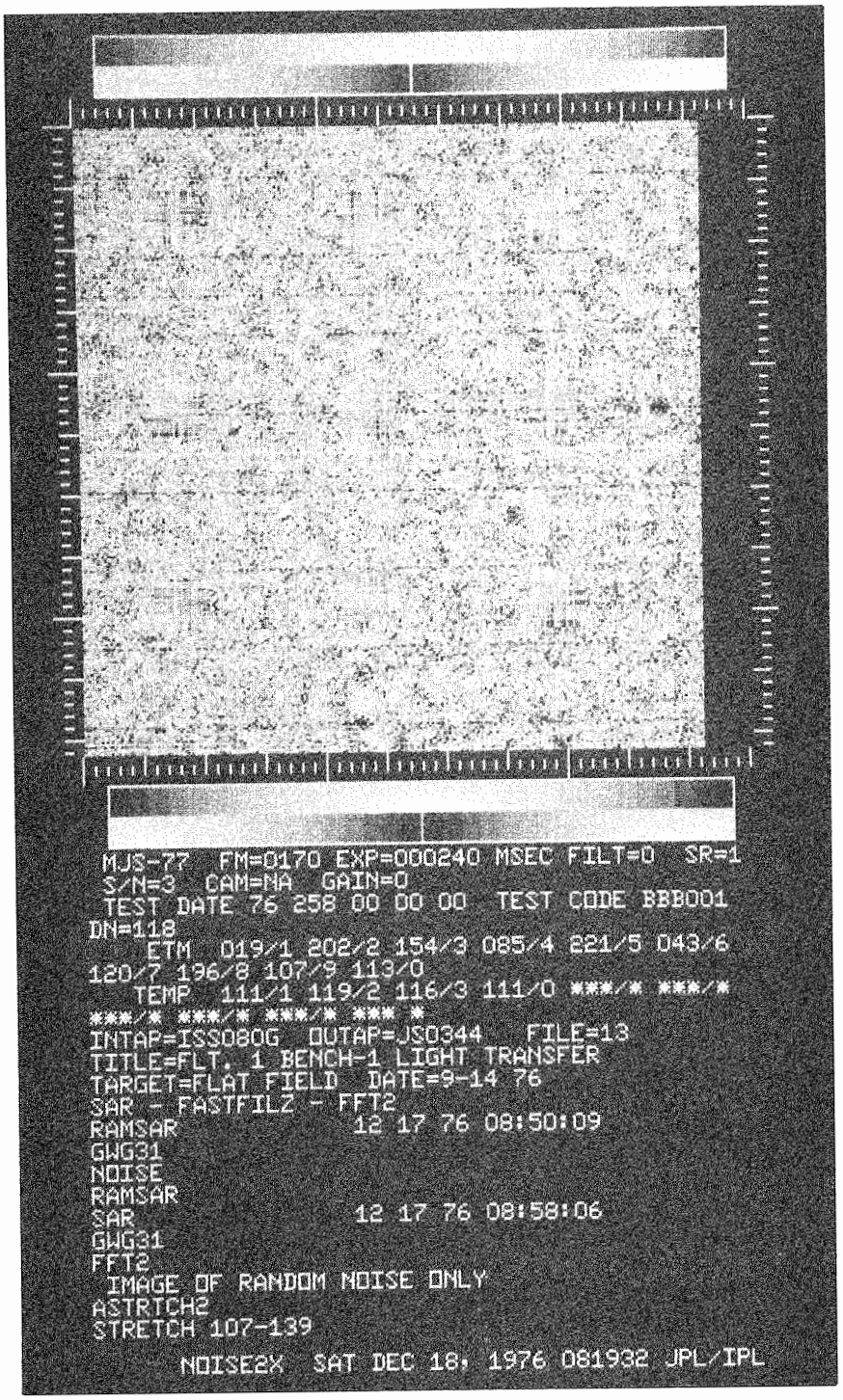

(c) ISS S/N 03

Figure 4-46 (contd)

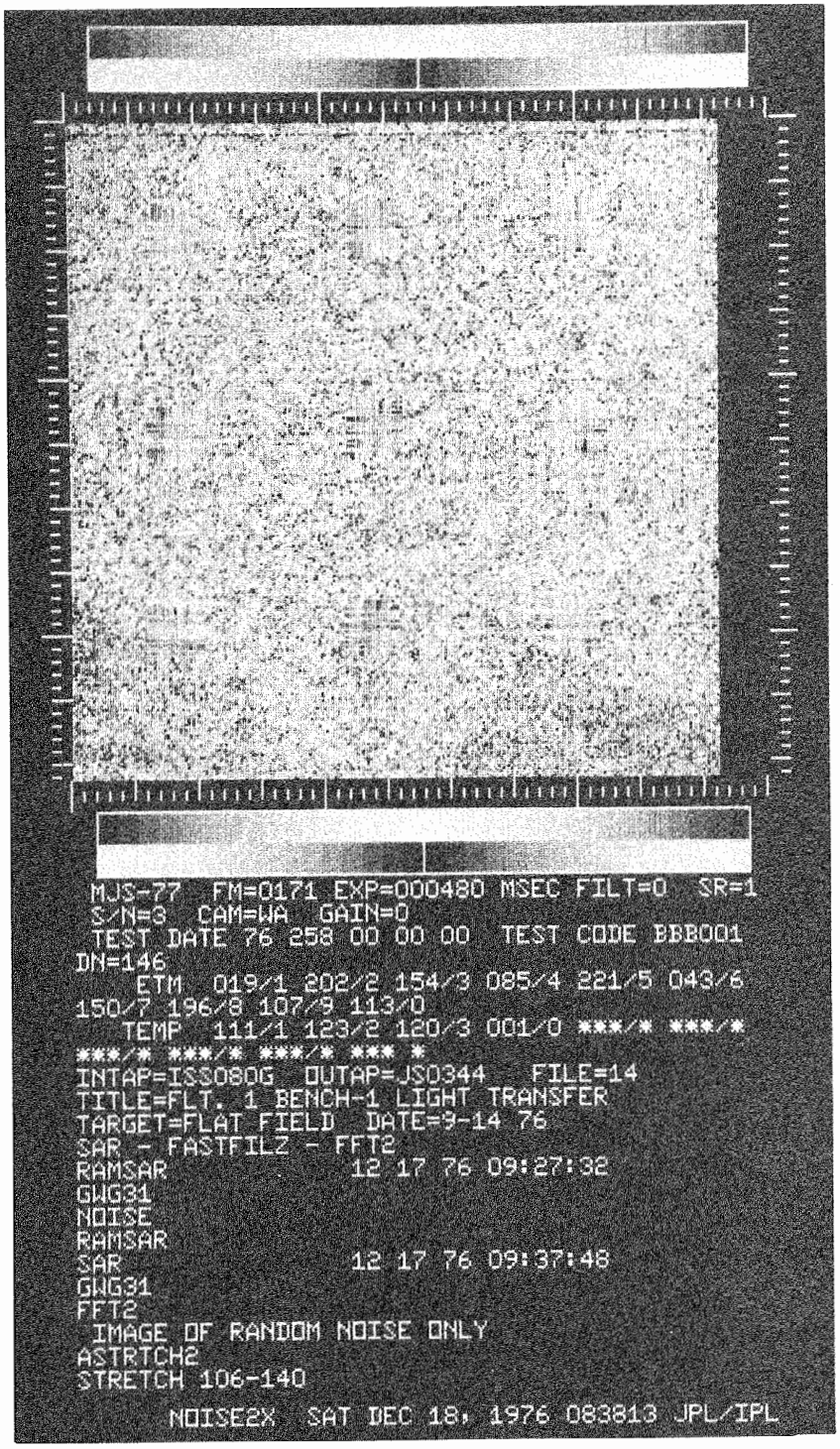

(d) ISS S/N 04

Figure 4-46 (contd)

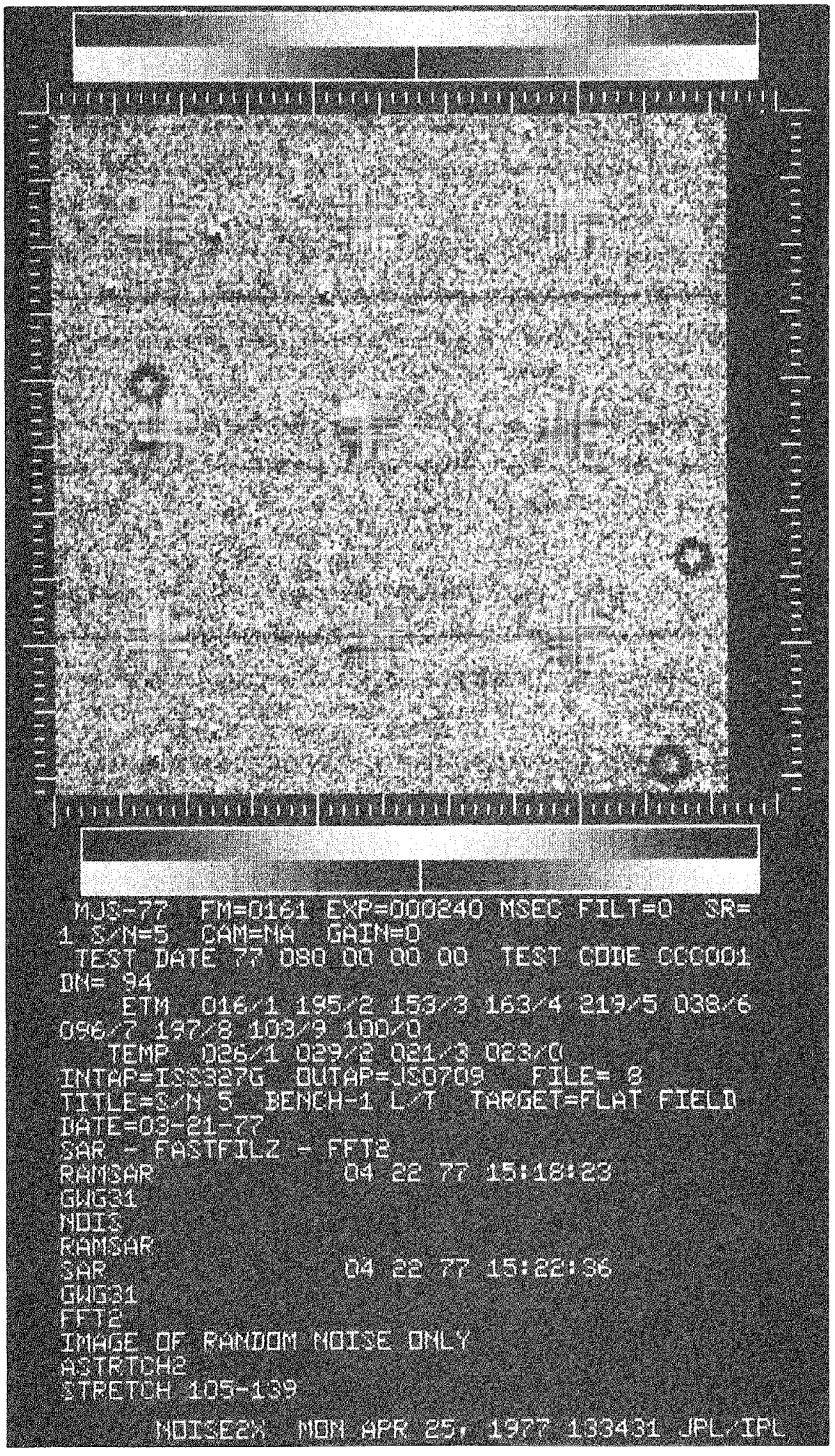

(e) ISS S/N 05

Figure 4-46 (contd)

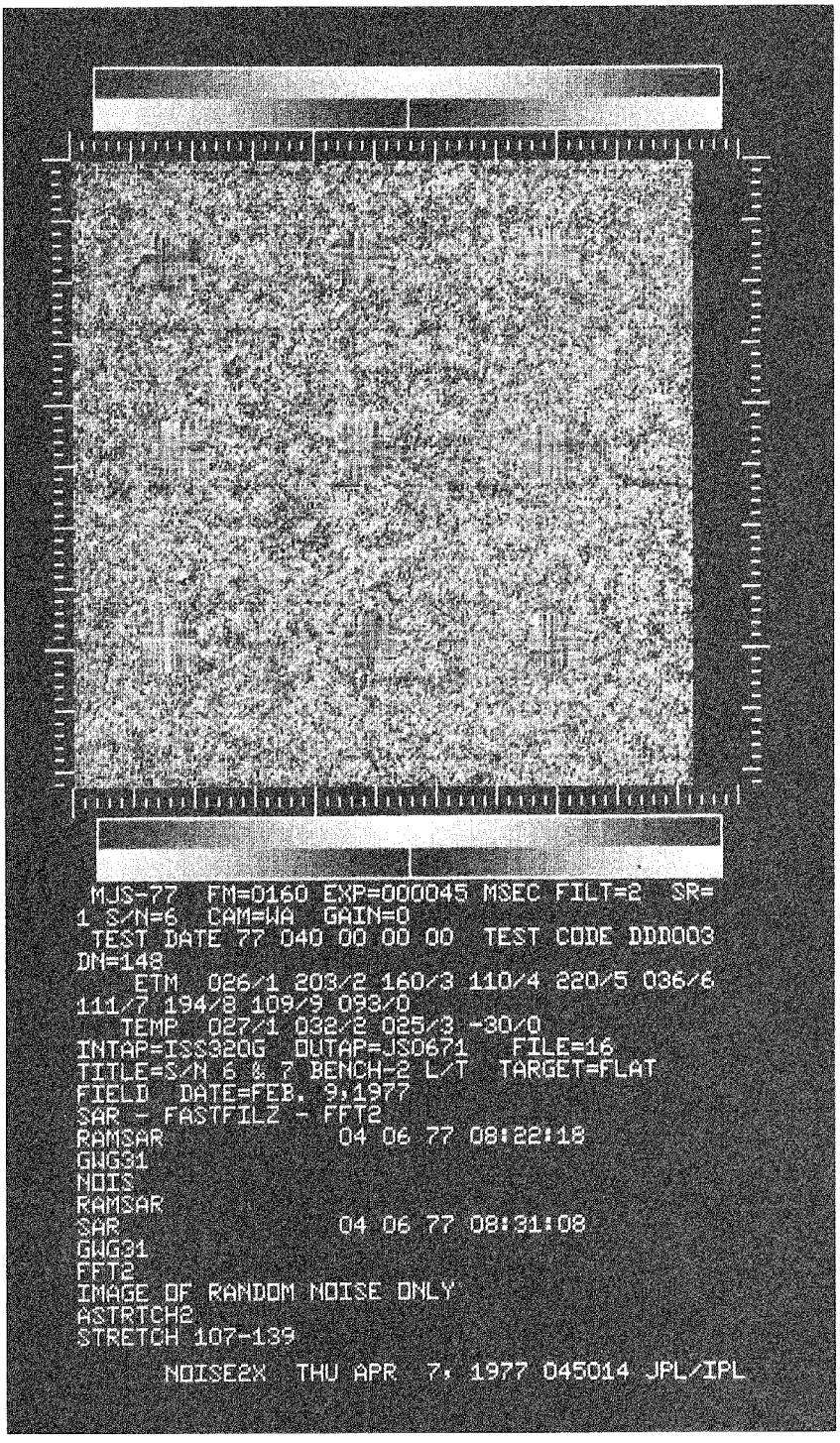

(f) ISS S/N 06

Figure 4-46 (contd)

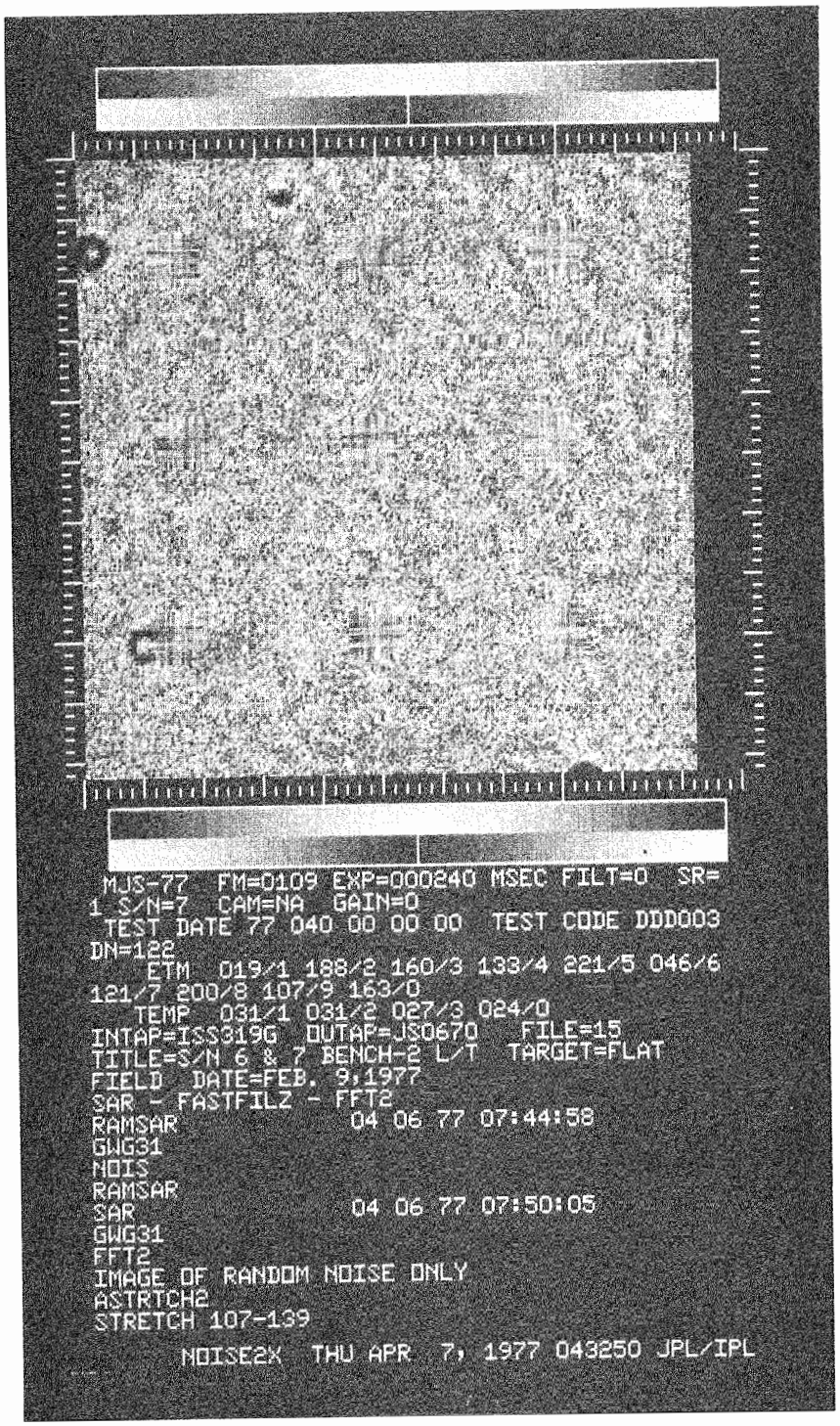

(g) ISS S/N 07

Figure 4-46 (contd)

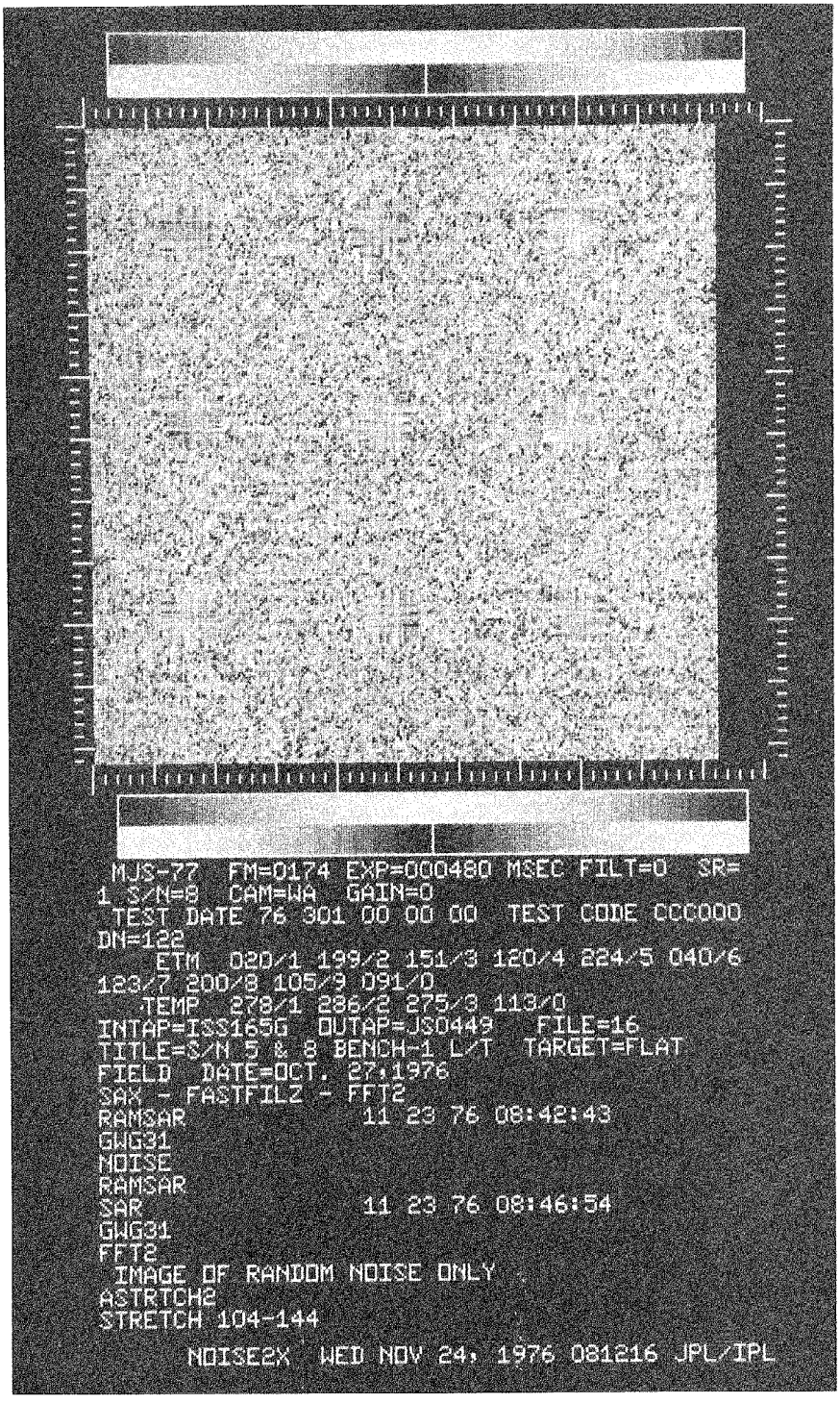

(h) ISS S/N 08

Figure 4-46 (contd)

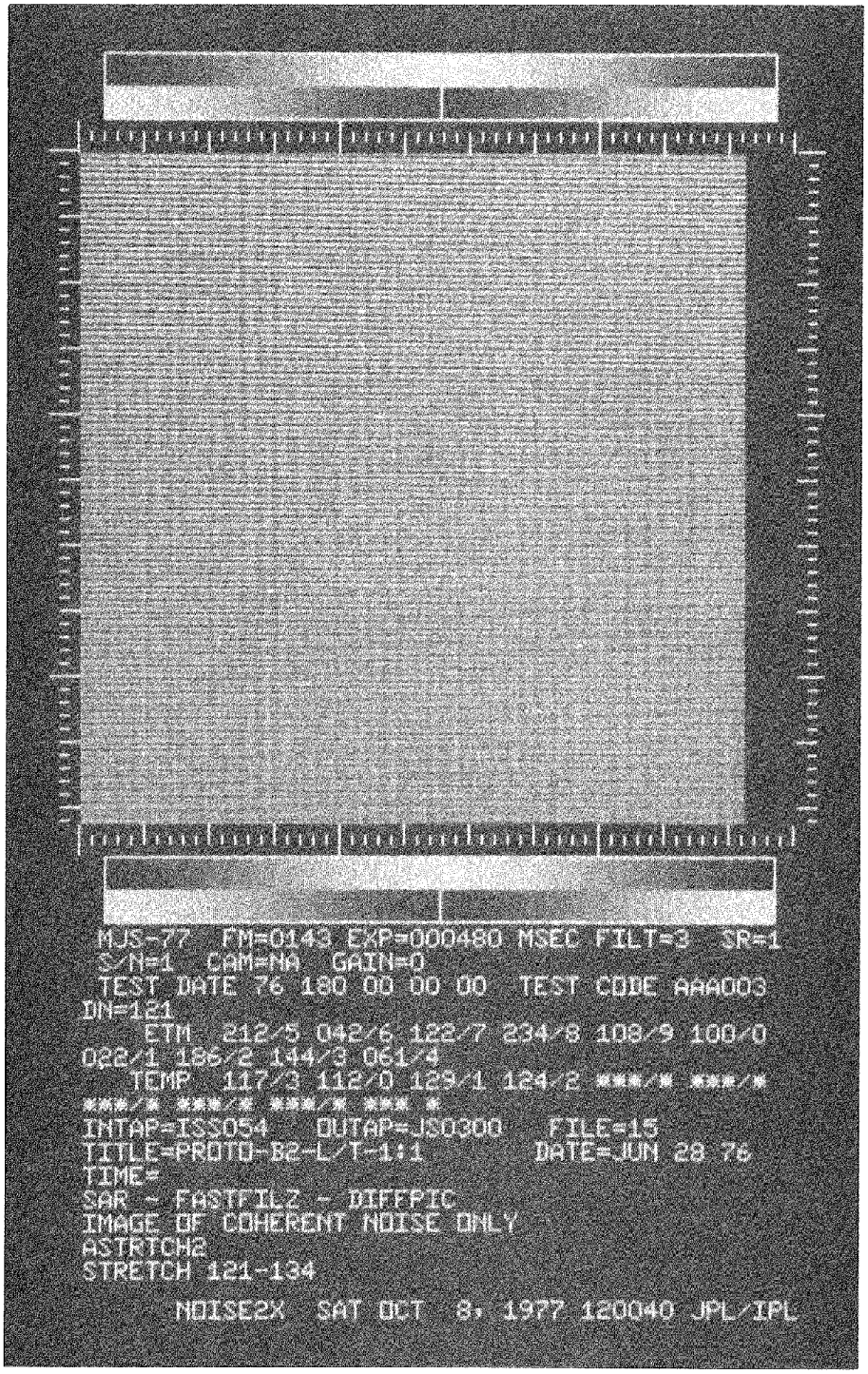

(a) ISS S/N 01

Figure 4-47. Periodic-noise image, ISS S/N 01 to 08

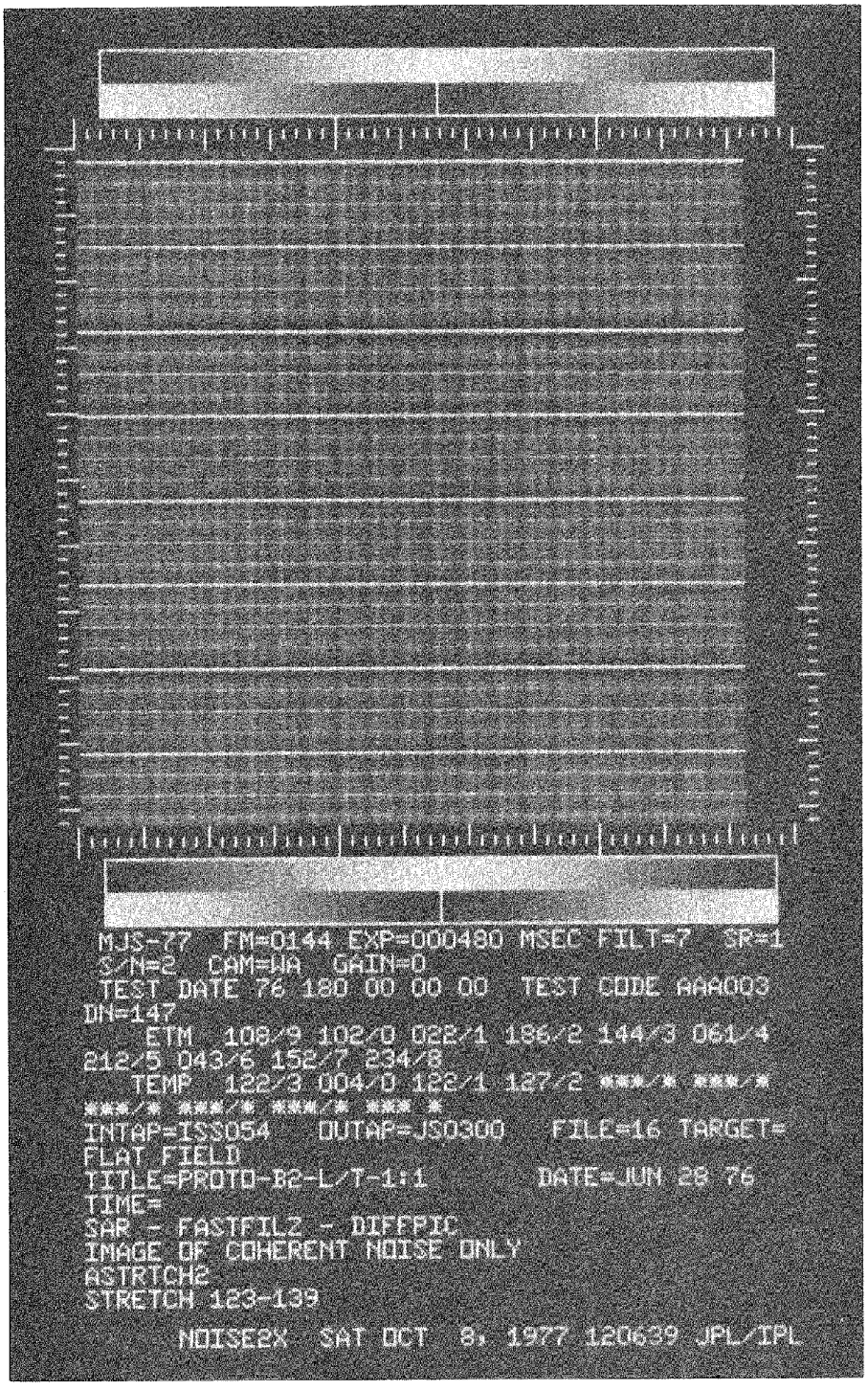

(b) ISS S/N 02

Figure 4-47 (contd)

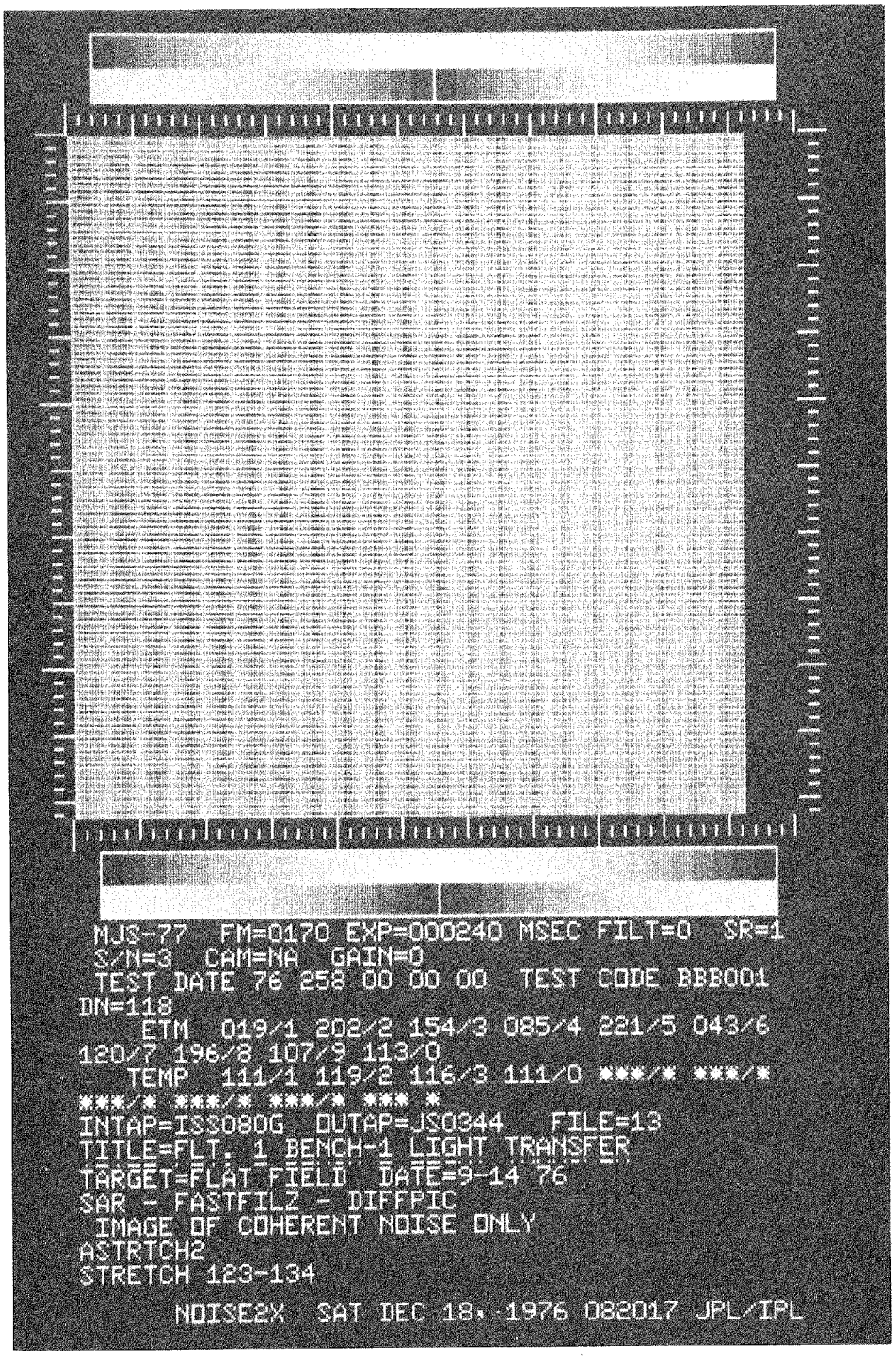

(c) ISS S/N 03

Figure 4-47 (contd)

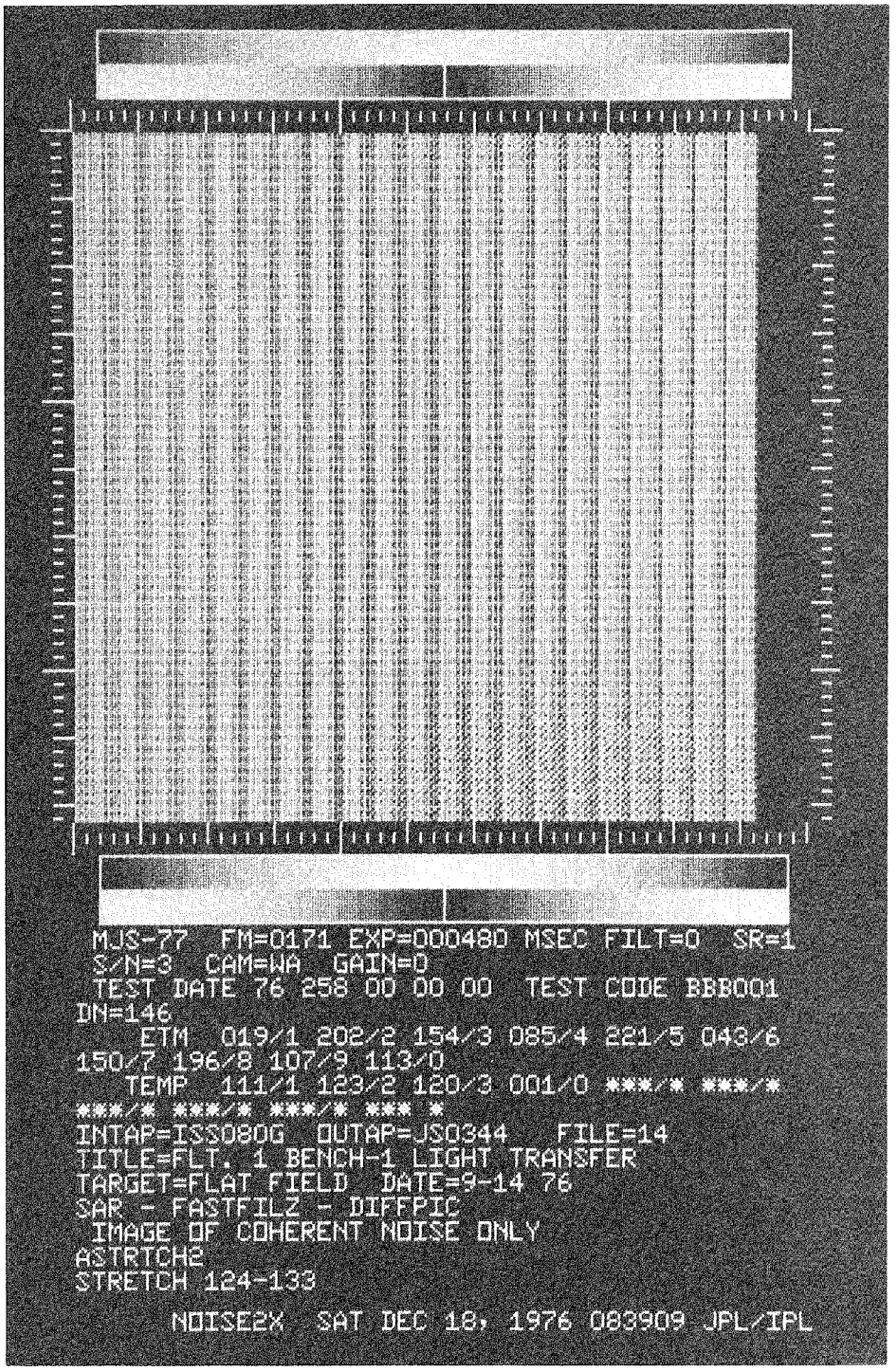

(d) ISS S/N 04

Figure 4-47 (contd)

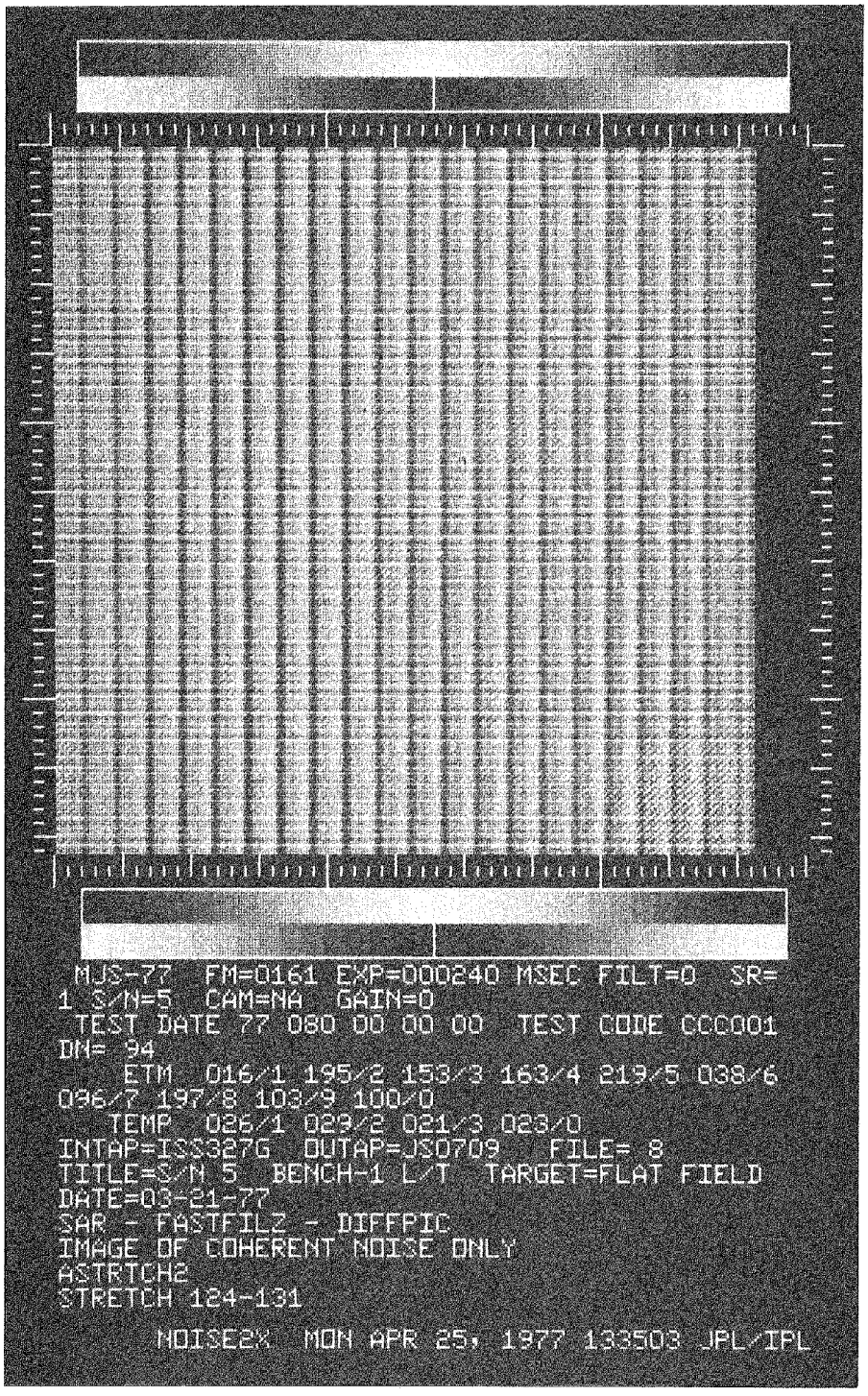

(e) ISS S/N 05

Figure 4-47 (contd)

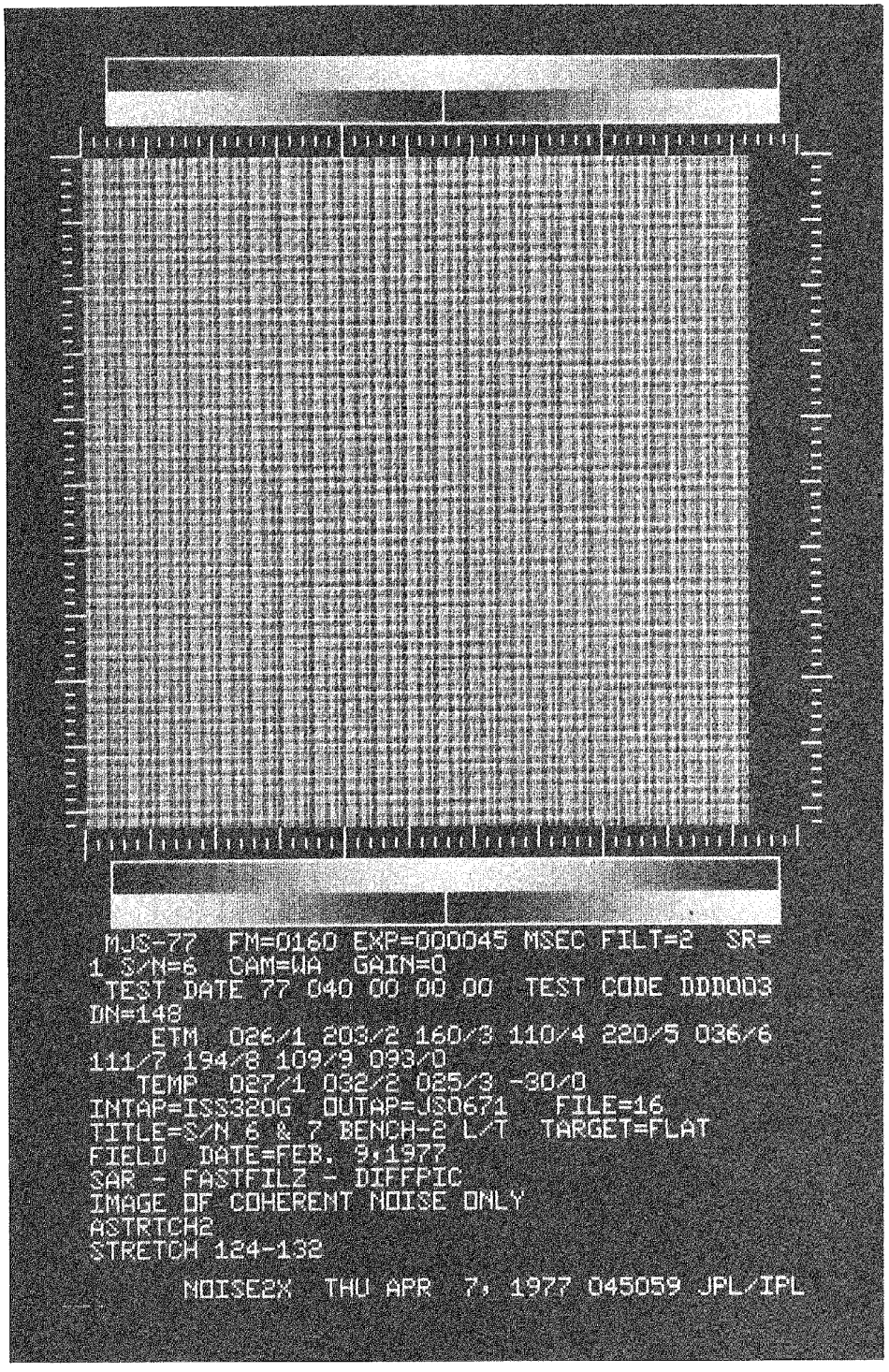

(f) ISS S/N 06

Figure 4-47 (contd)

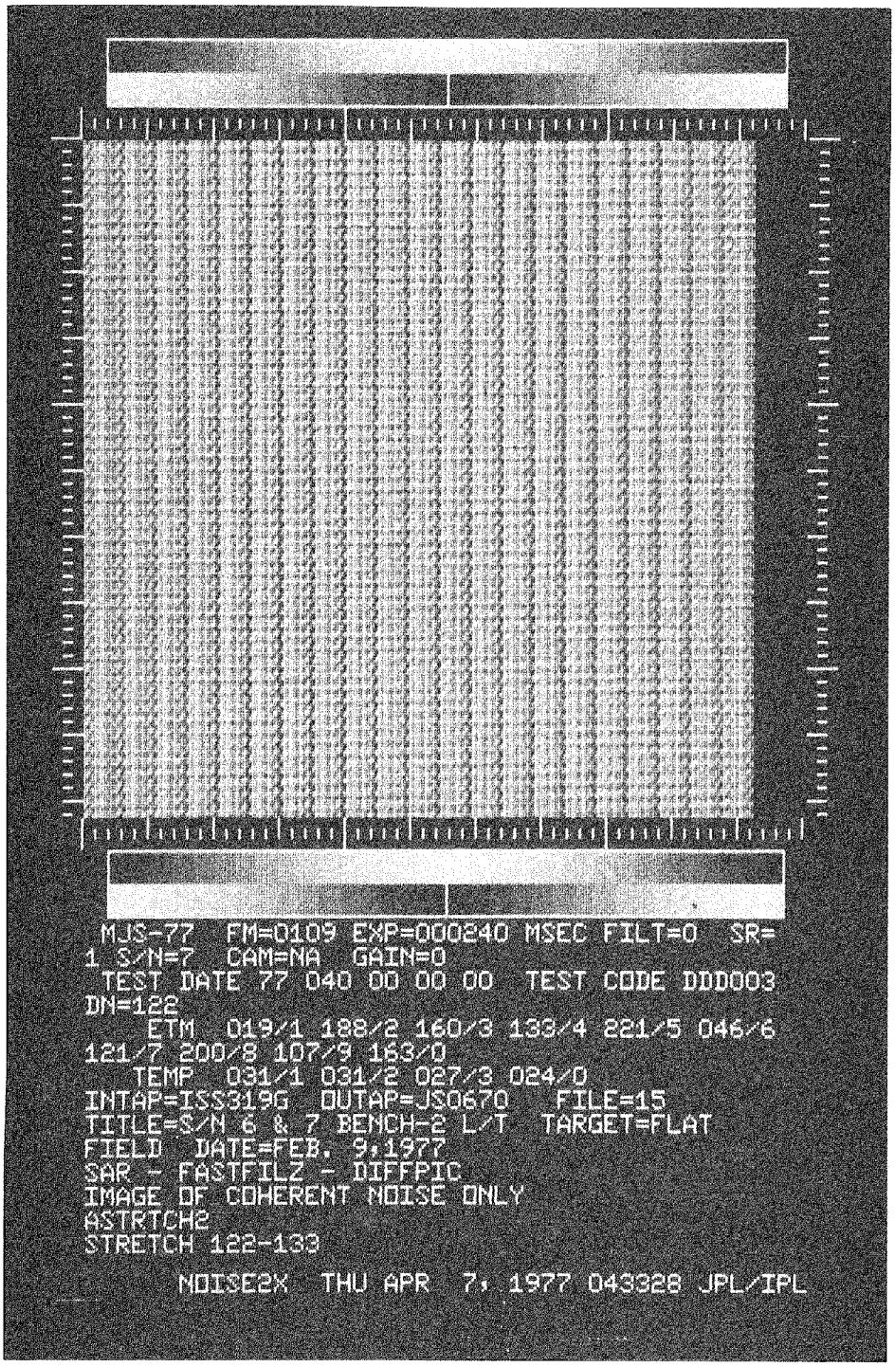

(g) ISS S/N 07

Figure 4-47 (contd)

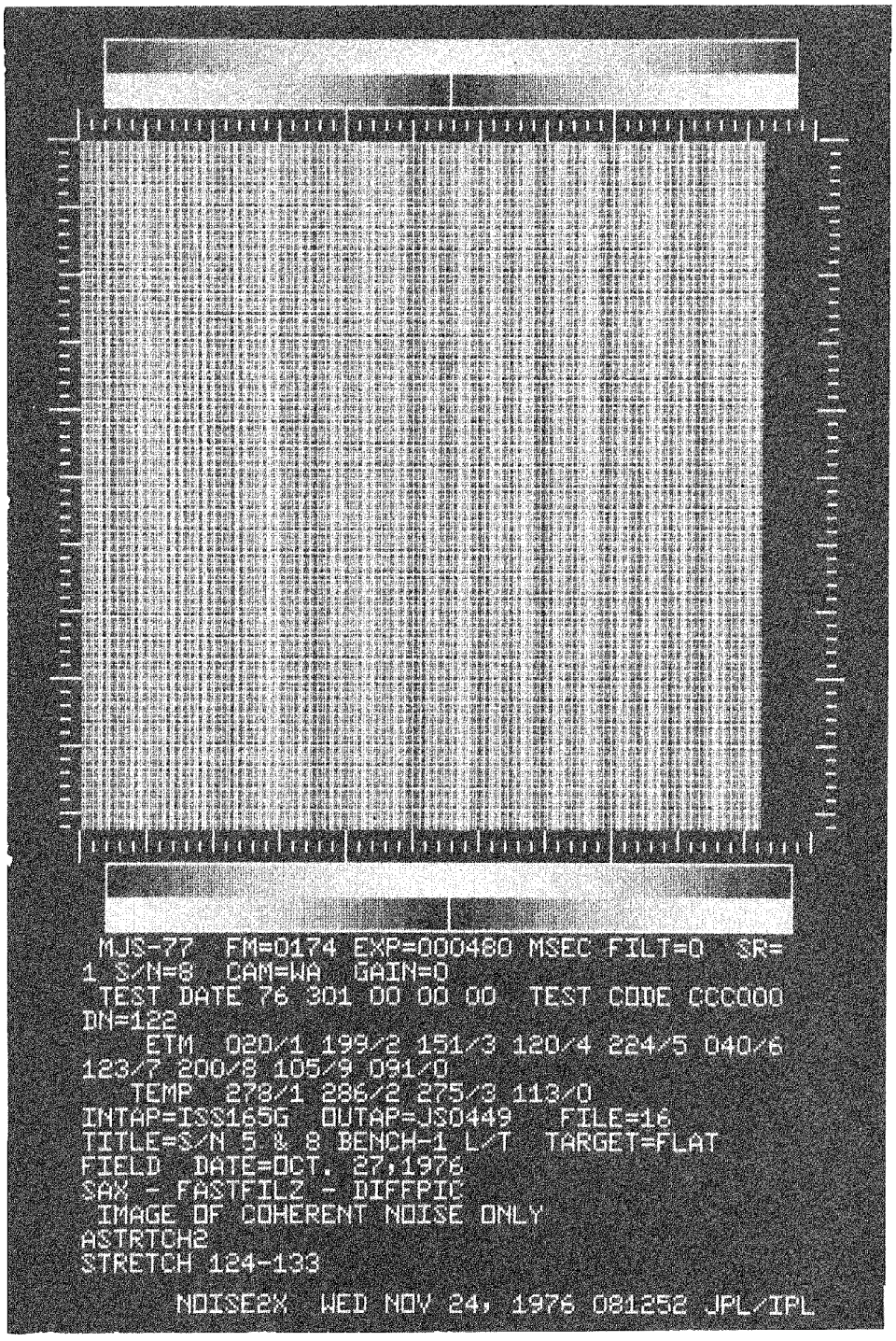

(h) ISS S/N 08

Figure 4-47 (cont)

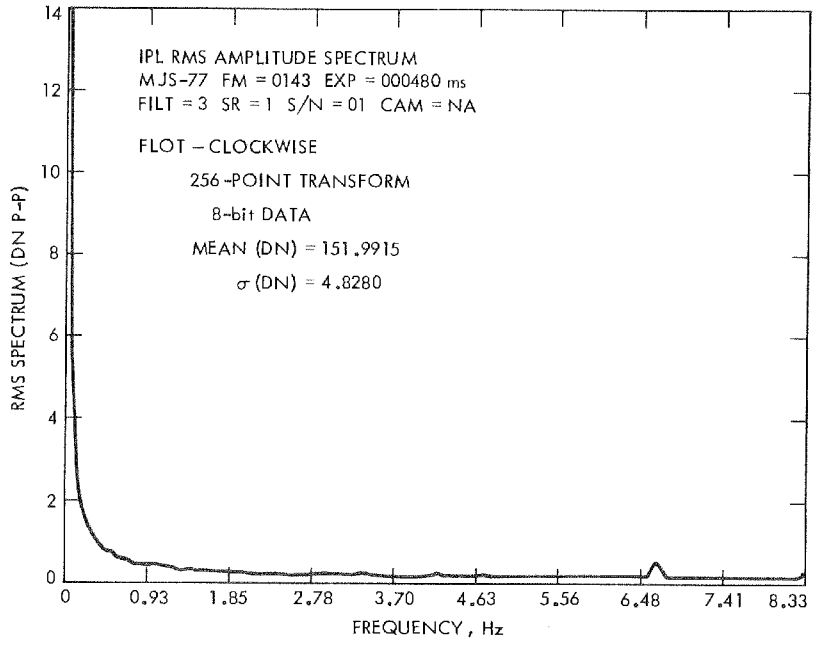

(a) ISS S/N 01

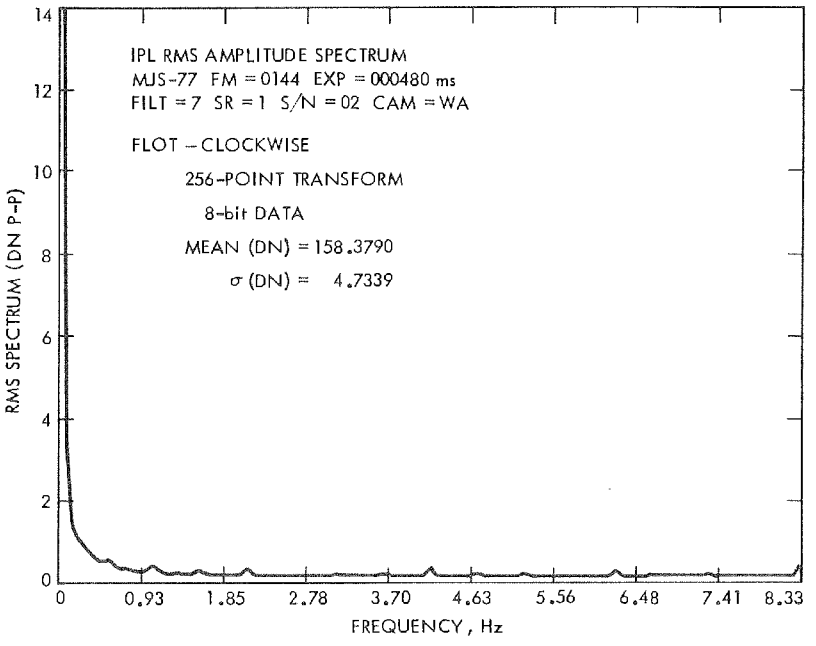

(b) ISS S/N 02

Figure 4-48. Plot of one-dimensional amplitude-spectrum line direction, ISS S/N 01 to 08

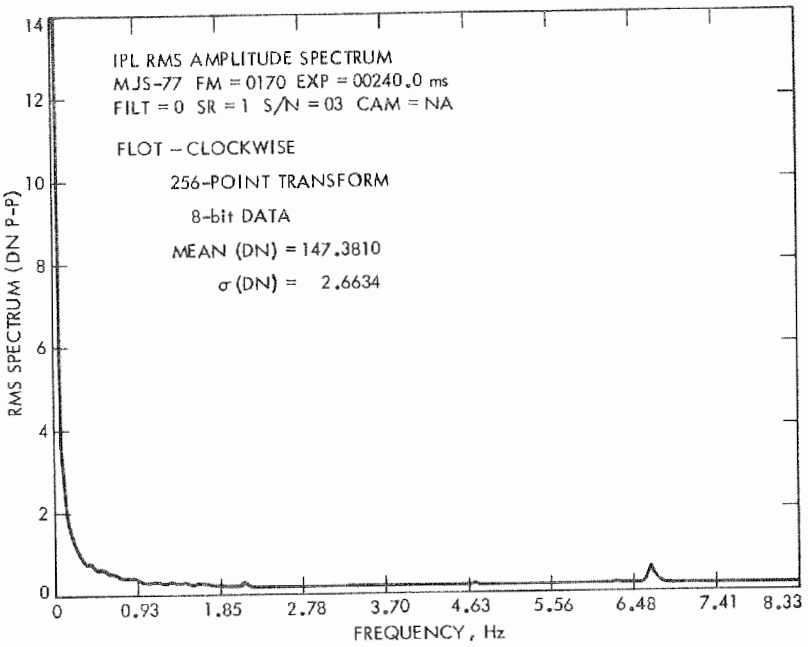

(c) ISS S/N 03

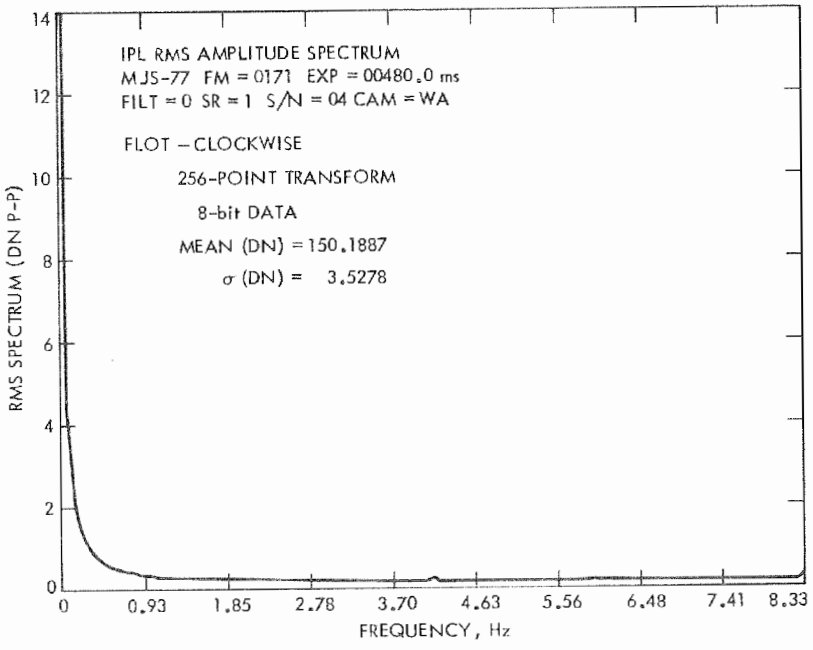

(d) ISS S/N 04

Figure 4-48 (contd)

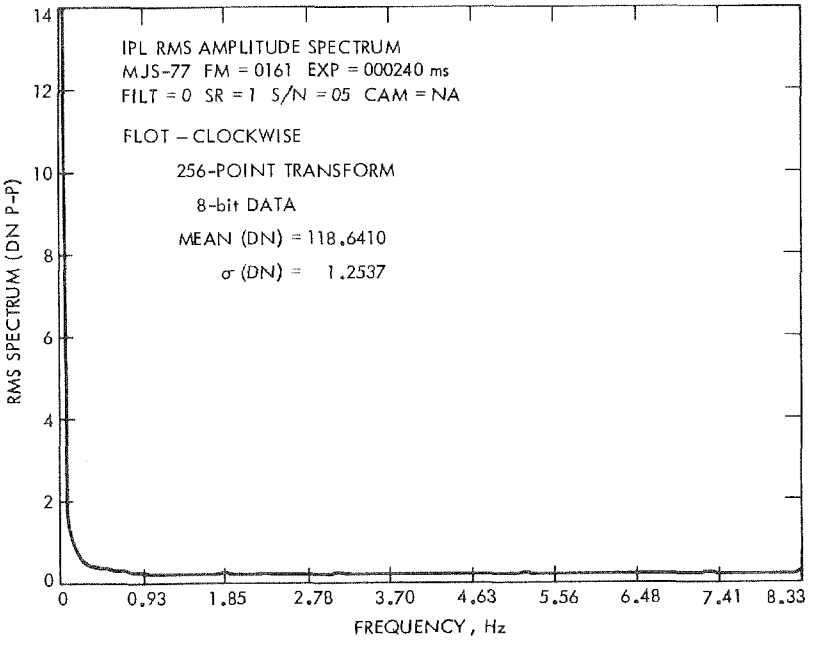

(e) ISS S/N 05

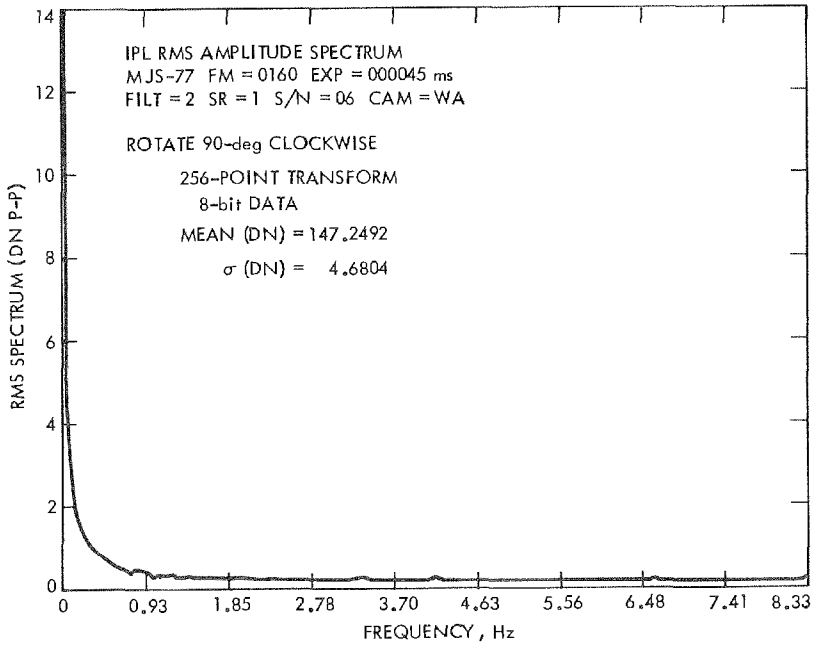

(f) ISS S/N 06

Figure 4-48 (contd)

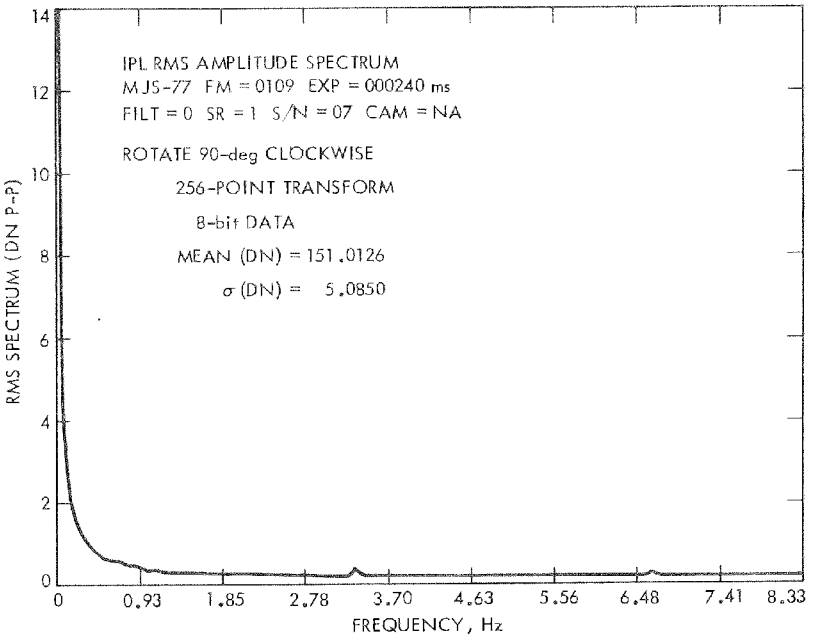

(g) ISS S/N 07

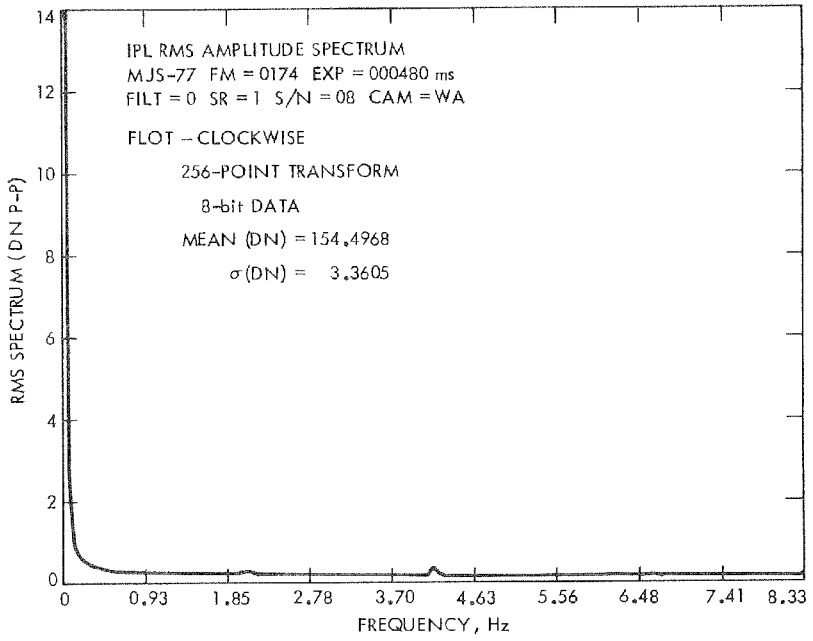

(h) ISS S/N 08

Figure 4-48 (contd)

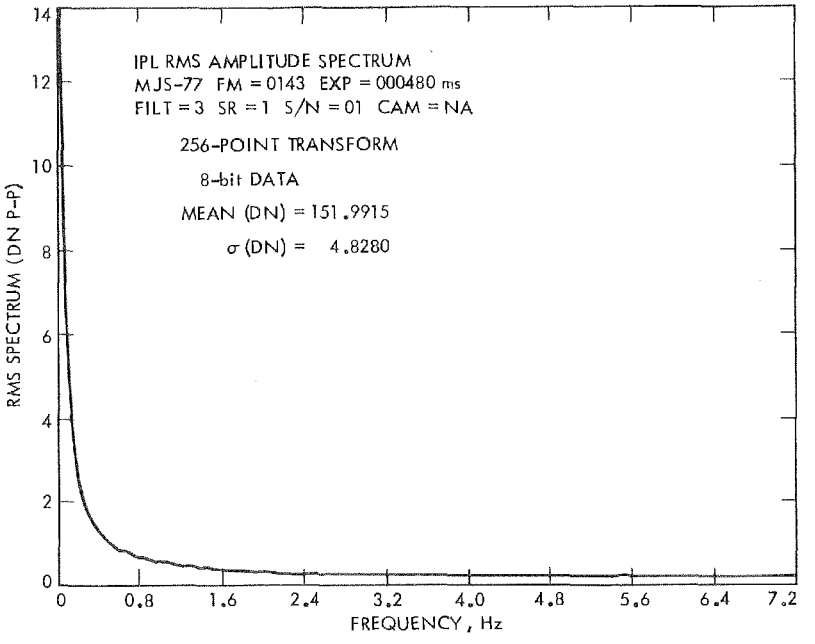

(a) ISS S/N 01

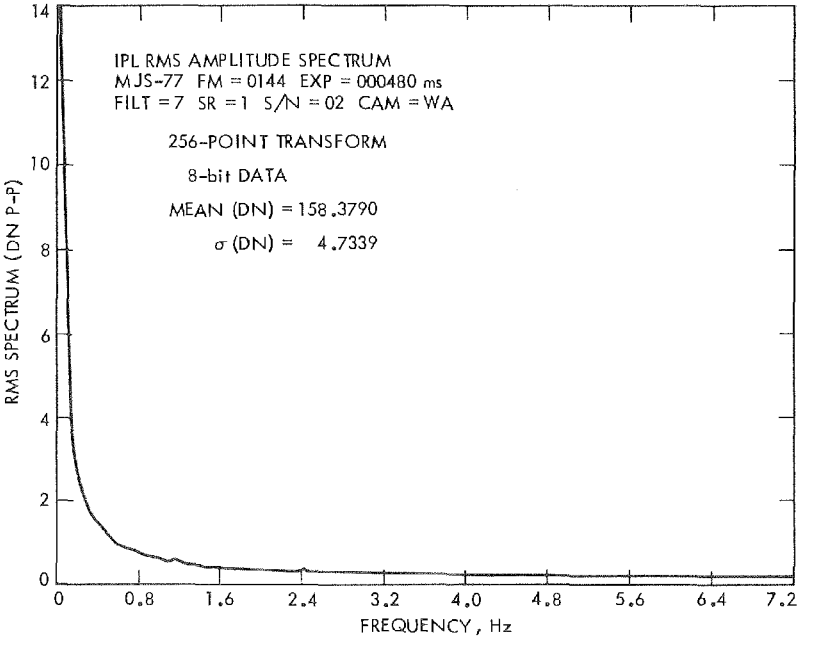

(b) ISS S/N 02

Figure 4-49. Plot of one-dimensional amplitude-spectrum sample direction, ISS S/N 01 to 08

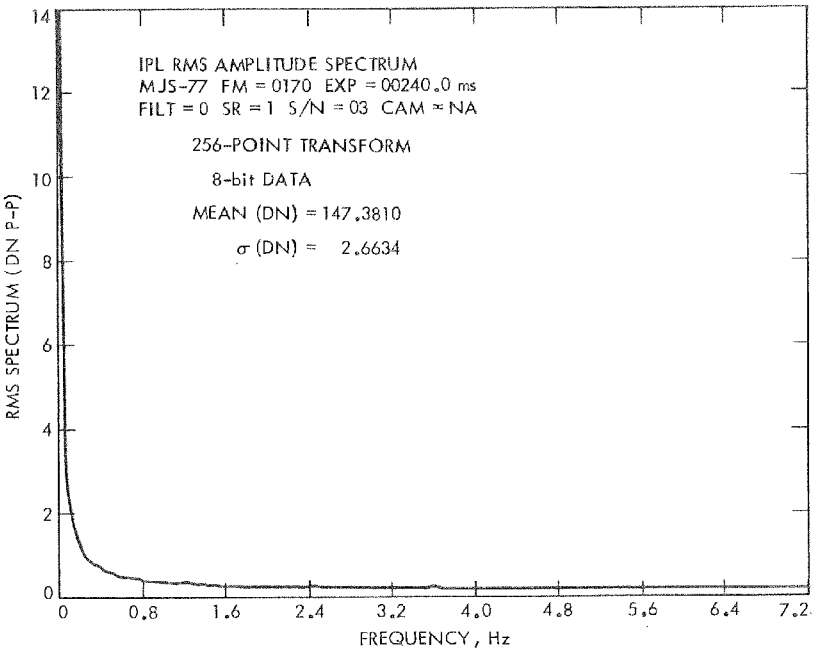

(c) ISS S/N 03

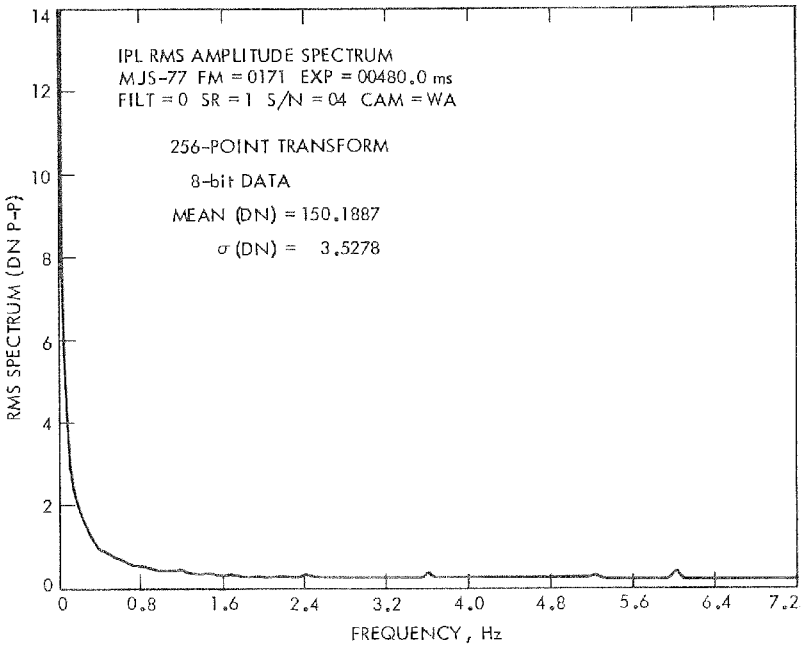

(d) ISS S/N 04

Figure 4-49 (contd)

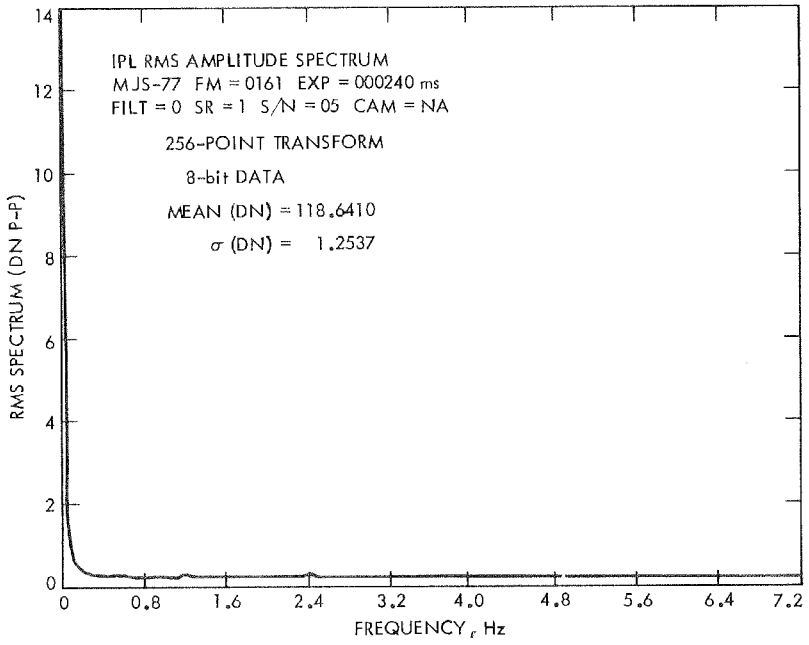

(e) ISS S/N 05

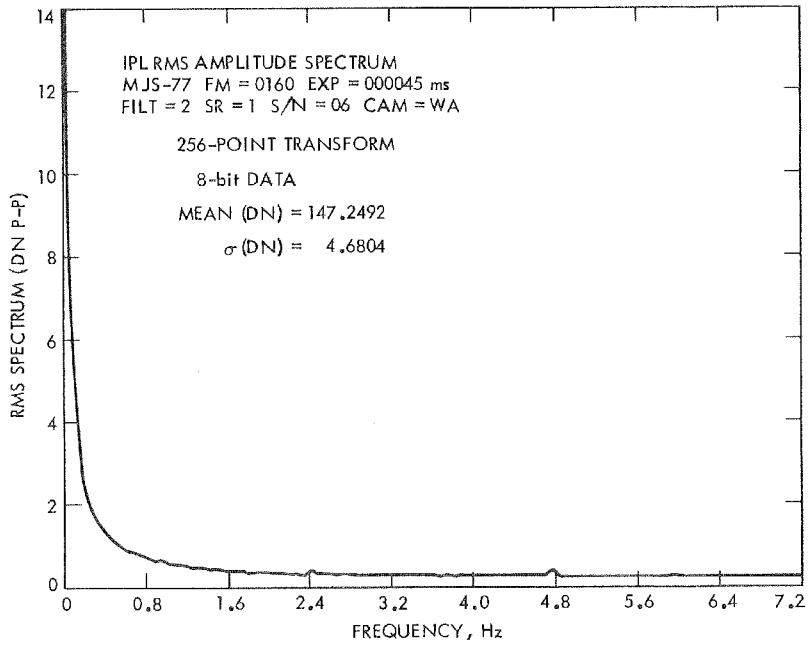

(f) ISS S/N 06

Figure 4-49 (contd)

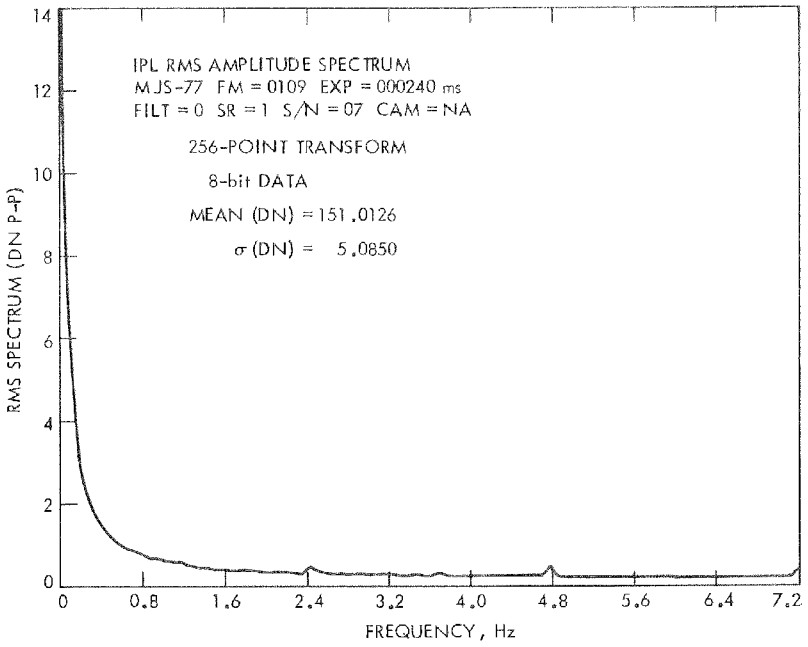

(g) ISS S/N 07

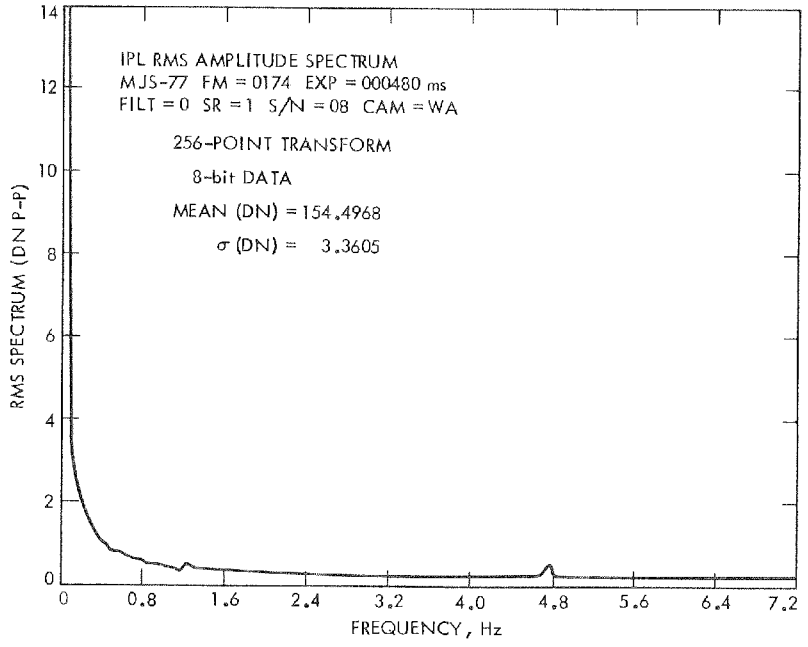

(h) ISS S/N 08

Figure 4-49 (contd)

(2) Environmental Calibration

(a) -15°C

(b) + 5°C

(c) +25°C

(3) Bench 2 Calibration

(4) In-flight analysis (S/N 04 only)

Average total random and periodic RMS (DN) noise signals (low gain) are summarized below for all calibrations:

ISS S/N	Total	Random	Periodic
01	0.6540	0.6481	0.0829
02	0.7889	0.7795	0.1153
03	0.6806	0.6624	0.1387
04	0.7216	0.6972	0.1631
05	0.8008	0.7906	0.1029
06	0.7421	0.7348	0.0895
07	0.7242	0.7065	0.1387
08	0.8877	0.8680	0.1540

Table 4-9 provides a complete breakdown by individual calibration type, mean DN of the images used, and by camera of all RMS noise-signals computed.

For each of the cameras, there are a number of periodic noise components, the frequencies of which can be identified; for example, there is a vertical component in all cameras at 2.4 kHz. However, since the peak-to-peak periodic noise amplitudes rarely exceed 0.5 DN, it was deemed unnecessary to isolate these individual components. An in-flight noise analysis was performed using the star-field images taken by the Voyager 2 wide-angle camera on day 240. The RMS results are tabulated below along with comparable bench data:

Noise	Star-Field Data	Bench 1 light transfer (high gain)
Total	2.241	2.602
Random	2.233	2.597
Periodic	0.1432	0.1277

Table 4-9. Noise characteristics of ISS cameras

ISS S/N	Test Title	Frame No.	Exposure, ms	Mean DN	Noise		
					Raw	Random	Periodic
01	TH/VAC	29	720	42.0	0.5158	0.5148	0.0348
	-20°C	31	1920	100.2	0.6526	0.6477	0.0837
		32	2880	140.6	0.7467	0.7330	0.1296
	BENCH 2	126	45	25.5	0.7025	0.7015	0.0451
		132	240	92.8	0.6915	0.6847	0.0964
		143	480	161.5	0.7488	0.7392	0.1176
	TH/VAC	470	180	37.9	0.5261	0.5249	0.0454
	-20°C	471	360	87.3	0.5831	0.5792	0.0709
		47	720	163.0	0.7433	0.7292	0.1336
	TH/VAC	1552	720	28.0	0.5958	0.5950	0.0498
	-29°C	1555	2880	118.7	0.6450	0.6389	0.0865
		1556	3840	153.3	0.6966	0.6892	0.1015
02	TH/VAC	2087	90	44.2	0.6153	0.6127	0.0632
	-20°C	2089	240	106.8	0.7669	0.7628	0.0829
		2090	360	150.1	0.8748	0.8683	0.1062
	TH/VAC	590	30	39.1	0.6141	0.6107	0.0710
	-20°C	592	90	121.9	0.9070	0.8919	0.1525
		593	120	156.6	1.0376	1.0160	0.2012
	TH/VAC	1632	60	38.4	0.6029	0.5985	0.0774
	-20°C	1634	180	109.5	0.8927	0.8754	0.1680
03	BENCH 1 (Low Gain)	164	60	57.5	0.6586	0.6493	0.1104
		166	120	92.0	0.7060	0.6829	0.1747
		170	240	155.9	0.8122	0.7602	0.2745
	BENCH 1 (High Gain)	742	5	91.9	2.0696	2.0660	0.1152
		746	22	105.3	2.0749	2.0647	0.1689
		750	60	132.7	2.1072	2.0946	0.1996
	TH/VAC	1545	60	43.8	0.6050	0.6011	0.0657
	-15°C	1546	120	80.5	0.6236	0.6141	0.0977
		1548	240	148.5	0.7411	0.7120	0.1787

Table 4-9 (contd)

ISS S/N	Test Title	Frame No.	Exposure, ms	Mean DN	Noise		
					Raw	Random	Periodic
03	TH/VAC	2987	60	44.5	0.5953	0.5903	0.0775
	+5°C	2988	120	80.3	0.6279	0.6189	0.0992
		2990	240	147.4	0.7556	0.7329	0.1697
04	BENCH 1	165	120	62.7	0.8839	0.8791	0.0823
	(Low Gain)	167	240	95.8	0.8361	0.8201	0.1482
		171	480	158.6	0.8432	0.8116	0.2050
	BENCH 1	743	5	101.2	2.6290	2.6257	0.1083
	(High Gain)	747	22	109.5	2.5885	2.5842	0.1218
		751	90	141.9	2.5889	2.5818	0.1530
	TH/VA	1878	22	42.3	0.5975	0.5908	0.0918
	-15°C	1881	60	100.1	0.6493	0.6155	0.2005
		1882	90	144.5	0.7209	0.6602	0.2814
	TH/VA	3263	22	43.4	0.6137	0.6094	0.0737
	+5°C	3266	60	99.4	0.6312	0.6114	0.1543
		3267	90	142.8	0.7188	0.6771	0.2305
05	BENCH 1	157	30	37.0	0.7314	0.7307	0.0432
	(Low Gain)	159	120	75.7	0.8171	0.8140	0.0727
		161	240	127.3	0.8644	0.8496	0.1425
	BENCH 1	163	5	116.4	2.6753	2.6715	0.1193
	(High Gain)	166	22	140.0	2.6657	2.6606	0.1489
		168	45	170.3	2.7179	2.7101	0.1697
	TH/VA	168	30	30.9	0.7202	0.7186	0.0488
	-15°C	170	120	79.9	0.7632	0.7554	0.1002
		172	240	144.3	0.9266	0.9083	0.1655
	TH/VA	3245	30	35.2	0.7004	0.6992	0.0484
	+5°C	3247	120	83.7	0.7572	0.7481	0.1071
		3249	240	147.4	0.9328	0.9029	0.2134
	TH/VA	1712	15	35.0	0.6758	0.6739	0.0475
	+25°C	1715	120	88.7	0.7898	0.7803	0.1044
		1717	240	149.1	0.9305	0.9067	0.1915

Table 4-9 (contd)

ISS S/N	Test Title	Frame No.	Exposure, ms	Mean DN	Noise		
					Raw	Random	Periodic
06	BENCH 1	166	5	41.0	0.8922	0.8918	0.0307
	(Low Gain)	170	12	66.0	0.8389	0.8367	0.0571
		178	45	150.5	0.7975	0.7824	0.1425
	BENCH 1	266	5	116.4	2.9851	2.9805	0.1199
	(High Gain)	270	12	129.8	3.0236	3.0221	0.0799
		276	30	160.2	3.0131	3.0090	0.1264
	TH/VA	2421	12	48.4	0.6424	0.6411	0.0458
	-15°C	2423	22	82.3	0.6520	0.6465	0.0825
		2425	45	152.1	0.7102	0.6938	0.1498
	TH/VA	3914	12	49.9	0.6406	0.6397	0.0462
	+5°C	3916	22	83.3	0.6541	0.6489	0.0853
		3918	45	152.8	0.7182	0.6994	0.1618
	TH/VA	6954	12	58.7	0.7369	0.7353	0.0543
	+25°C	6956	22	90.8	0.7263	0.7231	0.0705
		6958	45	156.9	0.7438	0.7333	0.1196
	BENCH 2	148	5	39.5	0.8248	0.8246	0.0267
		156	22	92.1	0.7722	0.7662	0.0937
		160	45	155.0	0.7821	0.7595	0.1762
07	BENCH 1	101	30	39.6	0.8002	0.7985	0.0594
	(Low Gain)	105	120	85.0	0.7435	0.7357	0.1059
		109	240	142.2	0.7740	0.7508	0.1775
	TH/VAL	2133	60	47.1	0.6135	0.6049	0.0943
	-15°C	2134	120	87.3	0.6691	0.6462	0.1643
		2136	240	159.3	0.7973	0.7317	0.3003
	TH/VAL	3654	60	46.8	0.6149	0.6125	0.0643
	+5°C	3655	120	86.0	0.6584	0.6479	0.1143
		3657	240	157.2	0.7542	0.7215	0.2109
	TH/VAL	6678	60	54.1	0.7037	0.7001	0.0660
	+25°C	6679	120	91.7	0.6965	0.6892	0.0985
		6681	240	159.3	0.7514	0.7330	0.1602

Table 4-9 (contd)

ISS S/N	Test Title	Frame No.	Exposure, ms	Mean DN	Noise		
					Raw	Random	Periodic
07	BENCH 2	101	30	37.4	0.7630	0.7602	0.0664
		105	120	90.7	0.7369	0.7188	0.1556
		109	240	155.1	0.7856	0.7464	0.2375
08	BENCH 1	162	15	50.1	1.2714	1.2692	0.0687
	(Low Gain)	170	240	104.6	1.0270	1.0175	0.1224
		174	480	157.6	0.9631	0.9330	0.2124
	TH/VAL	9360	15	44.9	0.7733	0.7667	0.0968
	-15°C	9362	30	78.7	0.7643	0.7464	0.1582
		9364	60	143.6	0.8121	0.7771	0.2137
	TH/VAL	918	15	47.3	0.7564	0.7541	0.0642
	+5°C	920	30	81.1	0.7561	0.7477	0.1083
		922	60	145.6	0.8092	0.7805	0.1824
	TH/VAL	6024	15	62.3	0.9116	0.9064	0.0860
	+30°C	6026	30	92.2	0.8836	0.8722	0.1349
		6028	60	149.4	0.8676	0.8414	0.1936
	BENCH 2	130	15	31.3	0.9174	0.9136	0.0852
		138	240	94.1	0.8868	0.8518	0.2384
		142	480	155.1	0.9149	0.8428	0.3442

In general, all RMS noise measures are consistent in character and magnitude from test to test and camera to camera; and they should have no negative impact on imaging plans.

The RMS measure for non-periodic noise is consistent with the planned random noise levels to be introduced to the ISS. The cameras are remarkably periodic-noise free. For example, in the Viking Orbiter cameras, VIS S/N 08 had an average RMS total noise level of 1.22, whereas the RMS total noise level for Voyager S/N 07 was only 0.724.

8. Witness Plate and Calibration Plaque Calibrations

The calibration plaque provides a direct way to perform radiometric in-flight calibrations along with the in-flight calibration lamps (see Section IV-A-5). The dimensions and technical properties of the plaque were described in Section II-D, and its spectral characteristics are shown in Figures 4-50, 4-51, and in Table 4-10. (The Lamp Standard ES-7402 was used for illumination of the calibration plaque.) The witness plate is a smaller segment of the complete plaque, which was used when the plaque itself was not available (see Section II-B). During

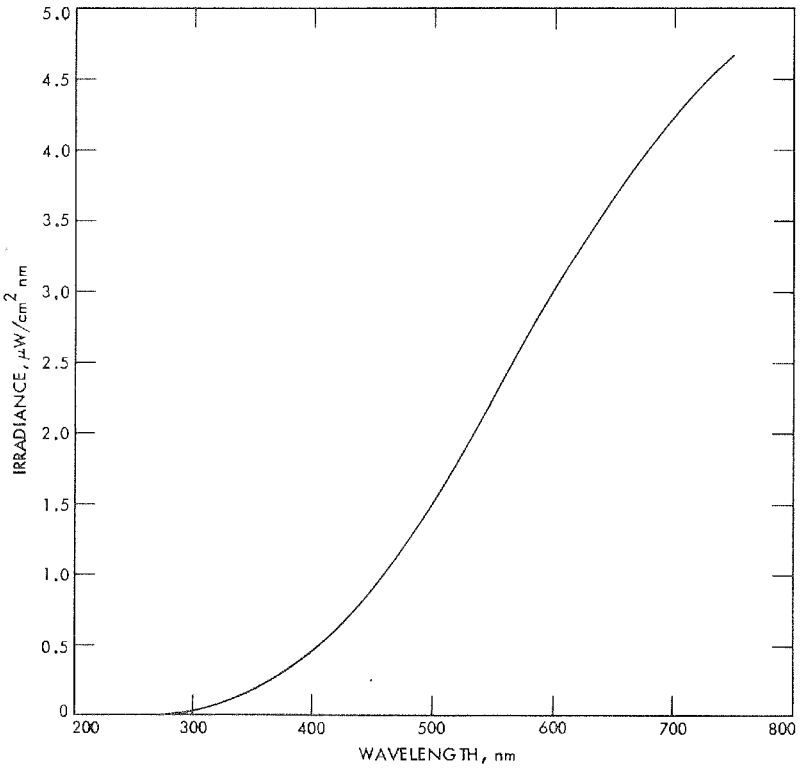

Figure 4-50. Spectral characteristics of the NBS 200-W quartz iodine lamp, standard ES 7402

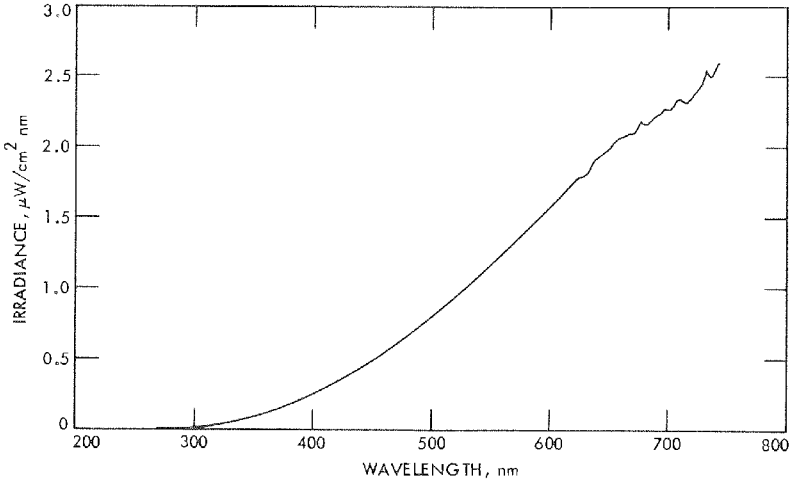

Figure 4-51. Spectral characteristics of the calibration plaque (illuminated with standard ES 7402)

Table 4-10. Standard ES-7402 and calibration plaque (spectral characteristics)

Wave, length, nm	Irradiance, $\mu W/cm^2$ nm		Wave-length, nm	Irradiance, $\mu W/cm^2$ nm		Wave-length, nm	Irradiance, $\mu W/cm^2$ nm	
	Standard ES-7042	Calibration Plaque		Standard ES-7042	Calibration Plaque		Standard ES-7402	Calibration Plaque
300	0.037	0.018	450	0.902	0.458	600	3.010	1.586
305	0.044	0.020	455	0.957	0.488	605	3.085	1.625
310	0.052	0.023	460	1.014	0.517	610	3.158	1.692
315	0.061	0.027	465	1.072	0.548	615	3.231	1.718
320	0.072	0.033	470	1.132	0.584	620	3.302	1.768
325	0.084	0.040	475	1.194	0.615	625	3.371	1.781
330	0.097	0.046	480	1.258	0.649	630	3.440	1.810
335	0.112	0.054	485	1.323	0.672	635	3.507	1.891
340	0.127	0.060	490	1.390	0.722	640	3.572	1.939
345	0.144	0.068	495	1.459	0.749	645	3.637	1.965
350	0.163	0.077	500	1.530	0.783	650	3.700	1.999
355	0.184	0.088	505	1.602	0.827	655	3.762	2.049
360	0.207	0.096	510	1.674	0.864	660	3.822	2.072
365	0.231	0.112	515	1.747	0.903	665	3.882	2.096
370	0.257	0.125	520	1.820	0.944	670	3.940	2.097
375	0.285	0.137	525	1.892	0.984	675	3.996	2.179
380	0.314	0.154	530	1.966	1.027	680	4.052	2.149
385	0.345	0.171	535	2.039	1.065	685	4.106	2.208
590	0.378	0.186	540	2.112	1.097	690	4.158	2.236
595	0.412	0.205	545	2.186	1.153	695	4.210	2.270
400	0.448	0.225	550	2.260	1.198	700	4.260	2.259
405	0.486	0.240	555	2.334	1.243	705	4.310	2.331
410	0.525	0.262	560	2.408	1.265	710	4.360	2.333
415	0.566	0.287	565	2.483	1.324	715	4.410	2.299
420	0.609	0.304	570	2.558	1.370	720	4.460	2.383
425	0.653	0.326	575	2.632	1.390	725	4.500	2.429
430	0.699	0.347	580	2.708	1.454	730	4.550	2.547
435	0.748	0.378	585	2.783	1.469	735	4.590	2.487
440	0.797	0.406	590	2.858	1.521	740	4.630	2.593
445	0.849	0.431	595	2.934	1.544	745	4.670	N/A

bench calibrations, both the plate and plaque were illuminated with the 30-cm light cannon No. 1, but, in flight, the Sun will serve as the light source.

Inasmuch as it is possible to generate only average response functions for the vidicon using the in-flight calibration lamps, as was explained in Section IV-A-5, complete decalibration files will have to be generated during the mission using the calibration plaque. The question of major importance to be answered is whether or not the plaque uniformly reflects sunlight. Unfortunately, this question could not be answered during ground-based calibrations because of limited accessibility of the calibration plaque and other technical, as well as organizational, problems; but the question will be answered in flight. The witness plate was used only for ISS S/N 03; and the calibration plaque, for ISS S/N 05 (the original S/N 05 before the cracked vidicon was replaced) and for S/N 08.

Some significant preliminary work was done, however, despite these limitations. Figure 4-52 shows the ISS S/N 03 light-transfer function using the witness plate and clear filter (see Figure 4-1 for explanation of subareas). The witness plate images were then compared with a flat-field image taken through the clear filter at the same average DN value. Dark current was subtracted from each picture and ratios determined. The results (Figure 4-53) show a slight global nonuniformity caused by either nonuniform illumination of the plate or by reflective inhomogeneity on the plate itself.

Since these results are most likely due to nonuniform illumination, as indicated in Figure 4-54, there is no reason to believe that the plate itself has nonuniform reflectance characteristics (see Section II-D).

Figure 4-55 shows the ISS S/N 08 four-point light-transfer curves using the calibration plaque for the clear, violet, and orange filters. The ratio of the ISS S/N 08 pictures of the calibration plaque with flat-field pictures taken through the same filters after dark currents were removed from each frame was determined. Figure 4-56 shows the relative lighting geometry of the plaque, showing clearly that the resulting ratio should display shading in the sample direction. Figures 4-57 to 4-59 show the predicted gradient for these three filters. There is also some shading in the line direction, which indicates that the plaque may not be uniformly reflecting after all, but the results are not conclusive.

In summary, it can be repeated that the results of the limited calibration activities on the calibration plaque and witness plate are useful but inconclusive. The plaque is needed, however, if the IPL in-flight decalibration files for shading corrections are to be generated.

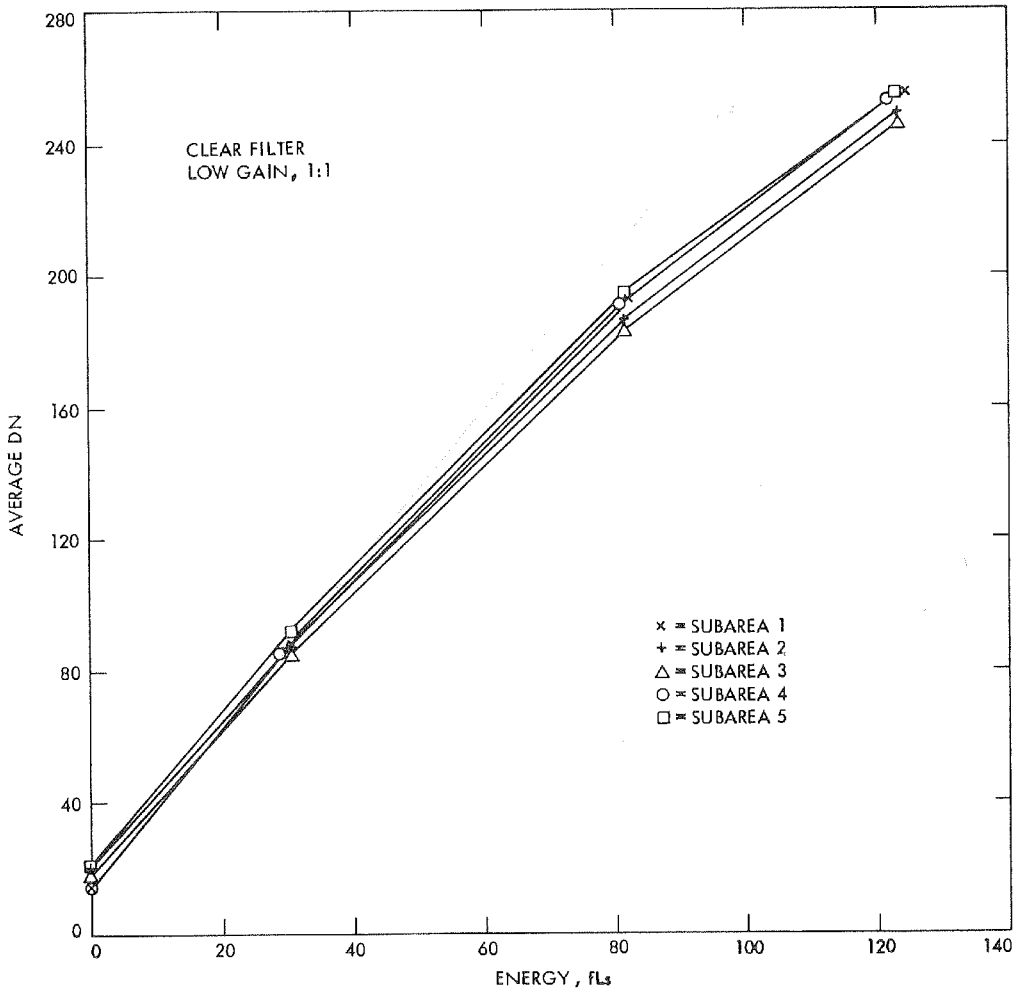

Figure 4-52. Light-transfer function using the witness plate (clear filter), ISS S/N 03

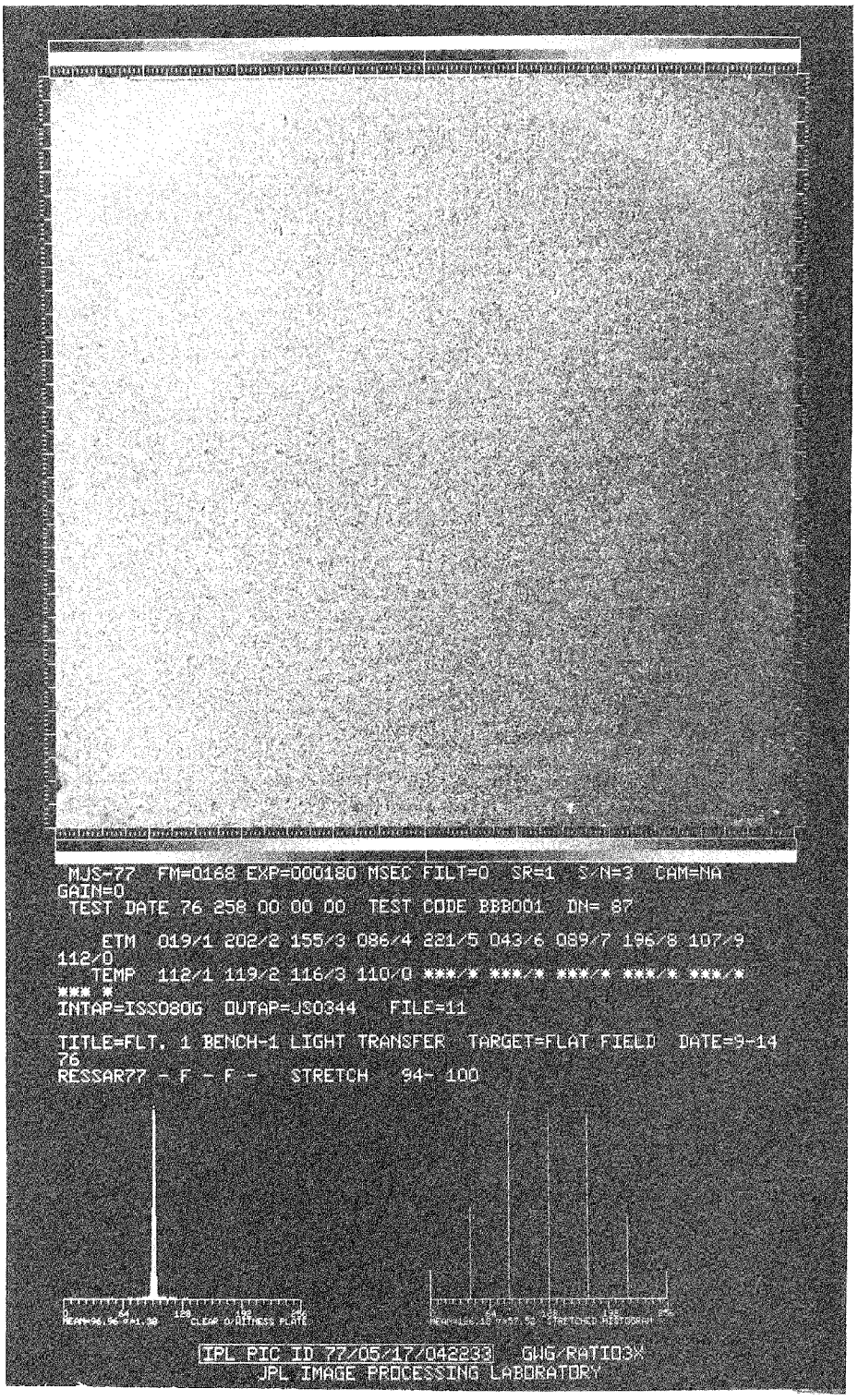

Figure 4-53. Ratio of witness plate image (clear filter), ISS S/N 03

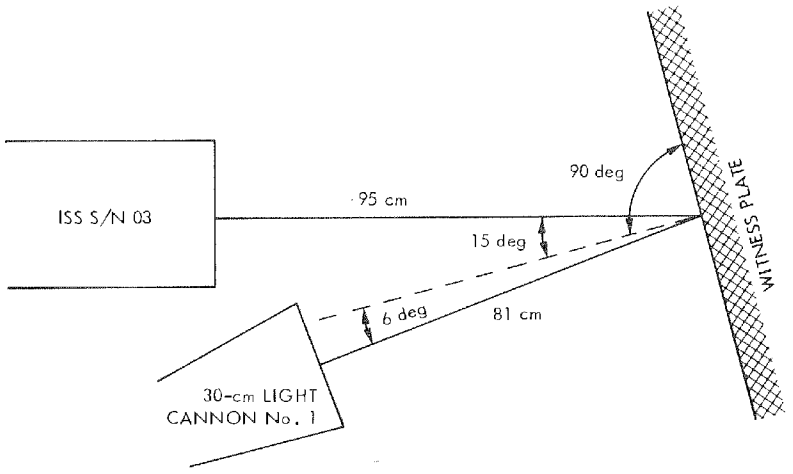

Figure 4-54. Lighting geometry of the witness plate

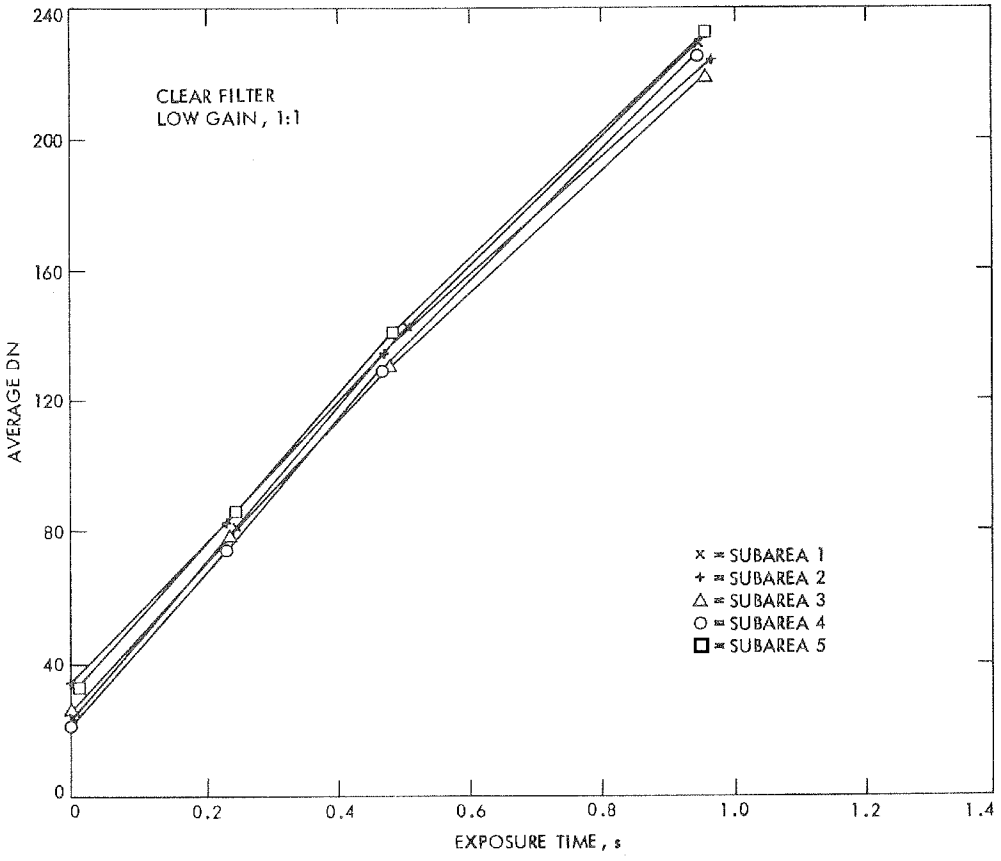

(a) Clear filter

Figure 4-55. Light-transfer functions using the calibration plaque (clear, violet, and orange filters), ISS S/N 08

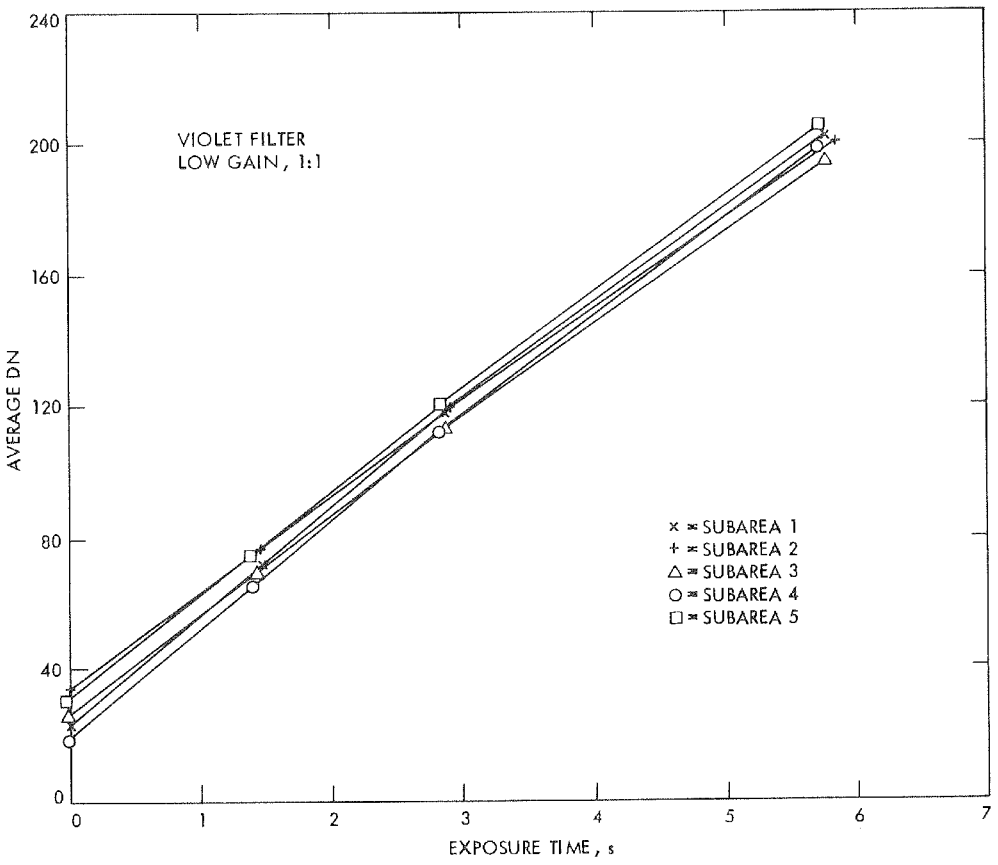

(b) Violet filter

Figure 4-55 (contd)

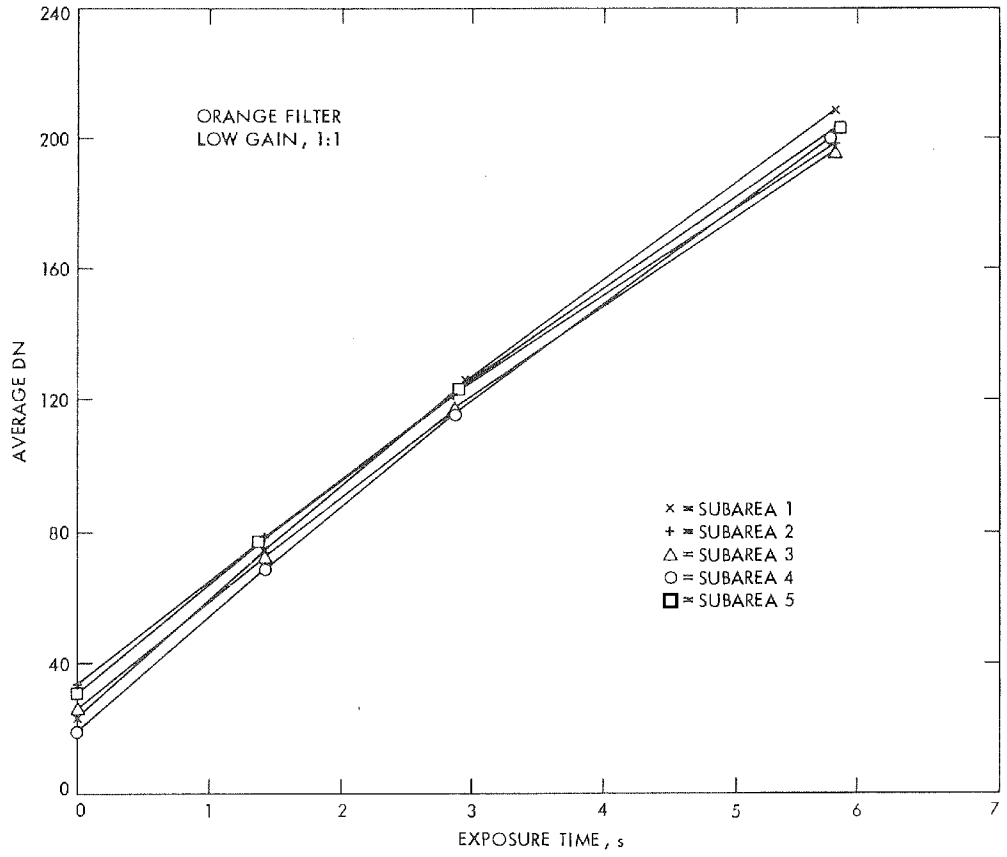

(c) Orange filter

Figure 4-55 (contd)

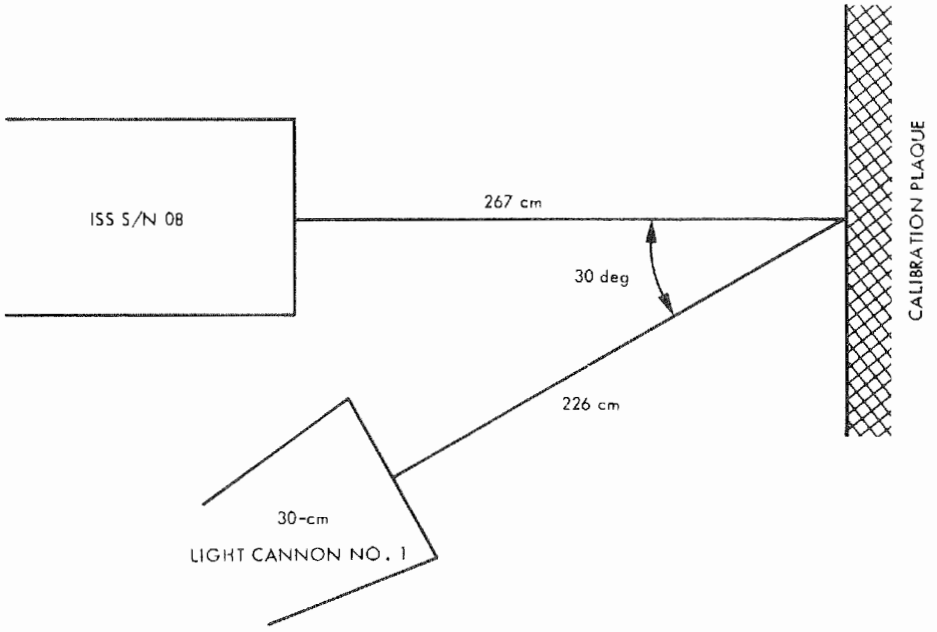

Figure 4-56. Lighting geometry of the calibration plaque

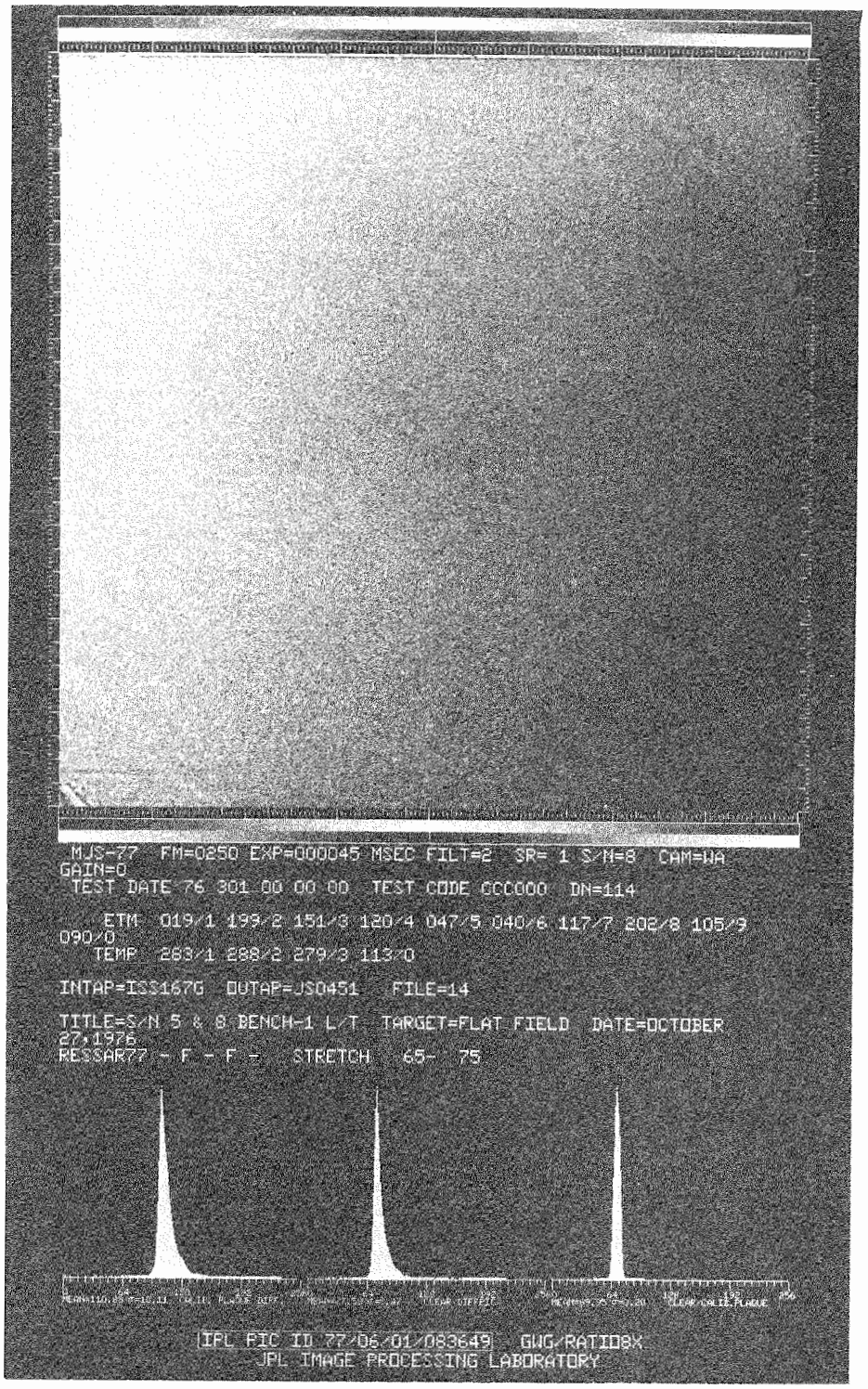

Figure 4-57. Ratio of calibration plaque image (clear filter), ISS S/N 08

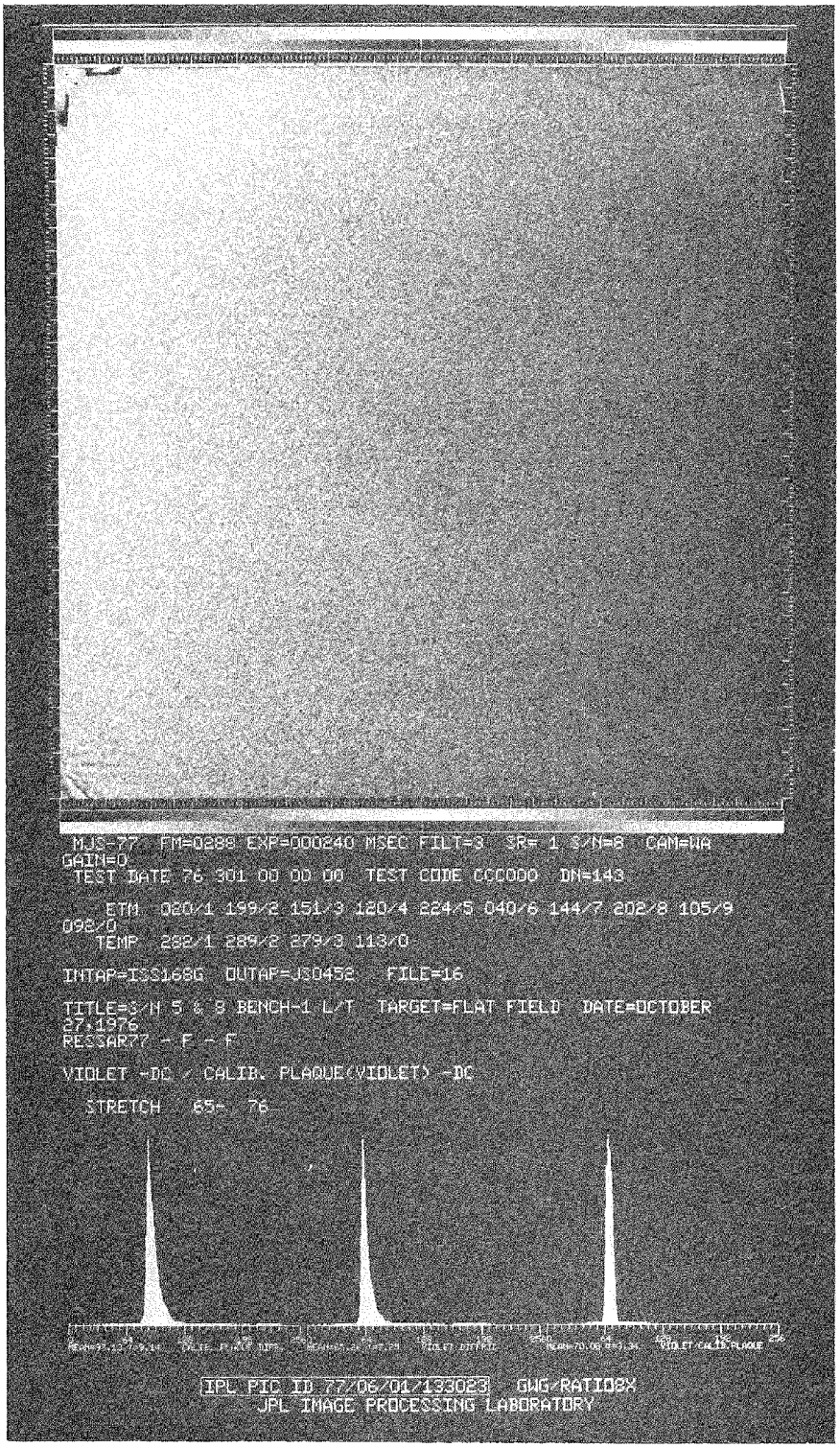

Figure 4-58. Ratio of calibration plaque image (violet filter), ISS S/N 08

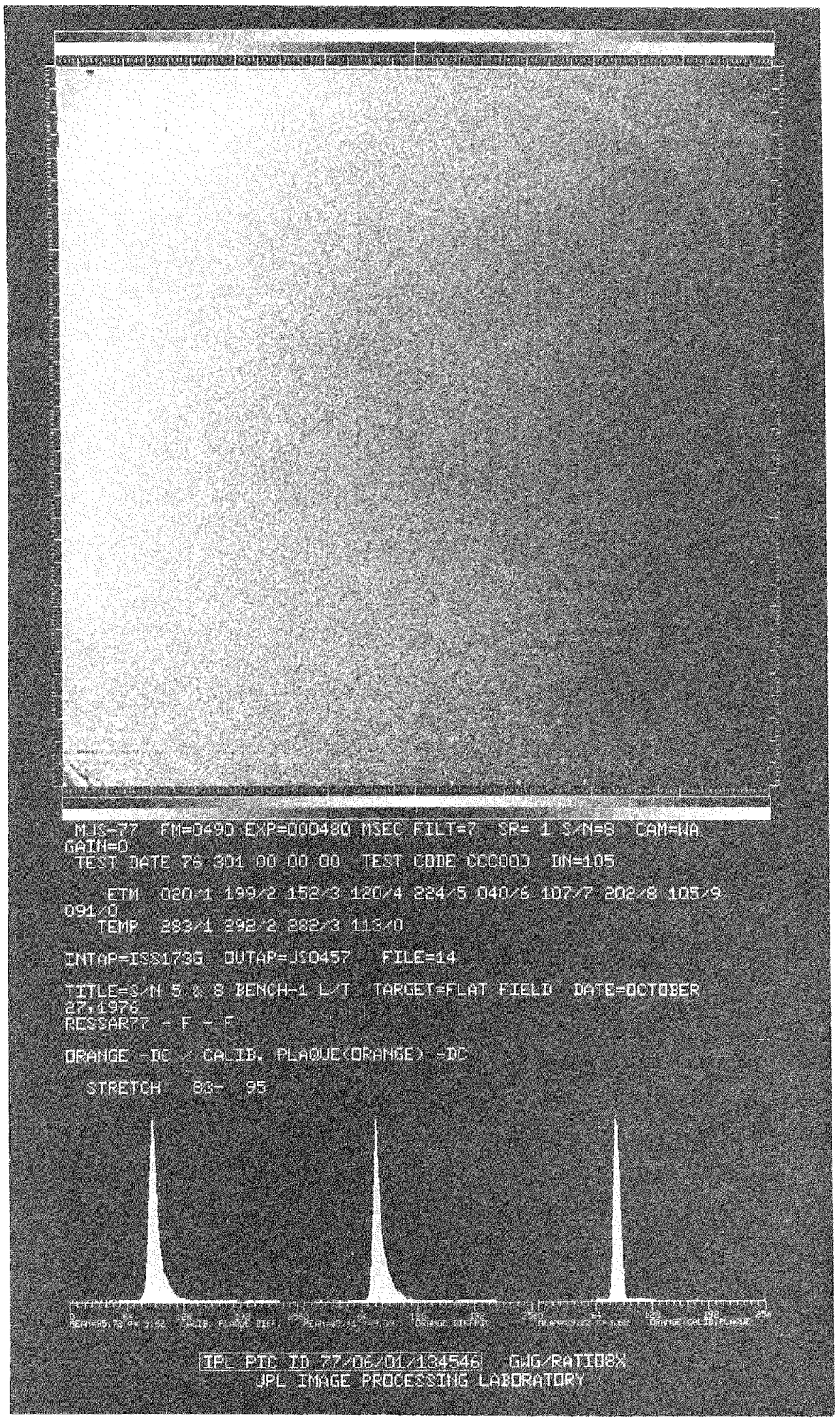

Figure 4-59. Ratio of calibration plaque image (orange filter), ISS S/N 08

B. FOCAL LENGTH

1. Geometry

Knowledge of the correct focal length establishes the on-axis scale factor of the object-to-image geometry and also is the determining factor for geometric distortion measurements.

The geometric quality of a photographic system is determined by the mutual relations of these four axes (Figure 4-60):

(1) Optical axis: The line connecting the front and rear nodal point.

(2) Vidicon normal: The perpendicular from the real nodal point to the vidicon faceplate.

(3) Boresight axis: The line connecting the rear nodal point and the center reseau mark.

(4) Mechanical axis: The axis of the camera mounting feet.

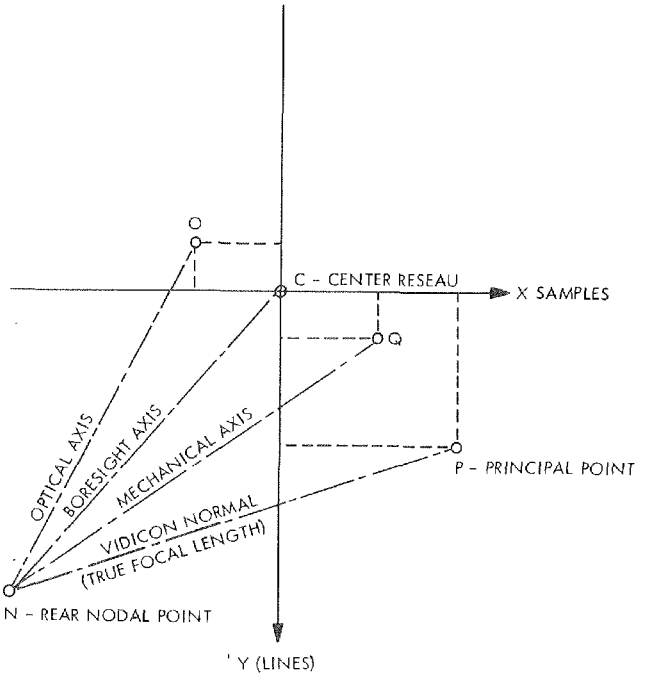

Figure 4-60. Geometry of a photographic system

In an ideal system, all four axes would be identical and perpendicular to the vidicon faceplate, but this is technically impossible to achieve. Therefore, the focal length is usually measured along the vidicon normal, and the coordinate difference between point C (center reseau mark) and point P (principal point) is defined as principal point eccentricity, which may play a role in camera pointing and in photogrammetric evaluations.

Determination of the principal point eccentricity is a very difficult, time consuming, and expensive operation. Thus, for the Viking and the MVM 1973 missions it was ignored, and the cameras were arbitrarily treated as an optomechanically ideal system in this respect. However, for the Voyager project, a new complex analytical method based on the principle of collinearity was designed and developed. This method yields not only the focal length, but the principal point eccentricity and the optical distortion of the system as well. Consequently, the ISS camera true focal length was measured along the vidicon normal as the distance between the rear nodal point and the principal point.

The determination of the focal length of each camera was based on direct theodolite observations of the vidicon reseau grid through the optics. The measured horizontal and vertical angles define space vectors that can be combined with the known reseau mark locations on the vidicon faceplate (see Section II-D-2). The focal length and other pertinent parameters can then be calculated as a result of complicated three-dimensional rotations and translations utilizing least squares adjustment.

The reseau angles were measured with a Wild T-3 theodolite, and each focal length result is based on two independent sets of measurements containing at least 90 reseaus spread evenly across the vidicon faceplate. The results obtained are given below. The first number indicates the focal length, and the two numbers in parentheses refer to principal point eccentricity, XPP and YPP:

ISS S/N 01 = 1499.12 mm (-0.080, -0.072)

ISS S/N 02 = 201.568 mm (-0.240, +0.234)

ISS S/N 03 = 1499.95 mm (-0.410, +0.083)

ISS S/N 04 = 201.640 mm (-0.064, + 0.134)

ISS S/N 05 = 1501.68 mm (-0.175, -0.057)

ISS S/N 06 = 201.498 mm (-0.088, + 0.028)

ISS S/N 07 = 1499.96 mm (-0.161, +0.048)

ISS S/N 08 = 201.326 mm (-0.030, +0.020)

The coordinate system is the same as described in Figure 3-39 (Section III-D-2). The average standard error of unit weight is ±0.23 mm

for the narrow-angle camera and ±0.04 mm for the wide-angle camera, which is within the accuracy limits defined in Reference 2-1 (±0.3 mm and ±0.04 mm). The optical distortion is insignificant for all practical purposes (it does not exceed 2.5 μm for the narrow-angle cameras and 4.0 μm for the wide-angle cameras in the farthest corner of the frame). The average standard error of the principal point eccentricity is ±0.051 mm for the narrow-angle cameras (limit ±0.050 mm) and ±0.023 mm for the wide-angle cameras (limit ±0.010 mm). As can be seen, the wide-angle-camera accuracy limit has been exceeded, but the determination of this parameter has turned out to be very difficult. However, the practical impact of this error is negligible.

The camera field of view is defined by the traditional nine basic vidicon format points. The corner format points 1, 3, 7, 9 are identical with reseau marks 2, 13, 190, 201, and the center point 5 is the same as center reseau mark 102 (boresight azis). Point 5′ denotes the principal point (vidicon normal ≡ optical axis). Format points 2, 4, 6, 8 lie between the corner points either on the X- or Y-axis (Figure 4-61). The results obtained are summarized in Table 4-11. The angles are calculated in the standard reseau grid coordinate system as the cross-cone component (X-axis direction), the cone component (Y-axis direction), and the diagonal space angles. Thus, the camera field of view is a function of the focal length and the reseau-mark coordinates. This information, together with the optomechanical alignment parameters (see Sections IV-B-3 and V-B), is essential for determination of the correct picture footprint geometry for the POINTER program, as well as for navigational purposes.

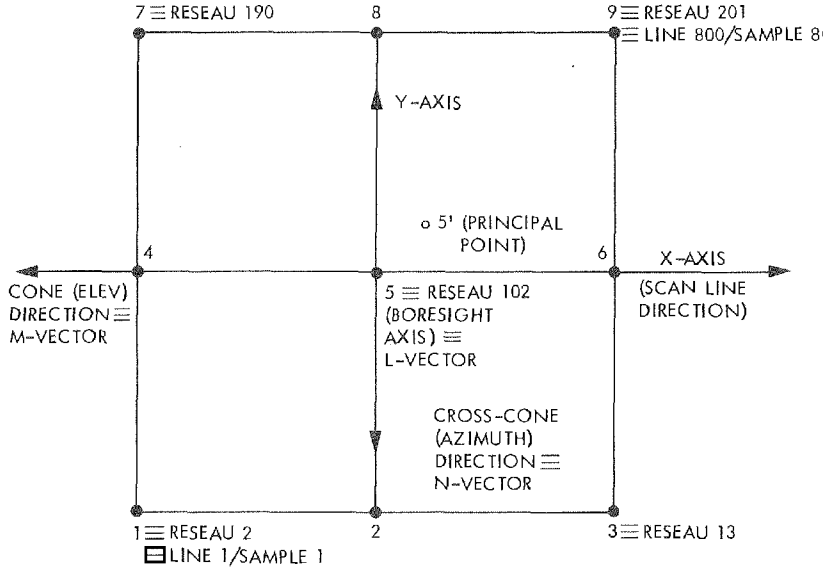

Figure 4-61. Basic nine vidicon-format points (looking into the camera)

Table 4-11. Field of view, ISS S/N 03 to 08

ISS S/N 03 (vidicon S/N 115 9880)				ISS S/N 04 (vidicon S/N 305 2719)			
Format Point	Half-angle field of view, deg			Format Point	Half-angle field of view, deg		
	Cone	Cross-cone	Diagonal		Cone	Cross-cone	Diagonal
1	+0.2074	+0.2075	0.2933	1	+1.5426	+1.5420	2.1810
2	0.0000	+0.2075	0.2075	2	0.0000	+1.5424	1.5424
3	-0.2075	+0.2075	0.2934	3	-1.5428	+1.5417	2.1810
4	+0.2074	0.0000	0.2074	4	+1.5428	0.0000	1.5428
5[a]	0.0000	0.0000	0.0000	5[a]	0.0000	0.0000	0.0000
5',[b]	+0.0157	-0.0032	0.0160	5',[b]	+0.0182	-0.0381	0.0422
6	-0.2075	0.0000	0.2075	6	-1.5428	0.0000	1.5423
7	+0.2074	-0.2074	0.2933	7	+1.5431	-1.5417	2.1812
8	0.0000	-0.2074	0.2074	8	0.0000	-1.5423	1.5423
9	-0.2075	-0.2074	0.2934	9	-1.5428	-1.5417	2.1810

ISS S/N 05 (vidicon S/N 225 1901)				ISS S/N 06 (vidicon S/N 115 9903)			
Format Point	Half-angle field of view, deg			Format Point	Half-angle field of view, deg		
	Cone	Cross-cone	Diagonal		Cone	Cross-cone	Diagonal
1	+0.2072	+0.2071	0.2929	1	+1.5434	+1.5428	2.1821
2	0.0000	+0.2071	0.2071	2	0.0000	+1.5434	1.5434
3	-0.2072	+0.2071	0.2929	3	-1.5439	+1.5428	2.1825
4	+0.2072	0.0000	0.2072	4	+1.5434	0.0000	1.5434
5[a]	0.0000	0.0000	0.0000	5[a]	0.0000	0.0000	0.0000
5',[b]	+0.0067	+0.0022	0.0070	5',[b]	+0.0250	-0.0080	0.0263
6	-0.2072	0.0000	0.2072	6	-1.5439	0.0000	1.5439
7	+0.2072	-0.2073	0.2930	7	+1.5434	-1.5428	2.1821
8	0.0000	-0.2073	0.2073	8	0.0000	-1.5434	1.5434
9	-0.2072	-0.2073	0.2930	9	-1.5439	-1.5428	2.1825

[a]Boresight axis.

[b]Principal points.

Table 4-11 (contd)

ISS S/N 07 (vidicon S/N 165 1402)				ISS S/N 08 (vidicon S/N 165 1407)			
Format Point	Half-angle field of view, deg			Format Point	Half-angle field of view, deg		
	Cone	Cross-cone	Diagonal		Cone	Cross-cone	Diagonal
1	+0.2074	+0.2073	0.2933	1	+1.5447	+1.5438	2.1838
2	0.0000	+0.2073	0.2073	2	0.0000	+1.5444	1.5444
3	-0.2075	+0.2073	0.2933	3	-1.5452	+1.5438	2.1842
4	+0.2074	0.0000	0.2074	4	+1.5447	0.0000	1.5447
5[a]	0.0000	0.0000	0.0000	5[a]	0.0000	0.0000	0.0000
5',[b]	+0.0061	-0.0018	0.0064	5',[b]	+0.0085	-0.0057	0.0103
6	-0.2075	0.0000	0.2075	6	-1.5452	0.0000	1.5452
7	+0.2074	-0.2074	0.2933	7	+1.5447	-1.5441	2.1840
8	0.0000	-0.2074	0.2074	8	0.0000	-1.5447	1.5447
9	-0.2075	-0.2074	0.2934	9	-1.5452	-1.5441	2.1844

[a]Boresight axis.
[b]Principal points.

The corresponding narrow-angle camera field-of-view accuracy is ±0.000009 rad and, for the wide-angle camera, ±0.000013 rad (required limits are ±0.000025 and ±0.00015 rad).

2. Geometric Distortion [14]

The purpose of distortion calibration was to characterize the combined geometric distortion introduced by ISS optics and electronics as a function of exposure level.

The optical distortion can be ignored for all practical purposes, as explained in Section IV-B-1, which means that geometric distortions of all ISS cameras can be ascribed entirely to their electronic influences.

[14]This section is based on information provided by G. Yagi in "Geometric Distortion Measurement for Voyager Vidicon S/N 01-08," 324-IPL/SIPG-79-199, September 23, 1977.

The procedure utilized was that developed for the Mariner 9 television subsystem (TVS) calibrations (see Reference 4-3). The procedure follows the basic strategy of comparing the geometric characteristics of a picture of a grid target recorded by an ISS camera with the known characteristics of the target. The geometric characteristics of the target were determined by using the JPL Fairchild collimator and a theodolite to carefully measure the location of each grid intersection (see Section II-D). The measurements, recorded in millimeters, are scaled to line and sample coordinates. These are the locations that would result, if the grid target were imaged through a geometrically perfect ISS imaging system. The values are referred to as "object space" coordinates.

The grid intersection locations in the picture of the grid target are determined by a series of hand and digital image processing calculations. These values will be referred to as the "raw image" coordinates. Figure 4-62 shows a typical grid-target image recorded with an ISS camera. Each grid intersection has been enclosed by a square, indicating the measured location of the intersection.

The raw image coordinates are compared with the theodolite measurements by applying a linear transformation which minimizes the RMS residual error between the two sets of data. Two RMS values are computed, the first by allowing the transformation to adjust for differences in scale, translation, and rotation between the two sets of data (four degrees of freedom); and the second, by allowing the transformation to correct also for differences in skew and aspect ratio (unconstrained case).

Let (x_i, y_i), $i = 1,2....,N$ be the raw image coordinates, and $(u_i, v_i,)$ be the corresponding theodolite measurements. In the unconstrained case, the RMS residual is defined as follows:

$$R = \sum_{i=i}^{N} \left[(ax_i + by_i + e - u_i)^2 + (cx_i + dy_i + f - v_i)^2 \right]^{1/2}$$

where the values of a, b, c, d, e, and f are chosen to minimize R. If only four degrees of freedom are permitted, the transformation is confined to a magnification, rotation, and offset by requiring that $a = d$ and $b = -c$.

Adjusting for rotation and offset errors reduces variables introduced by the arbitrary orientation of the grid target relative to the camera focal plane. Adjusting for scale eliminates errors in camera and collimator focal length measurements. The RMS value computed by allowing these four degrees of freedom is a measure of the total geometric distortion of the camera system, excluding measurement errors.

In the unconstrained case, the remaining two degrees of freedom, skew, and aspect ratio are also involved. The resulting RMS is a measure of the nonlinear component of the total geometric distortion.

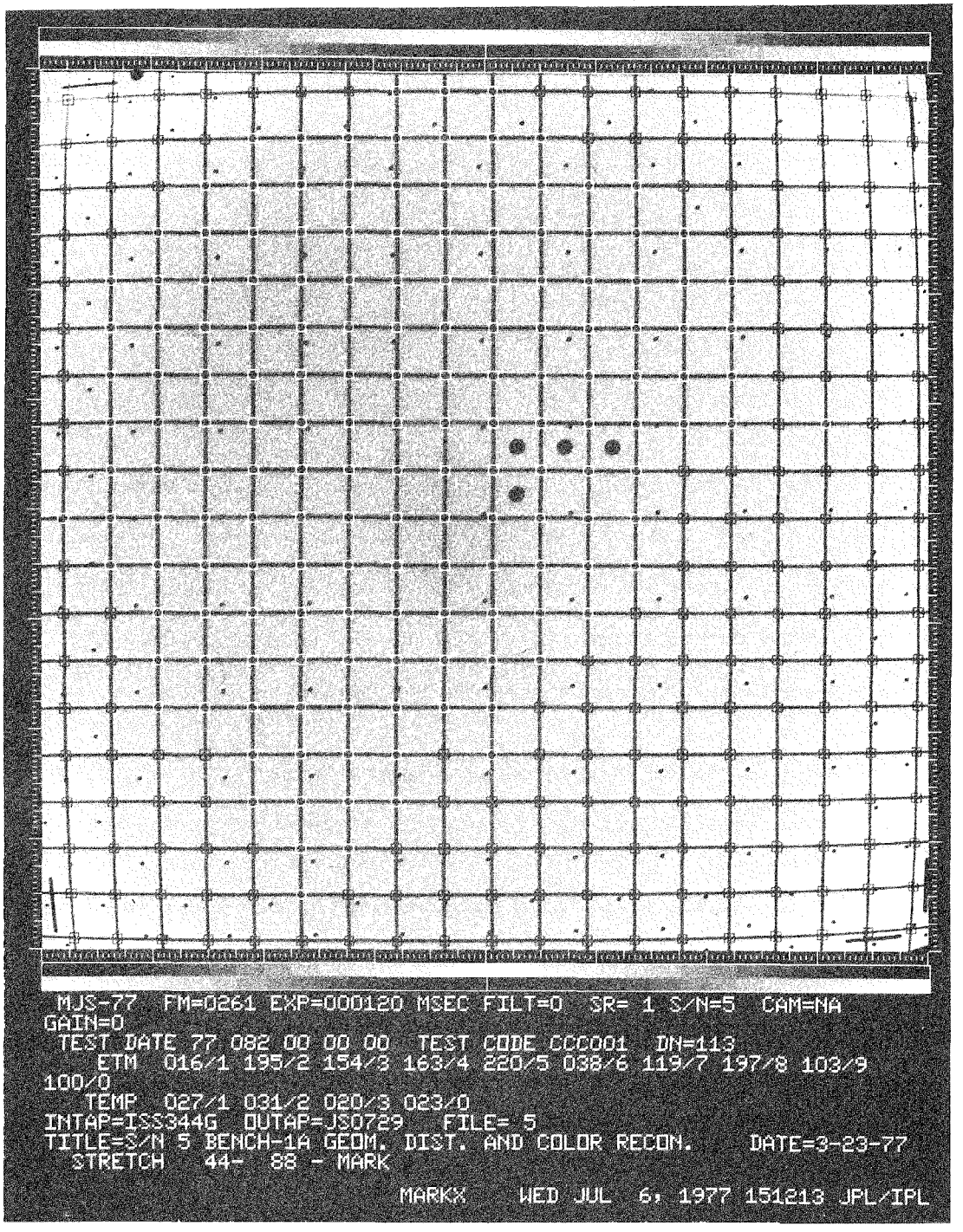

Figure 4-62. Geometric grid-target image with intersections marked

Table 4-12 lists the RMS residual errors representing the total and nonlinear geometric distortions for each of the ISS cameras. Also included is a measure of the maximum pixel distortion encountered in each frame. Measurements for a set of three frames from each camera are included, and they are an indication of the repeatability of the experiments.

Figure 4-63 is a synthesized picture showing the residual errors at each grid intersection when four degrees of freedom are applied. The "object space" coordinates are displayed as bright dots. Displacements have been magnified 2.5 x for better visibility. Figure 4-64 is a corresponding picture for the unconstrained case. A complete set of pictures for each camera is on file at IPL.

The Voyager cameras exhibit typical barrel distortions. The distortion increases radially from some internal point close to the center reseau mark and is greatest in the corners of the frame. The extent of this barrel distortion is more pronounced than that observed in the Viking Orbiter vidicons, as evidenced by the larger distortions measured in the corners. The average maximum displacement for the four flight Voyager cameras (S/Ns 04, 05, 06, and 07) is 13.9 pixels, as opposed to 8.2 pixels for Viking Orbiter. However, the Viking Orbiter cameras displayed a characteristic vertical crossover distortion near the left margin of the images, apparently because of some systematic beam sweep nonlinearity. As a result, the total geometric distortions are comparable for both systems. The average RMS is 2.83 pixels for Voyager versus 2.76 pixels for Viking Orbiter.

3. Optical/Mechanical Alignment and Vidicon Twist

An ideal optical/mechanical alignment of ISS cameras would be achieved, if:

(a) The boresight axis (see Figure 4-60 in Section IV-B-1) were parallel with the camera mounting feet and the spacecraft scan platform plane.

(b) The vidicon reseau grid were perpendicular to the spacecraft scan platform plane.

It is obvious that such a system is impossible to build. Thus, for Voyager applications, the following limits of angular deviations were set:

(a) Narrow-angle camera boresight axis ±1.8 min/arc for both the cross-cone and cone deviations.

(b) Wide-angle camera boresight axis ±8.0 min/arc for both the cross-cone and cone deviations.

Table 4-12. ISS vidicon geometric distortions

ISS S/N	Frame No.	Exposure time, ms	Total distortion, pixels		Non-linear distortion, pixels	
			RMS residual error	Maximum distortion	RMS residual error	Maximum distortion
	31	480	4.49	16.2	3.26	13.4
01	33	240	4.58	16.7	3.36	13.4
	35	90	4.38	15.0	3.06	12.7
	32	120	2.80	11.1	2.13	11.1
02	34	60	2.84	10.9	2.19	11.9
	36	30	2.85	11.9	2.17	10.5
	251	240	2.34	11.9	1.81	10.1
03	297	120	2.37	11.3	1.83	9.6
	341	360	2.31	11.0	1.78	9.2
	252	30	3.43	17.1	1.87	12.7
04	298	15	3.43	16.8	1.86	12.4
	334	45	3.39	16.6	1.84	12.3
	260	240	2.41	12.1	1.88	10.3
05	261	120	2.67	14.9	2.22	13.1
	262	360	2.40	12.0	1.85	10.1
	1878	30	2.58	12.5	2.21	13.1
06	1880	15	2.60	11.8	2.21	13.1
	1882	45	2.26	10.7	1.90	11.4
	1877	240	2.88	14.0	2.32	11.3
07	1879	120	2.59	12.2	2.04	9.6
	1881	360	2.88	13.8	2.30	11.1
	446	30	2.26	11.5	2.15	12.6
08	448	15	2.28	11.9	2.17	13.0
	450	45	2.29	14.2	2.18	15.2

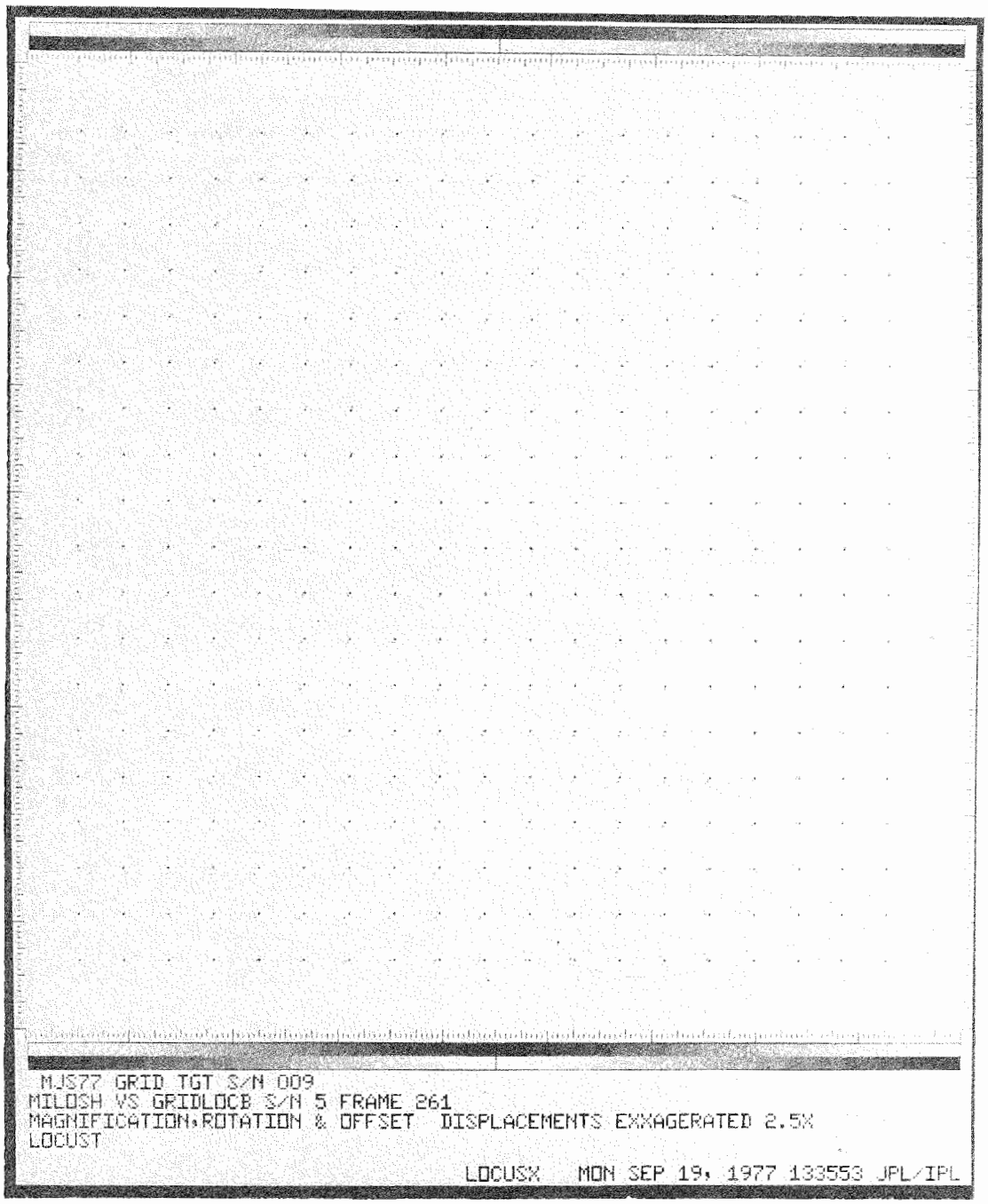

Figure 4-63. Synthesized picture of total distortion

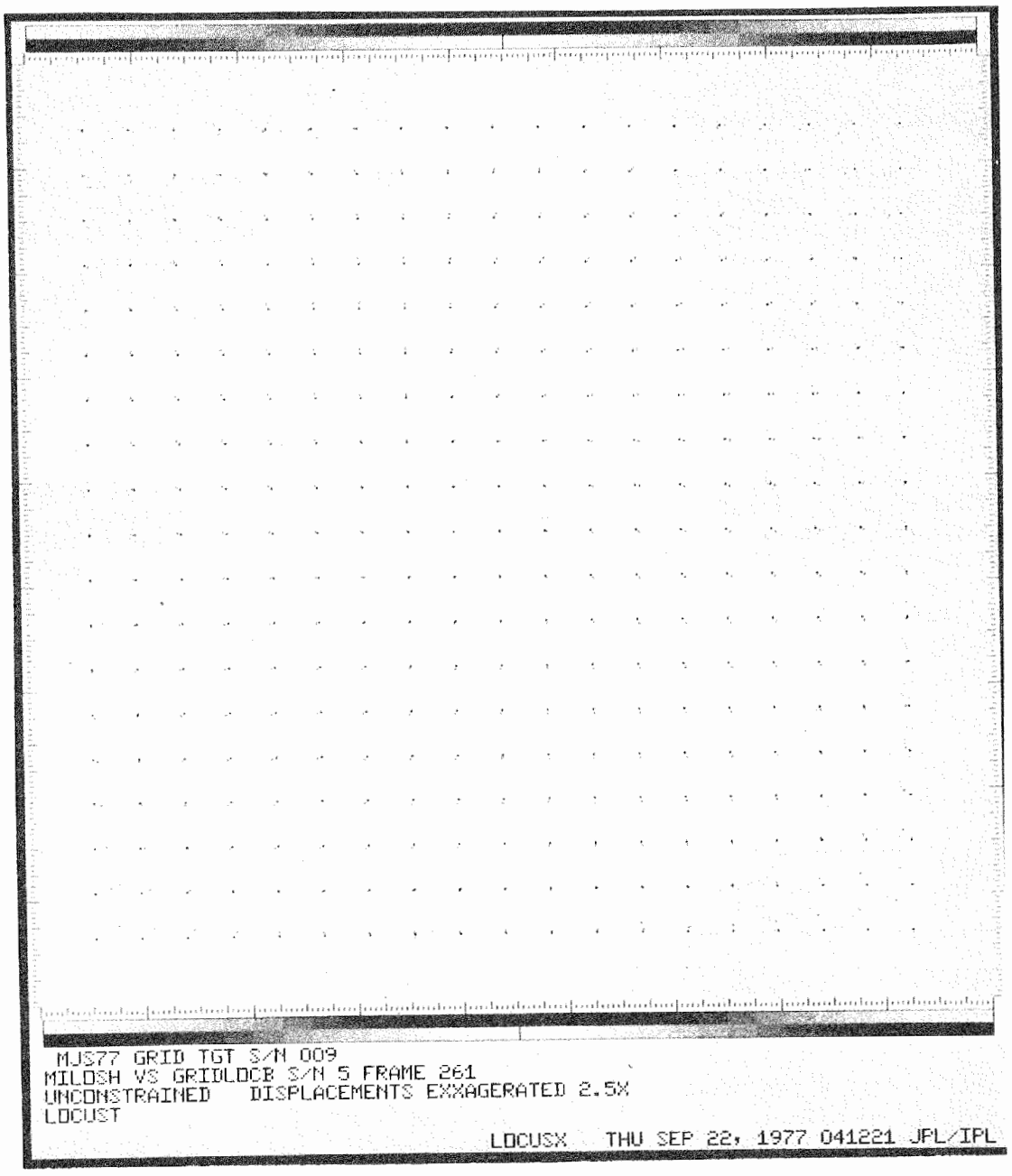

Figure 4-64. Synthesized picture of nonlinear distortions

No limits were specified for vidicon twist, but this deviation also had to be measured because it is an essential part of the picture footprint geometry used for camera pointing by the POINTER program.

The same method as described in Reference 2-3 was used, and each ISS camera was measured independently at least twice over a period of time. The results obtained are summarized in Table 4-13, and the sign convention of the angular deviations is explained in Figure 4-65.

The ISS cameras were built with great skill and expertise because, with only one minor exception (S/N 03), the cross-cone and cone deviations are well within the specified limits and the vidicon twist is also very small. To avoid any misunderstanding, it should be noted that reseau mark 1 (line one, sample one) appears, in this case, in the lower left-hand corner when the vidicon faceplate is viewed through the telescope (for comparison, see Figure 3-39, Section III-D-2).

4. Electron Beam Bending

During bench calibrations, light-transfer sequences were performed using a target of a full disc and a half-moon (the bull's-eye target described in Section II-D). The diameter of the disc, which was placed in the center of the frame, was approximately 400 pixels. Positions of the reseau marks and of the limb points were determined for each frame. In addition, reseau positions were also found for regular flat-field light-transfer sequences.

Table 4-13. ISS optical/mechanical alignment and vidicon twist

ISS S/N	Boresight axis		Vidicon reseau grid twist γ, min/arc
	Cone deviation α, min/arc	Cross-cone deviation β, min/arc	
03	+1.88 ±0.13	-0.38 ±0.10	-8.68 ±1.03
04	+1.14 ±0.27	-2.53 ±0.17	+7.40 ±0.42
05	+0.40 ±0.22	+0.13 ±0.11	-11.78 ±1.40
06	+1.39 ±0.13	-0.53 ±0.07	+29.76 ±2.60
07	+0.26 ±0.23	-0.11 ±0.01	+11.31 ±0.72
08	+0.98 ±0.10	-0.39 ±0.19	+4.44 ±2.99

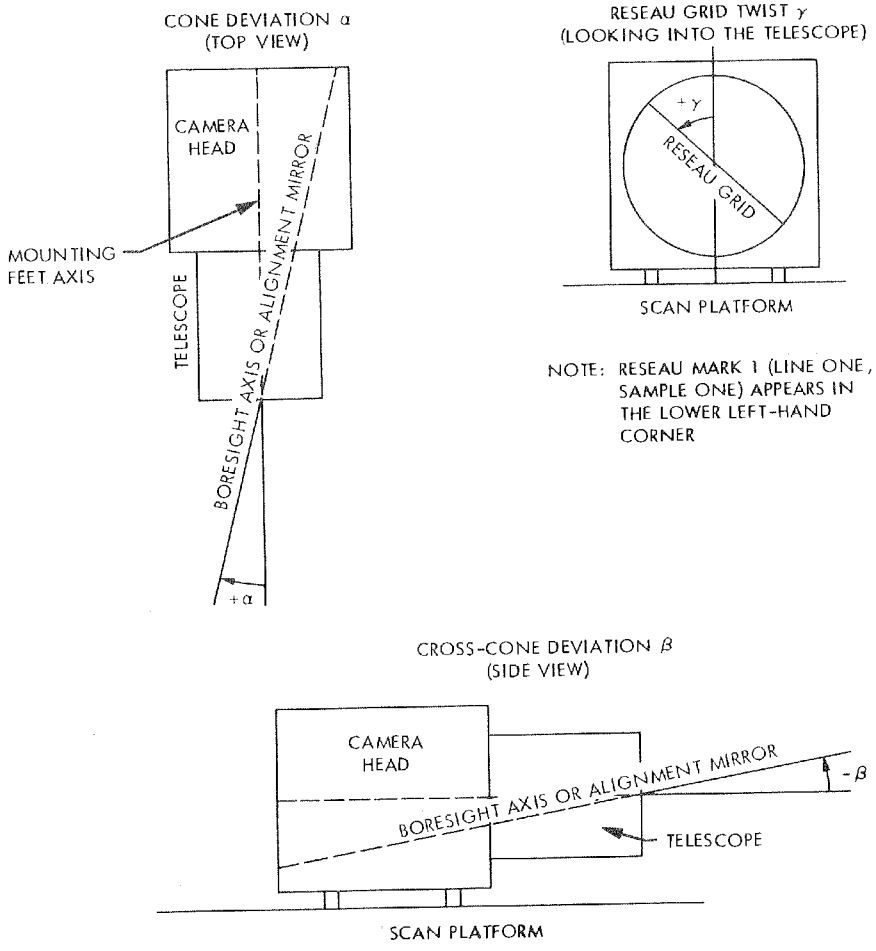

Figure 4-65. Sign convention of the optical/mechanical alignment deviations, Voyager ISS

It has been found that the position of the reseau marks, when imaged by the optics-electronics system of the ISS cameras, is a function of the exposure. Also, the shifts from the dark-current position are dependent upon the spatial shape of the image and upon its relative location with respect to the reseau mark.

For flat-field frames the shifts in reseau positions get larger with increasing exposure (i.e., increasing average DN), until maximum shifts are reached for nearly saturated frames, as shown schematically in Figure 4-66. However, light-transfer sequences using a disc target have a different shifting pattern of the reseau marks (see Figures 4-67 and 4-68). In this case, the reseau marks lying inside the illuminated disc, or very close to the limb, show shifts similar to those of flat-field frames, but there is no shift whatsoever for all reseaus lying more than one reseau spacing in the dark field.

To summarize the major beam-bending effects:

(a) The greatest reseau shifts occur near the top of the image (lower line number), and there is no shift at the bottom of the frame (close to line 800).

(b) The shifts increase monotomically with exposure or average DN.

(c) Qualitatively, it is as if the reseaus were "repelled" by the image with increasing image brightness.

(d) For the full disc and half-moon images, beam bending is noticeable only for reseaus lying inside the disc or located less than one reseau width from the limb in the dark field. This means that the effect is very local.

(e) The effect is even more noticeable when radial limb scans are performed on the image. In this case, limb points near the top of the disc are shifted radially outward by up to 4 pixels from the near dark-current frames to nearly saturated frames with average DN $\sim$ 255 (see Figures 4-69 and 4-70).

An empirical formula has been developed that predicts the increase in radius as a function of position angle θ and average DN of the image (Figure 4-71):

$$\Delta R = a(\theta) + b(\theta)*\overline{DN} \qquad (8)$$

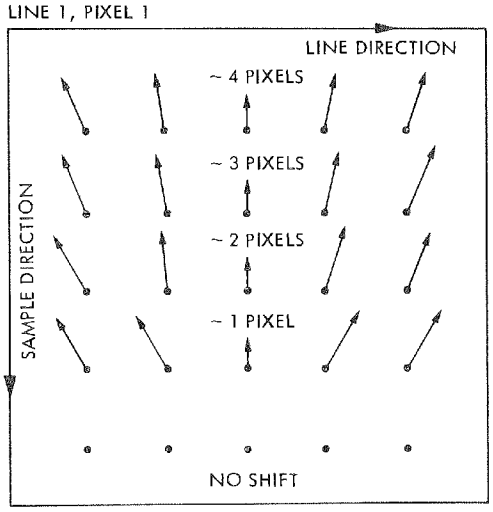

Figure 4-66. Reseau shift for a nearly saturated flat-field frame

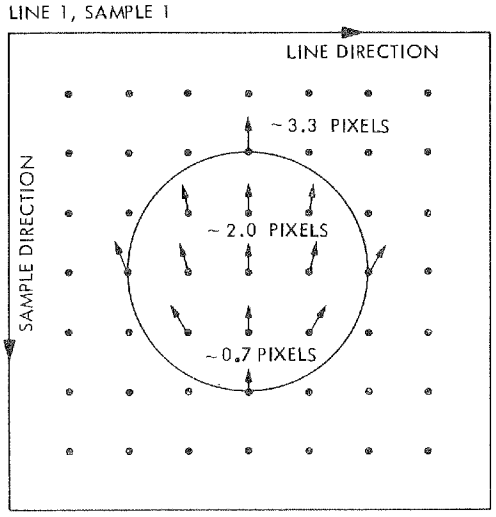

Figure 4-67. Reseau shift for a nearly saturated full-disc frame

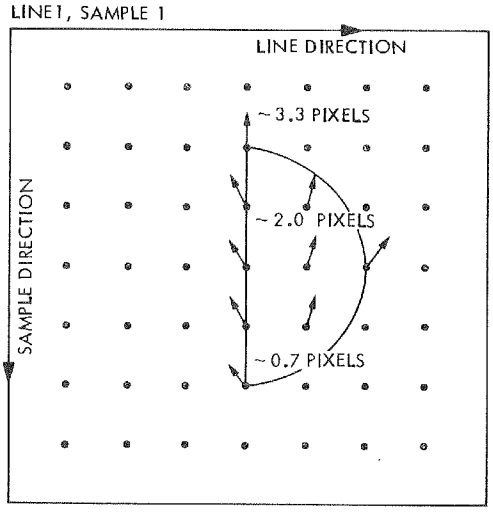

Figure 4-68. Reseau shift for a nearly saturated half-moon frame

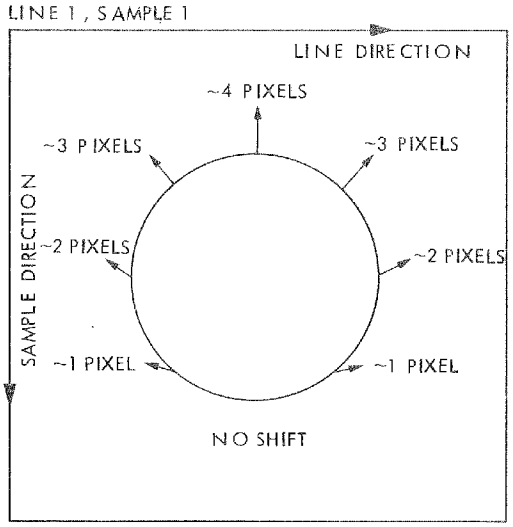

Figure 4-69. Limb-point shift for a nearly saturated full-disc frame

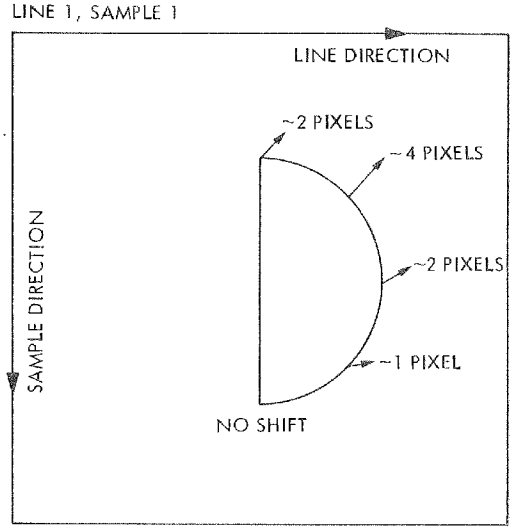

Figure 4-70. Limb-point shift for a nearly saturated half-moon frame

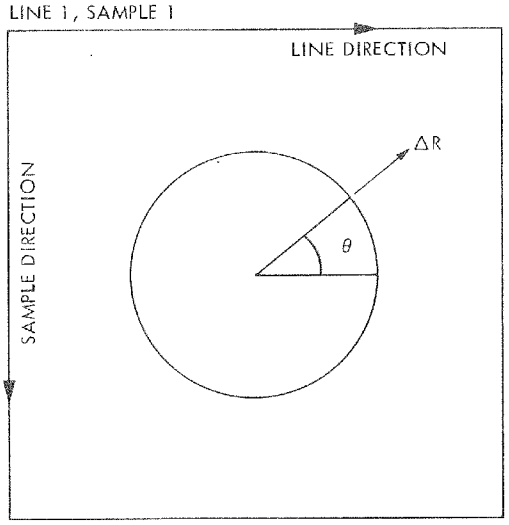

Figure 4-71. Definition of radial shift, ΔR, and position angle, θ

where

Δr = increase of radius

$\overline{DN}$ = average DN of disc

$a(\theta)$, $b(\theta)$ = coefficients which are quadratic functions of θ

This formula is based on 30 radial limb scans (i.e., 30 different angles, θ) for each frame of the light-transfer sequence. Except for two or three values, the predicted shift ΔR is within one pixel of the true increase of radius. A similar but different set of coefficients $a(\theta)$ and $b(\theta)$ was defined for the half-moon frames.

Rigorously, formula (8) is true only for images in the center of the frame, 400 pixels in diameter, and with an average brightness $\leq$255 DN.

The shifts of both the reseaus and the limb can be explained by an early or premature attraction of the scanning electron beam towards the point in question, as shown schematically in Figure 4-72. The greater the local image charge (average DN), the greater the effect of electron-beam bending.

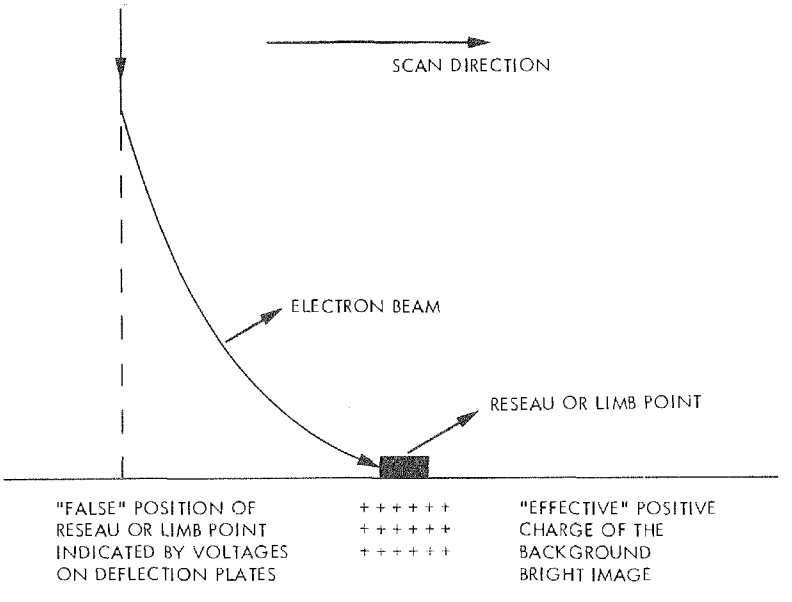

Figure 4-72. Principle of electron beam bending

A theoretical prediction for a particular image is difficult because of partial erasure of the image as it is scanned and an incomplete knowledge of the exact magnetic field in each vidicon. Therefore, corrections of ISS camera images are based on the empirical formula (8) described above.

C. OPTICAL TRANSFER FUNCTION

This section summarizes the optical transfer-function (OTF) analysis performed for the Voyager ISS cameras S/N 03 to 08. A brief discussion of the theoretical aspects is given along with the actual procedures followed. Results along with examples are presented.

1. Analysis

The techniques described below provide a measure of the OTF of an imaging instrument. A number of practical problems arise in the measurement. There is, of course, always the problem of noise biasing the signal. More importantly, however, the OTF is spatially dependent. The latter is not a serious problem as far as Voyager is concerned, since the Voyager vidicons are fairly stable and, if an appropriate area of the image is selected, the spatial stability is periodically monitored by measuring different areas of the image.

When the vidicon reads out an image, the beam performs a convolution with several pixels by virtue of the beam width. The image of a point object would represent the convolving function and is called the point spread function (PSF). The one dimensional equivalent quantity is the line spread function (LSF), which is defined in Eq. (9):

$$\mathrm{LSF}(x) = \int_{-\infty}^{\infty} \mathrm{PSF}(x,y)\,dy \qquad \text{for the x direction} \tag{9}$$

When a long vertical step function is imaged, the resulting horizontal profile S(x) will be a convolution of the step function with the LSF. To recover the LSF, one has to differentiate the blurred edge S as in Eq. (10):

$$\mathrm{LSF}(x) = \frac{d}{dx}\,S(x) \tag{10}$$

The OTF in the x direction can be obtained by taking the normalized Fourier transform of the LSF as in Eq. (11):

$$OTF(f_x) = \frac{\int_{-\infty}^{\infty} LSF(x)e^{-2\pi ifx}dx}{\int_{-\infty}^{\infty} LSF(x)dx} \tag{11}$$

From the OTF, one can obtain the MTF:

$$MTF(f_x) = |OTF(f_x)| = |a + ib| \quad \text{at each frequency} \tag{12}$$

Similarly, one can obtain the phase:

$$\text{Phase } (f_x) = \tan^{-1}(b/a) \tag{13}$$

In practice, many traces are made through the blurred edge S and many LSFs are computed. Each digital LSF is resampled using the Sampling Theorem so that the centroid C [Eq. (14)] of each LSF is centered on an integral pixel. [This process is called the integral line spread function (ILSF).]

$$C = \sum_{n=1}^{N} (n - 1)LSF_n \Big/ \sum_{n=1}^{N} LSF_n$$

$$ILSF_m = \sum LSF_n \frac{\sin(m - n)\pi}{(m - n)\pi} \tag{14}$$

where m is some integer distance from C.

Each ILSF is then processed by Eq. (11), and all of the complex OTFs are averaged. Interpolation, using the Sampling Theorem, is used to eliminate phase bias introduced by shifted LSF. The MTF is not affected, only the phase.

When the complex average is made, rather than the average of the MTFs, the resulting MTF is independent of the random noise level in the image.

2. Data Source

During bench calibration, a specifically designed MTF target (see Figure 4-73 and also Figure 2-22 in Section II-D) was imaged at three scan rates and a number of light levels. The target was also rotated (Figure 4-74) so that the vertical MTF also could be measured. MTF analysis was performed at three scan rates (1:1, 3:1, 10:1) at three exposure levels, and at both dark to light (ascending edge) and light to dark (descending edge) transitions. The DNs for the transitions were: low = Δ10 to 20 ΔDN, mid = 45 to 65 ΔDN, and high = 100 to 200 ΔDN.

Two areas near the center of the image were measured, one ascending and one descending. Reseaus were removed, if necessary. A 150-line by 35-sample area was used to reduce noise effects and produce a better measure of the mean MTF. Horizontal and vertical, 1:1-scan-rate plots of the average MTF and phase (Figures 4-75 and 4-76) were produced for ISS S/N 03 to 08.

3. Results

(a) For all cameras, the horizontal MTF is higher on the ascending edge than the descending edge.

(b) There is no significant difference between the vertical ascending and descending MTFs.

(c) The horizontally and vertically measured MTFs are spatially variant (see Figure 4-77). The MTF at the center is generally slightly better than at the edges of the image.

(d) There is no significant difference between the measured MTFs at different scan rates (see Figure 4-78).

(e) Vertically measured MTFs are higher than horizontally measured MTFs.

(f) The MTF is very dependent upon the height of the edge in DN. The higher the total DN difference, the lower the MTF.

(g) The MTF does not drop to zero at the Nyquist frequency. This indicates that a certain amount of aliasing is present. Frequencies near the Nyquist will be garbled.

(h) The phase function is generally negative on the ascending edge and positive on the descending. This indicates that the upper edge of a steep feature is rounded off more than the lower edge.

(i) The phase function becomes more pronounced as the amplitude of the edge increases. This indicates that very high frequencies will be uninterpretable in the vicinity of objects of high contrast.

(j) Different scan rates have no obvious impact on the phase function.

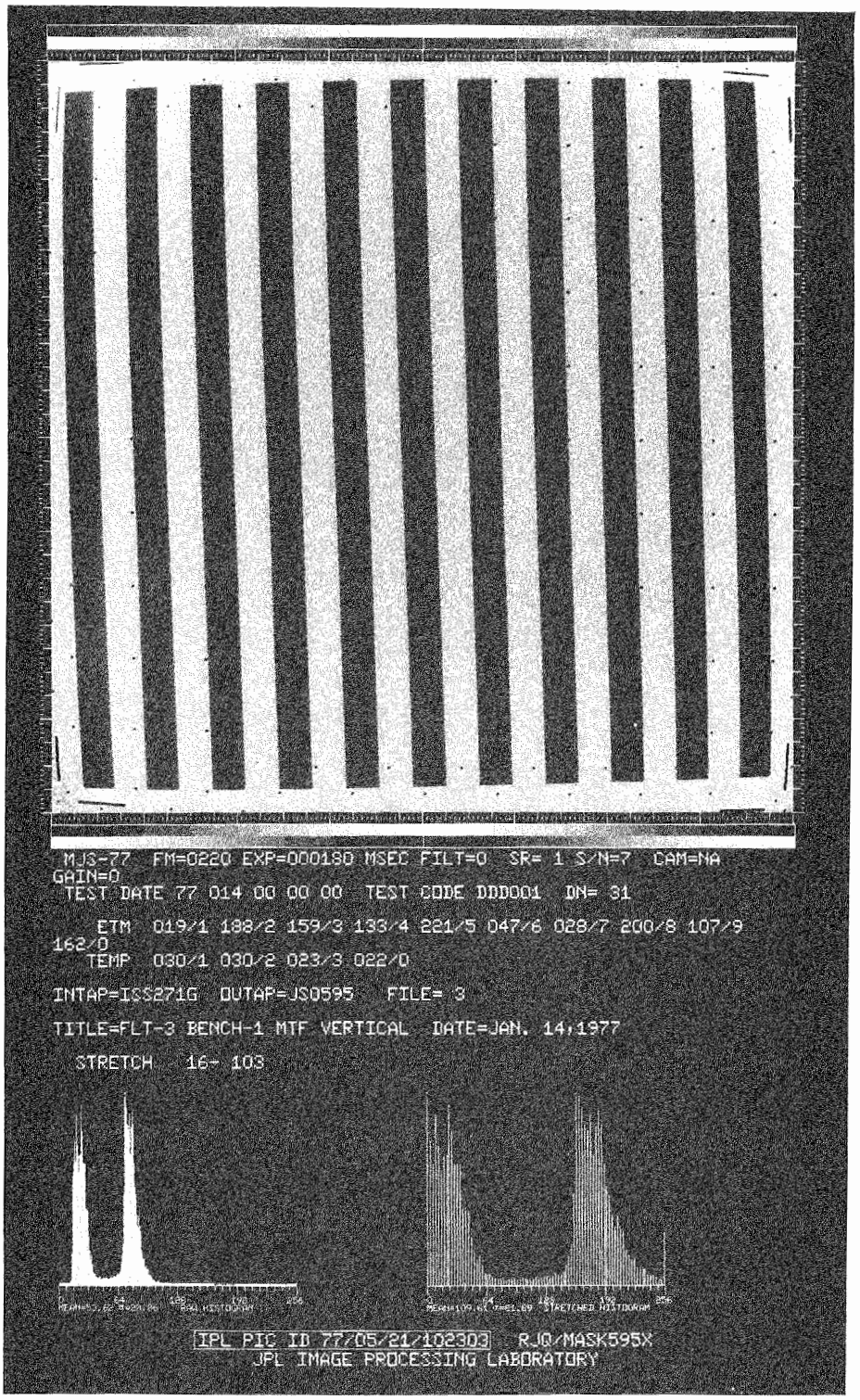

Figure 4-73. ISS image of the MTF vertical target

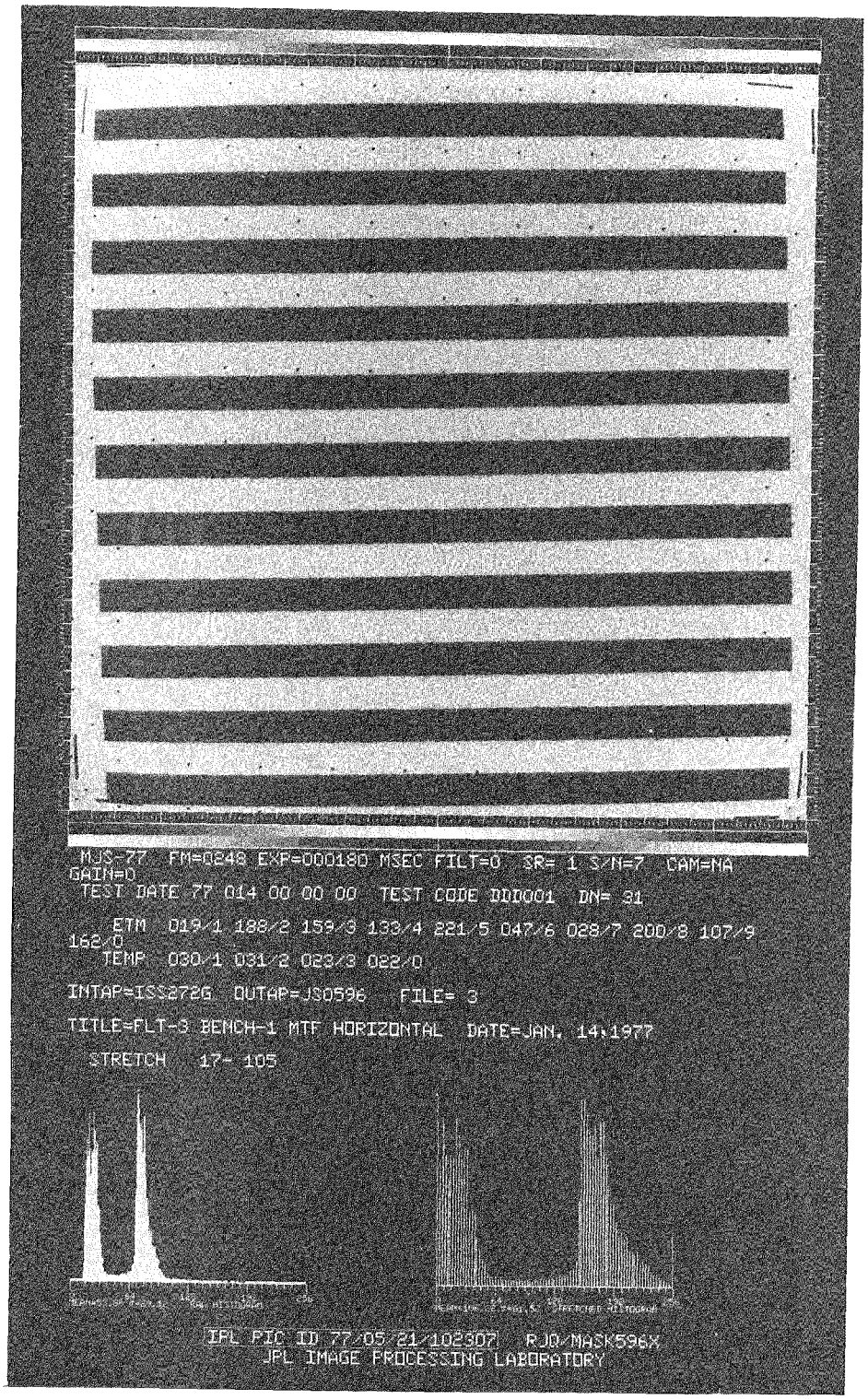

Figure 4-74. ISS image of the MTF horizontal target

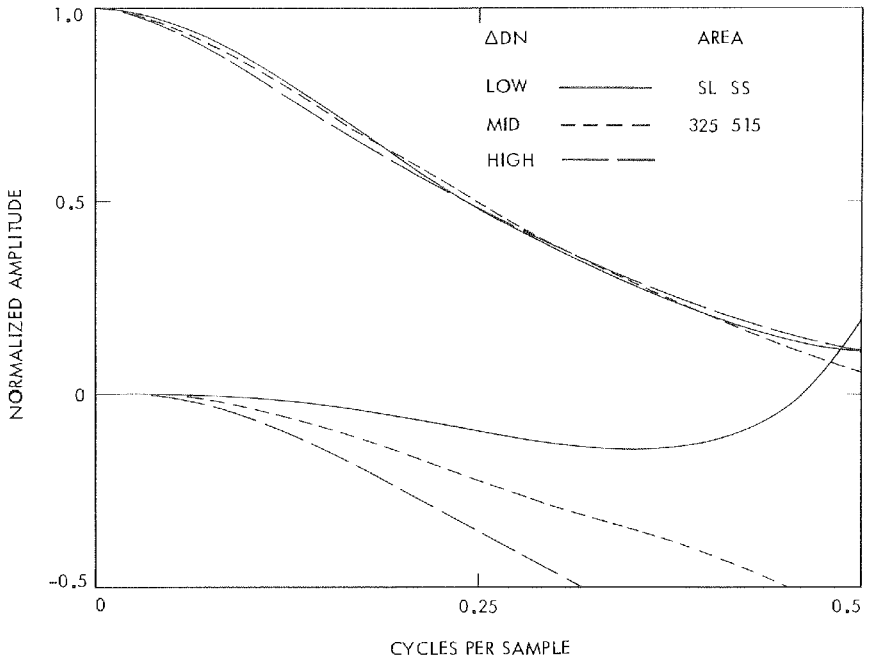

(a) ISS S/N 03, ascending

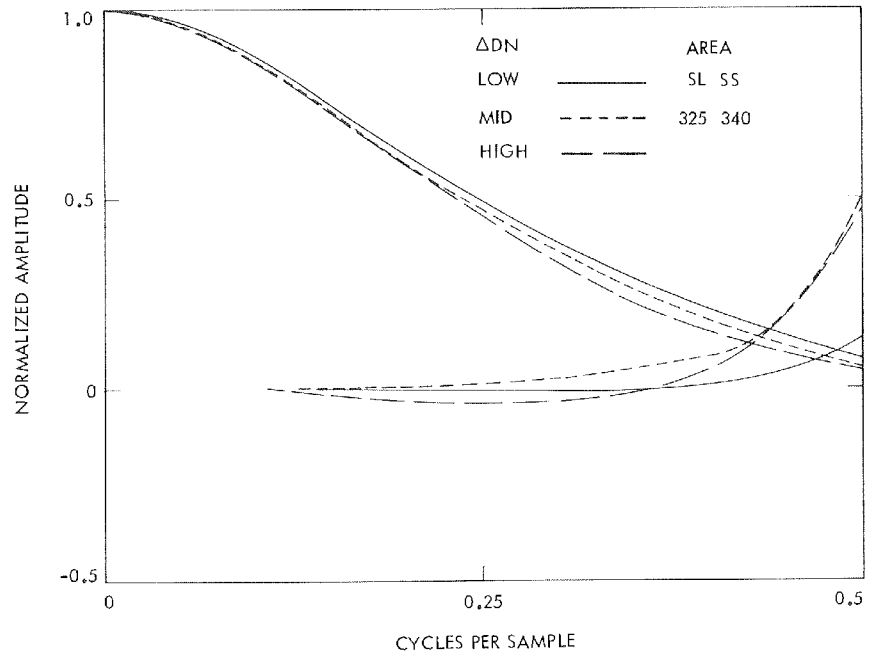

(b) ISS S/N 03, descending

Figure 4-75. Horizontal MTF (ascending and descending), ISS S/N 03 to 08

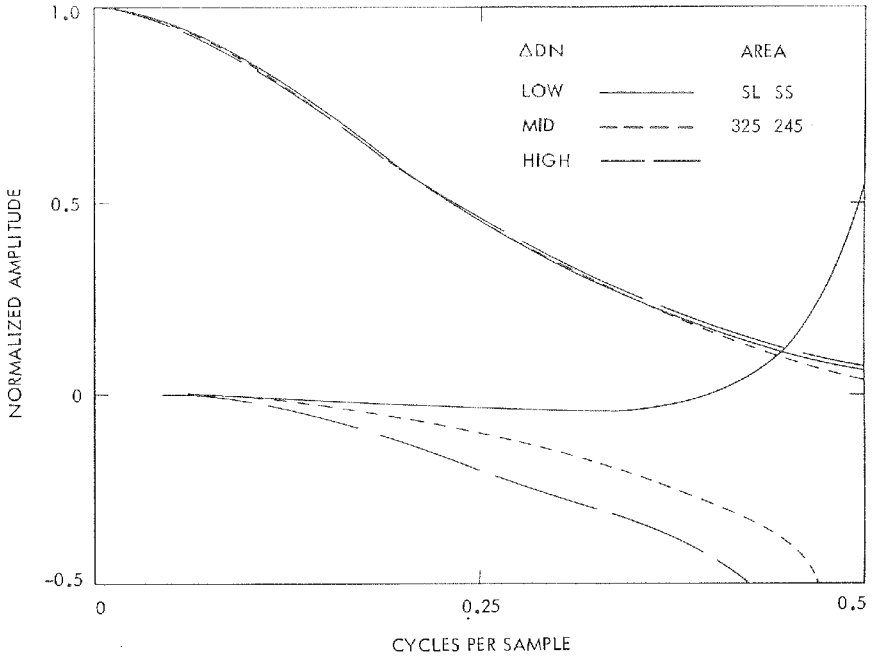

(c) ISS S/N 04, ascending

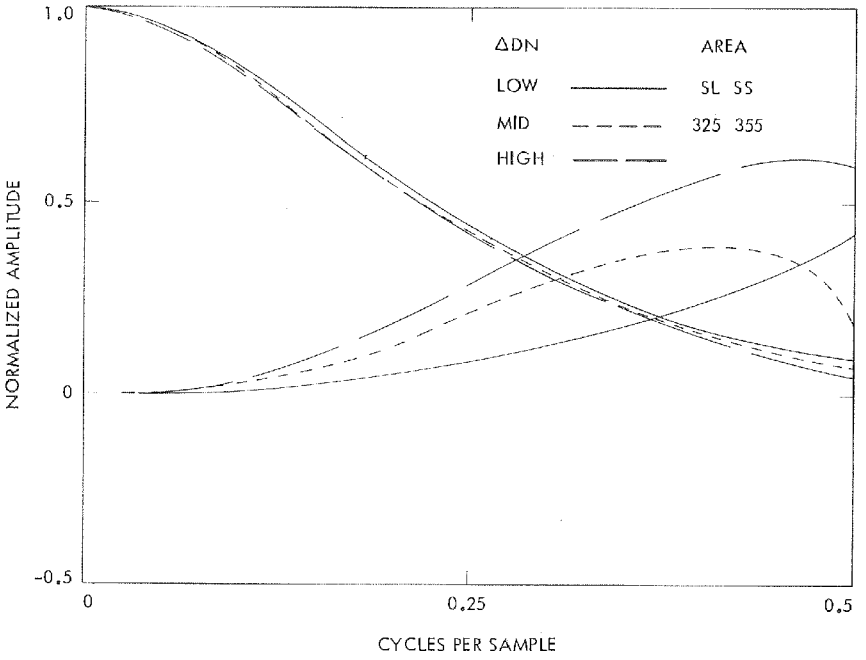

(d) ISS S/N 04, descending

Figure 4-75 (contd)

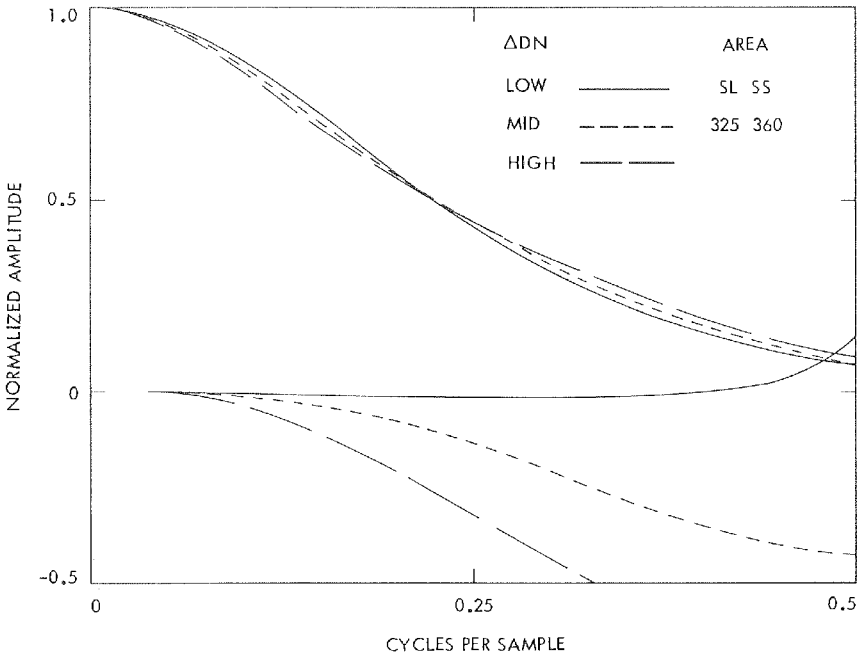

(e) ISS S/N 05, ascending

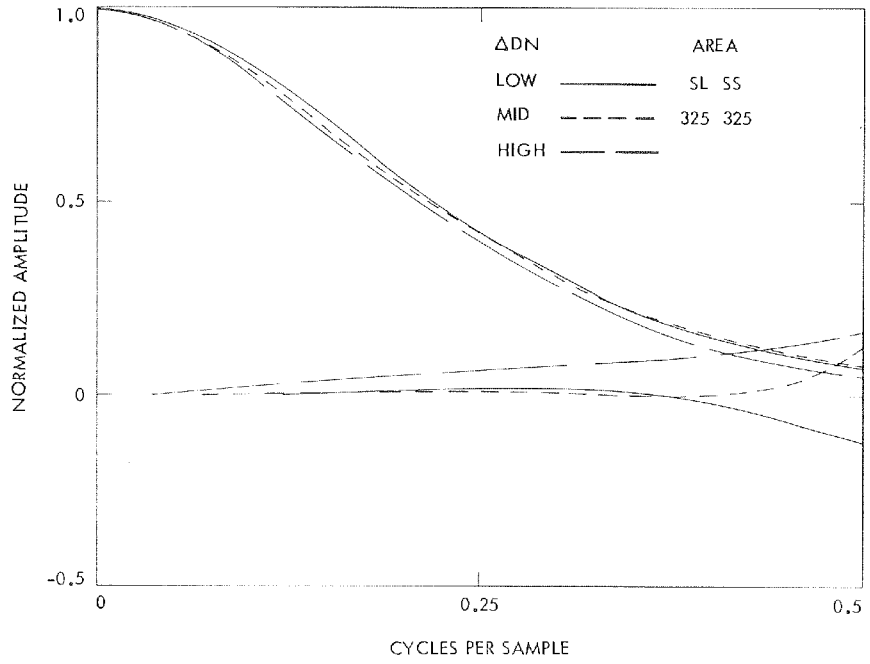

(f) ISS S/N 05, descending

Figure 4-75 (contd)

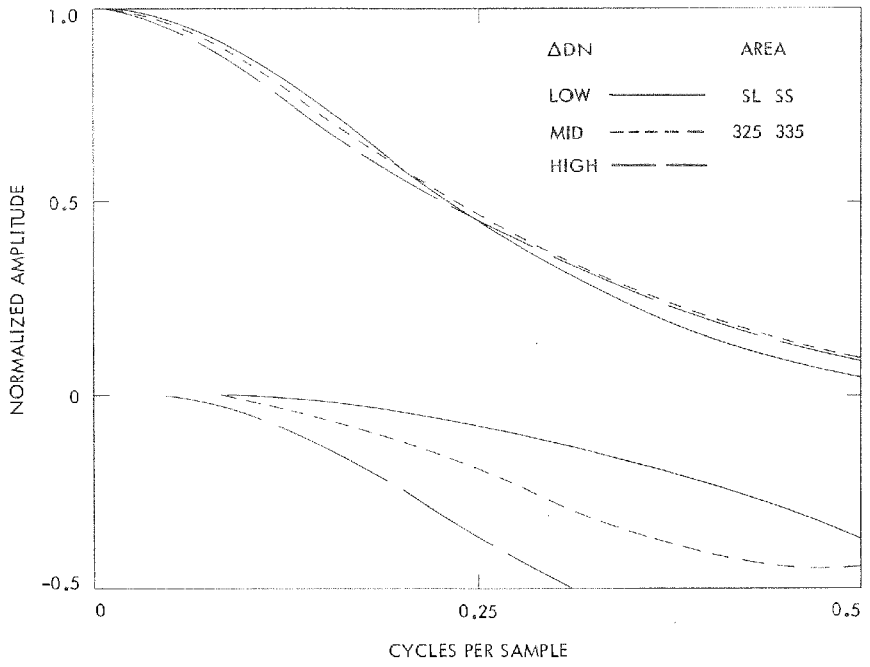

(g) ISS S/N 06, ascending

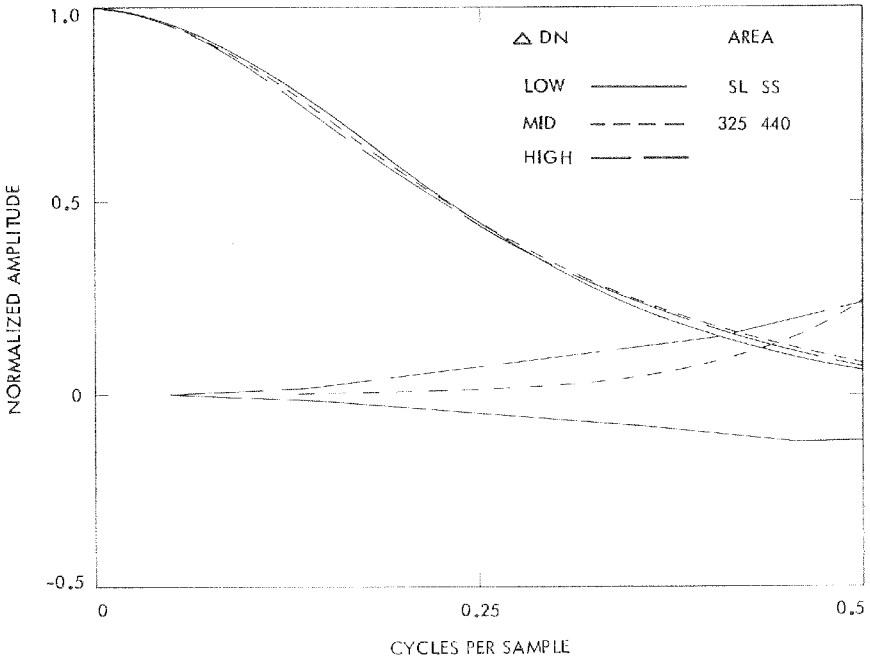

(h) ISS S/N 06, descending

Figure 4-75 (contd)

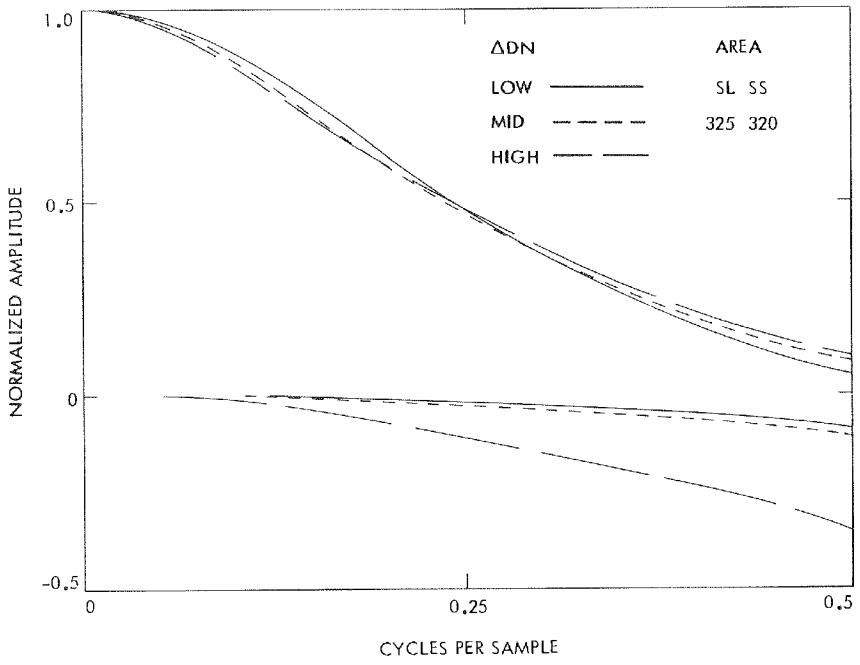

(i) ISS S/N 07, ascending

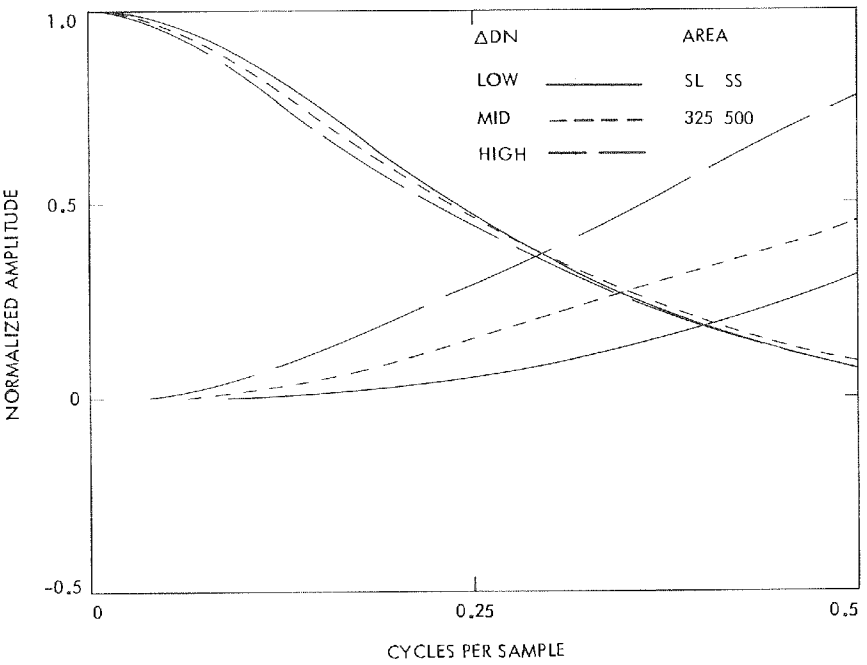

(j) ISS S/N 07, descending

Figure 4-75 (contd)

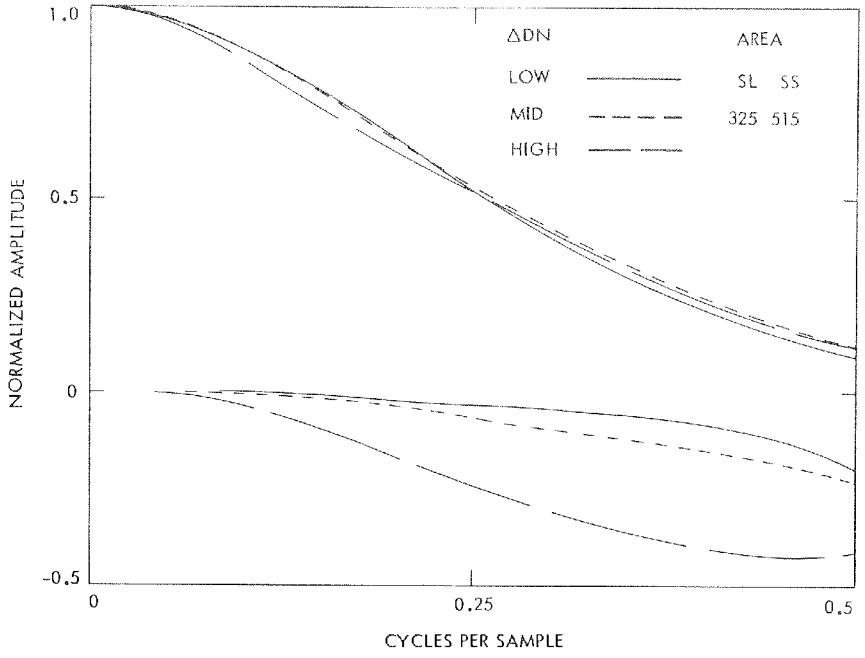

(k) ISS S/N 08, ascending

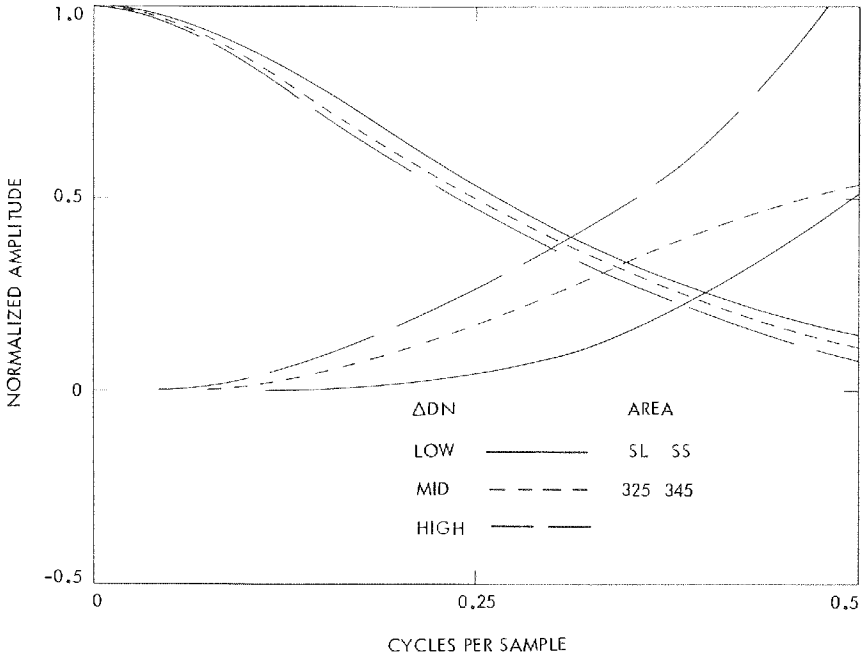

(l) ISS S/N 08, descending

Figure 4-75 (contd)

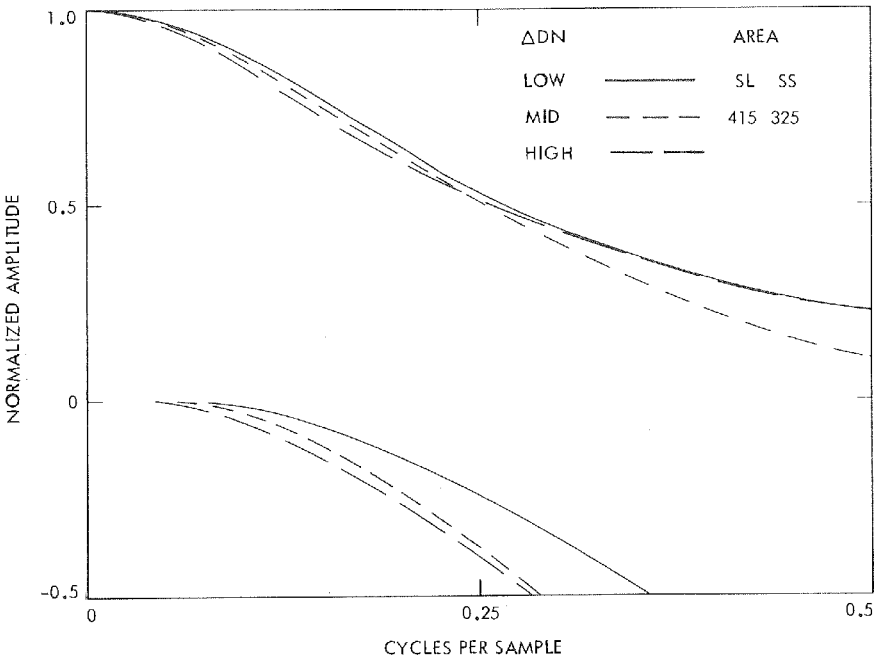

(a) ISS S/N 03, ascending

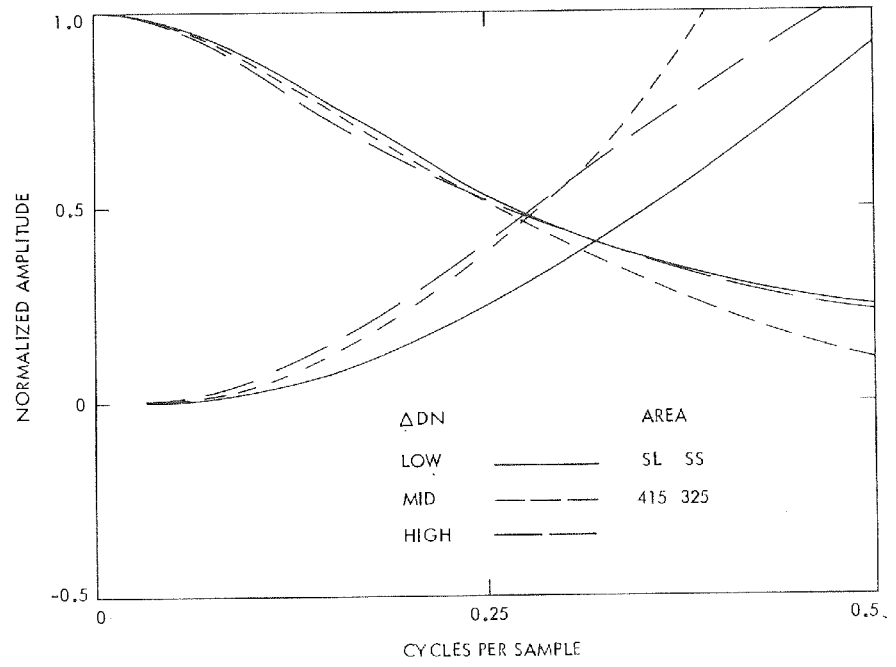

(b) ISS S/N 03, descending

Figure 4-76. Vertical MTF (ascending and descending), ISS S/N 03 to 08

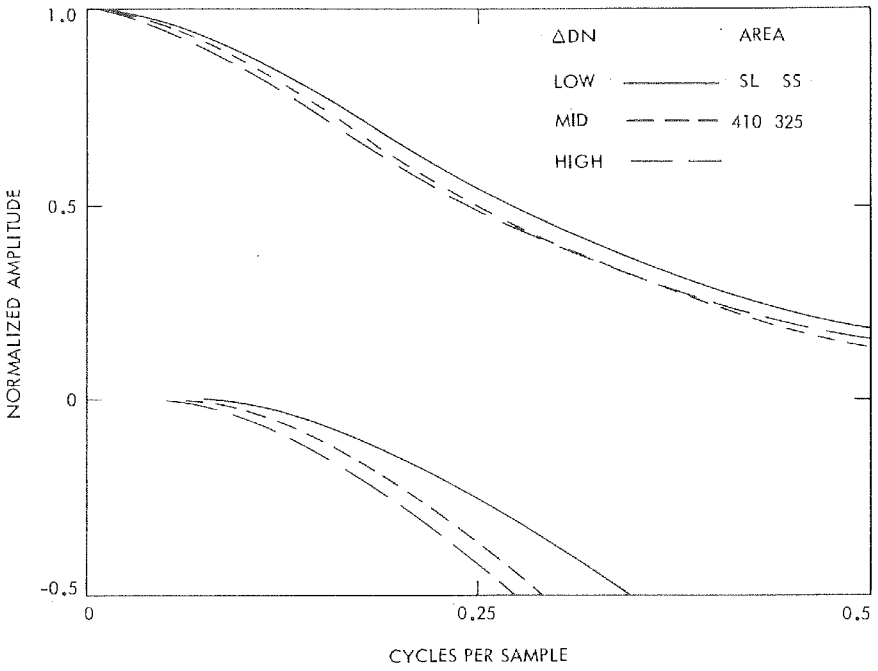

(c) ISS S/N 04, ascending

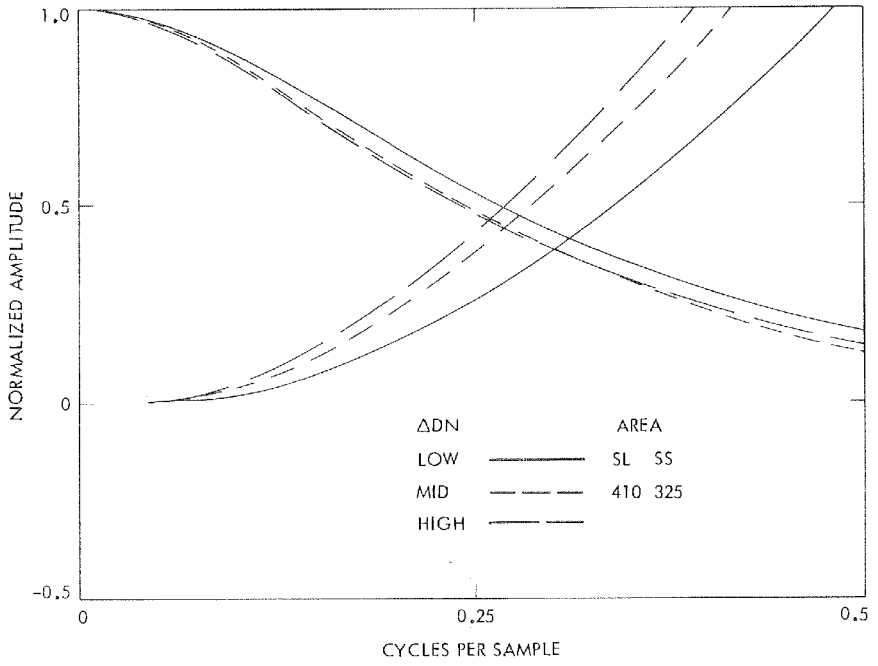

(d) ISS S/N 04, descending

Figure 4-76 (contd)

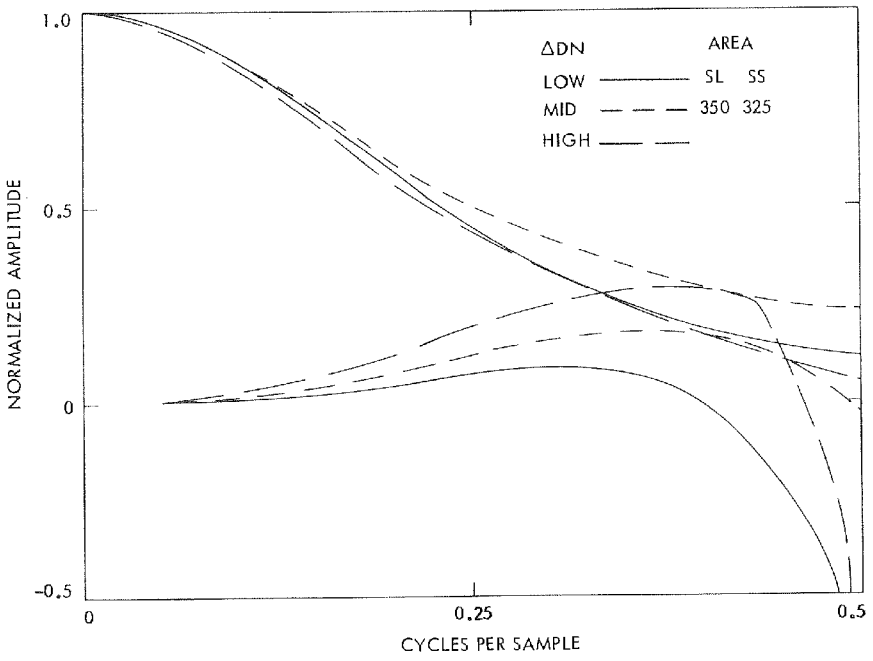

(e) ISS S/N 05, ascending

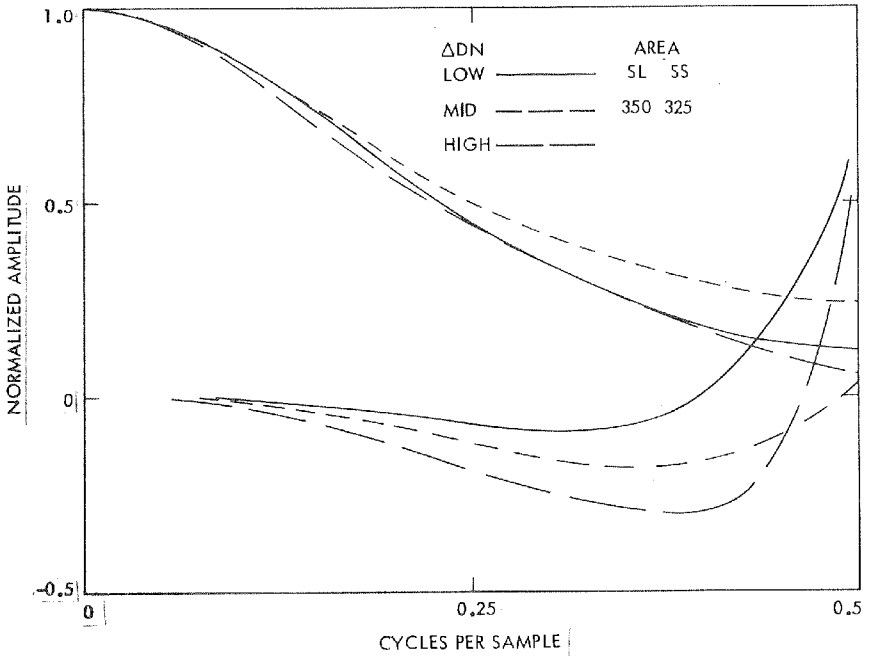

(f) ISS S/N 05, descending

Figure 4-76 (contd)

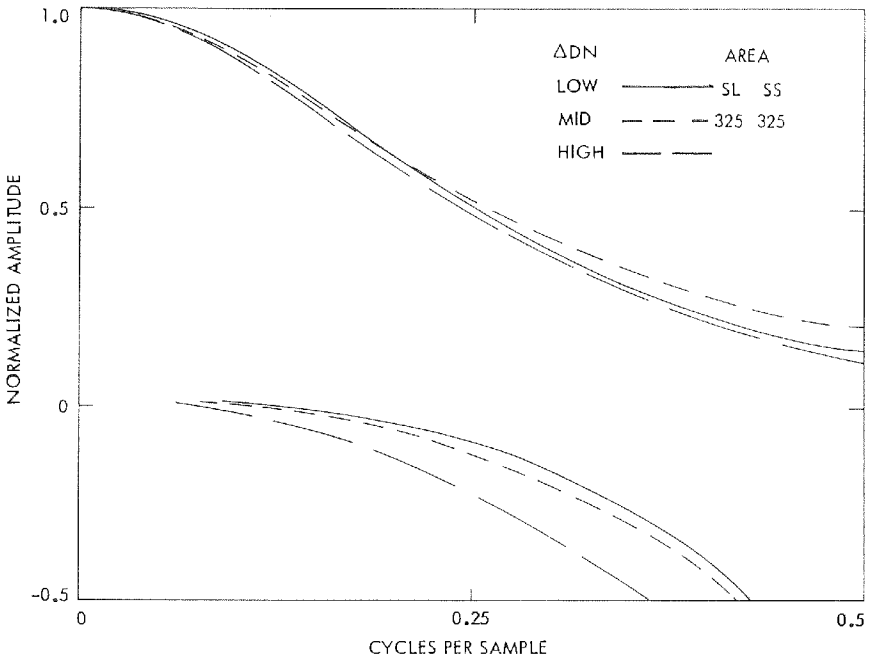

(g) ISS S/N 06, ascending

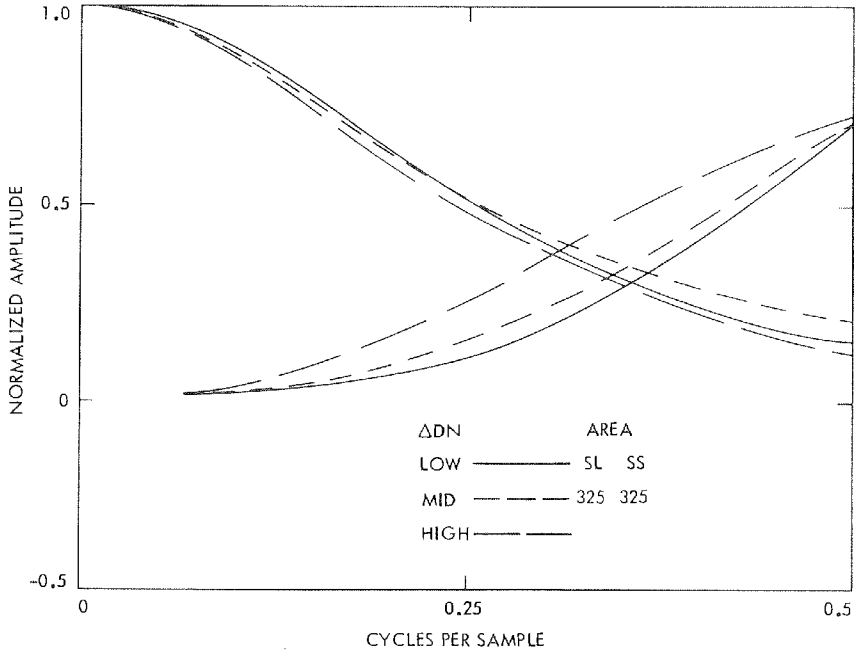

(h) ISS S/N 06, descending

Figure 4-76 (contd)

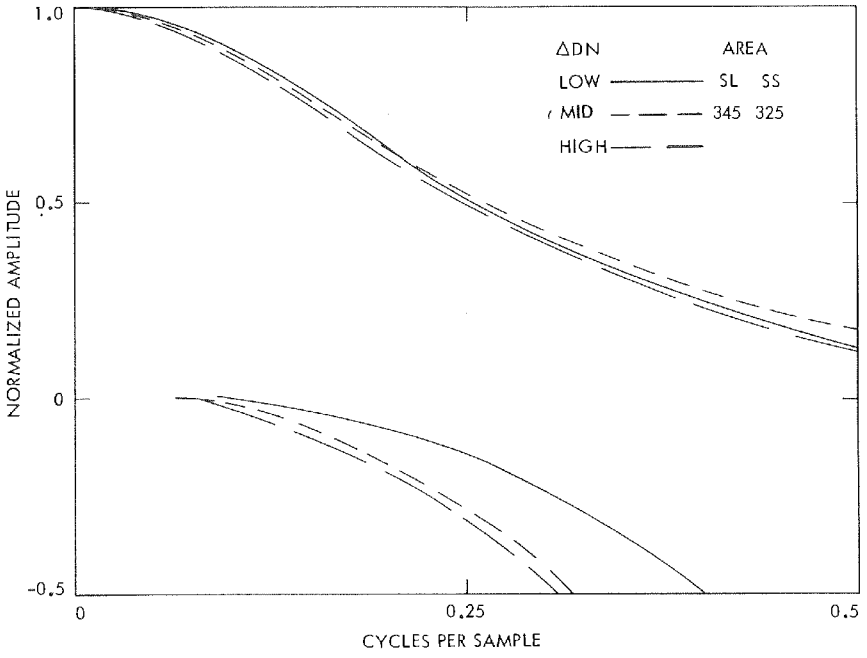

(i) ISS S/N 07, ascending

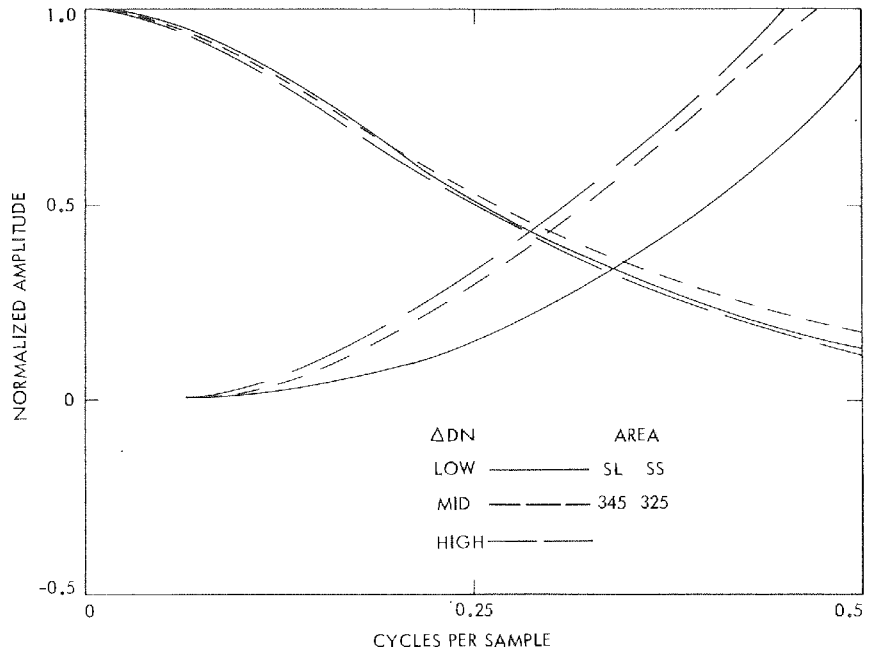

(j) ISS S/N 07, descending

Figure 4-76 (contd)

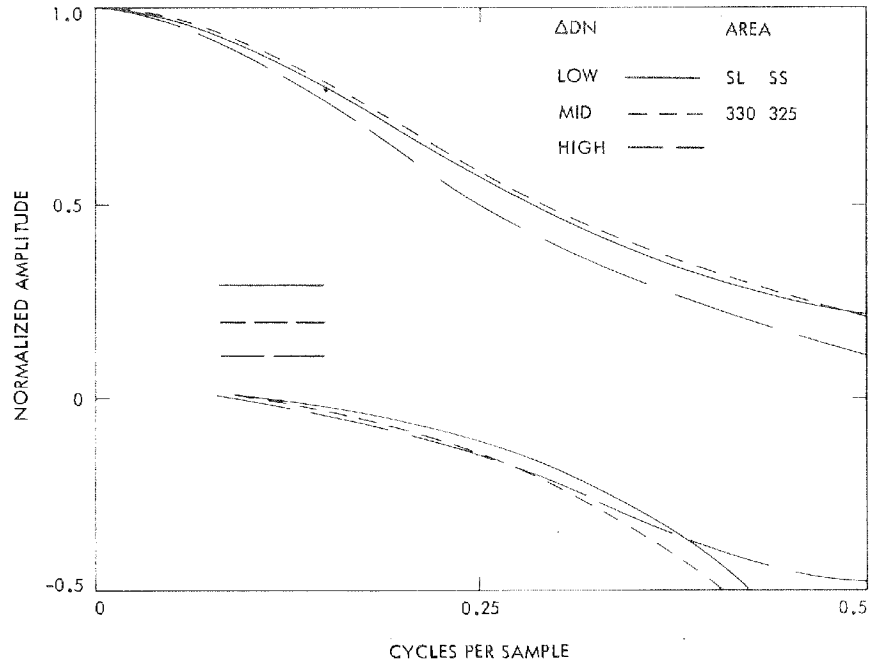

(k) ISS S/N 08, ascending

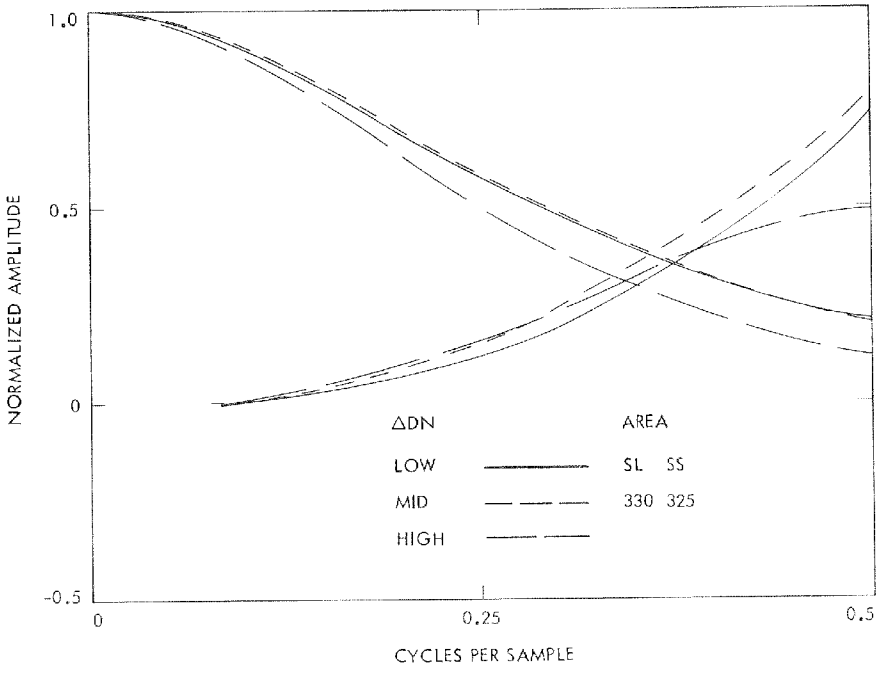

(l) ISS S/N 08, descending

Figure 4-76 (contd)

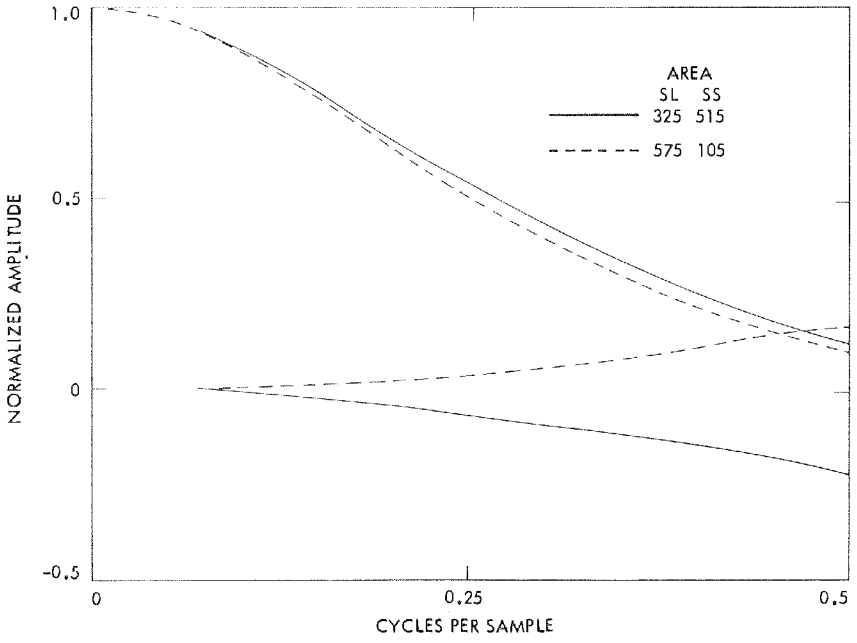

(a) Horizontal ascending

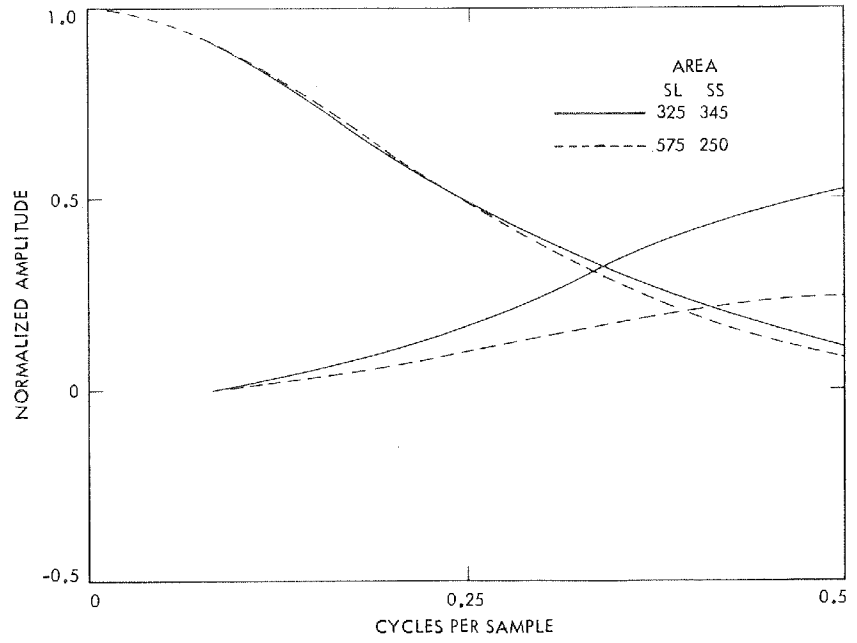

(b) Horizontal descending

Figure 4-77. Horizontal and vertical MTF spatial variation (ascending and descending), ISS S/N 08

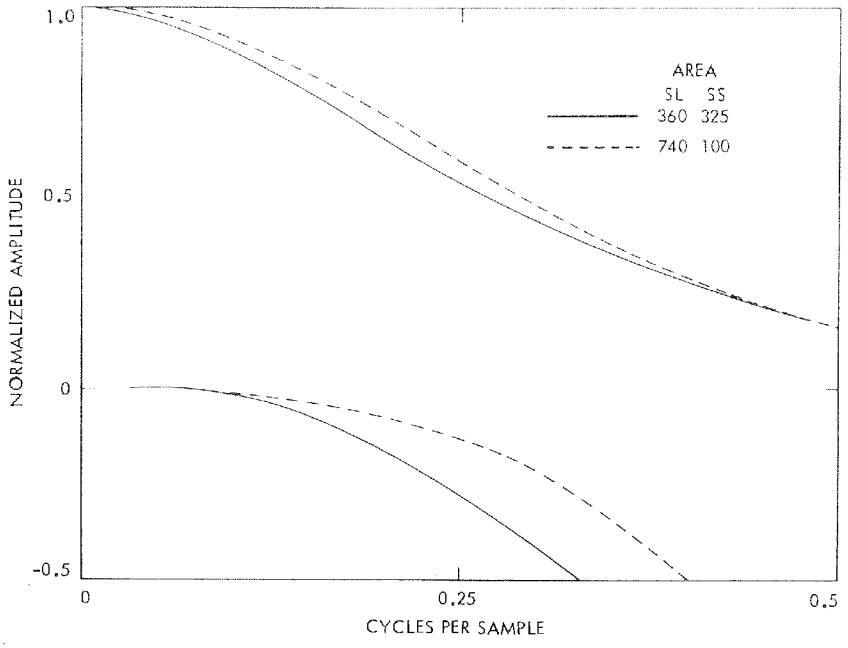

(c) Vertical ascending

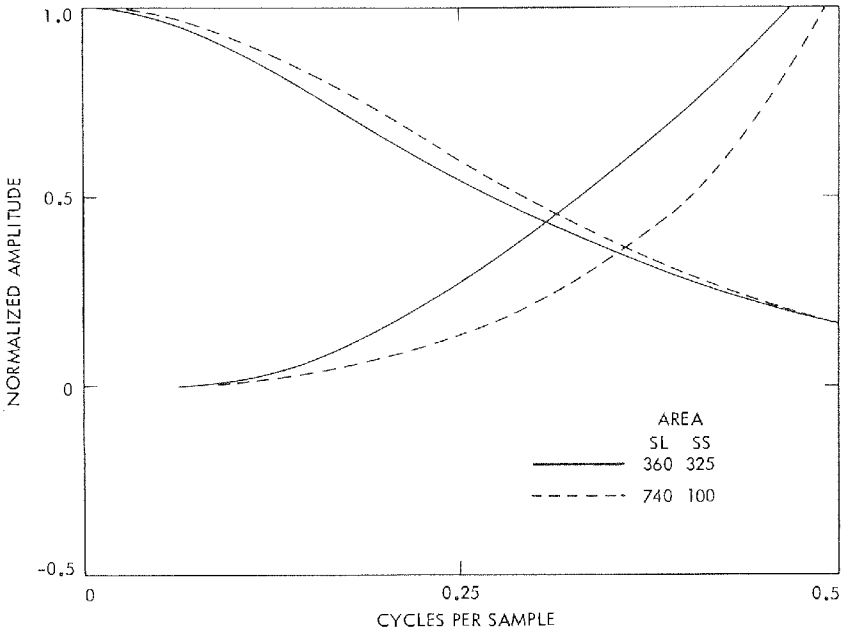

(d) Vertical descending

Figure 4-77 (contd)

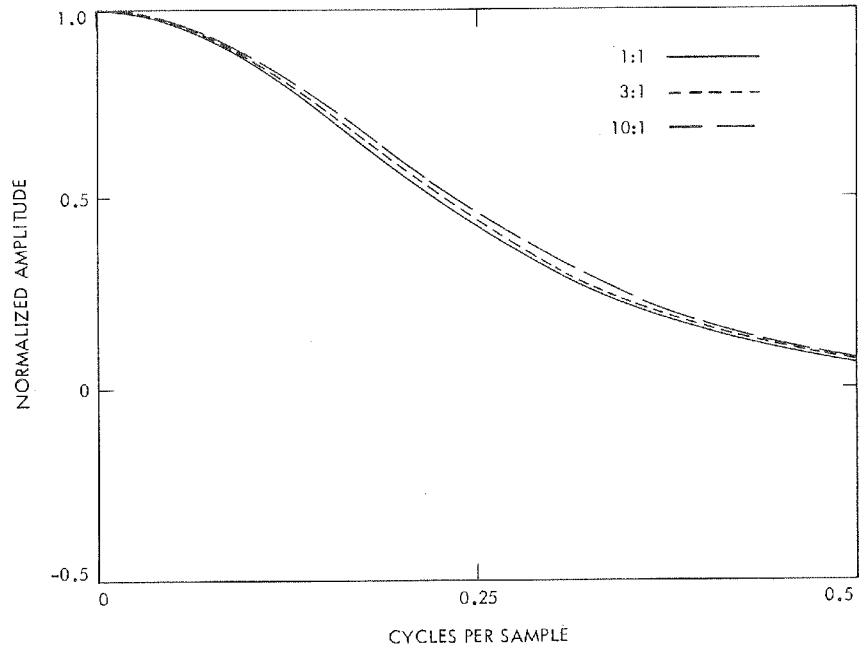

(a) Ascending

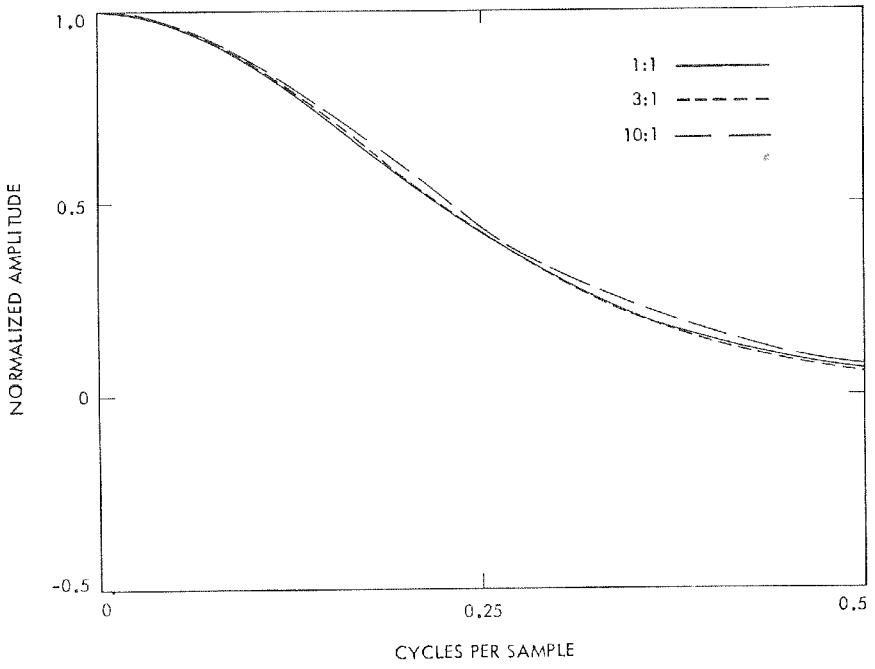

(b) Descending

Figure 4-78. Horizontal MTF scan-rate variation (ascending and descending), ISS S/N 05

4. Conclusion

The results of the MTF analysis are consistent with earlier results obtained for Mariner 10. In summary, there is no reason to believe that any of the cameras analyzed will pose any problem during the mission for MTF restoration or image interpretation from the restorations. Further, compensating filters have already been developed and applied to Voyager imaging (see Figure 4-79), and the results are satisfactory.

D. POINT-SPREAD FUNCTION (STAR SIMULATION)

The point spread function (star simulation) calibrations were performed for all ISS cameras and the data obtained were stored on magnetic tapes. However, the analysis of the obtained data has not been completed in time to meet the publication deadline of this report.

Therefore, this section will be discussed in full detail in the In-Flight Calibration Report, which will be written and published at a later date. Meanwhile the interested reader may want to contact Voyager Imaging Science Experiment Representative at JPL for the available intermediate and preliminary results.

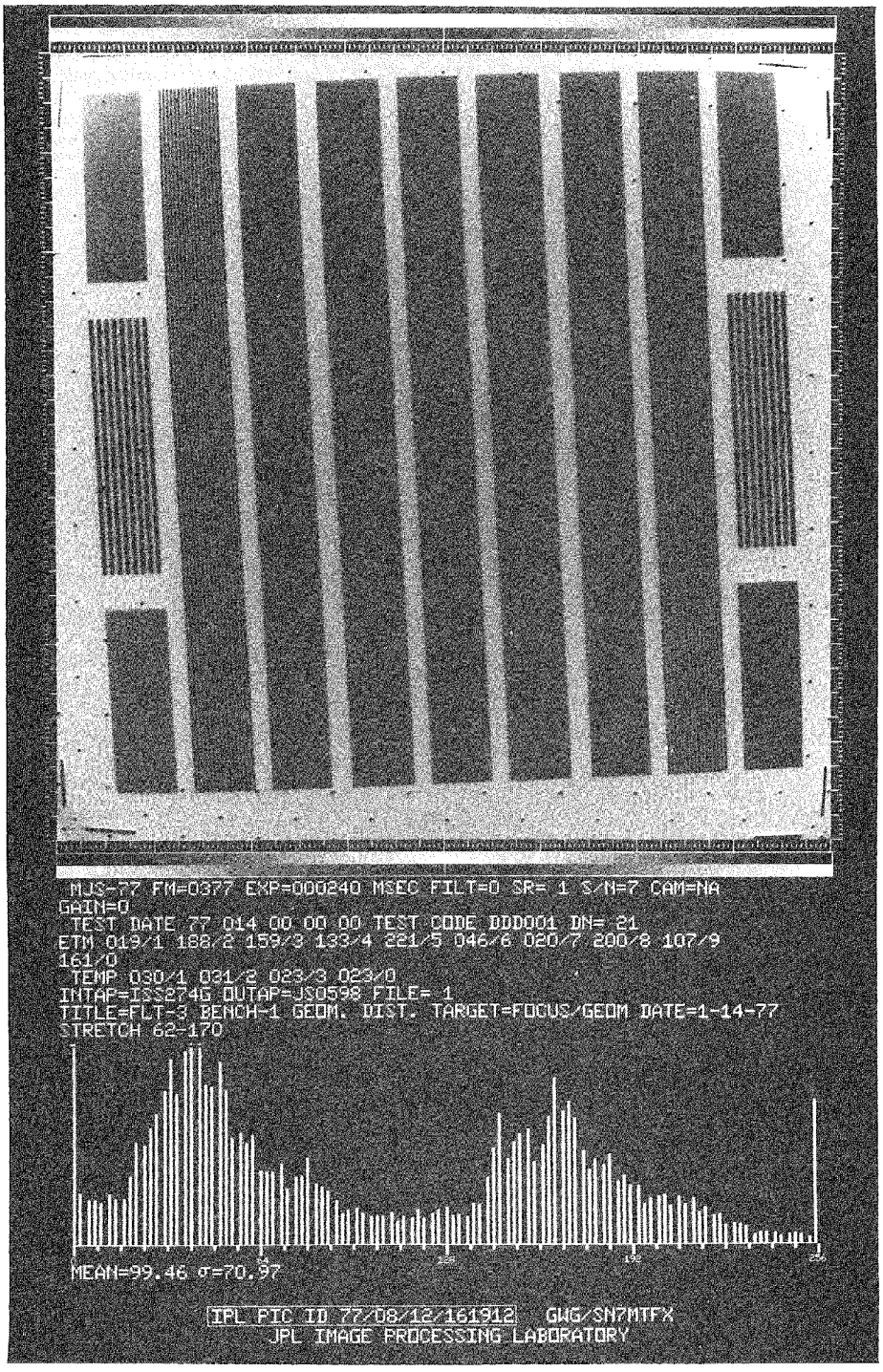

(a) Before correction

Figure 4-79. ISS image before and after MTF correction

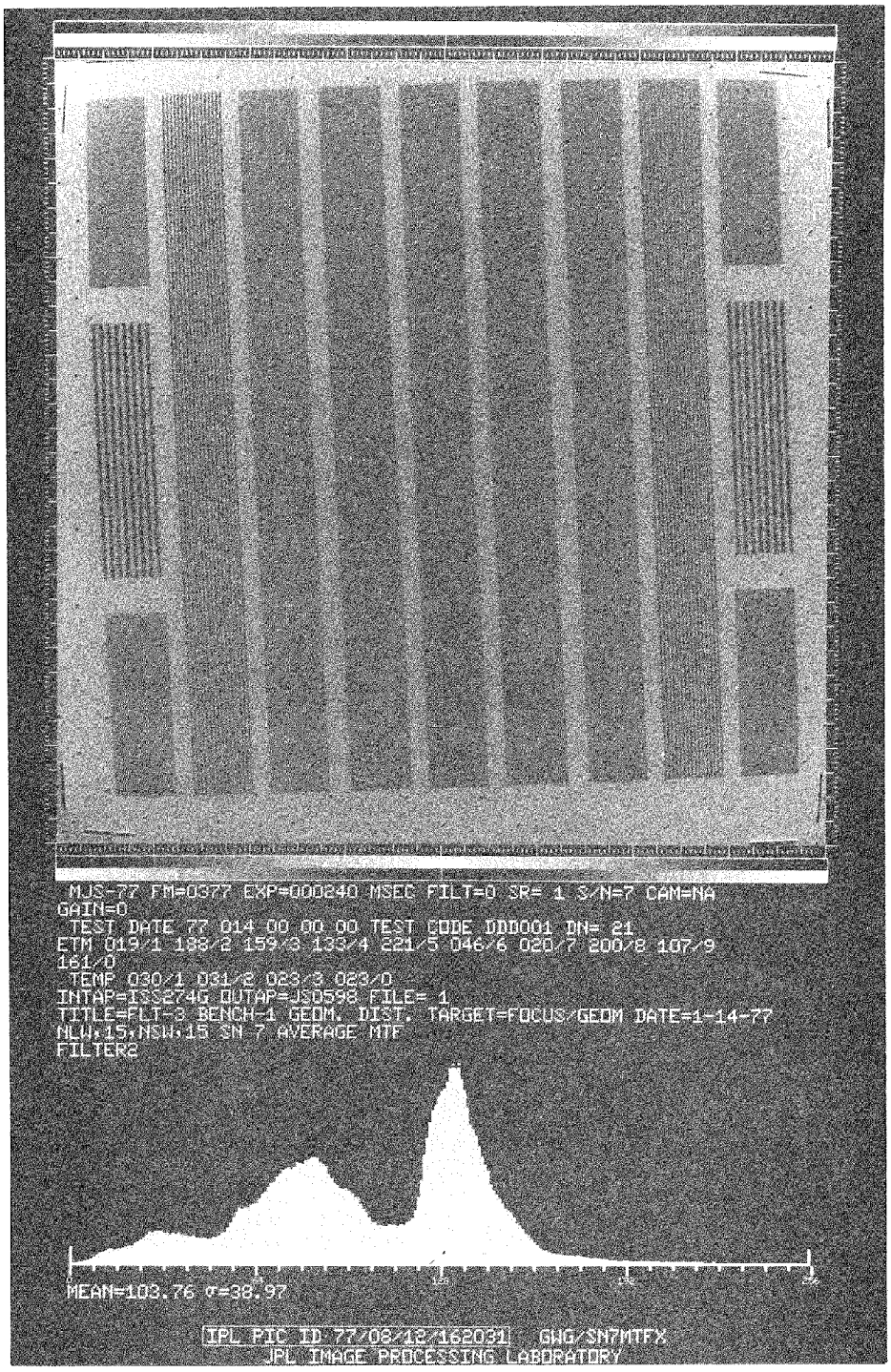

(b) After correction

Figure 4-79 (contd)

REFERENCES

4-1. M. Benesh, Subsystem-Level Test and Calibration Procedure, Viking Orbiter 1975 Visual Imaging Subsystem, JPL Document 611-101, March 21, 1974.

4-2. Judd and Wyszecki, Color in Business, Science, and Industry, John Wiley & Sons, Inc., N.Y., 1963, 2nd ed.

4-3 J. E. Kreznar, User's and Programmer's Guide to the MM '71 Geometric Calibration and Decalibration Programs, JPL Document 900-575, March 1973.

SECTION V

SYSTEM CALIBRATIONS

A. FLAT-FIELD LIGHT-TRANSFER VERIFICATION

During system tests, both SAF and ETR, the in-flight calibration lamps were used almost exclusively for calibration verification of the subsystem-level flat-field light-transfer functions. The lamps also successfully pinpointed the ISS S/N 08 vidicon failure prior to launch, thereby proving their usefulness (ISS S/N 08 was then replaced by ISS S/N 04).

The most important calibration verification for the flight units (ISS S/N 04 to 07, mounted on the spacecraft) and for the flight spare units (ISS S/N 03 and 08, mounted on optical bench) were performed immediately prior to launch. A set of light-transfer functions, based on the in-flight calibration lamps, was generated, as shown in Figure 5-1 (see Figure 4-1 for explanation of subareas). These data are consistent with earlier calibrations and will be used as a reference for comparison of the in-flight radiometric response of the flight ISS cameras during the mission (see Section IV-A-5).

In addition to the in-flight calibration lamps, a few system-level calibrations utilized the Celestron and Soligor collimators described in Section II-C. However, the radiometric properties of these light sources are not sufficiently known to permit a reliable evaluation of the data obtained. On the other hand, analysis of several geometric grid-target frames, mounted in the same collimators, did not reveal any significant changes from the results discussed in Section IV-B-2, which means that the subsystem-level geometric distortion parameters can be safely applied to all flight photographs.

B. FIELD-OF-VIEW ALIGNMENT

The results of geometric calibrations described in Sections IV-B-1 and IV-B-3 were used for the final alignment of flight ISS cameras mounted on the scan platform of each Voyager spacecraft.[16] The standard method of optical autocollimation, utilizing the ISS camera alignment mirror, was used for this purpose.

---

[16] See C. W. Odd, "Science Instrument Alignment Verification for Voyager 77-2 Spacecraft," JPL IOM VGR 77-34, FL, July 21, 1977, and "ISS W/A S/N 04 Alignment Verification for Voyager 77-3," JPL IOM 373 VGR 77-48, FL, August 11, 1977.

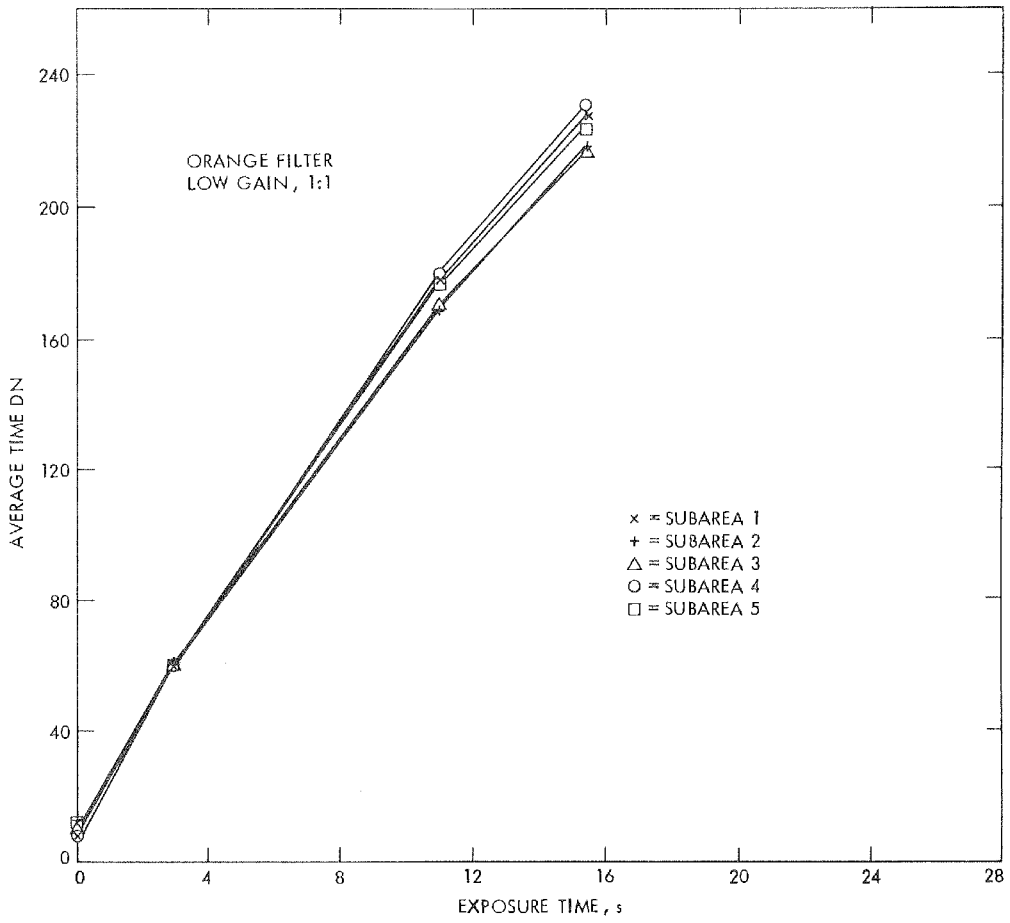

(a) ISS S/N 03

Figure 5-1. Light-transfer functions using the in-flight calibration lamps in mode 1 (vary shutter), ISS S/N 03 to 08

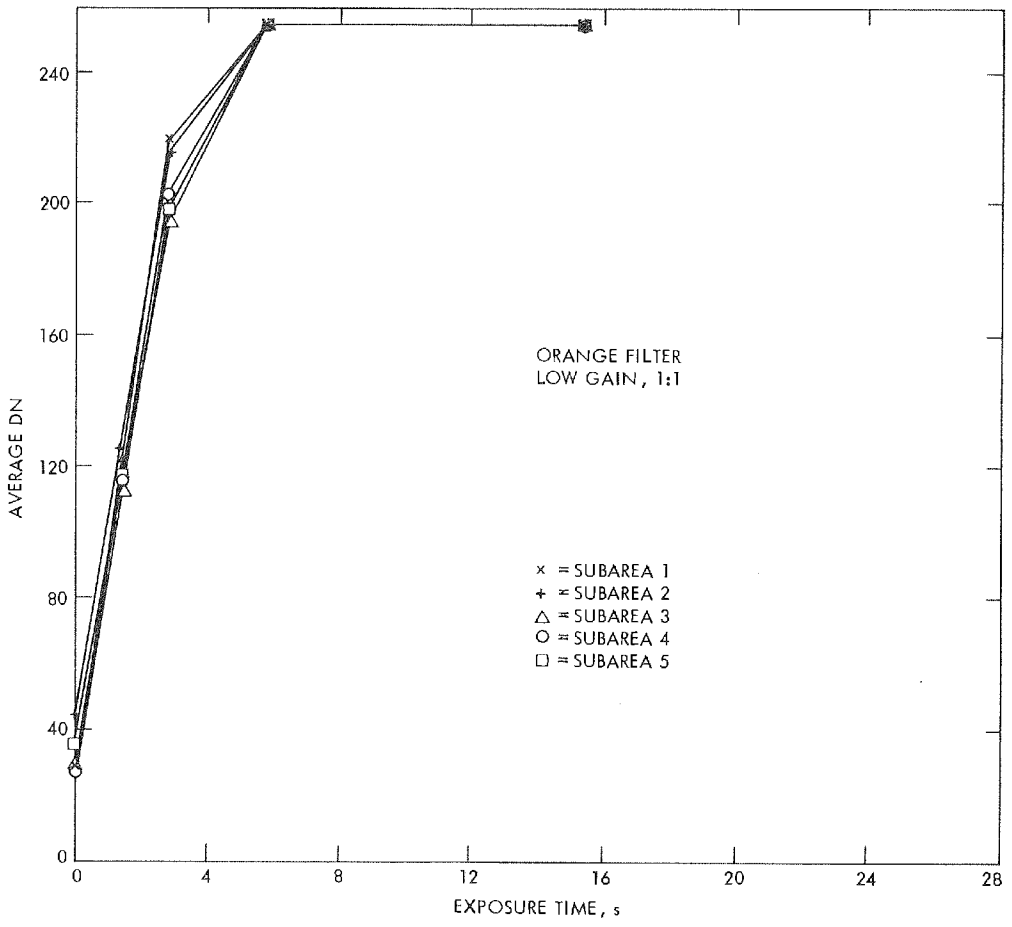

(b) ISS S/N 04

Figure 5-1 (contd)

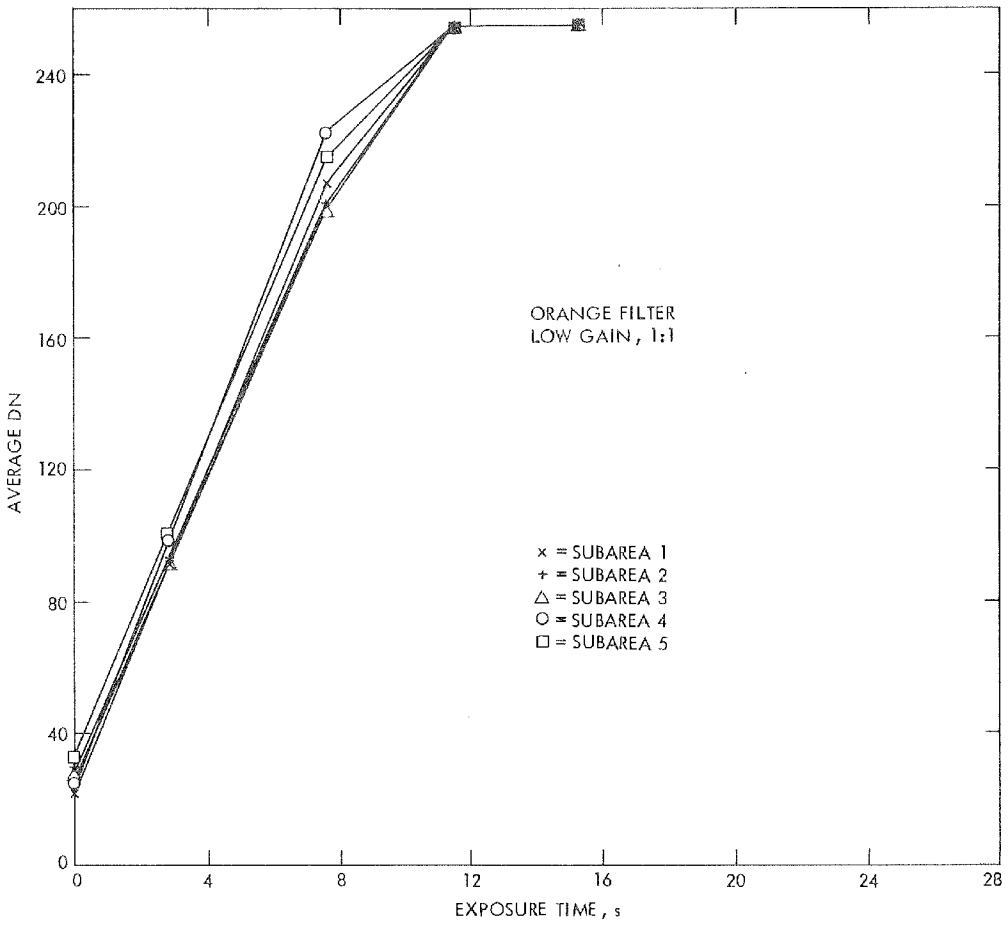

(c) ISS S/N 05

Figure 5-1 (contd)

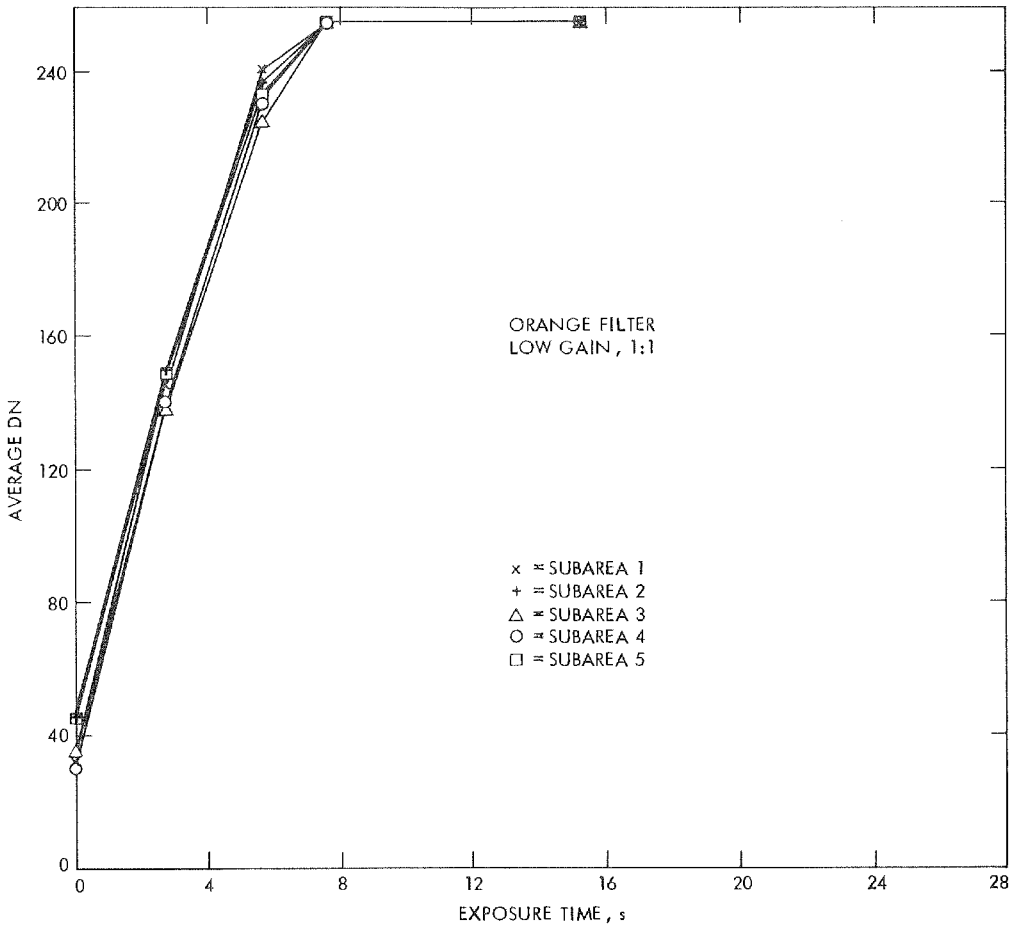

(d) ISS S/N 06

Figure 5-1 (contd)

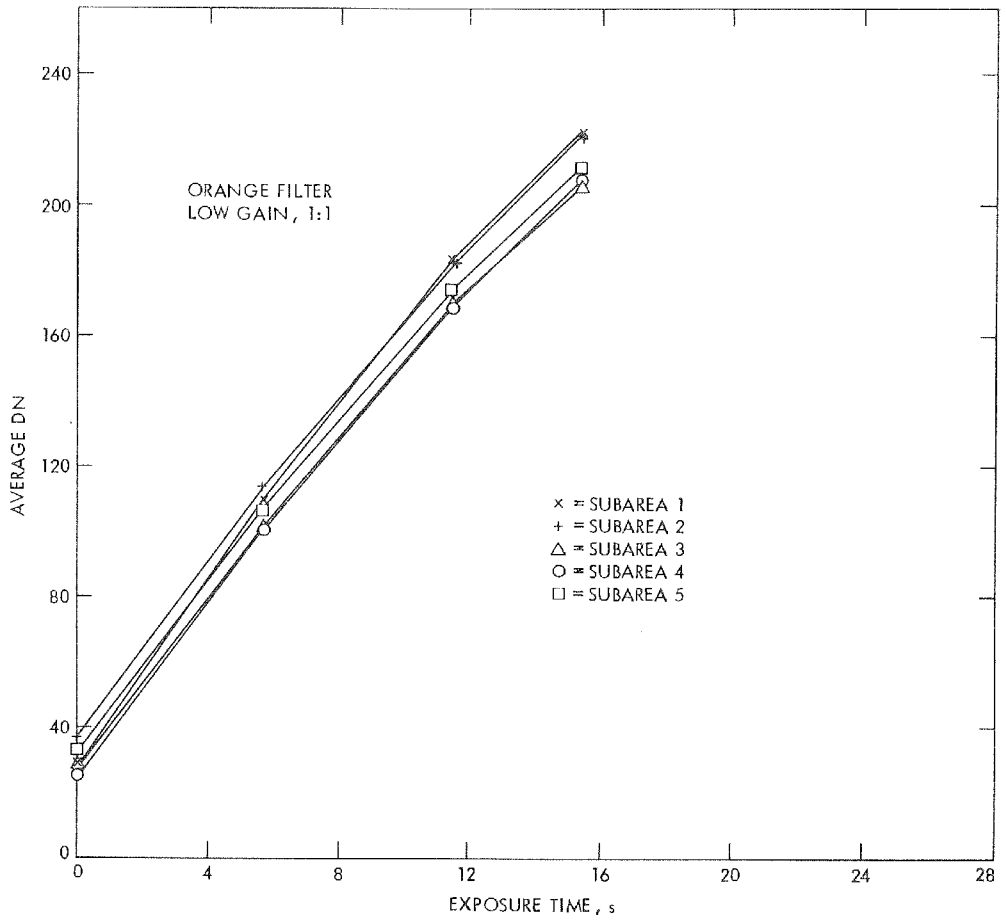

(e) ISS S/N 07

Figure 5-1 (contd)

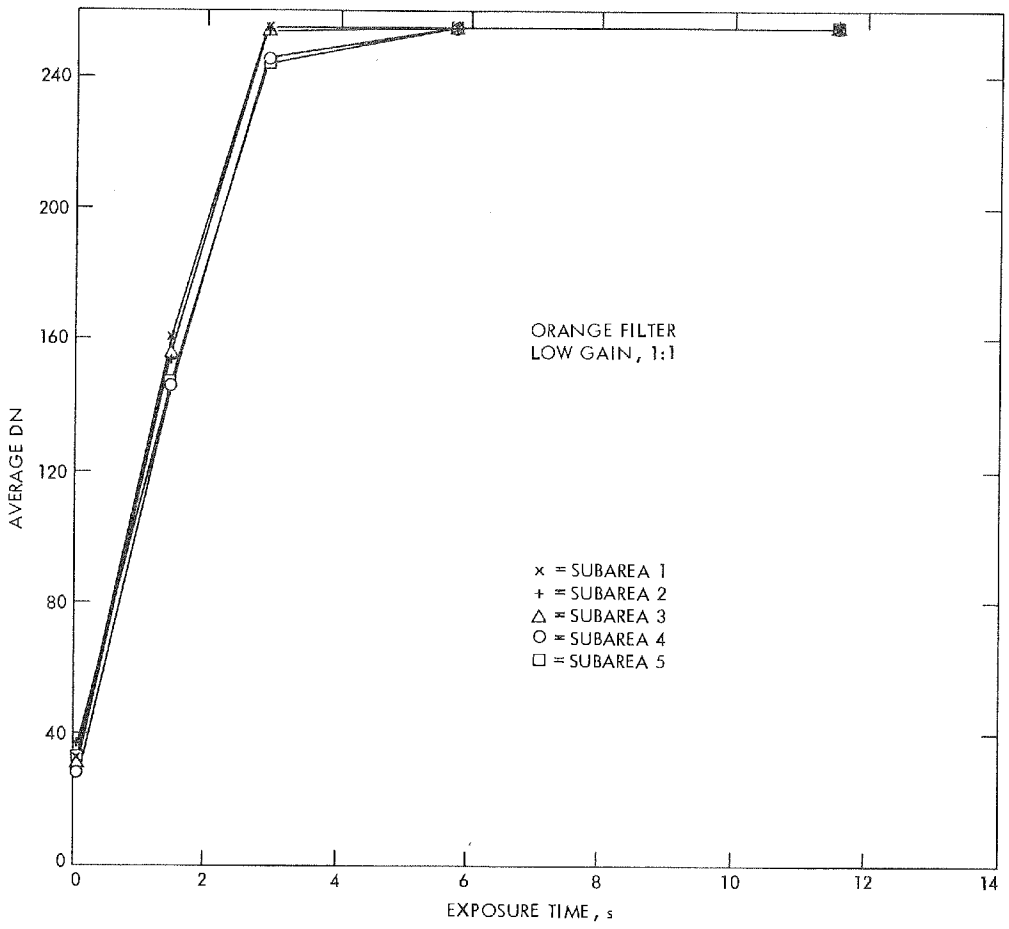

(f) ISS S/N 08

Figure 5-1 (contd)

Inasmuch as the boresight axis (line connecting the rear nodal point with the center reseau mark) of the narrow-angle camera defines the L-vector of the Voyager spacecraft, all that was necessary was to determine the cone (elevation) and cross-cone (azimuth) component of the wide-angle camera boresight-axis offset with respect to the narrow-angle camera.

The obtained results are summarized in Table 5-1, and they are all well within the required ±8.0 min/arc accuracy limit. However, it should be noted that only ISS S/N 06 deviations were actually measured at the ETR at Cape Canaveral, Florida. The ISS S/N 04 wide-angle camera replaced the original ISS S/N 08 camera shortly before the launch. This was an emergency action, which did not leave any time for the final alignment verification measurements. Consequently, the JPL SAF results, obtained when the ISS cameras were mounted on the PTM spacecraft, were used as final. Naturally, this invalidates to some degree the standard errors shown, but JPL experience indicates that such an operation usually changes the offset angles less than 1.0 min/arc (0.3 mrad).

The cone and cross-cone deviations documented in Table 5-1 are very important, but nevertheless they do not present the full story. The Voyager POINTER program requires the knowledge of nine standard vidicon format points (see Section IV-B-1 for their definition), which include not only the boresight-axis angular offset, but also the twist of the vidicon reseau grid. Therefore, the vectors of all these nine points were calculated and then rotated into their proper projected position.

The results obtained are summarized in Table 5-2. Point 5 of the narrow-angle cameras (boresight axis ≡ L-vector) was deliberately set to cone = 90 deg and cross-cone = 90 deg. The additional point 10 (point 5′ in Figure 4-61, Section IV-B-1) is the principal point (optical axis ≡ vidicon normal), which may be used for certain photogrammetric evaluations.

Table 5-1. ISS wide-angle camera boresight-axis offset

(a) Voyager 1

ISS S/N	Cone (elevation) offset, min/arc	Cross-cone (azimuth) offset, min/arc
07	Zero (L-vector)	Zero (L-vector)
06	+1.06 ±0.58	+3.09 ±0.65

(b) Voyager 2

ISS S/N	Cone (elevation) offset, min/arc	Cross-cone (azimuth) offset, min/arc
05	Zero (L-vector)	Zero (L-vector)
04	-0.52 ±0.55	-3.95 ±0.62

Table 5-2. Scan-platform alignment of ISS cameras

(a) Voyager 1

ISS S/N 07 (narrow-angle camera)			ISS S/N 06 (wide-angle camera)		
Vidicon format points (projected)	Cone angle (elevation), deg	Cross-cone angle (azimuth), deg	Vidicon format points (projected)	Cone angle (elevation), deg	Cross-cone angle (azimuth), deg
1	89.7933	89.7920	1	88.4878	88.4955
2	90.0007	89.7927	2	90.0312	88.5083
3	90.2082	89.7934	3	91.5750	88.5222
4	89.7926	89.9993	4	88.4745	90.0382
5 ≡ L-Vector	90.0000	90.0000	5	90.0178	90.0516
6	90.2075	90.0007	6	91.5616	90.0650
7	89.7919	90.2067	7	88.4611	91.5810
8	89.9993	90.2074	8	90.0044	91.5949
9	90.2068	90.2081	9	91.5483	91.6077
10	89.9939	90.0018	10	89.9927	90.0594

(b) Voyager 2

ISS S/N 05 (narrow-angle camera)			ISS S/N 04 (wide-angle camera)		
Vidicon format points (projected)	Cone angle (elevation), deg	Cross-cone angle (azimuth), deg	Vidicon format points (projected)	Cone angle (elevation), deg	Cross-cone angle (azimuth), deg
1	89.7921	89.7936	1	88.4521	88.3888
2	89.9993	89.7929	2	89.9947	88.3917
3	90.2065	89.7922	3	91.5375	88.3957
4	89.7928	90.0007	4	88.4489	89.9308
5 ≡ L-Vector	90.0000	90.0000	5	89.9914	89.9341
6	90.2072	89.9993	6	91.5342	89.9374
7	89.7935	90.2080	7	88.4450	91.4725
8	90.0007	90.2073	8	89.9881	91.4764
9	90.2079	90.2066	9	91.5309	91.4791
10	89.9933	89.9978	10	89.9731	89.9722